IMPROVED TURBULENCE MODELS BASED ON LARGE EDDY SIMULATION

OF HOMOGENEOUS, INCOMPRESSIBLE, TURBULENT FLOWS

by

J. Bardina

J. H. Ferziger

and

W. C. Reynolds

NASA-CR-166541
19840009460

Report No. TF-19

Thermosciences Division
Department of Mechanical Engineering
Stanford University
Stanford, California

May 1983

IMPROVED TURBULENCE MODELS BASED ON LARGE EDDY SIMULATION

OF HOMOGENEOUS, INCOMPRESSIBLE, TURBULENT FLOWS

by

J. Bardina, J. H. Ferziger, and W. C. Reynolds

Technical Report No. TF-19

Thermosciences Division
Department of Mechanical Engineering
Stanford University
Stanford, California 94305

May 1983

This Page Intentionally Left Blank

Acknowledgments

Abstract

The physical bases of large eddy simulation and the subgrid scale modeling it employs are studied in some detail. This investigation leads to a new scale-similarity model for the subgrid-scale turbulent Reynolds stresses. "Exact" tests of this model based on results of full simulations of homogeneous turbulent flows show that it correlates well with the subgrid-scale Reynolds stresses but does not correlate well with eddy viscosity models. This model is not dissipative; to obtain all of the desired properties, one needs to take a combination of this model with an eddy viscosity model. Tests of the combined model yield better correlations than a pure eddy viscosity model. The model also performs better in large eddy simulations.

A "defiltering" method for large eddy simulation has also been developed; it can predict accurately the full turbulent kinetic energy from the properties of large eddies and thus allows us to compare simulation results against experimental data. This method has been tested against experimental data for homogeneous turbulence with excellent results.

The effects of system rotation on isotropic turbulence have been studied, and apparently contradictory experimental results are explained. The main effect of rotation is to increase of the transverse length scales in the rotation direction, which results in a decrease of the rate of dissipation. Experimental results are shown to be affected by conditions at the turbulence-producing grid, which make the initial states a function of the rotation rate. A two-equation model which accounts for these effects of rotation has been proposed. This model predicts all of the experimental results accurately.

Large eddy simulations of homogeneous shear flows have been carried out with and without the scale-similarity model. The turbulence kinetic energy of Champagne, Harris, and Corrsin (1970) is predicted accurately. The large eddy simulation results presented are intended to complement the data. A closure Reynolds stress model for these flows has been proposed. This model compares well with experimental data and other turbulence models in homogeneous turbulence. Unlike previous models, this model accounts for the effects of system rotation.

Large eddy simulations of homogeneous shear flows with system rotation have been carried out. The results agree in general with those obtained by linear theory and other methods. However, two limiting cases with Richardson number zero which are predicted identically by linear theory are shown to be different. In these cases, nonlinear interactions cause significant changes in the statistical properties of the flows.

Table of Contents

List of Figures

Nomenclature

A_{ij} Mean velocity gradient tensor.

B_{ij} Coordinate transformation tensor, Section 2.2, Eqs. (2-8), (2-16), and (2-21).

b_{ij} Time-averaged Reynolds stress anisotropy tensor, Eq. (8-7),

$$\langle \tilde{u}_i \tilde{u}_j \rangle / \langle \tilde{u}_k \tilde{u}_k \rangle - \delta_{ij}/3$$

c Model constant, Eq. (4-15).

c_1 Model constant, Eqs. (7-8) and (8-8).

c_2 Model constant, Eqs. (7-8) and (8-8).

c_3 Model constant, Eq. (8-8).

c_4 Model constant, Eq. (8-7).

c_f Model constant, Eqs. (5-10) and (5-12).

c_m Model constant, Eqs. (6-10) and (6-14).

c_{p1} Model constant, Eq. (8-7).

c_{p2} Model constant, Eq. (8-7).

c_{p3} Model constant, Eq. (8-7).

c_q Model constant, Eqs. (6-10), (6-11), (6-14), and (6-24).

c_r Model constant, Eqs. (6-20), (6-30), and (6-33).

c_s Model constant, Eqs. (4-6), (6-6), (6-22), (6-26), and (6-32).

c_v Model constant, Eqs. (4-7) and (6-23).

c_z Model constant, Eq. (6-27).

D_{ij} Model tensor, Eq. (8-10).

d_{ij} Model tensor, Eq. (8-13).

E Three-dimensional energy spectrum of the full flow field.

E_f Three-dimensional energy spectrum of the filtered flow field, Eq. (2-51).

E_{SGS} Turbulent kinetic energy of subgrid scale flow field, Eq. (9-3).

G Filter function, Eqs. (2-31) and (2-32).

$\underline{k}$	Wave vector.
k_i	Component of the wave vector in the i-direction.
k	Wave number $(k_1^2 + k_2^2 + k_3^2)^{1/2}$.
L	Length scale of the large eddies of the full flow field, Eqs. (5-4) and (5-6).
L_f	Length scale of the large eddies of the filtered flow field, Eqs. (5-5) and (5-6).
$L_{ij,k}$	Integral length scale based on the two-point correlation of the velocities u_i and u_j in the k-direction.
L_1	Length of the computational box, Eqs. (2-44) and (2-45).
ℓ	Mixing length, Eqs. (9-1) and (9-3)
ℓ_o	Mixing length when $Ri = 0$, Eq. (9-1).
M	Experimental turbulence-generating grid size.
M_{ij}	Subgrid scale model tensor, Eqs. (2-39), (6-19), (6-10), (6-29), (6-30), (6-31), and (6-33).
N	Number of grid points in each direction.
n	Exponent for the decay of isotropic turbulence, Eqs. (8-16) and (8-17).
P	Production rate of turbulent kinetic energy per unit mass for the full flow field, Eqs. (4-9), (4-10), (8-11), and (9-4).
P_f	Production rate of turbulent kinetic energy per unit mass for the filtered flow field, Eqs. (4-9) and (4-10).
P_{ij}	Production rate of Reynolds stress, Eq. (8-9).
P_{ij}	Model tensor, Eq. (8-12).
$\tilde{p}$	Total pressure, Eq. (2-1).
p''	Pressure fluctuations, Eq. (2-5).
p	$\equiv p''/\theta + \overline{u_i u_i}/3$.
$\overline{p}$	$\equiv \overline{p''}/\rho + \overline{\bar{u}_i \bar{u}_i}/3$.
Q^2	Turbulence intensity of full flow field, $\langle u_i u_i \rangle$.
Q_o^2	Q^2 at $t = 0$.
Q_f^2	Turbulence intensity of filtered flow field, $\langle \bar{u}_i \bar{u}_i \rangle$.
q^2	Turbulence intensity of subgrid scale flow field, $Q^2 - Q_f^2$.

q_f^2 Turbulence intensity of the smaller eddies of the filtered flow field, Eqs. (6-10)-(6-14) and (6-19)-(6-26).

q_m^2 Turbulence intensity of the smaller eddies of the subgrid scale flow field, Eq. (6-10).

R Rotation rate, Eq. (9-5).

Ri Richardson number, Eq. (9-2)

R_{ij} Time-averaged Reynolds stress tensor, Section 8.4.

R_{SGS} Subgrid scale Reynolds number, $< |\overline{S}| \Delta_f/\nu >$.

R_λ Reynolds number based on transverse Taylor microscale, Eq. (8-2).

S Mean shear rate, Eq. (2-20).

S_{ij} Strain rate tensor, $\frac{1}{2}\left(\dfrac{\partial u_i}{\partial x_j} + \dfrac{\partial u_j}{\partial x_i}\right)$

$|\overline{S}|$ $\equiv (2\overline{S}_{ij}\overline{S}_{ij})^{1/2}$.

S_k Velocity-derivative skewness, Eq. (6-33).

$\tilde{t}$ Time.

t Time.

$\underset{\sim}{u}, \tilde{u}_i$ Total velocity.

$\underline{U}, U_i$ Mean velocity, $<\underline{U}>$, $<\tilde{u}_i>$.

$\underline{u}'', u_i''$ Fluctuating velocity, $\underset{\sim}{u} - \underline{U}$, $\tilde{u}_i - U_i$.

$\overline{\underline{u}}, \overline{u}_i$ Fluctuating velocity, Eq. (2-10).

$\overline{\underline{u}}, u_i$ Fluctuating velocity, Eq. (2-31).

$\underline{u}', u_i$ Subgrid-scale velocity, $\underline{u} - \overline{\underline{u}}$, $u_i - \overline{u}_i$.

$\overline{\overline{\underline{u}}}, \overline{\overline{u}}_i$ Velocity of larger or twice-filtered flow field, Diagram 6.2.

$\overline{\underline{u}}', \overline{u}_i'$ Velocity of smaller eddies of the filtered flow field, Eq. (6-7).

$\overline{\underline{u}}', \overline{u}_i'$ Velocity of larger eddies of subgrid-scale flow field, or filtered subgrid-scale flow field, Eq. (6-9).

$\tilde{x}_i$ Spatial coordinate of fixed frame.

x_i Spatial coordinate of moving frame.

Greek Letters

α Magnitude of rotation and shear rates defined in Table 9.1.

β Mixing length constant, Eq. (9-1).

Γ Mean strain rate, Section 8.4 and Eq. (9-5).

γ Exponent for homogeneous shear flows in rotating system, Eq. (9-5).

Δ Grid spacing.

Δ_f Filter width, 2Δ.

δ_{ij} $\equiv \begin{cases} 1, & i = j \\ 0, & i \neq j \end{cases}$

ϵ Dissipation rate of turbulent kinetic energy per unit mass for full flow field.

ϵ_o ϵ at $t = 0$.

ϵ_f Dissipation rate of turbulent kinetic energy per unit mass for filtered flow field.

ϵ_{fo} ϵ_f at $t = 0$.

ϵ_{ij} Dissipation rate of time-averaged Reynolds stress tensor, Eq. (7-1).

η Kolmogorov length scale, Eq. (6-3).

λ Transverse Taylor microscale of the velocity field in the mean flow direction.

$\lambda_{ij,k}$ Taylor microscale of the velocity field in k-direction

$$(< \overline{u}_i^2 > / < (\partial \overline{u}_i / \partial x_j^2) >)^{1/2} \quad \text{(no index summation)}$$

$\lambda_{ij,kf}$ Taylor microscale of the filtered velocity field in k-direction

$$(< \overline{u}_i^2 > / < (\partial \overline{u}_i / \partial x_j^2) >)^{1/2} \quad \text{(no index summation)}$$

ν Kinematic viscosity.

ν_τ Eddy viscosity.

ρ Density.

σ Dimensionless frequency, Eq. (7-4).

ϕ_{ij} Pressure-strain tensor, Eq. (7-1).

$\underline{\Omega}$ System rotation vector.

Ω Magnitude of system rotation vector, $\left|\underline{\Omega}\right|$.

Ω_{ij} Rotation rate tensor, $\dfrac{1}{2}\left(\dfrac{\partial U_i}{\partial \tilde{x}_j} - \dfrac{\partial U_j}{\partial \tilde{x}_i}\right)$.

$\bar{\omega}_i$ Vorticity vector of the filtered flow field.

$\left|\bar{\omega}\right|$ $\equiv \left(\bar{\omega}_i\bar{\omega}_i\right)^{1/2}$.

Other Symbols

$\langle \ \rangle$ Spatial or time average.

$\overline{(\ \ )}$ Filtered value.

$(\ )^*$ Complex conjugate.

Chapter I

INTRODUCTION

1.1 Motivation

The variety of turbulent flows is enormous, and knowledge of them has important engineering applications. Despite a century of work on turbulence, its behavior is not well understood.

The basic equations that govern turbulent flows are known, namely, those of conservation of mass, momentum, and energy. Due to their complexity, most information about turbulent flows is obtained from experiments. However, the increasing availability of large scientific computers has made numerical simulation of turbulent flows possible. The results of these simulations can be regarded as numerical experiments which add to the understanding of turbulence gained through laboratory experiments. The aim of this work is to use three-dimensional numerical simulations of turbulent flows to increase understanding of turbulence phenomena.

The large range of length and time scales present in turbulent flows makes full simulation of them impossible, except at low Reynolds numbers. To date, valid simulations of homogeneous turbulent flows at Reynolds numbers (based on the Taylor microscale) of less than 70 have been fully simulated (Orszag et al., 1971; Clark et al., 1977; Rogallo, 1980, 1981; Feiereisen et al., 1981; Shirani et al., 1981). Furthermore, these simulations require large, fast computers, such as the ILLIAC IV or CRAY-1. Since mean rotation, strain, and/or shear cause the size of the large eddies to increase more rapidly and to develop anisotropy, full simulations of flows containing these effects are limited to even smaller Reynolds numbers.

Experimental evidence indicates that the larger eddies of turbulence are flow-dependent, while the smaller ones are more universal. The larger eddies are responsible for most of the production, convection, and redistribution of the energy, while the smaller eddies are mainly responsible for the dissipation of the energy. These observations lead to the conclusion that large-eddy simulation (LES), which

resolves the large eddies and models the small ones, is an attractive and less expensive alternative to full simulation (Smagorinsky, 1963; Deardorff, 1970; Kwak et al., 1975; Shaanan et al., 1975; Mansour et al., 1978; Cain et al., 1981; Antonopoulos, 1981). The assumptions about the small eddies are not entirely correct in wall-bounded flows; however, LES has been successfully applied to channel and annular flows (Schumann, 1973; Grotzbach, 1976; Moin et al., 1978, 1981; Kim et al., 1980).

Most large eddy simulations have used simple eddy-viscosity models to model the small eddies of the turbulence. These models can produce the correct average energy removal from the large eddies, but they poorly represent the effects of the small eddies on the large eddies on a local basis (Clark et al., 1977; McMillan et al., 1979, 1980; Bardina et al., 1980). Thus, there is a need for improvement in modeling for LES.

A drawback of LES is that it does not compute the full turbulent flow field. Since experiments do provide the full turbulence quantities, comparisons between LES and experimental results can be difficult. A "defiltering" method which enables us to compare complete statistical quantities from LES and thus allow accurate comparison with experimental observations is required.

Simpler methods of predicting turbulent flows are usually used for practical applications. The most complex methods in common use at the present time are one-point closure methods. In these methods, time-averages at a single spatial point are computed, and all of the scales of the turbulence need to be modeled. There is a wide variety of such models; they can be classified according to the number of differential equations used in the model. Current state-of-the-art models are capable of predicting many flows with reasonable accuracy. The 1980-81 AFOSR-HTTM-Stanford Conference on Complex Turbulent Flows (Kline et al., 1981) showed some of the strong points as well as the shortcomings of these models. None of the models presented had any provision for the effects of mean rotation. As rotation affects many turbulent flows of technological significance, a model which accounts for it is a necessity.

2

1.2 Objectives

The main objectives of this research are:

1) to study the validity of existing subgrid scale models for large-eddy simulation;

2) to develop improved subgrid scale models;

3) to find methods of computing the complete one-point average quantities from large-eddy simulation results; and

4) to use the results of numerical simulations to improve one-point-closure turbulence models for flows with mean rotation.

The basic assumptions of large-eddy simulation will be analyzed. This analysis will lead to a method of predicting full turbulence quantities from large-eddy simulations. This analysis leads to consideration of the scales of the turbulence involved in the transfer of energy between the large and small eddies. In turn, this allows us to better understand subgrid scale models for large-eddy simulation and leads to the development of new subgrid scale models called scale-similarity models. These models shall be tested by using full simulations of homogeneous turbulence and by using them in large-eddy simulations.

Large-eddy simulations will be used to provide better understanding of the physical effects of rotation and shear on the turbulence. We shall use this knowledge to develop a one-point closure turbulence model which accounts for the effects of rotation. This model shall be tested against experimental observations of homogeneous turbulent flows.

Cases studied include isotropic turbulence, mean rotation and mean shear applied to initially isotropic turbulence, and mean shear of turbulence in a rotating coordinate frame.

Chapter II

MATHEMATICAL FORMULATION AND NUMERICAL METHOD

This chapter describes the governing system of equations and the numerical method used to simulate homogeneous turbulent shear flows in a rotating frame. This method is also able to simulate homogeneous isotropic turbulent flows and homogeneous turbulence in the presence of rotation and/or shear.

2.1 Mathematical Formulation

The basic equations of motion for an incompressible fluid having constant viscosity are the Navier-Stokes and Continuity equations:

$$\frac{\partial \tilde{u}_i}{\partial \tilde{t}} + \frac{\partial \tilde{u}_i \tilde{u}_j}{\partial \tilde{x}_j} = -\frac{1}{\rho} \frac{\partial \tilde{p}}{\partial \tilde{x}_i} + \nu \frac{\partial^2 \tilde{u}_i}{\partial \tilde{x}_j \partial \tilde{x}_j} \qquad (2\text{-}1)$$

$$\frac{\partial \tilde{u}_j}{\partial \tilde{x}_j} = 0 \qquad (2\text{-}2)$$

where $i,j = 1, 2, 3,$ and repeated indices in any term imply summation.

We are interested in flows in which both the statistical properties of the turbulent fluctuations and the gradients of the mean velocity are homogeneous, i.e., independent of position in the flow.

For homogeneous flows, the mean velocity field U_i must be linear in the spatial coordinates:

$$\langle \tilde{u}_i \rangle \equiv U_i = A_{ij} \tilde{x}_j \qquad (2\text{-}3)$$

where the tensor A_{ij} is constant or, possibly, a function of time.

The basic equations of motion for the turbulent component of the flow field are obtained by decomposing the flow quantities $(\tilde{u}_i \tilde{p})$ into mean $(U_i, \langle \tilde{p} \rangle)$ and fluctuating parts:

$$u_i'' = \tilde{u}_i - U_i \qquad (2\text{-}4)$$

5

$$p'' = \tilde{p} - \langle \tilde{p} \rangle \qquad (2\text{-}5)$$

Substituting these into the equations of motion and subtracting the mean equations, noting that $\partial \langle u_i'' u_j'' \rangle / \partial \tilde{x}_j = 0$ due to the assumption of homogeneity of the turbulence, we obtain the following equations for the fluctuating components:

$$\frac{\partial u_i''}{\partial \tilde{t}} + U_j \frac{\partial u_i''}{\partial \tilde{x}_j} + \frac{\partial u_i'' u_j''}{\partial \tilde{x}_j} + A_{ij} u_j'' = -\frac{1}{\rho} \frac{\partial p''}{\partial \tilde{x}_i} + \nu \frac{\partial^2 u_i''}{\partial \tilde{x}_j \partial \tilde{x}_j} \qquad (2\text{-}6)$$

$$\frac{\partial u_j''}{\partial \tilde{x}_j} = 0 \qquad (2\text{-}7)$$

There is no exact analytical solution of the equations of motion for the turbulence fluctuations, and numerical approximations are required. In particular, the simulations will be carried out in a finite domain with specified boundary and initial conditions; these are described in Sections 2.7 and 2.10, respectively. In this section, we shall only mention that we have chosen to apply a coordinate transformation to the equations of motion in order to permit use of periodic boundary conditions. Another option could have been to specify some sort of random boundary conditions, but the assumption of homogeneity of the turbulence fluctuations imposes too many restrictions and makes this difficult even in the simplest (statistically) case of isotropic turbulence, for which $A_{ij} = 0$. Therefore, we prefer to use periodic boundary conditions. This cannot be done to Eq. (2-6), because the coefficient U_j is not constant in space. A coordinate transformation which transforms these equations into a system with constant coefficients is described in the next section. These equations admit periodic boundary conditions.

2.2 Coordinate Transformation

The coordinate transformation required to admit periodic solutions is based on Batchelor's (1953) rapid distortion theory. This transformation was first applied to the solution of the incompressible Navier-Stokes equations by Rogallo (1977) and, more recently, it was used by Rogallo (1981), Feiereisen et al. (1981), and Shirani et al. (1981). This transformation transforms the fixed coordinate system $(\underset{\sim}{x})$ into a

6

convected coordinate system $(\underline{x})$; i.e., one moving with the mean velocity field.

The transformation is represented by

$$x_i = B_{ij}(t)\, \tilde{x}_j \tag{2-8}$$

and

$$t = \tilde{t} \tag{2-9}$$

where the tensor B_{ij} is only a function of time and the magnitude of the constant mean velocity gradient. The velocity field u_i'' is transformed by:

$$u_i'' = B_{ij}^{-1} u_j \tag{2-10}$$

which, together with the coordinate transformation (2-8), implies that the continuity equation (2-7) becomes

$$B_{kj} \frac{\partial B_{jn}^{-1} u_n}{\partial x_k} = 0 \tag{2-11}$$

or simply

$$\frac{\partial u_j}{\partial x_j} = 0 \tag{2-12}$$

because the tensor B_{ij} is independent of the spatial coordinates and $B_{ij} B_{jn}^{-1} = \delta_{in}$.

Under these transformations, Eqs. (2-8), (2-9), and (2-10), the momentum equations (2-6) become:

$$\left(B_{ik}^{-1} \frac{\partial u_k}{\partial t} + B_{ik}^{-1} \frac{dB_{nj}}{dt} \tilde{x}_j \frac{\partial u_k}{\partial x_n} + \frac{dB_{ik}^{-1}}{dt} u_k + B_{ik}^{-1} \frac{\partial u_k u_j}{\partial x_j} \right) +$$

$$+ \left(B_{ik}^{-1} B_{n\ell} A_{\ell j} \tilde{x}_j \frac{\partial u_k}{\partial x_n} \right) + \left(A_{ij} B_{jk}^{-1} u_k \right) = \tag{2-13}$$

$$= - \left(\frac{1}{\rho} B_{ji} \frac{\partial p''}{\partial x_j} \right) + \left(\nu\, B_{ik}^{-1} B_{\ell j} B_{nj} \frac{\partial^2 u_k}{\partial x_\ell \partial x_n} \right)$$

where the terms in parentheses are in one-to-one correspondence with the terms of Eq. (2-6). Multiplying Eq. (2-13) by the tensor B_{ri},

7

rearranging terms, and interchanging the names of the dummy indices r and i, we get

$$\frac{\partial u_i}{\partial t} + \frac{\partial u_i u_j}{\partial x_j} + \left(\frac{dB_{nj}}{dt} + B_{n\ell}A_{\ell j}\right) \tilde{x}_j \frac{\partial u_i}{\partial x_n} +$$

$$+ B_{ir}\left(\frac{dB_{rk}^{-1}}{dt} + A_{rj}B_{jk}^{-1}\right) u_k = -\frac{1}{\rho} B_{ir}B_{jr}\frac{\partial p''}{\partial x_j} + \nu\, B_{\ell j}B_{nj}\frac{\partial^2 u_i}{\partial x_\ell \partial x_n} \qquad (2\text{-}14)$$

Following Rogallo (1977), the transformation tensor B_{ij} is chosen to be the solution of the following set of ordinary differential equations:

$$\frac{dB_{ij}}{dt} + B_{ik}A_{kj} = 0 \qquad (2\text{-}15)$$

subject to the convenient initial conditions:

$$B_{ij} = \delta_{ij} \quad \text{at} \ \ t = 0 \qquad (2.16)$$

Thus, the coefficient of the third term of Eq. (2-14) is made zero. The fourth term of Eq. (2-14) can also be simplified by noting that

$$B_{ij}B_{jk}^{-1} = \delta_{ik} \qquad (2\text{-}17)$$

Differentiating by parts with respect to time, we get

$$B_{ij}\frac{dB_{jk}^{-1}}{dt} + \frac{dB_{ij}}{dt}B_{jk}^{-1} = 0 \qquad (2\text{-}18)$$

Multiplying times the tensor B_{ri}^{-1} gives

$$\frac{dB_{rk}^{-1}}{dt} + B_{ri}^{-1}\frac{dB_{ij}}{dt}B_{jk}^{-1} = 0 \qquad (2\text{-}19)$$

and combining with Eq. (2-15), we get:

$$\frac{dB_{rk}^{-1}}{dt} - A_{rj}B_{jk}^{-1} = 0 \qquad (2\text{-}20)$$

Therefore, the momentum equation (2-14) becomes:

$$\frac{\partial u_i}{\partial t} + \frac{\partial u_i u_j}{\partial x_j} + 2B_{ir}A_{rj}B_{jk}^{-1}u_k = -\frac{1}{\rho}B_{ir}B_{jr}\frac{\partial p''}{\partial x_j} + \nu\, B_{\ell j}B_{nj}\frac{\partial^2 u_i}{\partial x_\ell \partial x_n} \qquad (2\text{-}21)$$

8

which has constant coefficients in space and therefore admits periodic solutions.

2.3 Homogeneous Rotating Flow

Here, the linear transformation of the preceding section is particularized to the case of a constant rate of rotation (Ω) about the x_3-axis.

The mean velocity gradients for this case are

$$A_{ij} = \Omega\left(-\delta_{i1}\delta_{j2} + \delta_{i2}\delta_{j1}\right) \tag{2-22}$$

The transformation tensor obtained by solving Eqs. (2-15) and (2-16) is:

$$B_{ij} = \begin{pmatrix} \cos\Omega t & \sin\Omega t & 0 \\ -\sin\Omega t & \cos\Omega t & 0 \\ 0 & 0 & 1 \end{pmatrix} \tag{2-23}$$

and the system of equations in a rotating frame is:

$$\frac{\partial u_i}{\partial x_i} = 0 \tag{2-24}$$

$$\frac{\partial u_i}{\partial t} + \frac{\partial\left(u_i u_j - \frac{1}{3} u_k u_k \delta_{ij}\right)}{\partial x_j} = -\frac{\partial P}{\partial x_i} + 2\Omega\left(u_2\delta_{i1} - u_1\delta_{i2}\right) + \nu\frac{\partial^2 u_i}{\partial x_j\partial x_j} \tag{2-25}$$

where the reduced pressure P is

$$P = \frac{p}{\rho} + \frac{u_k u_k}{3} \tag{2-26}$$

The second term on the right-hand side of Eq. (2-25) represents the Coriolis force. The centrifugal force is compensated by mean pressure gradients (see Greenspan, 1968, pp. 5-6).

9

2.4 Homogeneous Shear Flow in a Rotating Frame

Here, the linear transformation is particularized to the case of a constant shear rate in the rotating frame of the previous section. We thus obtain the equations describing homogeneous shear flow in a rotating frame, which is an idealization of turbulent flows that occur in geophysics, oceanography, and turbomachinery. We emphasize that these equations do not represent a flow with rotation and shear in a fixed frame. Equations for this case can be obtained directly from Eqs. (2-21).

The mean-velocity gradients in the rotating frame are:

$$A_{ij} = S \, \delta_{i1} \delta_{j2} \tag{2-27}$$

The transformation tensor obtained by solving Eqs. (2-15) and (2-16) is:

$$B_{ij} = \begin{pmatrix} 1 & -St & 0 \\ 0 & 1 & 0 \\ 0 & 0 & 1 \end{pmatrix} \tag{2-28}$$

The system of equations for the fluctuating components of the velocity with respect to the convective frame is obtained by applying the velocity decomposition and linear transformations to Eqs. (2-24) and (2-25). The only significant differences between Eqs. (2-24) and (2-25) and the original system of equations (2-1) and (2-2) are the terms representing the effects of the coriolis force in Eqs. (2-25). However, these terms are not affected by the coordinate transformation, because they are linear in the velocity components; they are affected only by the velocity transformation, Eq. (2-10), which is a straightforward transformation. Therefore, the system of equations with respect to the convective frame is obtained from Eqs. (2-12) and (2-21) directly, except for the coriolis force terms, whose fluctuating components transform according to Eq. (2-10). Consequently, Eq. (2-25) becomes:

$$\frac{\partial u_i}{\partial t} + \frac{\partial \left(u_i u_j - \frac{1}{3} u_k u_k \delta_{ij} \right)}{\partial x_j} =$$

$$= -\frac{\partial P}{\partial x_j} \left[\delta_{ij} - St \delta_{i1} \delta_{j2} - St \delta_{i2} \delta_{j1} + s^2 t^2 \delta_{i1} \delta_{j1} \right]$$

$$+ \left[2(\Omega - S) u_2 + 2\Omega St (u_1 + St\ u_2) \right] \delta_{i1}$$

$$- 2\Omega (u_1 + St\ u_2) \delta_{i2}$$

$$+ \nu \frac{\partial u_i}{\partial x_j \partial x_k} \left(\delta_{jk} - 2St\ \delta_{j1} \delta_{k2} + s^2 t^2 \delta_{j1} \delta_{kl} \right) \quad (2-29)$$

which are to be solved together with the continuity equation (2-24).

This system of equations contains as special cases homogeneous isotropic turbulence ($S = \Omega = 0$), homogeneous rotating turbulence ($S = 0$), and homogeneous shear flows ($\Omega = 0$), where Ω is the frame rotation and S is the mean shear rate in the rotating frame.

2.5 Definition of Filtered and Subgrid-Scale Fields

In large-eddy simulation, each flow variable is decomposed in a filtered (or large-scale) component and a residual (or subgrid-scale SES) This decomposition is represented as:

$$\underline{u} = \underline{\bar{u}} + \underline{u}' \quad (2-30)$$

where the large-scale component is defined according to Leonard (1974) as:

$$\underline{\bar{u}}(\underline{x}) = \int G(\underline{x} - \underline{y}; \Delta_f)\ \underline{u}(\underline{y})\ d\underline{y} \quad (2-31)$$

and the integral extends over the whole flow field, $G(\underline{x} - \underline{y}; \Delta_f)$ is the filter function, and Δ_f is the width or characteristic length scale of the filter.

The selection of the filter function is an important step in large-eddy simulation. Kwak et al. (1975) analyzed several filter functions and found that a Gaussian filter is physically and mathematically convenient; we shall adopt it. The energy in the filtered flow field is a function of the filter width and the Reynolds number and is often less

11

than half the total energy (Kwak et al., 1975), Shaanan et al., 1975).
Calculation of the full-energy spectrum from the filtered-energy spectrum is unreliable, because the process amplifies numerical errors excessively. However, the Gaussian filter is smooth and produces filtered energy spectra similar to the energy spectra of flows at lower Reynolds numbers and makes the filtered velocity field behave like a real flow field. Also, unlike sharp filters, which may lead to an initial reduction of the length scales in homogeneous turbulence, Gaussian filters always produce growth of the large-length scales.

The Gaussian filter is:

$$G(\underline{x} - \underline{y}; \Delta_f) = \left(\sqrt{\frac{6}{\pi}} \frac{1}{\Delta_f}\right)^3 \exp\left(-6(\underline{x} - \underline{y})^2/\Delta_f^2\right) \qquad (2\text{-}32)$$

2.6 Governing Equations of the Filtered Flow Field

The governing equations of the filtered flow field are obtained by applying the filter function, Eq. (2-32) to the equations of motion of the full field, Eqs. (2-24) and (2-29). The resulting equations are:

$$\frac{\partial \overline{u}_i}{\partial t} = H_i - \frac{\partial \overline{P}}{\partial x_j}\left(\delta_{ij} - St\,\delta_{i1}\delta_{j2} - St\,\delta_{i2}\delta_{j1} + S^2 t^2 \delta_{i1}\delta_{j1}\right) \qquad (2\text{-}33)$$

where

$$H_i \equiv -\frac{\partial\left(\overline{\overline{u}_i\overline{u}_j} - \frac{1}{3}\overline{\overline{u}_k\overline{u}_k}\,\delta_{ij}\right)}{\partial x_j} + \left[2(\Omega\text{-}S)\,\overline{u}_2 + 2\Omega\,St\left(\overline{u}_1 + St\,\overline{u}_2\right)\right]\delta_{i1}$$

$$- 2\Omega\left(\overline{u}_1 + St\,\overline{u}_2\right)\delta_{i2} + \nu\frac{\partial^2 \overline{u}_i}{\partial x_j \partial x_k}\left(\delta_{jk} - St\,\delta_{j1}\delta_{k2} - St\,\delta_{j2}\delta_{k1} + S^2 t^2\delta_{j1}\delta_{k1}\right)$$

$$- \frac{\partial \tau_{ij}}{\partial x_j} \qquad (2\text{-}34)$$

and the SGS Reynolds stresses, τ_{ij}, are

$$\tau_{ij} = R_{ij} - \frac{1}{3}R_{kk}\delta_{ij} \qquad (2\text{-}35)$$

where

$$R_{ij} = \overline{u_i u_j} - \overline{\overline{u}_i\overline{u}_j} = \overline{u_i'u_j'} + \overline{u_i'\overline{u}_j} + \overline{\overline{u}_i u_j'} \qquad (2\text{-}36)$$

12

The continuity equation for the filtered field is:

$$\frac{\partial \overline{u}_i}{\partial x_i} = 0 \qquad (2\text{-}37)$$

It is convenient to replace the continuity equation (2-38) by a Poisson equation for the reduced pressure. The latter is obtained by taking the divergence of Eq. (2-33) and applying the continuity equation:

$$\frac{\partial^2 \overline{P}}{\partial x_i \partial x_j} \left(\delta_{ij} - 2St\, \delta_{i1}\delta_{j2} + S^2 t^2\, \delta_{i1}\delta_{j1} \right) = \frac{\partial H_i}{\partial x_i} \qquad (2\text{-}38)$$

Equations (2-33), (2-37) and (2-38) constitute a closed system of partial differential equations, except for the Reynolds stresses τ_{ij} which need to be modeled.

Models of the Reynolds stresses shall be presented and analyzed in the following chapters. For now, we note that the models represent τ_{ij} in terms of derivatives of the filtered velocity field. The models we shall investigate have the form:

$$\tau_{ij} = -2\nu_\tau S_{ij} + M_{ij} \qquad (2\text{-}39)$$

where ν_τ is an eddy viscosity, which, following Smagorinsky (1963), is given by:

$$\nu_\tau = \left(c_s \Delta_f \right)^2 \sqrt{2 S_{ij} S_{ij}} \qquad (2\text{-}40)$$

S_{ij} is the strain rate. M_{ij} will be defined later.

The governing equations now become:

$$\frac{\partial \overline{u}_i}{\partial t} = H_i - \frac{\partial \overline{P}}{\partial x_j} \left(\delta_{ij} - St\, \delta_{i1}\delta_{j2} - St\, \delta_{i1}\delta_{j1} + S^2 t^2 \delta_{i1}\delta_{j1} \right) \qquad (2\text{-}41)$$

and

$$\frac{\partial^2 \overline{P}}{\partial x_i \partial x_j} \left(\delta_{ij} - 2St\, \delta_{i1}\delta_{j2} + S^2 t^2 \delta_{i1}\delta_{j1} \right) = \frac{\partial H_i}{\partial x_i} \qquad (2\text{-}42)$$

with

13

$$H_i = -\frac{\partial \left(\overline{u_i u_j} - \frac{1}{3} \overline{u_k u_k}\, \delta_{ij} \right)}{\partial x_j} - \frac{\partial M_{ij}}{\partial x_j} +$$

$$+ \left[2(\Omega - \delta)\, \overline{u}_2 + 2\Omega\, St(\overline{u}_1 + St\, \overline{u}_2) \right] \delta_{i1} +$$

$$- 2\Omega(\overline{u}_1 + St\, \overline{u}_2)\, \delta_{i2} +$$

$$+ \frac{\partial}{\partial x_j} \left[(\nu + \nu_\tau) \frac{\partial \overline{u}_i}{\partial x_k} \left(\delta_{jk} - St\, \delta_{j1}\delta_{k2} - St\, \delta_{j2}\delta_{k1} + s^2 t^2 \delta_{j1}\delta_{k1} \right) \right]$$

$$(2\text{-}43)$$

where various models of the eddy viscosity, ν_τ, and scale-similarity models, M_{ij}, shall be considered in the next chapters.

2.7 Boundary Conditions

Numerical simulation of homogeneous turbulent flows in a finite domain requires the specification of boundary conditions. Since turbulent motions at any point of the flow affect the motions through all the domain due to the pressure field, the boundary conditions will affect all the numerical results. The choices of boundary conditions are also restricted by the assumptions of turbulence and homogeneity of the turbulent fluctuations. One option could be to specify some sort of random boundary conditions; however, turbulent motions are not random. From a statistical point of view, the assumption of homogeneity on the turbulent fluctuations implies that the mean value of functions of the turbulent fluctuations must be independent of spatial position. According to Townsend (1976), "even in the simplest (statistically) of turbulent flows--isotropic turbulence--the number of these functions necessary in the theory is large and, for normal turbulent flows whose asymmetry imposes still more organization, an even larger number seems to be necessary." Therefore, in order not to violate the assumptions of turbulence and homogeneity, it is convenient to specify the boundary conditions as functions of the variables in the numerical domain. Following previous simulations (Mansour et al., 1977; Rogallo, 1977 and 1981; Ferziger et al., 1981; Shirani et al., 1981, and many others), we have chosen to specify periodic boundary conditions; thus, the assumptions of turbulence and homogeneity are preserved. These boundary conditions are also consistent with the system of equations developed

14

earlier in this chapter. for the x_1-direction, their mathematical formulation is:

$$\underline{u}(x_1,x_2,x_3;t) = \underline{u}(x_1 + L_1,x_2,x_3;t) \qquad (2-44)$$

$$\overline{p}(x_1,x_2,x_3;t) = \overline{p}(x_1 + L_1,x_2,x_3;t) \qquad (2-45)$$

where L_1 is the length of the computational domain in the x_1-direction. Similar conditions are applied in the other two directions.

2.8 Approximation of Spatial Derivatives

Approximations which compute the spatial partial derivatives in terms of the data located at grid points in the numerical domain are required. The computational grid spacing will be uniform and half the filter width, as recommended by McMillan and Verziger (1979). Since the system of equations admits periodic solutions, we shall use the pseudo-spectral method, which has been used frequently in simulations of homogeneous turbulence and is fast and accurate. Since this method is applied independently in each direction, we shall consider only the one-dimensional case in this section. Thus, any function $u(x_j)$ is approximated by a discrete Fourier series:

$$u(x_j) = \sum_{m=-N/2+1}^{N/2} \hat{u}(k_m) e^{ik_m x_j} \qquad (2-46)$$

and its spatial derivative is given by another related discrete Fourier series:

$$\frac{\partial u}{\partial x}(x_j) = \sum_{m=-\frac{N}{2}+1}^{N/2} ik_m \hat{u}(k_m) w^{ik_m x_j} \qquad (2-47)$$

where

$$\hat{u}(k_m) = \frac{1}{N} \sum_{j=o}^{N-1} u(x_j) e^{-ik_m x_j} \qquad (2-48)$$

and

$$N = \text{number of grid points}$$

$$x_j = \Delta j \quad , \quad j = 0, 1, 2 \ldots, N-1$$

$$k_m = \frac{2\pi}{N\Delta} m \quad , \quad m = -\frac{N}{2} + 1, -\frac{N}{2} + 1, \ldots, 0, \ldots, \frac{N}{2}$$

This method is made efficient by the Fast Fourier Transform algorithm developed by Cooley and Tukey (1965), which is particularly efficient for $N = 2^n$, where n is an integer. In this case, since N is an even number, the Fourier component $\hat{u}(k_{N/2})$ is set equal to zero, due to the lack of information about it.

2.9 Time Advancement

The time-advancement is the fourth-order Runge-Kutta method, which is stable and accurate (see Feiereisen et al., 1981, pp. 29-30). The time step is variable and is determined by requiring the Courant number to be 0.5. The fourth-order Runge-Kutta method used is:

$$\underline{\overline{u}}^{(1)} = \underline{\overline{u}}^{(n)} + \frac{\Delta t}{2} \frac{\partial \underline{\overline{u}}^{(n)}}{\partial t}$$

$$\underline{\overline{u}}^{(2)} = \underline{\overline{u}}^{(n)} + \frac{\Delta t}{2} \frac{\partial \underline{\overline{u}}^{(1)}}{\partial t}$$

$$\underline{\overline{u}}^{(3)} = \underline{\overline{u}}^{(n)} + \Delta t \frac{\partial \underline{\overline{u}}^{(2)}}{\partial t}$$

$$\underline{\overline{u}}^{(n+1)} = \underline{\overline{u}}^{(n)} + \frac{\Delta t}{6} \left[\frac{\partial \underline{\overline{u}}^{(n)}}{\partial t} + 2 \frac{\partial \underline{\overline{u}}^{(1)}}{\partial t} + 2 \frac{\partial \underline{\overline{u}}^{(2)}}{\partial t} + \frac{\partial \underline{\overline{u}}^{(3)}}{\partial t} \right] \quad (2.49)$$

where the superscript (n) denotes the time step, and the superscripts (1), (2), and (3) denote time substeps.

2.10 Alias Removal

The nonlinearity of the equations of motion introduces the possibility of aliasing errors in numerical simulations. In a line of length $N\Delta$, where N is the number of mesh points and Δ is the width of the mesh, we can resolve nondimensional wave-numbers in the

interval $\left(-\frac{N}{2} + 1, \frac{N}{2}\right)$. On the other hand, the nonlinear terms introduce wave numbers outside this domain, and these are erroneously allocated to wave-numbers inside the computational domain. To remove the aliasing, we use the "2/3 rule", which requires eliminating all components at wave numbers outside the range $\left(-\frac{N}{3}, \frac{N}{3}\right)$. The results of all remaining products inside the domain $\left(-\frac{N}{3}, \frac{N}{3}\right)$ are alias-free (see Rogallo, 1981, pp. 46-47).

2.11 Remeshing the Computational Domain

The linear coordinate transformation applied to the governing equations moves the system of coordinates with the mean flow. The initial cubic computational box is distorted by the shear. This causes one dimension of the computational domain to become smaller than the large scales of the turbulence and the simulation is no longer accurate. To avoid this problem, the computational box is remeshed, as shown in Fig. 2.1. This process is a coordinate transformation which is performed when the total shear reaches the value $St = 1/2$ and is given by

$$\left(x_1\right)_{St=-\frac{1}{2}} = \left(x_1 + 2St\ x_2\ \delta_{11}\right)_{St=\frac{1}{2}} \qquad (2\text{-}50)$$

Fig. 2.1. Remeshing.

This transformation produces Fourier modes outside the computational domain in the 2-direction. These aliased terms are removed by applying the "2/3 rule" described in the previous section. This procedure has been successfully applied in full simulations of homogeneous shear flows (see Feiereisen et al., 1981, pp. 32-33; Shirani et al., 1981, p. 18).

2.12 Initial Conditions

Full and large-eddy simulations require an initial turbulent velocity field. Experimental results do not provide this information, and we have to provide a velocity field which is consistent with whatever information is available. Of course, for incompressible fluids, the initial velocity field must also be divergence-free.

In order to generate the initial velocity field, we have developed a procedure which is easier and more efficient than the ones used in previous simulations. The basic steps are:

a) A random number is assigned to each component of a vector stream function at every grid point. The random values can be biased to produce an anisotropic velocity field.

b) A divergence-free velocity field is constructed by taking the curl of the vector stream function. The numerical operator used to take the curl must be the one used to define the divergence.

c) The velocity field is Fourier transformed, and its three-dimensional energy spectrum is obtained by averaging the kinetic energy over spherical shells

$$E_f(k) = 2\pi k^2 < \hat{\bar{u}}_i(\underline{k}) \, \hat{\bar{u}}_i^*(\underline{k}) > \qquad (2\text{-}51)$$

where $< \hat{\bar{u}}_i(\underline{k}) \, \hat{\bar{u}}_i^*(\underline{k}) >$ is twice the average kinetic energy per unit mass in the spherical shell.

d) Each Fourier mode in a spherical shell is multiplied by a constant which gives this shell the desired energy content.

e) The velocity field is transformed back into real space.

Since most experimental results do not provide the three-dimensional energy spectrum of the turbulence, we shall use the one of Comte-Bellot and Corrsin (1971). The case chosen had a free-stream velocity of 10 m/s, a generating grid size $M = 0.0508$ m, and the initial position was at $x/M = 42$ downstream of the generating grid. This energy spectrum was nondimensionalized with the turbulent kinetic energy and the rate of energy-dissipation. This normalization makes the large-scale part of the energy spectrum independent of Reynolds numbers in isotropic turbulence, according to Tennekes and Lumley (1972, p. 267). Since filtering removes the small-scale part of the energy spectrum, we should have an initial three-dimensional energy spectrum which is representative of filtered isotropic turbulence.

Chapter III

COMPUTER PROGRAMS ON ILLIAC IV

3.1 The ILLIAC IV Processor

The numerical simulations were performed on the ILLIAC IV, a very fast parallel computer. ILLIAC IV consisted of a control unit and 64 parallel processors and was capable of performing as many as 10^7 arithmetic operations per second. Each processor had 2096 words of local memory, and the system contained a disk memory with a capacity of about 32×10^6 words. The performance of a code was largely determined by the management of the data transfer between the disk and the processor memories. The data-management system chosen was the "Pencil System" developed by Pulliam and Lomax (1979). This system transfers arrays of $8 \times 16 \times N$ words at a time, where N is the number of mesh points in a given direction, which can be 16, 32, or 64. We chose N = 32 in order to have enough resolution to simulate the large scales of various flows.

3.2 Computer Programs

Several computer codes were used in the numerical simulations. One code generated the initial turbulent velocity field, according to the procedure described in Section 2.10.

The main code advanced the velocity field using the fourth-order Runge-Kutta method described in Chapter II. Various statistics were computed at each time step.

A third code computes spectra and statistics derived from the velocity field generated by the main code.

Finally, various codes do data reduction and prepare data for plotting. These ran on a CDC 7600 computer.

The main ILLIAC code with $32 \times 32 \times 32$ mesh points required a running time of less than 1.5 seconds per time sub-step. This running time is about 40% faster than the codes used by Feiereisen et al. (1981) for full simulations of compressible, homogeneous shear flows, and Shirani et al. (1981) for full simulations of mixing of a passive scalar

in homogeneous shear flows. The improvement in the running time was due to the design of the code according to suggestions made by Drs. R. Rogallo, E. Shirani, W. Feiereisen, P. Moin, and J. Kim.

3.3 Tests of the Main Code

Several tests were performed in order to check the performance of the codes. We shall describe some of the most significant tests of the main code:

- Simulations of two-dimensional, incompressible Taylor-Green vortices were performed. The solution has the following form:

$$u_1 = -k_2 \cos(k_1 x) \sin(k_2 y) e^{-(k_1^2 + k_2^2)\nu t}$$

$$u_2 = k_1 \sin(k_1 x) \cos(k_2 y) e^{-(k_1^2 + k_2^2)\nu t}$$

Several values of the wave-numbers k_1 and k_2 and all three combinations of coordinates were tested. The filter width and the model constants were set to zero. The solution showed no change when the kinematic viscosity was set equal to zero. This is the correct result.

The solution showed less than $10^{-4}\%$ difference with respect to the exact value of the velocity components after 100 time steps in the viscous cases.

- The shearing transformation was tested by performing a full simulation of a homogeneous shear flow. The time development of the components of the turbulence kinetic energy and shear stress compares well qualitatively with those of Shirani et al. (1981) and Feiereisen et al. (1981). This transformation was also tested by simulating the experimental results of Champagne, Harris, and Corrsin (1970) with accuracy. This simulation is described further in Chapter VIII.

- The filtering process and the Smagorinsky model were tested by simulating the experiment of Comte-Bellot and Corrsin (1971) on the decay of homogeneous isotropic turbulence; the experimental

results are predicted with great accuracy. This will be described further in Chapter V.

3.4 General Comments About the Simulations

All simulations require some approximations, which produce errors. In our case, the main approximations are due to modeling of the Reynolds stresses and the size of the computational domain. Comparisons with experimental data are also affected by insufficient information about the initial turbulence velocity field. Various models will be presented and tested in the following chapters; their differences will be discussed later. The initial velocity field is computed as described in Section 2.10 and initial velocity field does not have all the turbulence statistics of an experimental flow field. Higher-order statistics require time to develop; the velocity-derivative skewness reaches experimental levels only after a number of time steps. The length of this development time is a function of the model of the Reynolds stresses, the shape of the initial energy spectra, and the size of the computational domain.

The behavior in the development region of the turbulence intensity and velocity-derivative skewness (see Figs. 6.9 and 6.11) agree with large-eddy simulations performed by Kwak et al. (1975) and Shaanan et al. (1975), who used the Smagorinsky model, and by Mansour et al. (1977), who used the vorticity model.

The size of the computational domain determines the size of the largest eddies that can be simulated. Since the eddies tend to grow with time in many turbulent flows, the largest eddies will eventually exceed the size allowed by the computational domain, and the periodic boundary conditions and the calculation becomes invalid. The region of validity of the simulation can be monitored by examining the length scales during the simulation; the simulation must be stopped when these scales exceed these limits.

Chapter IV

THE BASIS OF LARGE-EDDY SIMULATION

This chapter will analyze the basic assumptions of large-eddy simulation (LES). We shall also look at some unresolved issues, especially those relating to subgrid-scale (SGS) modeling. Understanding of these issues is essential if we are to find improved models for LES.

4.1 Basis of Large-Eddy Simulation

The main objective of large-eddy simulation (LES) is to simulate turbulent flows. In LES, the large-scale motions are resolved, so no model is needed for them. However, modeling the effect of the small eddies on the large eddies is required. LES is less sensitive to turbulence modeling than the more commonly used one-point closure methods, in which all turbulent scales are represented by models.

Turbulent flows contain eddies of various sizes, and there is no single length scale which differentiates large and small eddies. At high Reynolds numbers there is an inertial sub-range in the energy spectrum in which there is neither significant energy production nor dissipation, and the distinction is easier to make. In this case, filtering the energy spectrum so as to retain all of the structures below some wavenumber in the inertial subrange provides a natural definition of the large eddies. When there is no inertial subrange, the distinction is necessarily more arbitrary. A schematic of the decomposition of the velocity field is shown in Diagram 6.1.

Full Field $(\underline{u})$

Large-scale field $(\underline{\bar{u}})$ ⟷ Interactions via Reynolds Stresses ⟷ Small-scale field $(\underline{u}' = \underline{u} - \underline{\bar{u}})$
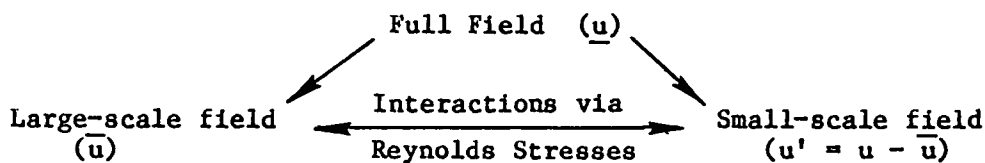
Diagram 6.1. Flow field decomposition.

The effects of the small eddies are represented by the Reynolds stresses in the equations of motion for the large-scale field; cf. Section 2.6.

LES requires large and fast computers. Since the range of scales of turbulent motions increases with Reynolds number, computer capacity may not allow resolution of the large-scale motions according to the definition above. The scales of motion represented in LES is shown in Diagram 6.2.

Full Flow Field $(\underline{u})$

Filtered Flow Field $\xleftarrow{\text{Interaction via}}$ $\xrightarrow{}$ Subgrid-scale Flow Field
$(\overline{\underline{u}})$ $\overline{\text{Subgrid Scale Model}}$ $(\underline{u}' = \underline{u} - \overline{\underline{u}})$
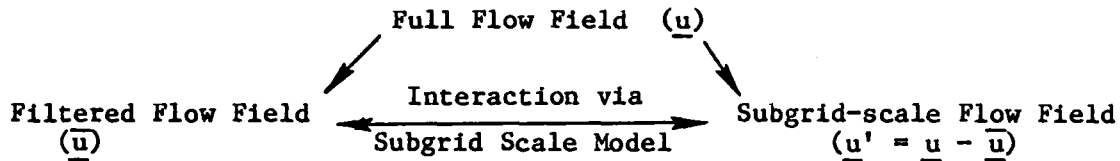
Diagram 6.2. Flow field decomposition in LES.

The filtered field $\overline{\underline{u}}$ is obtained by filtering the full flow field $\underline{u}$; cf. Section 2.5. The SGS flow field $\underline{u}'$ is obtained by subtracting the filtered field from the full field. The interaction between the filtered and SGS fields is represented by a model of the Reynolds stresses. The difference between the definitions used in Diagrams 6.1 and 6.2 lies mainly in the SGS model and the choice of filter width or cutoff eddy size.

LES requires the model to represent the effects of the SGS field on the filtered field. Furthermore, estimation of complete turbulence quantities from the results of LES also requires modeling of the SGS field. The assumptions made in this model must be consistent with those made in the Reynolds stress model.

4.2 Usual Assumptions of Eddy-Viscosity Models

Subgrid scale models for LES have been based on ideas used in one-point closure models. However, the differences between the methods are significant and require careful consideration.

The simplest and most popular model in LES is the eddy-viscosity model, which assumes that the SGS Reynolds stress deviator tensor, τ_{ij}, is proportional to the local strain rate tensor of the filtered field, $\overline{S}_{ij}$, so that:

$$\tau_{ij} = -2\nu_\tau \overline{S}_{ij} \qquad (4\text{-}1)$$

where ν_τ is the eddy viscosity.

26

The eddy viscosity is assumed to be proportional to the product of the characteristic length and time scales of the SGS turbulence,

$$\nu_\tau \sim \Delta_f q \qquad (4\text{-}2)$$

The filter width, Δ_f, is used because it is the length-scale of the largest and, presumably, the most important SGS turbulence eddies. The velocity-scale q is related to the kinetic energy of the SGS motions by:

$$E_{SGS} = \frac{1}{2} \rho q^2 \qquad (4\text{-}3)$$

Furthermore, if the SGS turbulence is assumed to be in local equilibrium with the large-scale field, a reasonable approximation is:

$$q \sim \Delta_f |\overline{S}| \qquad (4\text{-}4)$$

where

$$|\overline{S}| = \sqrt{2\overline{S}_{ij}\overline{S}_{ij}} \qquad (4\text{-}5)$$

is the magnitude of the strain rate of the filtered field. Combining these equations, we have the eddy viscosity first proposed by Smagorinsky (1963):

$$\nu_\tau = (c_s \Delta_f)^2 |\overline{S}| \qquad (4\text{-}6)$$

Mansour et al. (1978) proposed replacing Eq. (4-6) with:

$$\nu_\tau = (c_v \Delta_f)^2 |\overline{\omega}| \qquad (4\text{-}7)$$

where $|\overline{\omega}|$ is the magnitude of the local vorticity of the large scale field.

The main advantage of eddy-viscosity models is that they are dissipative, i.e., they are guaranteed to take energy out of the large scale

27

field. For the Smagorinsky model, the net rate of transfer of energy out of the filtered flow field is:

$$\varepsilon_f \equiv \langle -\tau_{ij} \overline{S}_{ij} \rangle = \langle \nu_\tau \overline{S}^2 \rangle \qquad (4-8)$$

and is clearly positive. These models also produce accurate predictions of filtered quantities in at least some flows with just a single model constant, cf. Kwak et al. (1975), Shaanan et al. (1975), Mansour et al. (1978), and Moin et al. (1978, 1981).

4.3 Some Unresolved Issues in Large-Eddy Simulation

Some unresolved issues on LES were discussed by Herring (1977) and Ferziger and Leslie (1979). The chief of these are described in this section.

4.3.1 Eddy Viscosity Models

Eddy-viscosity models can be tested by using full simulations or by comparison with experimental observations. Full simulations of homogeneous turbulent flows allow us to make detailed comparisons of model predictions and exact values. However, at the present time, full simulations are restricted to low Reynolds numbers and simple flows, where periodic boundary conditions can be used. Experimental observations have neither of these restrictions but are not sufficiently detailed to permit detailed comparisons with models; indirect approaches must then be employed.

Tests using full simulations show that eddy-viscosity models are able to maintain the correct mean energy balance of the large scale flow field while giving poor representations of the Reynolds stresses on a local basis (Clark et al., 1977). It thus appears that some of the assumptions on which eddy-viscosity models are based may be incorrect.

We shall now look at some of these.

28

a. Stress-strain proportionality

Clark et al. (1977), McMillan et al. (1979, 1980), and Bardina et al. (1980) have shown that the principal axes of the SGS Reynolds stresses are not aligned with the principal axes of the strain rate of the large-scale or filtered turbulence. These tests will be described in more detail in Chapter VI.

b. Velocity scale in the model

The velocity scale in the eddy-viscosity model has been assumed to be the velocity scale of the SGS turbulence, cf. Eqs. (4-2)-(4-4) and Lilly (1967), Deardorff (1971), Clark et al. (1977), and Moin et al. (1978). The Smagorinsky (4-6) and vorticity (4-7) models do not use this velocity scale explicitly, but the matter deserves to be looked at.

To study the problem of the velocity scale in more detail, we shall use LES of the decay of homogeneous isotropic turbulence. Figure 4.1 gives the time history of the decay of the full and filtered turbulence intensities for the one case of the experiment of Comte-Bellot and Corrsin (1971). Figure 4.2 gives the initial filtered experimental spectrum, which served as the initial condition of the LES, while Figure 4.3 gives the filtered-energy spectrum obtained both experimentally and by LES at the last station. The excellent agreement between LES and experiment indicates that the Smagorinsky model is able to maintain the correct energy balance and spectrum in this flow. In order to test the SGS velocity relation (4-4), we looked at the SGS turbulent kinetic energy (TKE); Figure 4.4 gives its time history. The "exact" SGS TKE was obtained by subtracting the filtered TKE from the full TKE, while the estimated SGS TKE has been obtained by using Eq. (4-4). The results have been normalized with their values at the last station in order to eliminate the influence of the model constant. Figure 4.4 indicates that the actual SGS TKE decays faster than the one obtained from the model. Thus, we conclude that the velocity scale of the eddy-viscosity model is not truly the velocity scale of the SGS turbulence. Although the Smagorinsky model appears to be valid for this case, at least one of Eqs. (4-2) and (4-4) must be incorrect.

A new velocity scale for the eddy viscosity will be proposed in Chapter VI.

c. "Production equals dissipation"

The argument that the production and dissipation of turbulent kinetic energy are equal in equilibrium flows has been used to derive turbulence models in one-point closure methods. In LES, this argument becomes the notion that the net rate of energy transfer from the large-scale field equals the rate of dissipation of SGS energy. This is essentially the argument used to derive Eq. (4-4). However, this argument may not be valid in all flows. The SGS energy-dissipation rate may be greater or less than the rate of energy transfer to the SGS field in time developing flows. Figure 4.5 gives the time history of the rates of energy transfer and SGS energy dissipation in the isotropic turbulence experiment of Comte-Bellot and Corrsin. The rate of energy transfer is assumed equal to the rate of energy loss of the filtered field, because viscous dissipation accounts for less than 5% of the energy loss of the filtered field. The total energy dissipation rate is initially six times the rate of energy loss of the filtered field; this ratio decreases to about three at the later time. The difference between the rate of energy dissipation and energy transfer from the filtered field to the SGS field is due to the decay of the kinetic energy that was in the SGS initially.

That the rate of energy transfer is almost always smaller than SGS dissipation in isotropic homogeneous turbulence can be shown by analyzing the energy balance of the SGS flow field. This energy balance states that the rate of change of SGS TKE equals the net SGS production minus the net SGS dissipation; i.e.,

$$\frac{\partial q^2/2}{\partial t} = (P - P_f) - (\varepsilon - \varepsilon_f) \qquad (4-9)$$

where $q^2/2$ is the SGS turbulent kinetic energy, $P - P_f$ is the net production of SGS TKE by mean strain, if any is imposed, $\varepsilon - \varepsilon_f$ is the net SGS dissipation of TKE; i.e., dissipation of SGS TKE minus the rate of energy transfer from the filtered field. Note that ε_f, the energy transfer from the filtered field to the small-scale field, appears as dissipation to the filtered field.

30

In the decay of homogeneous isotropic turbulence, production of TKE is zero:

$$P = P_f = 0 \qquad (4\text{-}10)$$

and the SGS TKE normally decays with time; i.e.,

$$\frac{\partial q^2/2}{\partial t} < 0 \qquad (4\text{-}11)$$

Thus, SGS energy dissipation in this flow is always greater than the rate of energy transfer from the filtered field; i.e.,

$$\varepsilon > \varepsilon_f \qquad (4\text{-}12)$$

Furthermore, we anticipate that this will be the case in other homogeneous turbulent flows as well.

d. Smagorinsky constant

The constant in the Smagorinsky model has been determined from theoretical arguments by Lilly (1967) as ~ 0.2. Similar values were found through a full simulation of a low Reynolds number homogeneous isotropic turbulence by Clark et al. (1977), and by fitting the decay of homogeneous isotropic turbulence in LES by Kwak et al. (1975) and Shaanan et al. (1975). On the other hand, Deardorff (1970), Schumann (1975), and Moin and Kim (1981) found that this value of the parameter produces too much dissipation in the simulation of channel flow. Moin and Kim found a constant of 0.065 was needed to maintain the turbulence in this flow, in conjunction with other model changes.

The causes of the variation of the Smagorinsky parameter are not well understood. Deardorff (1971) stated that changing the numerical techniques requires a different value of the constant. Mansour et al. (1978) showed that use of a second-order central-difference method for evaluating the model requires a constant of the order 10% greater than use of a pseudospectral method. McMillan and Ferziger (1979) found evidence that the effect of mean shear is to decrease the net rate of energy transfer to small scales.

We shall show in Chapter VII that one of the effects of rotation is to decrease the net rate of energy transfer to the small scales. These results could explain some of the discrepancy.

e. Length scale for anisotropic filters

Since wall-bounded flows are inhomogeneous and require a nonuniform numerical grid, the definition of the characteristic length scale used in the model is no longer simple. Moin and Kim (1981) used the following definition for the mean filter width:

$$\Delta_f = (\Delta_{f1} \Delta_{f2} \Delta_{f3})^{1/3} \tag{4-13}$$

while Bardina et al. (1980) showed that a better definition of the mean filter width in homogeneous turbulent flows with anisotropic filters is

$$\Delta_f = \frac{(\Delta_{f1}^2 + \Delta_{f2}^2 + \Delta_{f3}^2)^{1/2}}{3} \tag{4-14}$$

Eddy viscosity models require a different model constant in order to keep the proper balance of energy, if the mean filter width is obtained from Eq. (4-14) instead of Eq. (4-13). Therefore, the definition of the mean filter width in inhomogeneous turbulent flows is very significant when comparisons of model constant are performed.

4.3.2 Defiltering

LES predicts filtered turbulent quantities; however, for comparison with experiments we need the full turbulent quantities. We define defiltering as any method of obtaining full turbulent quantities from filtered ones.

Two defiltering methods have been proposed:

● Eddy viscosity method

Lilly (1967) and Moin et al. (1978) assumed that the velocity scale used in the eddy viscosity is the velocity scale of the SGS turbulence, cf. Eq. (4-2). The SGS TKE can therefore be obtained from Eq. (4.2):

$$\frac{q^2}{2} \approx \frac{v_\tau^2}{c\Delta_f} \quad , \quad c \approx 0.094 \tag{4-15}$$

However, we have seen in the previous section that the velocity scale of
the eddy viscosity is not the velocity scale of the SGS turbulence.
Figure 4.6 shows that Eq. (4-15) underpredicts the SGS TKE by 37% at the
initial station.

● Energy spectrum method

Cain (1981) proposed to calculate the full TKE by integrating the
(defiltered) three-dimensional energy spectrum. The (defiltered) energy
spectrum is obtained by applying the inverse of the filter to the re-
solvable or filtered three-dimensional energy spectrum up to the maximum
resolvable wave number. At high wave numbers Pao's (1965) spectrum is
used and is matched to the computed spectrum at the maximum resolvable
wave number.

The main problem of this method is that it introduces large errors
because the filtered energy spectrum is very uncertain near the maximum
wavenumber, and the inverse of the filtering function is relatively
large at those wavenumbers. The result is also sensitive to the numeri-
cal method used. For example, Mansour et al. (1977) showed that chang-
ing the numerical method could produce differences as large as 400% in
the filtered energy spectrum at the maximum resolvable wave number.

In the next chapter, an accurate "defiltering" method will be pro-
posed. This method is based on the physical assumptions of large-eddy
simultion and will be tested against experimental data.

Chapter V

BASIC RELATIONSHIPS AND DEFILTERING METHOD IN LARGE-EDDY SIMULATION

The analysis presented in this chapter sheds some light on the unresolved issues described in the preceding chapter. It primarily analyzes the behavior of the characteristic turbulence scales in the decay of homogeneous isotropic turbulence at high Reynolds numbers, and leads to a new defiltering method. This method is tested against experimental results on isotropic, rotating, and sheared turbulence.

5.1 Energy Balance and the Defiltering Method

The prime requirement placed on turbulence models is to provide the proper energy balance. We therefore begin by analyzing the energy balance in turbulent flows.

Figure 5.1 is a schematic representation of the three-dimensional energy spectra and energy balances of the full, filtered, and SGS flow fields in the decay of homogeneous isotropic turbulence. The energy spectrum of the filtered field is obtained by filtering the full energy spectrum, while the SGS energy spectrum is obtained by subtracting the filtered energy spectrum from the full energy spectrum. The energy balances may be written

Full Field: $$\frac{\partial Q^2/2}{\partial t} = - \varepsilon \qquad (5-1)$$

Filtered Field: $$\frac{\partial Q_f^2/2}{\partial t} = - \varepsilon_f \qquad (5-2)$$

SGS Field: $$\frac{\partial q^2/2}{\partial t} = - (\varepsilon - \varepsilon_f) \qquad (5-3)$$

where $0.5\ Q^2$, $0.5\ Q_f^2$, and $0.5\ q^2$ are the turbulent kinetic energy per unit mass of the full, filtered, and SGS flow fields, respectively; ε is the rate of turbulence energy dissipation per unit mass; and ε_f is the rate of turbulence energy transfer per unit mass from the filtered flow field to the SGS flow field.

Since viscous dissipation of the large scale or filtered flow field is negligible at high turbulence Reynolds numbers, we may neglect it.

Dimensional analysis and heuristic physical arguments for the full and filtered fields at high Reynolds numbers lead to the following relationships:

Full Field: $$\varepsilon \sim \frac{Q^3}{L} \qquad\qquad (5\text{-}4)$$

Filtered Field: $$\varepsilon_f \sim \frac{Q_f^3}{L_f} \qquad\qquad (5\text{-}5)$$

Tennekes and Lumley (1978) consider that this "...is one of the cornerstone assumptions of turbulence theory; it claims that large eddies lose a significant fraction of their kinetic energy $\frac{1}{2} Q^2$ within one "turnover" time L/Q."

The relationship (5-4) has been used frequently to get an estimate of the average length-scale of the energy-containing large eddies, L, and is about 4.5 times the longitudinal integral length scale, according to the experimental results of Comte-Bellot and Corrsin (1971), when a constant of unity is assumed in (5-4). Furthermore, Tennekes and Lumley (1978, p. 267) show that this length scale makes the normalized large scale spectrum of the turbulence energy independent of Reynolds number.

Since the filtered flow field contains the same large eddies as the full flow field, we expect that

$$L_f \sim L \qquad\qquad (5\text{-}6)$$

Therefore, combining relationships (5-4), (5-5), and (5-6), we have:

$$\varepsilon \sim \varepsilon_f \frac{Q^3}{Q_f^3} \qquad\qquad (5\text{-}7)$$

This tells us that the dissipation rate, ε, is larger than the rate of energy transfer from the resolved scales to the smaller scales, ε_f, since filtering ensures that $Q^2 > Q_f^2$. The difference between these two quantities, i.e., $\varepsilon - \varepsilon_f$, represents the net rate of decay of SGS turbulence and may be quite large. One cannot apply the "production equals dissipation" argument to the small scales if this is the case.

The SGS field is defined as the difference between the full field and the filtered field. The principal quantities for the subgrid scales are the turbulence kinetic energy per unit mass $q^2/2$, dissipation rate per unit mass ε, and the filter width Δ_f, which is their natural length scale. Dimensional analysis suggests that, if the Reynolds number is high enough that there is no significant viscous dissipation of eddies of size Δ_f, then these scales are related by

$$\varepsilon \sim \frac{q^3}{\Delta_f} \tag{5-8}$$

Combination of relationships (5-7) and (5-8) gives the SGS turbulent kinetic energy as a function of the full turbulence kinetic energy and filtered quantities, i.e.,

$$q^2 \sim (\Delta_f \varepsilon_f)^{2/3} \frac{Q^2}{Q_f^2} \tag{5-9}$$

which may also be written as

$$q^2 = c_f (2\Delta_f \varepsilon_f)^{2/3} \frac{Q^2}{Q_f^2} \tag{5-10}$$

where c_f is the constant of proportionality. This constant depends on the filter function and energy spectrum of the turbulence. The Gaussian filter and energy spectra of Comte-Bellot and Corrsin (1971) suggest $c_f = 1.04$.

Since the full turbulence kinetic energy is equal to the sum of the filtered and SGS energies, i.e.,

$$Q^2 = Q_f^2 + q^2 , \tag{5-11}$$

the combination of Eqs. (5-10) and (5-11) gives the proposed defiltering equation for the full turbulence kinetic energy as:

$$Q^2 = \frac{Q_f^4}{Q_f^2 - c_f (2\Delta_f \varepsilon_f)^{2/3}} \tag{5-12}$$

which is a function only of filtered quantities. This procedure will be tested in the following subsections against experimental data on homogeneous isotropic, rotating, and shear turbulence.

5.2 Tests of the Scaling Relationships

In this section we shall test the scaling relationships presented in the preceding section against the experimental results of Comte-Bellot and Corrsin (1971) on the decay of homogeneous, isotropic turbulence. The turbulence Reynolds number based on the Taylor microscale was $R_\lambda \approx 73$ in this experiment. The simulations are LES with the Smagorinsky model, and the model constant is $c_s = 0.21$, and a $32 \times 32 \times 32$ computational grid is used. The numerical method is pseudospectral, except for the turbulence model, which is evaluated with second-order central differences. The filter width, $\Delta_f = 0.03$ m, is twice the computational mesh size, and the initial energy spectrum is shown in Fig. 4.2. The filtered quantities are obtained from the simulation, while the full quantities are obtained from the experiment.

Firstly, the assumption that the average length-scales of the filtered flow field, $L_f \equiv Q_f^3/\varepsilon_f$, and full flow field, $L \equiv Q^3/\varepsilon$, are equal is tested. Figure 5.2 gives the time history of the ratio of these length scales, L/L_f, and indicates that they are nearly equal. In this simulation over half of the energy is in the SGS turbulence. We conclude that the assumption of equality of large length scales in the full and filtered fields is accurate for this flow.

Secondly, the scaling relationship for the small scales is tested. Figure 5.3 gives the time history of $q^2/(2\Delta_f \varepsilon)^{2/3}$, which Eq. (5-5) suggests should be constant, and indicates that this is also a good approximation in the decay of turbulence at high Reynolds numbers.

5.3 Tests of the Defiltering Method

In this section the full turbulence kinetic energy is calculated by using Eq. (5-12) and comparing it to experimental results on isotropic, rotating, and sheared turbulence. The filtered turbulence quantities are obtained by LES, as described above, and the constant of Eq. (5-12) is kept at $c_f = 1.04$.

5.3.1 Homogeneous Isotropic Turbulence

LES of the decay of homogeneous isotropic turbulence of Comte-Bellot and Corrsin (1971) has been presented above and in Chapter IV. In particular, Fig. 4.1 shows the prediction of the time history of the resolvable energy, and Fig. 4.3 shows the prediction of the resolvable three-dimensional energy spectrum. We shall use this simulation to test the defiltering relationship (5-12).

Figure 5.4 shows the time history of the full and filtered turbulence energies obtained from the experiment and the simulation. The prediction of the decay of the full turbulence energy obtained from Eq. (5-12) is within 5% of the experimental data.

5.3.2 Homogeneous Rotating Flows

The defiltering method shall be used to predict the experimental data of Wigeland and Nagib (1978) on the decay of homogeneous turbulence in the presence of constant rate of rotation. As we have observed in Chapter II, extension of the isotropic turbulence code to include frame rotation is straightforward.

Figure 5.5 compares the experimental and simulated turbulence energies of the full and filtered flow fields. The only modification is the inclusion of the Coriolis force in the momentum equations and the centrifugal potential in the mean reduced pressure.

The initial three-dimensional energy spectrum is the one used to simulate isotropic turbulence but is scaled to match the initial turbulence kinetic energy and dissipation rate of the flow being simulated, as explained in Section 2.10.

Figure 5.5 gives the comparison between the predicted and the experimental time history of the inverse of the full turbulence energy with rotation rates of 0, 20, and 80 sec^{-1}, respectively (see Table 7.3). The turbulence Reynolds number based on Taylor microscale is about 15. The inverse of the turbulence energy has been plotted in order to emphasize the differences at later times due to the long decay time of these experimental results. The effects of rotation on the rate of decay of the turbulence will be analyzed in detail in Chapter VII.

The predictions compare very well with the experimental observations. The small differences observed at the high rotation rate of 80 sec^{-1} can be attributed to several reasons, such as experimental uncertainties which are larger at higher rates of rotation, initial conditions of the simulation, and non-inclusion of the Rossby number in the scaling relationships.

5.3.3 Homogeneous Shear Flows

We shall apply the defiltering method to simulations aimed at the experimental results by Champagne, Harris, and Corrsin (1970) for homogeneous turbulent shear flow. In this experiment, the shear rate was $S = 12.9$ sec^{-1}, the turbulence Reynolds number based on Taylor microscale was about 130, and $St = 3.2$.

The extension of the method necessary to simulate homogeneous shear flows is given in Chapter II. The initial conditions are the ones used to simulate isotropic turbulence, scaled to match the initial turbulence kinetic energy and dissipation rate, as explained in Section 2.10.

Figure 5.6 shows the time history of the resolvable turbulent energy obtained from LES, together with the comparison between the predicted and the experimental full turbulent energies. The agreement is very good.

The experimental results by Harris, Graham, and Corrsin (1977) for homogeneous turbulent shear flow are not used, due to computer limitations. In this experiment, the shear rate was $S = 44$ sec^{-1}, the turbulence Reynolds number based on Taylor microscale was about 230, and $St = 12.7$. LES with a $32 \times 32 \times 32$ grid was not valid after $St = 4$, due to the growth of the length scales. A meaningful simulation of this flow requires at least a $128 \times 128 \times 128$ grid and several hours of computational time, and the resources were not available to this work.

5.4 Analysis of the Scaling Relationships

The results presented above show that the scaling relationships and the defiltering method are accurate for several homogeneous turbulent flows. We emphasize that it was not assumed that the net rate of transfer of energy from the resolvable turbulent scales to the subgrid scales is equal to the dissipation rate. Rather, the key assumption is that the average large length scales of the full and filtered field are equal. These length scales are proportional to the integral length scales in isotropic turbulence; however, there is no known relationship between them when there is anisotropy in the length scales. Since measurements of integral length-scales have relatively large experimental uncertainties (see Champagne, Harris, and Corrsin, 1970, p. 105), and there is no agreement on the proper definition of the integral length scales when the two-point velocity correlation function contains positive and negative values, it seems reasonable to use Q^3/ε as the proper length scale.

Chapter VI

NEW SUBGRID-SCALE TURBULENCE MODELS FOR LARGE-EDDY SIMULATION

The physical bases of large eddy simulation (LES) and some unre-
solved issues on subgrid-scale (SGS) turbulence modeling were analyzed
in Chapter IV. Basic relationships for the characteristic turbulence
scales in LES were developed in Chapter V. In this chapter, improved
SGS turbulence models for LES are developed, analyzed, and tested.
These models not only keep the proper mean energy balance, but represent
SGS Reynolds stresses much better. These models are tested by using
full and large eddy simulations of homogeneous, isotropic, rotating, and
sheared turbulent flows.

6.1 Subgrid-Scale Reynolds Stresses

A good SGS turbulence model should accurately represent all the
effects of the SGS Reynolds stresses on the filtered flow field. Exper-
imental and numerical evidence indicates that the most significant ef-
fect of the SGS Reynolds stresses is to transfer energy from the large
eddies to the SGS eddies.

We can study these effects in the decay of homogeneous isotropic
turbulence. In this case, the mean energy balance of the full flow
field is Eq. (5-1) and the mean energy balance of the filtered flow
field is Eq. (5-2). At high turbulence Reynolds numbers, the rate of
decay of the filtered turbulent kinetic energy is well approximated by:

$$\varepsilon_f \approx \langle - \tau_{ij} \overline{S}_{ij} \rangle \qquad (6\text{-}1)$$

It is evident from Eq. (6-1) that the part of the local SGS Reynolds
stress tensor which contributes to the transfer of energy is diagonal in
a coordinate system aligned with the principal axis of the local fil-
tered strain rate tensor, $\overline{S}_{ij}$. Eddy viscosity models account for this
effect by assuming that the entire SGS Reynolds stress deviator is pro-
portional to $\overline{S}_{ij}$:

$$\tau_{ij} = - 2 \nu_\tau \overline{S}_{ij} \qquad (6\text{-}2)$$

43

The proportionality factor is the eddy viscosity ν_τ. This kind of model provides the proper energy balance of the filtered flow field in the mean but not in detail. The success of eddy viscosity models has been demonstrated in a number of simulations (see Kwak et al., 1975, Shaanan et al., 1975, Mansour et al., 1978, Kim et al., 1979, and Moin et al., 1978, 1981). All these simulations used Smagorinsky's (1963) model (see Eq. (4-6)) or the vorticity model (see Eq. (4-7)) for the eddy viscosity. We have already shown in Chapter IV that some of the basic assumptions used to derive these models are wrong. Therefore, it is useful to provide a derivation of the Smagorinsky model that is not based on these assumptions. This derivation provides insight into the limitations and capabilities of the Smagorinsky model and guidance as to how to devise improved SGS models.

6.2 Smagorinsky Model

The energy-dissipation rate of the full turbulent kinetic energy is given by definition of η:

$$\varepsilon = \frac{\nu^3}{\eta^4} \qquad (6-3)$$

where ν is the kinematic viscosity and η the Kolmogorov length scale. By analogy, we shall assume that the net rate of energy transfer out of the filtered flow field (large eddies) is given by:

$$\varepsilon_f \sim \frac{<\nu_\tau>^3}{\Delta_f^4} \qquad (6-4)$$

where Δ_f is the filter width which is also the length scale of the smallest eddies of the filtered flow field. Combining Eqs. (6-1), (6-2), and (6-4), we have:

$$\frac{<\nu_\tau>^3}{\Delta_f^4} \sim \varepsilon_f \sim <2\nu_\tau \overline{S}_{ij}\overline{S}_{ij}> \qquad (6-5)$$

The Smagorinsky model for the eddy viscosity is obtained if relationship (6-5) is applied locally, i.e.,

$$\nu_\tau = (c_s\Delta_f)^2\left(\sqrt{2\,\overline{S}_{ij}\overline{S}_{ij}}\right)^{1/2} \qquad (6-6)$$

44

where c_s is the constant of proportionality. Tests of this model based on full simulations show that neglecting the spatial variations of the eddy viscosity does not make much difference (see McMillan et al., 1978, and Section 6.6 below). The Smagorinsky model (Eq. (6-6)) is able to maintain the proper energy balance of the mean filtered flow field, because its spatial average is consistent with relationship (6.5).

6.3 The Transfer Flow Field

A basic assumption of the previous section is that the net rate of energy transfer from the filtered flow field to the SGS flow field is determined by eddies whose size is the filter width. These eddies are simultaneously the smallest eddies of the filtered flow field and the largest eddies of the SGS flow field.

The definition of large and small eddies in LES is based on filtering. By analogy to the method used to decompose the full flow field, we may decompose the filtered and SGS flow fields. This decomposition provides a three-level flow field decomposition, as shown in Diagram 6.2.

Full Flow Field, u_i

$(Q^2 = \langle u_i u_i \rangle)$

Filtered Flow Field, $\overline{u}_i$ SGS Flow Field, $u_i' = u_i - \overline{u}_i$

Larger Flow Field   Transfer Flow Field   Smaller Flow Field

$\overline{\overline{u}}_i$ $\overline{u}_i' = \overline{u}_i - \overline{\overline{u}}_i$ $u_i'' = u_i' - \overline{u_i'}$
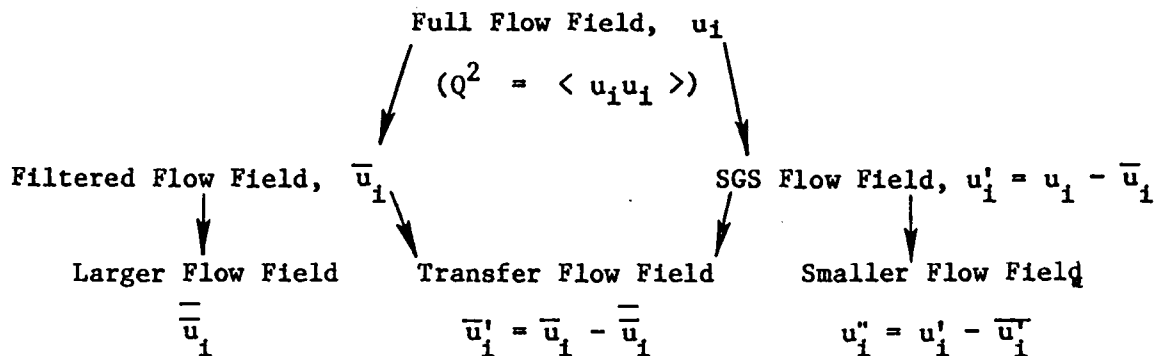
Diagram 6.2. Three-level flow field decomposition using a smooth filter
function

The larger flow field $\overline{\overline{u}}_i$ contains the larger eddies of the filtered flow field. The smaller eddies of the filtered flow field are obtained by subtraction:

$$\underline{\overline{u}}' = \underline{\overline{u}} - \underline{\overline{\overline{u}}} \qquad (6-7)$$

which is analogous to:

$$\underline{u}' = \underline{u} - \underline{\bar{u}} \qquad (6-8)$$

The larger eddies of the SGS flow field are obtained by filtering Eq. (6-8).

$$\underline{\bar{u}}' = \underline{\bar{u}} - \underline{\bar{\bar{u}}} \qquad (6-9)$$

However, Eqs. (6-7) and (6-9) are identical, so that the smaller eddies of the filtered flow field are also the larger eddies of the SGS flow field and will be called the transfer flow field, as indicated in Diagram 6.2. The identity of these two fields holds if the filter function is smooth; the Gaussian filter is in this category.

We assume that most of the energy transfer between the filtered flow field and the SGS flow field takes place through the transfer flow field. We shall use this idea to formulate new SGS turbulence models. It is consistent with the concept of energy-cascade, cf. Tennekes and Lumley (1972) and Leonard (1974). Finally, if a filter which is a step-function in Fourier space is used, the smaller eddies of the resolvable flow field can be defined by increasing the filter width or decreasing the cut-off frequency of the step-function; however, we do not recommend sharp filters for reasons given in Section 2.5.

6.4 Improved Eddy-Viscosity Models

Here we shall use the ideas of the previous section to formulate improved eddy-viscosity SGS models. We expect that the smaller and larger components of the SGS should affect the large-scale motions differently. Therefore, we propose the following "two-component" model of the eddy viscosity:

$$\nu_\tau = c_q q_f \Delta_f + c_m q_m \Delta_f \qquad (6-10)$$

where c_q and c_m are model constants and q_f^2 and q_m^2 are the turbulence intensities associated with the transfer and smaller flow fields, respectively.

The large eddies are expected to interact more strongly with the large SGS eddies than with the smaller SGS eddies, so we expect $c_q >$ c_m. Moreover, if the average length scale of the large eddies is much larger than the filter width, i.e., if $L \gg \Delta_f$, the effects of the smaller SGS eddies should be negligible, and Eq. (6-10) reduces to a turbulent kinetic energy (TKE) model.

$$\nu_\tau = c_q q_f \Delta_f \qquad (6\text{-}11)$$

If this model is applied locally, q_f should be defined as

$$q_f = |\overline{u_i \overline{u}_i} - \overline{\overline{u}_i \overline{u}_i}|^{1/2} \qquad (6\text{-}12)$$

The Smagorinsky model can also be derived. Following the arguments used above, the net rate of energy transfer from the filtered flow field to the SGS flow field should be:

$$\varepsilon_f \sim \frac{q_f^3}{\Delta_f} \qquad (6\text{-}13)$$

which in combinat on with Eqs. (6-1), (6-2), and (6-11) leads to the Smagorinsky model.

A combination of the TKE and Smagorinsky models provides the following model:

$$\nu_\tau = \frac{c_q^2}{c_m} q_f^2 (\overline{S}_{ij} \overline{S}_{ij})^{-1/2} \qquad (6\text{-}14)$$

which does not contain the filter width Δ_f explicitly. This model may be useful for inhomogeneous turbulent flows.

Tests of these eddy viscosity models based on full simulations, LES, and experimental observations will be presented at the end of this chapter. These tests show no significant differences among any of the eddy viscosity models presented in this section, but they do confirm the contention that the velocity scale of the eddy viscosity is that of the larger SGS or smaller resolvable eddies.

6.5 Scale-Similarity Model

The arguments made above suggest that we model the SGS Reynolds stresses directly in terms of the transfer flow field. Since the SGS velocity field is:

$$u_i' = u_i - \bar{u}_i \qquad (6\text{-}15)$$

we might expect

$$u_i' \simeq \overline{u_i^r} = \bar{u}_i - \bar{\bar{u}}_i \qquad (6\text{-}16)$$

which is the transfer velocity field. This suggests that

$$\overline{u_i' u_j'} \simeq (\bar{u}_i - \bar{\bar{u}}_i)(\bar{u}_j - \bar{\bar{u}}_j) \qquad (6\text{-}17)$$

However, this ignores the "cross terms" of Eq. (2-37). Modeling of each term of the SGS Reynolds stress tensor R_{ij} in terms of the transfer $\overline{u_i^r}$ and larger $\bar{u}_i$ velocity filds suggests that

$$\overline{u_i^r u_j^r} \simeq \overline{u_i^r}\,\overline{u_j^r} = (\bar{u}_i - \bar{\bar{u}}_i)(\bar{u}_j - \bar{\bar{u}}_j)$$

$$\overline{u_i' \bar{u}_j} \simeq \overline{u_i^r}\,\bar{u}_j = (\bar{u}_i - \bar{\bar{u}}_i)\,\bar{u}_j$$

$$\overline{\bar{u}_i u_j'} \simeq \bar{u}_i\,\overline{u_j^r} = \bar{u}_i(\bar{u}_j - \bar{\bar{u}}_j)$$

and

$$R_{ij} = \overline{u_i' u_j'} + \overline{u_i' \bar{u}_j} + \overline{\bar{u}_i u_j'} \simeq \overline{\bar{u}_i \bar{u}_j} - \bar{\bar{u}}_i \bar{\bar{u}}_j \qquad (6/18)$$

might be a better model.

We call Eq. (6-18) a scale-similarity model. It is not an eddy viscosity model and does not ensure a positive net rate of energy transfer to the small scales. Tests of this model presented in the next section show that it correlates well with the SGS Reynolds stresses locally, but does not dissipate energy. Simulations of decay of homogeneous isotropic turbulence with the scale similarity model and without the eddy viscosity model do not lost energy. To obtain the best

features of both models, we consider the following linear combination model:

$$\tau_{ij} = - 2\nu_\tau \overline{S}_{ij} + M_{ij} \qquad (6-19)$$

where

$$M_{ij} = c_r \left(\overline{\overline{u}_i \overline{u}_j} - \overline{\overline{u}}_i \overline{\overline{u}}_j - \frac{1}{3} \delta_{ij} \left(\overline{\overline{u}_n \overline{u}_n} - \overline{\overline{u}}_n \overline{\overline{u}}_n \right) \right) \qquad (6-20)$$

This model will also be tested in the following sections.

6.6 Tests of Subgrid-Scale Turbulence Models

Clark et al. (1977) proposed the evaluation of SGS turbulence models by using fully simulated turbulent flows. These simulations of three-dimensional and unsteady homogeneous turbulent flows are limited to low Reynolds numbers, $R_\lambda < 40$ for a $64 \times 64 \times 64$ grid and $R_\lambda < 63$ for a $128 \times 128 \times 128$ grid. McMillan and Ferziger (1979) used this technique to analyze various aspects of eddy viscosity models. Their results indicate that eddy viscosity models correlate poorly with "exact" SGS Reynolds stresses.

We have used this technique to test eddy viscosity and scale-similarity models. This work was done in conjunction with Dr. O. J. McMillan at Nielsen Engineering and Research, Inc., and Dr. R. S. Rogallo at NASA-Ames Research Center.

Rogallo (1977, 1981) has fully simulated homogeneous turbulent flows using $64 \times 64 \times 64$ and $128 \times 128 \times 128$ grid points on the ILLIAC IV computer. The velocity field ($\underline{u}$) was stored on a magnetic tape and processed on a CDC-7600 computer. A filtered velocity field is computed on a $16 \times 16 \times 16$ grid. The difference between the "exact" and filtered velocity field gives the SGS velocity field. Once these velocity fields are known, the "exact" SGS Reynolds stresses are calculated. The model of the SGS Reynolds stresses can also be calculated using only the filtered velocity field ($\overline{u}$). The models and exact results are then compared.

Comparisons can be made at the tensor level (comparing τ_{ij} and M_{ij}), vector level ($\partial\tau_{ij}/\partial x_j$ and $\partial M_{ij}/\partial x_j$) and/or the scalar level ($\overline{u}_i(\partial\tau_{ij}/\partial x_j)$ and $\overline{u}_i(\partial M_{ij}/\partial x_j)$).

49

A computer program was developed to make least-squares comparisons between the "exact" and the SGS Reynolds stresses models. The equations for the least-squares correlation coefficients, partial correlation coefficients, constant coefficients, standard deviations, t-statistics, and various other statistics are given in Johnston (1972); they are also described in many other statistics texts. Appendix A gives the equations of the correlation coefficients and model constants for the multiple component models analyzed in this chapter.

Exact tests were performed for the models using one field of homogeneous isotropic turbulence at $R_\lambda = 38$ and $R_{SGS} = 180$, and one field of homogeneous turbulence in the presence of mean shear $S = 34$ sec^{-1} at $R_{SGS} = 204$, where $R_{SGS} = S\Delta_f^2/\nu$ is the SGS Reynolds number. The same fields were used my McMillan et al. (1980) and Bardina et al. (1980) in tests of SGS models.

6.6.1 Eddy Viscosity Models

The eddy viscosity models all have the form:

$$\tau_{ij} = -2\nu_\tau \overline{S}_{ij} \qquad (6\text{-}21)$$

The models tested are:

- Smagorinsky model: $\quad \nu_\tau = (c_s \Delta_f)^2 \left(2\overline{S}_{ij}\overline{S}_{ij}\right)^{1/2} \qquad (6\text{-}22)$

- Vorticity model: $\quad \nu_\tau = (c_v \Delta_f)^2 \left(\overline{\omega}_i\overline{\omega}_i\right)^{1/2} \qquad (6\text{-}23)$

- TKE model: $\quad \nu_\tau = c_q q_f \Delta_f \qquad (6\text{-}24)$

  where $\quad q_f = \left|\overline{u_i u_i} - \overline{u}_i\overline{u}_i\right|^{1/2}$. $\qquad (6\text{-}25)$

- Smagorinsky-TKE model: $\quad \nu_\tau = \dfrac{c_s^2}{c_q} q_f^2 / \left(2\overline{S}_{ij}\overline{S}_{ij}\right)^{1/2} \qquad (6\text{-}26)$

- Hybrid model: $\quad \nu_\tau = c_z \left(\overline{u}_k - \overline{\overline{u}}_k\right)\left(\overline{u}_k - \overline{\overline{u}}_k\right) / \left(2\overline{S}_{ij}\overline{S}_{ij}\right)^{1/2} \qquad (6\text{-}27)$

- Constant eddy viscosity:

$$\nu_\tau = \begin{array}{l} \text{spatial average value of any of} \\ \text{the above eddy viscosity models.} \end{array} \qquad (6.28)$$

The average correlation coefficients between the "exact" and the eddy viscosity model of the SGS Reynolds stresses are shown in Table 6.1 and Table 6.2 for homogeneous isotropic turbulence and homogeneous sheared turbulence, respectively. All cases are calculated with a Gaussian filter and a filter width $\Delta_f = 2\Delta$, where Δ is the computational grid spacing. These are values recommended by McMillan and Ferziger (1979).

Table 6.1

Average Correlation Coefficient between "Exact" and Eddy Viscosity Model SGS Reynolds Stresses in Homogeneous Isotropic Turbulence at $R_\lambda = 38$ and $R_{SGS} = 180$

Eddy Viscosity Model	Tensor Level	Vector Level	Scalar Level
Smagorinsky, Eq. (6-22)	.24	.20	.36
Vorticity, Eq. (6-23)	.24	.22	.38
TKE, Eq. (6-24)	.24	.18	.36
Smagorinsky-TKE, Eq. (6-26)	.22	.14	.36
Hybrid, Eq. (6-27)	.24	.19	.37
Constant, Eq. (6-28)	.25	.22	.39

Table 6.2

Average Correlation Coefficient between Exact and Eddy-Viscosity Model SGS Reynolds Stresses in Homogeneous Turbulence in the Presence of Mean Shear, $S = 34$ sec^{-1} at $R_{SGS} = 204$

Eddy Viscosity Model	Tensor Level	Vector Level	Scalar Level
Smagorinsky, Eq. (6-22)	.05	.04	.05
Vorticity, Eq. (6-23)	.03	.04	.06
TKE, Eq. (6-24)	.03	.04	.04
Smagorinsky-TKE, Eq. (6-25)	.03	.06	.02
Hybrid, Eq. (6-27)	.03	.06	.04
Constant, Eq. (6-28)	.04	.04	.05

Tables 6.1 and 6.2 show that all these eddy viscosity models give similar correlation coefficients; all are quite low. Moreover, the correlation coefficients between the various models are more than 0.8 at the tensor and vector levels and more than 0.9 at the scalar level. Therefore, these models are essentially equivalent. These results are consistent with those of Clark et al. (1977) and McMillan et al. (1978). They indicate that no eddy viscosity model is better than any other, but some may have numerical advantages. All eddy viscosity models give poor levels of correlation for homogeneous isotropic turbulence, and almost zero level of correlation for homogeneous sheared turbulence.

The weakness of the eddy viscosity models is also shown in Figs. 6.1 and 6.2. These figures show the "exact" and the Smagorinsky model values of the SGS Reynolds stresses at the tensor, vector, and scalar levels for homogeneous isotropic and sheared turbulence. For an exact model, the plotted symbols would lie on a line bisecting the axes. We see that eddy viscosity models are not able to represent the local values of the SGS Reynolds stresses, but they can fit the mean energy loss of the resolvable scales.

6.6.2 Scale-Similarity Model

The scale-similarity model

$$\tau_{ij} = M_{ij} - \frac{1}{3} M_{kk} S_{ij} \tag{6-29}$$

where

$$M_{ij} = c_r \left(\overline{\overline{u}_i \overline{u}_j} - \overline{\overline{u}_i}\, \overline{\overline{u}_j} \right) \tag{6-30}$$

has been subjected to the test procedures described in the previous section.

Tables 6.3 and 6.4 show the average correlation coefficient between the "exact" and model values of the SGS Reynolds stresses for homogeneous isotropic and sheared turbulence, respectively. The values for the Smagorinsky and linear combination models are also shown for comparison.

Table 6.3

Average Correlation Coefficient between Exact and Model Values
of the SGS Reynolds Stresses in Homogeneous Isotropic Turbulence
at $R_\lambda = 38$ and $R_{SGS} = 180$

Model	Tensor Level	Vector Level	Scalar Level
Smagorinsky model	.24	.20	.36
Scale-similarity model	.80	.71	.50
Smagorinsky and scale-similarity model	.83	.74	.60

Table 6.4

Average Correlation Coefficient between "Exact" and Model Values
of the SGS Reynolds Stresses in Homogeneous Turbulence in the
Presence of Mean Shear, $S = 34 \text{ sec}^{-1}$ at $R_{SGS} = 204$

Model	Tensor Level	Vector Level	Scalar Level
Smagorinsky model	.05	.04	.05
Scale-similarity model	.80	.75	.58
Smagorinsky and scale-similarity model	.80	.75	.58

The values of the model constants are presented in the next subsection, 6.6.3. The correlation coefficients for the Smagorinsky and scale-similarity models are independent of the model constants. For the combined model, the Smagorinsky and scale-similarity model, the influence of the model constants in the values of the correlation coefficients are insignificant, due to the poor correlation between the Smagorinsky model and the "exact" values.

Table 6.3 shows very high correlation coefficients between the exact and scale similarity values in homogeneous isotropic turbulence; they are much higher than those for eddy viscosity models.

Table 6.4 is even more impressive. The correlation coefficients for homogeneous sheared turbulence are as high as those for homogeneous isotropic turbulence, while, as noted above, the eddy viscosity models show almost zero correlation coefficients in the shear flow.

53

Figures 6.3 and 6.4 show the exact and the scale-similarity values of the SGS Reynolds stresses at the tensor, vector, and scalar levels for homogeneous isotropic and sheared turbulence, respectively. The distributions are what one expects of a good model at the tensor level but are poorer at the scalar level.

LES of homogeneous turbulent flows using the scale-similarity model shows that this model is not dissipative. This can also be inferred from the exact results. The scale-similarity model constants obtained from the least-squares statistics at the scalar level are 0.9 and 1.2 for homogeneous isotropic and sheared turbulence, respectively. However, the constants of this model obtained from the ratio between the mean exact and model values at the scalar level are 22 and 25 for homogeneous isotropic and sheared turbulence, respectively.

Since eddy viscosity models provide the proper mean energy balance and the scale-similarity model gives a good representation of the local SGS Reynolds stress but does not provide the mean energy balance, the linear combination of the two may be a desirable SGS model. The correlation coefficient between the scale-similarity and eddy viscosity models is almost zero at all levels for both flows, so adding them should yield the best features of each. Thus correlation coefficients shown for the combined model in Tables 6.3 and 6.4 are equal to or higher than those obtained from the simple scale-similarity model. Figures 6.5 and 6.6 show the exact and linear combination model values of the SGS Reynolds stresses, and the good behavior is obvious.

In conclusion, tests based on full simulations of homogeneous isotropic and sheared turbulent flows indicate that the linear combination of the scale-similarity and eddy viscosity models gives a good representation of the SGS Reynolds stresses and has the desired dissipative property.

6.6.3 Model Constants

The full simulations used in the previous sections are also able to provide estimates of the values of the model constants.

First consider the constant (c_s) of the Smagorinsky model (Eq. (6-21). A good estimate of this constant is the one which makes the ratio of the spatially averaged exact and model scalar values equal to unity, because the main objective of eddy-viscosity models is to provide proper dissipation. The values of c_s obtained in this way are 0.20 and 0.09 for homogeneous isotropic and sheared turbulence, respectively. The values of c_s obtained from least squares analysis at the scalar level are 0.17 and 0.06 for the two flows. In the shear flow, the mean velocity gradient did not contribute to the model. These results provide evidence that the Smagorinsky constant decreases in the presence of mean shear. McMillan et al. (1980) found that the Smagorinsky constant does not change in the presence of irrotational mean strain. Thus, it seems that the rotational effects of the shear are responsible for the decrease in the Smagorinsky constant. This is also consistent with the results of the next chapter.

The values of c_s also agree reasonably well with the values of $c_s = 0.21$ found by Mansour et al. (1978) by LES of the homogeneous isotropic turbulence and $c_s = 0.065$ found by Moin et al. (1981) by LES of turbulent channel flow.

Further studies of the influence of mean shear on the Smagorinsky constant are required. Such a study is currently being made by McMillan.

For the linear combination model (6-19), the constants were found to be $c_s = .19$ and $c_r = 1.1$, when second-order central difference is used for the model terms. These were obtained by a combination of least squares fitting and small adjustments to make LES fit experimental data. The reduced value of c_s (.19) as compared to the value for the pure Smagorinsky model is due to the slight dissipation produced by the scale similarity component of the model. The model constants were found to be $c_s = 0.165$ and $c_r = 1.1$ when the pseudo-spectral method is used for the model terms.

For completeness, the linear combination model of the SGS Reynolds stresses is rewritten:

$$\tau_{ij} = R_{ij} - \frac{1}{3} R_{kk} \delta_{ij}$$

and

$$R_{ij} = -2 \nu_\tau S_{ij} + M_{ij} \qquad (6\text{-}31)$$

where

$$\nu_\tau = (c_s \Delta_f)^2 \; \overline{2\overline{S}_{ij} \overline{S}_{ij}} \qquad (6\text{-}32)$$

and

$$M_{ij} = c_r (\overline{\overline{u}_i \overline{u}_j} - \overline{\overline{u}}_i \overline{\overline{u}}_j) \qquad (6\text{-}33)$$

6.6.4 Other SGS Reynolds Stress Models

Several other SGS Reynolds stress models were tested by using the method described in the previous sections. Most showed no improvement with respect to the linear combination of the scale-similarity and eddy-viscosity models; some of these models are given in Appendix B.

In this section, we shall comment on only two further turbulence models. The first is Eq. (6-17). This model is highly correlated with the scale-similarity model, Eq. (6-18), and gives correlation coefficients almost as high as the latter one. The least-squares model constant is 1.2. It could be considered an alternative to the scale similarity model.

The second model considered is:

$$R_{ij} \sim \Delta_f^2 (\overline{S}_{ik} \overline{\Omega}_{kj} + \overline{S}_{jk} \overline{\Omega}_{ki}) \qquad (6\text{-}34)$$

where

$$\overline{\Omega}_{ij} = \frac{1}{2} \left(\frac{\partial \overline{u}_i}{\partial x_j} - \frac{\partial \overline{u}_j}{\partial x_i} \right) \qquad (6\text{-}35)$$

56

This is similar to the turbulence model of Wilcox and Rubesin (1980). Significant improvements were found when it was added to the Smagorinsky and scale-similarity models.

Tables 6.5 and 6.6 show the correlation coefficients between exact and model quantities in homogeneous isotropic and sheared turbulence, respectively. The improvements in the level of the correlation coefficients when Eq. (6-34) is added to the Smagorinsky and scale-similarity model are significant, and use of this "triple" model may be worthwhile. The least-squares model constant of this new term is 0.065.

Table 6.5

Average Correlation Coefficient between "Exact" and Model Values of the SGS Reynolds Stresses in Homogeneous Isotropic Turbulence at $R_\lambda = 38$ and $R_{SGS} = 180$

Model Level	Tensor Level	Vector Level	Scalar
Eq. (6-31) .31	.13	.43	
Smagorinsky and scale-similarity .83	.74	.50	
Smagorinsky, scale-similarity, and Eq. (6-31)	.88	.78	.70

Table 6.6

Average Correlation Coefficient between "Exact" and Model Values of the SGS Reynolds Stresses in Homogeneous Turbulence in the Presence of Mean Shear, $S = 34 \text{ sec}^{-1}$ at $R_{SGS} = 204$.

Model	Tensor Level	Vector Level	Scalar Level
Eq. (6-31) .27	.10	.53	
Smagorinsky and scale-similarity .80	.75	.58	
Smagorinsky, scale-similarity, and Eq. (6-31)	.85	.78	.68

Clark et al. (1977) found almost no correlation between Eq. (6-34) and exact values in homogeneous isotropic turbulence. However, Clark's correlations were made without subtracting the spatial averages and are therefore unreliable.

6.6.5 Further Tests of the Scale-Similarity Model

McMillan et al. (1980) performed tests of the scale-similarity model in homogeneous turbulent flows in the presence of mean strain and shear. Their results indicate that the correlation coefficients in homogeneous strained flow are nearly as large as those obtained in homogeneous shear flows, cf. Table 6.4. The correlation coefficients are reduced to 0.13-0.29 when a sharp cut-off filter in Fourier space is used instead of a smooth filter. However, more tests are required, because the filter kept only the lowest three wavenumbers in each direction.

6.7 Tests of Subgrid-Scale Turbulence Models Using Large-Eddy Simulations

In this section, scale-similarity and eddy viscosity models are tested by performing large eddy simulations of homogeneous turbulence. These simulations used the methods described in Chapter II. The results are compared against the experimental results of Comte-Bellot and Corrsin (1971), Wigeland and Nagib (1978), and Champagne, Harris, and Corrsin (1970) in homogeneous isotropic, rotating, and shear turbulent flows, respectively.

6.7.1 Homogeneous Isotropic Turbulence

The experimental results of Comte-Bellot and Corrsin (1971) on the decay of homogeneous isotropic turbulence are simulated in the way described in Section 4.3. The numerical results obtained with each turbulence model are compared to the experimental data for the resolvable turbulent kinetic energy and three-dimensional energy spectra shown in Figs. 4.1, 4.2, and 4.3, respectively.

● Eddy Viscosity Models

All of the eddy-viscosity models of Section 6.6.1 are able to simu-
late this flow well. Figure 6.7a shows the decay of the spatially aver-
aged eddy viscosity obtained from LES using the Smagorinsky, vorticity,
and TKE models given by Eqs. (6-22), (6-23), and (6-24) with model
constants $c_s = 0.21$, $c_v = 0.21$, and $c_q = 0.16$, respectively. The
numerical method used to calculate the spatial derivatives is pseudo-
spectral, except for the model terms where second-order central differ-
ences are used.

Figure 6.7b shows similar results, except that all partial deriva-
tives were computed by the pseudospectral method. The model constants
had to be reduced 10% in order to fit the experimental data.

Figure 6.8 compares the three-dimensional energy spectra using the
Smagorinsky model with both numerical methods for the model terms.
Neither result shows significant differences with the experimental
spectrum. The pseudospectral method underpredicts the experimental
results at high wavenumbers, while the second-order central difference
method predicts the experimental results accurately in this region.

● Scale-Similarity and Eddy-Viscosity Models

Large-eddy simulations (LES) of the decay of homogeneous isotropic
turbulence using the combined scale-similarity (Eqs. (6-29) and (6-30))
and Smagorinsky (Eqs. (6-22) models are considered in this section.

Figure 6.9 shows the decay of the (filtered) turbulent intensity,
using the Smagorinsky model with and without the scale-similarity model.
The experimental values of Comte-Bellot and Corrsin (1971) at the ini-
tial and final stations are also shown. Figure 6.10 shows the experi-
mental and both numerical three-dimensional energy spectra at the final
time. The results shown in Figs. 6.9 and 6.10 indicate that the com-
bined model performs as well as or better than the Smagorinsky model
alone. This is not surprising. However, the numerical prediction of
higher-order turbulence statistics does improve when the scale-
similarity model is included. One significant turbulence statistic in
homogeneous isotropic turbulence is the velocity-derivative skewness:

$$S_k = \frac{\langle \frac{\partial \bar{u}}{\partial x}^3 \rangle}{\langle \frac{\partial \bar{u}}{\partial x}^2 \rangle^{3/2}} \qquad (6\text{-}36)$$

which measures the degree of asymmetry of the velocity-derivative distribution and determines the rate of vorticity production by stretching of vortex lines (see Townsend, 1976, pp. 126-129). Batchelor (1953) measured the skewness in homogeneous isotropic turbulence and found an approximately constant value of -0.4. A number of other authors find similar values at the Reynolds numbers of interest here.

Figure 6.11 shows the time history of the velocity-derivative skewness. When the Smagorinsky model is used, the skewness starts at zero, decreases with time, and is nearing the value of -0.4 at the last time step. On the other hand, when the combined model is used, the skewness starts at zero, decreases to -0.4 in few time steps, and remains there through the simulation. This result clearly favors the combined model.

6.7.2 Rotating Homogeneous Turbulent Flows

The effects of rotation on turbulence will be analyzed in Chapter VII. In this section, we shall consider only the effects of the scale-similarity model in the LES of rotating flows.

In general, the results of simulations of homogeneous turbulent flows in the presence of rotation are similar to those of the previous section. Therefore, we shall consider only the decay of the turbulent kinetic energy and the time history of the velocity-derivative skewness.

The analysis will be based on the cases shown in Figs 5.4 and 5.5. Figure 5.5 shows good agreement between the LES results obtained by using the Smagorinsky model and the experimental results of Wigeland and Nagib (1978).

Figure 6.12 shows the time history of the (filtered) turbulence intensity obtained from LES using the Smagorinsky model with and without the scale-similarity model. The numerical method is pseudospectral, except for the turbulence model terms for which second-order central differences are used. The results are nearly identical.

60

Figures 6.13a and 6.13b show the time history of the three velocity-derivative skewnesses. In contrast to the case of homogeneous isotropic turbulence, these skewness factors decrease to −0.2 in few time steps, and then remain constant or increase slowly. The absolute magnitudes of these skewness factors are smaller when the combined model is used.

There are no experimental data of the skewness factor in homogeneous rotating turbulent flows. However, the smaller magnitudes of the skewness factors in the presence of rotation can be attributed to the inhibition of energy transfer from the large scales to the smaller scales of the turbulence. The smaller magnitudes obtained with the scale-similarity model seem more reliable.

6.7.3 Sheared Homogeneous Turbulent Flows

Now consider sheared homogeneous turbulence. Figures 6.14a and 6.14b show the time history of the turbulence intensities of the experimental results of Champagne, Harris, and Corrsin (1970), together with the filtered and "defiltered" turbulence intensities obtained from LES using the Smagorinsky and combined models. The agreement between the experimental and numerical results is slightly better for the combined model.

It is important to recall that LES starts with artificial initial conditions. Turbulence statistics similar to the experimental ones develop faster in the simulations with the combined model.

6.8 Conclusions

A scale-similarity subgrid-scale turbulence model has been developed in this chapter. This model represents the effects of the SGS turbulence on the large eddies much better than the traditional eddy-viscosity models. It is consistent with the physical assumptions of LES.

Exact tests based on full simulations of homogeneous flows show a high level of correlation between the exact SGS Reynolds stresses and the scale-similarity model predictions. On the other hand, eddy-viscosity models show little correlation in similar tests.

However, the scale-similarity model is nearly non-dissipative, so we suggested a linear combination of an eddy-viscosity model and the scale-similarity model.

LES of homogeneous isotropic and rotating turbulent flows using the Smagorinsky and combined models show little differences in the level of the turbulence intensities. However, higher-order turbulence statistics develop faster and more accurately when the scale-similarity model is included.

LES of homogeneous sheared turbulent flows with and without the scale-similarity model show some differences even at the level of the turbulence intensities. The agreement with the experimental observations is better when the scale-similarity model is included. We thus conclude that, for homogeneous flows, the combined model performs better than the Smagorinsky model, but the differences are not great.

Chapter VII

HOMOGENEOUS TURBULENCE UNDERGOING ROTATION

7.1 Introduction

Rotation has profound effects in fluid mechanics. Shear flows are well known to be stabilized or destabilized by rotation. Some of the various effects of rotation are described in the book by Greenspan (1968).

The effects of rotation on isotropic turbulence are subtle and not well understood. Three experiments in this area differ in their conclusions with respect to the effect of the rotation on the decay of the turbulence.

The first experiment, by Traugott (1958), is similar in design to that of Wigeland and Nagib (1978) described below. For this reason and because only one case is presented, we shall not discuss this experiment in detail. The primary conclusion is that rotation decreases the rate of decay of the turbulence.

Ibbetson and Tritton (1975) used a unique apparatus in which a grid was dropped through a rotating chamber to produce the turbulence. They found that the turbulence decayed more rapidly when the apparatus was rotating than when it was not. However, in this experiment, the chamber was small and the measurements were made at relatively long times. The walls of the chamber probably affected the decay of the turbulence, which should therefore not be regarded as homogeneous. This experiment cannot be used for our purposes, but it should be an interesting target for future work.

The most recent experiment in this area was performed by Wigeland and Nagib (1978), hereafter referred to as WN. They used an open circuit wind tunnel of 0.15 m diameter, of the kind typically used in homogeneous isotropic turbulence experiments. A uniform flow was passed through a rotating honeycomb and a rotating grid in order to superimpose a solid-body rotation on the uniform flow and to generate the turbulence. Afterwards, the flow was passed through a stationary test section, where the decay of the rotating turbulence was then studied.

Unlike previous experiments, thermal insulation was provided by an inside foam lining, which minimized buoyancy effects.

The primary purpose of the experimental work of WN was to resolve the apparently contradictory conclusions of the previous experiments of Traugot (1958) and Ibbetson and Tritton (1975), and to analyze the dominant physical process which caused the effects of solid-body rotation. Thus, WN utilized a number of different flow conditions in which the flow speed, turbulence-generating grid, and rotation rate were changed. The range of the principal parameters utilized in these experiments is shown in Table 7.1; Ro is the Rossby number.

Table 7.1

Parameter Range of Experiments

Parameter	Traugott (1958)	Ibbetson & Tritton (1975)	Wigeland & Nagib (1978)
Ω sec^{-1}	210	1-6.4	6-80
x/M	17.5-27.5	133-3600	20-180
t sec	0.008-0.014	4-100	0.005-0.083
$Re_M = UM/\nu$	5500	1200	900-3800
$Ro_M = U/M\Omega$	10	28-180	10-600
$Re_\lambda = \overline{q^2}/3 \, \lambda/\nu$	30	?	7-23
$Ro_\lambda = \overline{q^2}/3 \, \lambda\Omega$	1.65	?	0.23-26
$\Omega \overline{q^2}/\varepsilon$	3.6	?	0.07-16

WN's results show at least two effects of the rotation. In most cases, the turbulence intensity decays slower in the presence of increasing rates of rotation, and the change is a smooth and monotone function of the rotation rate. The integral time scales of the turbulence velocity also increase with increasing rotation. In other cases, the turbulence intensity decays faster in the presence of small rotation rates and slower in the presence of larger rates of rotation. In those cases in which the turbulence intensity decays faster in the presence of rotation, the integral time scale of the normal components of the turbulence velocity showed no increase or decrease relative to the case of no rotation. The predominant effect of rotation seems to be

the decrease in the rate of decay of the turbulence with increasing rotation rate. The increasing rates of decay sometimes seen at low rotation rates appear to be a secondary effect.

We shall show that rotation indeed decreases the rate of decay of the turbulence and that the relative increase of the rates of decay of the turbulence in some of the experimental results are explained by variations of the conditions at the entrance of the experimental test section. The latter are due to the interaction of the rotation with the wakes of the turbulence-generating grid.

The current state of the art in turbulence modeling is described in the Evaluation Committee Report of the 1980-81 AFOSR-HTTM-Stanford Conference on Complex Turbulent Flows, which states, "The fact that none of the present methods is influenced by rotation of the turbulent flow is an indication that present models are deficient in this respect." Turbulence models which take rotation into account have been proposed by Rodi (1979) and Launder et al. (1977). Rodi's model contains a term proportional to the gradient of the rotation rate, which is zero if the rotation rate is constant and therefore has no effect on the flows considered here. The model proposed by Launder et al. (1977) is not well behaved at high rates of rotation, because the energy-dissipation rate can become negative.

The effects of rotation on turbulence are both multifold and subtle. In this chapter, those effects which occur only in the presence of mean strain are excluded, and we shall study the remaining ones. For example, the Reynolds stress equations for a homogeneous turbulent flow in uniform rotation about the x_3-axis expressed in a rotating frame, i.e., the frame in which the mean flow velocity is zero, are:

$$\frac{1}{2} \left\langle \frac{du_1^2}{dt} \right\rangle = 2\Omega \langle u_1 u_2 \rangle + \phi_{11} - \varepsilon_{11}$$

$$\frac{1}{2} \left\langle \frac{du_2^2}{dt} \right\rangle = -2\Omega \langle u_1 u_2 \rangle + \phi_{22} - \varepsilon_{22}$$

$$\frac{1}{2} \left\langle \frac{du_3^2}{dt} \right\rangle = + \phi_{33} - \varepsilon_{33} \qquad (7\text{-}1)$$

$$\left\langle \frac{du_1 u_2}{dt} \right\rangle = 2\Omega \langle u_2^2 - u_1^2 \rangle + \phi_{12} - \varepsilon_{12}$$

where

$\langle \ \rangle$ means time or spatial average,

ϕ_{ij} is the pressure-strain or redistribution, and

ε_{ij} is the rate of dissipation.

When the first three of these equations are summed, the resulting equation for twice the turbulence energy $(Q^2 = \langle u_1^2 + u_2^2 + u_3^2 \rangle)$ shows no <u>direct</u> effect of rotation. Furthermore, if the turbulence is isotropic, the rotation terms disappear entirely from Eqs. (7-1). These equations seem to imply that the effect of rotation is merely to redistribute energy among unequal Reynolds stress components. Rotation enters the equations for the components of the dissipation in a fashion almost identical to the way it enters the Reynolds stress equations, so no direct effects of rotation are found here either.

Greenspan (1968) made a linear analysis of the Fourier components of the turbulence velocity and showed that rotation alters the phases but not the amplitudes of Fourier modes. Hence, rotation has no direct effect on any quadratic statistical quantity. However, odd moments of the turbulence velocities may be affected by rotation. In the equation for the energy-dissipation,

$$2 \left\langle \frac{\partial \left(2\nu S_{ij} S_{ij} \right)}{\partial t} \right\rangle = - \left\langle 2\nu \frac{\partial u_j}{\partial x_j} \frac{\partial u_i}{\partial x_i} \frac{\partial u_i}{\partial x_j} \right\rangle - \left\langle 2\nu^2 \frac{\partial S_{ij}}{\partial x_i} \frac{\partial S_{ij}}{\partial x_j} \right\rangle \qquad (7-2)$$

the first term in the right-hand side is affected by rotation and thus gives rise to an indirect effect on the dissipation.

In this chapter, we shall use numerical simulation of the interaction of homogeneous isotropic turbulence in uniform rotation as a tool for investigating the phenomena observed in the WN experiment and shall show that it is possible to duplicate the effects they observed. By taking advantage of the greater control over initial conditions that one has in computer simulations, we shall be able to offer explanations of their results.

7.2 Approach

We shall use large eddy and full simulations in this chapter. These have been described earlier. Large-eddy simulations use the Smagorinsky model. The parameters of importance are $c_s = 0.21$, $16 \times 16 \times 16$ and $32 \times 32 \times 32$ grids, and the pseudospectral method for spatial derivatives, except for model terms in which second-order central difference was used. The initial spectrum is that of Comte-Bellot and Corrsin (1971), and the initial energy and dissipation match the WN cases with Reynolds number based on the Taylor microscale 15. The experimental flow exhibited a small anisotropy that was not modeled in the computation, so comparisons between the experiment and the computational results cannot be completely quantitative. Full (defiltered) turbulence quantities were calculated from these simulations using the method developed in Chapter V. The filter width for all the cases had the same nondimensional value, $\Delta_f \varepsilon_o / Q_o^3 = 0.244$, as the one used in the simulation of homogeneous isotropic turbulence shown in Fig. 4.1; where Q_o^2 and ε_o are the initial turbulence intensity and rate of dissipation, respectively.

The second approach was full simulation. Since this approach eliminates the uncertainty that arises from the subgrid-scale model in large eddy simulation, it is the preferred method for investigating the details of the effects of rotation on turbulence. For these simulations, the initial energy spectrum had a square shape and was allowed to decay in time until turbulence statistics of homogeneous isotropic turbulence were developed. The resulting turbulent velocity field was used as initial velcoity field in all the full simulations with a $64 \times 64 \times 64$ grid. The full simulations were performed by Dr. Robert Rogallo especially for this work, and are gratefully acknowledged.

7.3 Computational Results

The first exploratory simulations were large eddy simulations and were aimed at determining the feasibility of this approach. We selected one of the WN experimental cases which shows the turbulence intensity decaying faster for small rotation rate and slower for large rotation rate. The experimental results were obtained with rotation rates of 0,

6, 20, 40, 60, and 80 sec^{-1}; the fastest decay of the turbulence was observed at $\Omega = 20$ sec^{-1}, and the slowest one decay at $\Omega = 80$ sec^{-1}; therefore, we elected to simulate the cases with $\Omega = 0$, 20, and 80 sec^{-1}. The initial turbulence intensities, initial energy-dissipation rates, constant mean-streamwise velocity, generating grid mesh size, range of Reynolds number, and range of Rossby number of these cases are shown in the following table.

Table 7.2

Experimental Data of Wigeland and Nagib (1978)

Ω	s^{-1}	0	20	80
Us	m/s	5.3	5.45	5.7
M	m $\times 10^{-3}$	6.25	6.25	6.25
X/M		20-70	20-70	20-70
Re$_\lambda$		17.4-15.1	15.9-13.8	18.0-16.0
Ro$_\lambda$		(infinite)	6.3-1.2	1.4-0.4
$\Omega q^2/\epsilon$		0	0.5-2.7	2.4-15.7
Us/Q	(at X/M = 20)	334.1	329.1	327.9
E	m^2/s^3	2.60	3.58	3.38
	(at X/M = 20)			

It was discovered that large eddy simulations with $16 \times 16 \times 16$ grids are incapable of simulating the case with rotation rate (Ω) of 80 s^{-1} for a long enough period of time, because the length scales grow rapidly and invalidate the use of periodic boundary conditions.

The next simulations used a $32 \times 32 \times 32$ grid. Figure 7.1 shows the time history of the square of the streamwise velocity divided by the turbulence intensity, together with the WN experimental results. The inverse of the turbulence intensity is plotted to emphasize the differences of the turbulence energy levels at the later times. The results of the simulation agree with the experimental data, especially if we consider that the turbulence energy levels were calculated by using the "defiltering" process given by Eq. (5-12), which introduces small errors. As in the WN experimental results, at the small rotation rate ($\Omega = 20$ sec^{-1}), the decay of the turbulence is faster than in the

unrotated flow, while at the high rotation rate ($\Omega = 80$ sec^{-1}), the decay of turbulence is slower than in the unrotated flow.

It is important to observe that the initial turbulence intensities and rates of dissipation are not independent of rotation rate in any of WN's cases, including the ones presented above. In othr words, the effects of rotation on the turbulent flow in the test section are mixed with the effects of the initial condition. In general, both the initial turbulence intensity and initial rate of dissipation increase with increasing rotation rate. The increase of the initial turbulence intensity is nearly proportional to the increase in the square of the mean-streamwise velocity. In the absence of any other effect of the rotation, the changes in the initial conditions would increase the rate of decay of the turbulence intensity. On the other hand, we shall show that a slower decay of the turbulence intensity with increasing rotation rate should be observed if the initial conditions of the turbulence of all the cases are the same at the entrance of the test section. For small rotation rates, the effects of the initial conditions may be more significant than the effects of rotation on the flow in the test section. In the case presented in Table 7.2 and Fig. 7.1, the faster decay of turbulence intensity in the presence of the relatively small rate of rotation of 20 s^{-1} is due to the larger initial rate of dissipation, while the slower decay of the turbulence intensity at 80 s^{-1} is due to the effects of the rotation on the turbulence. Most of WN's experimental data show that the initial turbulence intensity and initial rate of dissipation increase with increased rate of rotation; however, the data of Table 7.2 show that the initial dissipation rate at $\Omega = 20$ s^{-1} is larger than the one obtained at $\Omega = 80$ s^{-1}. A possible explanation may be that the dissipation rate at $\Omega = 80$ s^{-1} has already been reduced by the effects of the strong rotation in the test section.

In order to test the hypothesis that the primary effect of rotation on isotropic turbulence is to decrease the rate of dissipation, a further set of simulations was made. Initial conditions identical to those used in the no-rotation case shown in Fig. 7.1 were used for all rotation rates. Figure 7.2 shows the time history of the decay of turbulence intensity with rotation rates of 0, 20, and 80 sec^{-1}. The

results confirm the hypothesis. Figure 7.3 shows that the average length scale of the energy containing eddies, $L = Q^3/\varepsilon$, grows more rapidly with increased rotation rate.

Full simulations were used to investigate the effects of rotation on the turbulence in further detail. In these runs, the turbulence was allowed to develop in the absence of rotation for some time. When the skewness of the velocity derivative reached its equilibrium value, the rotation was "turned on." This, of course, is an impossibility in the experiment, because it violates Helmholtz's theorem, but there is no reason why one cannot simulate it. All the full simulations reported in this section had the same initial conditions; the nondimensional initial turbulence intensity was 4.88, the nondimensional rate of energy dissipation was 16.78, and the initial Reynolds number based on the Taylor microscale was 15.4. Rotation rates of 0, 20, 40, and 80 s^{-1} were superimposed on the isotropic turbulent flow. The range of Reynolds and Rossby numbers of these full simulations were 15-10 and 0.015-(infinite), respectively. Figure 7.4 shows the time history of the decay of the turbulence intensity. The turbulence intensity and the time have been nondimensionalized with the initial turbulence intensity and rate of dissipation; therefore, all the initial nondimensional turbulence intensities of Fig. 7.4 are unity at time zero. These results further confirm the hypothesis that rotation decreases the rate of decay of the turbulence.

It is reasonable to expect that rotation produces anisotropy. This is easily checked; as shown in Fig. 7.5, there are no significant difference among the components of the velocity fluctuation, but they appear to exchange energy with each other. The exchange is not periodic, but the time scale appears to be approximately the inverse of the rotation rate; this could be anticipated from the Reynolds stress equations (7-1).

We noted above that the length scales grow more rapidly when rotation is present. To investigate this in more detail, we computed the integral length scales:

$$L_{ij,1} = Q_{ij}(x_1,0,0)\ dx_1/Q^2$$

$$(7\text{-}3)$$

$$L_{ij,3} = Q_{ij}(0,0,x_3)\ dx_3/Q^2$$

where $Q_{ij}(x_1,x_2,x_3)$ is the two-point correlation function of the velocity components u_i and u_j, and Q^2 is the turbulence intensity. The results for the zero rotation case are shown in Fig. 7.6a. As expected, $L_{ij,1} \simeq L_{ij,3} \simeq 2L_{11,3} \simeq 2L_{33,1}$ in this case; all of these length scales appear to grow approximately linearly in time over the range studied. The results for $\Omega = 80s^{-1}$ are shown in Fig. 7.6b. In this case, the most dramatic increase is in the length scale in the rotation direction, involving velocity components perpendicular to the rotation axis, $L_{11,3}$.

7.4 Theory

We shall now give a plausible explanation of the results described in the previous section. As with nearly all problems in turbulence, it is not possible to give a quantitative theory of the phenomenon, but it is possible to explain the main features.

It is well known (Greenspan, 1968) that inertial waves are generated in a rotating fluid; so far as is known, this is the only essentially new feature caused by rotation. In the absence of these waves, energy is cascaded from large eddies to small ones. The cascade process requires the turbulent eddies to be correlated in phase. It is proposed that the transport of energy by the inertial waves destroys the phase coherence and so inhibits energy transfer from large eddies to small ones; dissipation is thereby diminished, and the length scales are increased relative to what they would be in the absence of rotation.

To see how this picture fits together, we note that linear inviscid equations for rotating flows have wave solutions of the form

$$\hat{\underline{u}}(kL,Qt/L)\ \exp(-i(\underline{k}\cdot\underline{x} + \sigma|\underline{\Omega}|t))$$

with nondimensional frequency σ,

$$\sigma = 2\underline{\Omega}\cdot\underline{k}/|\underline{\Omega}||\underline{k}|$$

$$(7\text{-}4)$$

71

As in all turbulent flows, spectral transfer of energy to a wave with frequency σ at wave vector k can be caused by wave interactions with frequencies σ' and σ'' at corresponding wave vectors $\underline{k}'$ and $\underline{k}''$ only if

$$\underline{k}' \pm \underline{k}'' = \underline{k} \qquad (7\text{-}5)$$

However, the transferred energy must be in phase with the existing wave at wavenumber $\underline{k}$ to be effective. Thus we must also have

$$\sigma' \pm \sigma'' = \sigma \qquad (7\text{-}6)$$

In this case, we have resonant interactions. Non-resonant interactions are weak compared to the resonant interactions.

Rogallo (pp. 11-12, 1981) examined the contribution of the nonlinear terms to the time derivative of the wave and found that, "...only interactions between waves $\underline{k}$, $\underline{k}'$, and $\underline{k}''$ having ... $\sigma \pm \sigma' \pm \sigma'' \ll 1$ ... are significant on the long-time scale".

Pedlovsky (section 3.26, 1979) analyzed nonlinear interactions for two-dimensional inviscid shallow-water theory and also found equations (7-5) and (7-6) as necessary conditions for resonant interactions.

Thus, system rotation diminishes the effectiveness of the nonlinear transfer of energy; the net result is a decrease in the amount of energy cascaded from the large eddies to the small eddies and therefore a reduced rate of decay of the turbulence energy.

Finally, we observe that waves whose wave vectors are perpendicular to the rotation direction are not restricted by Eq. (7-6); Thus, system rotation should generate anisotropy in the length scales of the turbulence. From a physical point of view and considering the turbulence as composed of vortex filaments, Reynolds (1983) suggests that mean rotation produces gyroscopic forces on vortex filaments and tends to align them along the mean-rotation direction; thus, axisymmetric statistics of the small-scale fluctuations might be expected. Greenspan (1968) shows that at very low Rossby numbers the waves tend to organize themselves in the two-dimensional manner required by the Taylor-Proudman theory. The observed effects in the simulations accord with the theory: the correlations along the rotation direction of the transverse velocity are more

affected than that of the longitudinal velocity; the length scales increase with increased rotation rates, but those in the rotation direction increase faster, a reflection of the Taylor-Proudman type of organization.

7.5 Implications for Turbulence Modeling

The great majority of calculations of turbulent flows use averaged equations, which require modeling for closure; for reviews of this subject see Reynolds (1976) and Rodi (1981). We restrict ourselves to the part of the subject needed for the flow under study here.

Since the evidence indicates that the components of the turbulence remain nearly equal when rotation is imposed, there is no need for a model which computes any more than the turbulence intensity, Q^2. On the other hand, we found that the length scales of the turbulence become anisotropic under the influence of rotation. One model which allows for anisotropy of the length scales is based on the tensor volume of turbulence (Lin and Wolfstein (1980)), but Reynolds (1982) has shown that some of the quantities in this model may not be finite in all situations, so we prefer not to use it. Another model based on the integral length scales of the turbulence (Donaldson, 1973; Sandri et al., 1981) is currently at an early stage of development in which the length scales are assumed isotropic.

For these reasons, we shall use a model of the turbulence based on differential equations for the turbulence intensity Q^2 and dissipation ε; these are related to the length scale ℓ by $\ell = Q^3/\varepsilon$, a common assumption in turbulence modeling. The equation for the turbulence intensity is both simple and exact:

$$\frac{dQ^2}{dt} = -2\varepsilon \tag{7-7}$$

The dissipation equation must be modified to account for the effects of rotation. From the results of Fig. 7.3, one might guess that the effect is linear in the rotation rate, suggesting that the dissipation be modeled by:

$$\frac{d\varepsilon}{dt} = - c_1 \frac{\varepsilon^2}{Q^2} - c_2 \Omega\varepsilon \qquad (7\text{-}8)$$

where Ω is the rotation rate. For applications in inhomogeneous flows, the rotation rate may be replaced by $(\Omega_{ij}\Omega_{ij}/2)^{1/2}$, where

$$\Omega_{ij} = \frac{1}{2}\left(\frac{\partial U_i}{\partial x_j} - \frac{\partial U_j}{\partial x_i}\right)$$

is the rotation tensor of the mean flow. For $\Omega = 0$, Eq. (7-8) reduces to a commonly used two-equation model. The constant c_1 is obtained by requiring the model to predict the decay of isotropic turbulence at high Reynolds number; Reynolds (1976) found $c_1 = 11/3$. The new term causes the turbulence intensity to decay more slowly as the rate of rotation increases. Furthermore, if the rotation rate is high enough, the turbulence intensity does not decay. The system of equations (7-7) and (7-8) has the following analytical solution:

$$Q^2 = Q_o^2 \left(1 + \frac{2}{n}\frac{\varepsilon_o}{Q_o^2}\left(\frac{1 - e^{-c_2\Omega t}}{c_2\Omega}\right)\right)^{-n} \qquad (7\text{-}9)$$

where $n = 2/(c-2)$.

This two-equation model with $c_2 = 0.15$ has been tested against all of the WN experimental results, with excellent agreement. The initial values of Q and ε, together with Reynolds numbers and Rossby numbers of three test cases are shown in Table 7.3.

In Figs. 7.7 we shall show the prediction of the model for the three sets of WN cases described in the above table. Figure 7.7a shows the prediction of the two-equation model for Case A, in which the turbulence intensity appears to decay at a slower rate as the rotation rate is increased. Figure 7.7b shows the prediction of the two-equation model for Case B, in which the turbulence intensity appears to decay faster at a rotation rate of 20 s^{-1} and slower at a rotation rate of 80 s^{-1}; as shown earlier, the faster decay of the turbulence intensity in the presence of a rotation rate of 20 s^{-1} is really an effect of the initial conditions. Figure 7.7c shows the prediction of the two-equation model for the WN Case C, which was used as a test case in the 1980-81 AFOSR-Stanford-HTTM Conference on Complex Turbulent Flows. No

entry to the conference was able to predict this flow, but the model suggested here has no difficulty with it.

Table 7.3

Experimental Data of Wigeland and Nagib (1978)

Case A, M 0.0039 m			
Ω (s^{-1})	0	20	80
U (m/s)	8.69	8.66	8.82
U_s (m/s)	8.69	8.67	8.96
Q^2 (m^2/s^2) at Ut/M = 20	0.2125	0.2021	0.2314
ε (m^2/s^3) at Ut/M = 20	17.67	16.45	18.19
Re	17-14	17-14	18-15
Ro	∞	13.5-1.7	3.6-0.6
$\Omega Q^2/\varepsilon$	0	0.25-1.9	1.0-9.5
Case B, M = 0.00625 m			
Ω (s^{-1})	0	20	80
U (m/s)	5.33	5.45	5.48
U_s (m/s)	5.33	5.46	5.71
Q^2 (m^2/s^2) at Ut/M = 20	0.0850	0.0906	0.0994
ε (m^2/s^3) at Ut/M = 20	2.649	3.591	3.300
Re	17-15	16-14	18-16
Ro	∞	6.3-1.2	1.5-0.4
$\Omega Q^2/\varepsilon$	0	0.5-2.7	2.9-15.7
Case B, M = 0.00254 m			
Ω (s^{-1})	0	20	80
U (m/s)	8.51	8.58	8.79
U_s (m/s)	8.51	8.59	8.93
Q^2 (m^2/s^2) at Ut/M = 20	0.1770	0.1774	0.1969
ε (m^2/s^3) at Ut/M = 20	24.27	22.56	224.2
Re	12-9	12-10	14-11
Ro	∞	16-1.2	4-0.4
$\Omega Q^2/\varepsilon$	0	0.16-1.9	0.07-8.4

The rotation term in Eq. (7-8) may play an important role in shear flows. As shown by Ferziger and Shaanan (1976), the effect of the rotation tensor inherent in the flow (which is equivalent to the vorticity) adds to the externally imposed rotation. It is possible that the new term proposed here will help in explaining differences between strained and sheared flows. Calculations of these flows are shown in Chapter IX.

7.6 Conclusions

We have shown that full and large eddy simulation can be used to aid understanding the effect of rotation on homogeneous isotropic turbulence. The primary effect of rotation on the turbulence is a decrease in the dissipation and increase of the length scales, principally those in the direction of the axis of rotation. In the experimental results, there is a complex interaction between rotation and turbulence in the generation of rotating turbulence, which decreases the initial length scales of the turbulence and increases the initial turbulence intensity; the details of this interaction are not understood. The primary effect of rotation on turbulence is a decrease in dissipation, leading to an increase in the length scales, principally those in the direction of the axis of rotation.

The observed effects can be explained in terms of inertial waves created by the turbulence transporting energy and thus destroying the phase coherence needed to cascade energy to the small scales.

Finally, a two-equation model which is capable of reproducing the observed effects has been offered.

Chapter VIII

HOMOGENEOUS TURBULENT SHEAR FLOW

8.1 Introduction

Most flows of engineering interest are high Reynolds number turbulent shear flows. In these flows there is production of turbulence due to the gradients of the mean velocity field.

Homogeneous turbulence with mean shear S is a simple shear flow in which one can investigate the effect of shear on the turbulence. Several researchers have studied homogeneous shear flows using linear rapid distortion theory, with apparent success. Deissler (1961, 1970, 1972), Townsend (1976), and Rogallo (1981) are examples of such analyses. Any shear S can be decomposed into a plane strain $\Gamma = S/2$ and a rotation $\Omega = S/2$. Most of the effects predicted by linear theory are due to the strain. For small strain ratios Γt, the linear theory shows that the behavior of initially isotropic turbulence changes in the same way whether shear or strain are applied (see Townsend (1976), p. 77, Eq. (3.1.9) and p. 84, Eq. (3.12.5)). For large strain ratios Γt, differences appear; however, the results are questionable, because non-linear effects become important and the theory is no longer valid.

Experimental investigations of homogeneous turbulent shear flows have been carried out by Rose (1966, 1970), Champagne, Harris, and Corrsin (1970), Mulhearn and Luxton (1975), Harris, Graham, and Corrsin (1977), and Tavoularis and Corrsin (1981).

Champagne et al. and Mulhearn et al. found that the components of the turbulence intensity reach an apparently asymptotic state in which turbulence production and dissipation are equal. However, the integral length scales and Taylor microscales develop anisotropy and continue to increase with shear ratio, St.

For large shear ratios, Harris et al. and Tavoularis et al. find that the components of the turbulence intensity and the length scales increase continually with the shear ratio. The Reynolds numbers R_λ based on the Taylor microscale and the magnitude of the turbulent

velocity in the shear direction vary from about 70 to 300 in their experiments.

Another approach to investigating these flows is full simulation. This approach is limited to $R_\lambda < 70$ on present computers. Rogallo (1981), Feiereisen et al. (1981), and Shirani et al. (1981) have obtained results qualitatively similar to the experiments by this technique. The normal components of the Reynolds stress tensor develop anisotropy and appear to reach a state in which their ratios remain constant, but the off-diagonal components increase continually with shear ratio. Rogallo's results show good quantitative agreement with the Reynolds stress anisotropy of Tavoularis et al.

Large eddy simulation should be able to reproduce the experimental results at higher Reynolds numbers. Shaanan et al. (1976) used this technique to simulate the experimental results of Champagne et al. (1971). Qualitative agreement was obtained, but their simulation did not use proper boundary conditions. Also, they did not filter the experimental results or defilter the numerical results in order to allow quantitative comparisons, and they were limited to a $16 \times 16 \vee 16$ numerical grid.

We shall simulate the experimental results of Champagne et al. The defiltering method developed in Chapter V will be used to predict the development of the turbulence intensity, and the results will be compared to experimental data. These results will also be used to analyze turbulence models.

Understanding of homogeneous turbulent shear flows is useful in the development of turbulence models. We used these flows in Chapter IV to test subgrid scale models for large eddy simulation. Here we shall use them to determine some of the constants of time average models. These models are able to reproduce data for homogeneous strained flows, but they have no provision for rotation. Since shear is a combination of plane strain and rotation and we presented a model for rotation in Chapter VII, it is natural to investigate whether the addition of rotation to the model has any effect on the predictions of models for homogeneous shear flow.

8.2 Approach

We shall use large eddy simulation of homogeneous turbulence experiencing a constant mean shear $S = \partial U_1 / \partial \tilde{x}_2$, as the main tool in this chapter. The initial shape of the three-dimensional energy spectrum is that of Comte-Bellot and Corrsin (1971). The initial turbulence intensity and energy-dissipation rate are chosen to match the experimental results of Champagne, Harris, and Corrsin (1971), hereafter referred to as CHC.

Taylor's hypothesis is invoked in order to compare the time history results of the simulation with the downstream development of the experiment. There is little doubt of its validity in these flows. The subgrid scale turbulence is modeled using the Smagorinsky model with and without the scale similarity model described in Chapter VI. The simulations are alias-free and were run with a $32 \times 32 \times 32$ grid on the ILLIAC-IV at NASA-Ames Research Center.

8.3 Large Eddy Simulation Results

Figures 8.1a and 8.1b show the time history of the CHC turbulence intensity, together with the filtered and defiltered turbulence intensities obtained by large eddy simulation with and without the scale-similarity model. The shear rate $S = 12.4$ s^{-1} in all cases. Defiltering was accomplished using Eq. (5-12). The agreement between the numerical and experimental results is very good, especially in the cases in which the scale-similarity model is included.

Figures 8.2a and 8.2b show the time history of the anisotropy of the Reynolds stresses of the filtered flow field. The anisotropy of the Reynolds stresses is defined as

$$b_{ij} = (< \overline{u}_i \overline{u}_j > - \tfrac{1}{3} Q_f^2 \delta_{ij})/Q_f^2 \qquad (8\text{-}1)$$

Lacking a defiltering process for the anisotropic component of the flow field, we cannot compare these statistics with the experiment. Figure 8.2c shows the time history of the b_{ij} obtained by CHC. The full flow field shows less anisotropy than the filtered flow field, since the smaller eddies are more isotropic than the larger ones.

79

Figure 8.3a and 8.3b show the time history of each term of the turbulent kinetic energy budget of the filtered flow field. As in the experiment of CHC, the turbulence production and dissipation almost balance after $St = 3$; there is a slow growth of the turbulence intensity in the prediction based on the scale-similarity model.

Figures 8.4, 8.5, and 8.6 show the time history of the budget for $< \overline{u_1^2} >$, $< \overline{u_2^2} >$, and $< \overline{u_3^2} >$, respectively. In the $< \overline{u_1^2} >$ budget, the turbulence production and the pressure-strain term balances the turbulence dissipation. On the other hand, the turbulence dissipation tends to balance the pressure-strain term in the $< \overline{u_2^2} >$ and $< \overline{u_3^2} >$ equations. The production, pressure-strain, and dissipation terms are smaller than the respective terms of CHC. The differences between the full and filtered flow fields can be ascribed to differences in the Reynolds and shear numbers. The full field has a Reynolds number

$$R_\lambda = \frac{\lambda_{22,1}}{\nu} \sqrt{\frac{Q^2}{3}} \approx 130 \qquad (8-2)$$

and a shear number

$$\frac{S\lambda_{22,1}}{\sqrt{Q^2/3}} \approx 0.71 \qquad (8-3)$$

at $St = 3$, while the filtered flow field has a Reynolds number

$$R_{\lambda_f} = \frac{\lambda_{22,1f}}{(\nu + \nu_\tau)} \sqrt{\frac{Q_f^2}{3}} \approx 10 \qquad (8-4)$$

and a shear number

$$\frac{S\lambda_{22,1f}}{\sqrt{Q_f^2/3}} \approx 3 \qquad (8-5)$$

The larger shear number of the filtered flow field explains the stronger anisotropy, while the smaller Reynolds number explains the smaller magnitudes of the components of the energy budget.

8.4 One-Point Reynolds Stress Closure Model

Here, we shall apply our numerical results to Reynolds stress models because this flow is highly anisotropic. Specifically, we shall consider the turbulence models of Launder, Reese, and Rodi (1975), hereafter referred to as LRR, Wilcox and Rubesin (1980), hereafter referred to as WR, and Reynolds (1976), hereafter referred to as R. For homogeneous turbulent flows, these three models have the same structural form, and differ only in the values of the model constants. For this case, these models reduce to a set of six equations. These are:

Kinetic energy equation:

$$\frac{dQ^2}{dt} = 2P - 2\varepsilon \tag{8-6}$$

Anisotropy equations (5):

$$\frac{db_{ij}}{dt} = - \frac{2P + (C_4 - 2)\varepsilon}{Q^2} b_{ij} - (1 - C_{p1})P_{ij} - C_{p2}D_{ij} - C_{p3}S_{ij} \tag{8-7}$$

Dissipation equation:

$$\frac{d\varepsilon}{dt} = - \left(C_1 + C_2 \frac{\Omega Q^2}{\varepsilon} - C_3 \frac{P}{\varepsilon}\right)\frac{\varepsilon^2}{Q^2} \tag{8-8}$$

where

$$P_{ij} = - R_{i\ell}\frac{\partial U_j}{\partial \tilde{x}_\ell} - R_{j\ell}\frac{\partial U_i}{\partial \tilde{x}_\ell} \tag{8-9}$$

is the production and

$$D_{ij} = - R_{i\ell}\frac{\partial U_\ell}{\partial \tilde{x}_j} - R_{j\ell}\frac{\partial U_i}{\partial \tilde{x}_i} \tag{8-10}$$

$$P = 2P_{ii} = 2D_{ii} \tag{8-11}$$

$$P_{ij} = \left(P_{ij} - \frac{2}{3}\delta_{ij}P\right)/Q^2 \tag{8-12}$$

$$d_{ij} = \left(D_{ij} - \frac{2}{3}\delta_{ij}P\right)/Q^2 \tag{8-13}$$

$$\Omega_{ij} = \frac{1}{2}\left(\frac{\partial U_i}{\partial \tilde{x}_j} - \frac{\partial U_j}{\partial \tilde{x}_i}\right) \tag{8-14}$$

is the rotation and

$$\Omega = \sqrt{\Omega_{ij}\Omega_{ij}/2} \tag{8-15}$$

The constants of the three models mentioned above and the new proposed model are given in Table 8.1.

Table 8.1

MODEL CONSTANTS FOR REYNOLDS STRESS MODELS

Model	C_1	C_2	C_3	C_4	C_{p1}	C_{p2}	C_{p3}
LRR	3.8	0	2.88	3	8.4/11	$8C_{p1} - 6$	$6C_{p1} - 4.4$
WR	11/3	0	35/11	9	0.5	0.5	2/3
R	11/3	0	2.0	2.5	2.3/3	$8C_{p1} - 6$	$6C_{p1} - 4.9$
Proposed	11/3	0.15	3	2.5	2.3/3	$8C_{p1} - 6$	$6C_{p1} - 6.9$

The new model is an extension of model R to include the rotation term in the ε-equation proposed in Chapter VII. It also includes a modification of the value of the model constant C_3 based on the experimental results of homogeneous strained turbulence. Each model constant has been determined from experimental results. We shall briefly describe their significance.

● C_1 determines the rate of decay of the turbulence intensity in homogeneous isotropic turbulence. All models predict

$$Q^2 = Q_o^2 \left(1 + \frac{2\varepsilon_o}{2Q_o^2} t\right)^{-n} \tag{8-16}$$

where

$$n = \frac{2}{C_1 - 2} \tag{8-17}$$

The experimental results of Comte-Bellot and Corrsin (1971) and others indicate that $1.1 \leq n \leq 1.3$ so that $3.5 \leq C_1 \leq 3.8$. Reynolds (1976) proposed $C_0 = 11/3 = 3.67$ based on a theoretical argument that leads to $n = 1.2$.

- C_2 determines the rate of decay of the turbulence intensity in homogeneous rotating flows, as shown in Chapter VIII. The value found there is $C_2 = 0.15$. None of the other models uses this constant.

- C_3 determines the rate of change of the turbulence intensity in homogeneous strained turbulent flows.

Figure 8.7 shows the time history of the turbulence intensity and anisotropy of the Reynolds stresses of Tucker and Reynolds (1976) with a plane strain rate $\Gamma = 4.45$ s^{-1} and initial dissipation $\varepsilon_0 = 0.63$ m^2/s^3, together with the prediction of the four models LRR, WR, R, and the new model. All models give a good prediction of the experimental results.

Figure 8.8 shows the experimental results obtained from Gence and Mathieu (1979) with a much larger plane strain rate $\Gamma = 32.23$ s^{-1} and initial dissipation $\varepsilon_0 = 5.5$ m^2/s^3. Models LRR and the new model produce excellent predictions of the experimental results, while models WR and R are not as satisfactory. Changes of the initial energy-dissipation rate do not improve the predictions of models WR and R.

- C_4 determines the rate of return to isotropy of homogeneous turbulence. In the absence of mean strain or rotation, all of the models predict

$$b_{ij} = \left(\frac{Q^2}{Q_0^2}\right)^{-(C_4-2)/2} b_{ij_0} \qquad (8\text{-}18)$$

Thus, return to isotropy $(b_{ij} = 0)$ is obtained as $C_4 > 2$.

None of the turbulence models tested in the 1980-81 AFOSR-HTTM-Stanford Conference on Complex Turbulent Flows was able to predict accurately the return to isotropy of Uberoi and Wallis (1966) and Tucker and Reynolds (1968). Lumley (1978) proposed making C_4 a function of the Reynolds number and the second and third invariants of the anisotropy of the Reynolds stresses, i.e., $b_{ij}b_{ij}$ and $b_{ij}b_{jn}b_{ni}$. However, there

are serious doubts that a model with a single length scale can predict all these cases, as the length scales are known to be anisotropic.

C_{p1}, C_{p2}, and C_{p3} model the rapid part of the pressure strain terms. LRR proposed the relationships given in Table 8.1, which relate C_{p2} and C_{p3} to C_{p1}. The value of C_{p1} is determined by comparison with experimental results. In particular, Reynolds (1976) determined C_{p1} using the experimental results of Champagne, Harris, and Corrsin (1970).

The results for homogeneous sheared turbulence are highly sensitive to the initial conditions, especially the initial dissipation ε_o, which is usually not reported in the experimental results. Following Launder (1975), we shall determine ε_o by fitting to the data.

Figures 8.9 shows the time evolution of the Reynolds stresses of Champagne, Harris, and Corrsin (1970), together with the predictions of the models. Model LRR with $\varepsilon_o = 0.91$ m^2/s^3 gives a good prediction of shear stress $< -u_1u_2 >$, and the normal stresses $< u_2^2 >$ and $< u_3^2 >$; however, it underpredicts $< u_1^2 >$ by 20%, and the turbulence intensity Q^2 by 10% at $St = 2$. Since the LRR model predicts the production of turbulence accurately, the underprediction of the turbulence intensity must be due to the overprediction of the dissipation rate. The proposed model with $\varepsilon_o = 1.06$ m^2/s^3 gives predictions similar to those of LRR. Models WR and R with $\varepsilon_o = 0.65$ and 1.14, respectively, are also shown for comparison.

Figures 8.10 shows the time history of the Reynolds stresses of Harris, Graham, and Corrsin (1977), together with the predictions of the models. The initial dissipation ε_o has been determined by fitting the numerical calculations to the experimental turbulence production. Models B, LRR, WR, and the new model R used $\varepsilon_o = 1.5$, 2.6, 4.3, 3.0 m^2/s^3, respectively. In this case, the predictions seem better, but this is largely because the experimental data contain considerable uncertainty.

Chapter IX

HOMOGENEOUS SHEARED TURBULENCE IN ROTATING FLOWS

In this chapter, we shall analyze the effects of rotation on turbulence production in homogeneous shear flows. These flows are of relevance in geophysics and turbomachinery. The main effect of rotation is an increase or decrease of the turbulence production, depending on the relative directions and magnitudes of the rotation and the shear.

An analogy between system rotation, streamline curvature, and buoyancy in turbulent shear flows was made by Bradshaw (1969), and the results for rotating flows may therefore apply to other flows as well.

9.1 Introduction

The augmentation or suppression of the turbulence production by rotation in shear flows has been shown both experimentally and numerically. Halleen and Johnston (1967) found these effects in a fully developed flow in a rotating rectangular duct. Their results can be fit using a modified mixing length model proposed by Bradshaw (1969).

$$\frac{\ell}{\ell_o} = 1 - \beta \, Ri \qquad (9-1)$$

where β is a constant $(2 < \beta < 6)$, and Ri is the local gradient Richardson number defined by

$$Ri = -2\Omega(S - 2\Omega)/S^2 \qquad (9-2)$$

where Ω is the system rotation rate, and $S = \partial U_1/\partial \tilde{x}_2$ is the rate of shear and Ω is the rotation rate about the x_3-axis.

The mixing length is defined by

$$\ell \equiv \langle -u_1 u_2 \rangle^{1/2}/S^3 \qquad (9-3)$$

and the production of turbulence P is

$$P \equiv \langle -u_1 u_2 \rangle S = \ell^2 S^3 \qquad (9-4)$$

85

Equation (9-1) indicates that the local stability parameter is the Richardson number defined by Eq. (9-2). For $Ri < 0$ ($\frac{\Omega}{S} < 0$ or $\frac{\Omega}{S} > \frac{1}{2}$), the rotation destabilizes the turbulence, i.e., it increases the mixing length, production, and turbulence intensity. Maximum production obtains when $R_i = -1/4$ ($\frac{\Omega}{S} = \frac{1}{4}$).

Large eddy simulations of Shaanan et al. (1975) with a $16 \times 16 \times 16$ grid, shear rate $S = 12.9 \text{ s}^{-1}$, and various Richardson numbers, gave results which are in qualitative agreement with the experimental data. They found Eq. (9-1) valid with $\beta \simeq 1.7$. However, Shaanan et al. improperly used periodic boundary conditions.

Ferziger and Shaanan (1976) analyzed the two-dimensional Reynolds stress equations with constant shear and rotation rates while neglecting the pressure redistribution and dissipation terms. In this case, the Reynolds stresses have exponential solutions of the form $e^{\gamma t}$, where

$$\gamma = \pm\sqrt{\Gamma^2 - R^2} \qquad (9-5)$$

$\Gamma \equiv S/2$ is the plane strain component of the shear rate, and

$R \equiv S/2 - 2\Omega$ represents the rotation component of the shear rate minus the superimposed rotation, which can be shown to be 2Ω.

Maximum production results when $R = 0$ ($\frac{\Omega}{S} = \frac{1}{4}$), which is the case of pure strain in the fixed frame. Any rotation relative to this case inhibits production; in particular, there is no production for $R^2 > \Gamma^2$ ($\frac{\Omega}{S} < 0$ or $\frac{\Omega}{S} > \frac{1}{2}$). The growth parameter γ can be expressed as $\gamma = 2S \sqrt{-Ri}$.

Tritton (1981) disputed some of the statements made by Ferziger and Shaanan (1976). In particular, he argues that, "They then show that the most vigorous turbulence production occurs in the case of zero mean flow vorticity (for a given mean flow rate-of-strain)" and that they claim "the effect of externally imposed rotation (i.e., Coriolis forces) simply adds to the rotation tensor, so the case we are considering is quite general." Therefore, Tritton argues that, "If correct, this statement would imply that the configuration ... would be most strongly destabilized when $\Omega = -S/2$. There is thus a discrepancy, "because a

linear superposition of a constant shear rate S and a constant rotation rate Ω on a turbulent flow has zero mean flow vorticity when Ω/S = 1/2 and maximum production is obtained when Ω/S = 1/4."

This discrepancy is resolved if we recall that the Reynolds stress equations show a linear superposition of a constant shear rate S and a constant rotation rate 2Ω, not Ω, in a fixed frame. Then zero mean flow vorticity is obtained when Ω/S = 1/4 (Ri = -0.25) in a fixed frame of reference. Tritton is correct in saying that, "A linear superposition of a shear flow and a rigid-body rotation ... in an inertial frame ... is not equivalent to a shear flow with externally imposed rotation." However, Ferziger and Shaanan show that both flows yield the same Reynolds stress equations, when the magnitude of the superimposed rigid-body rotation in a fixed frame is twice the magnitude of the externally imposed rotation in the rotating frame. This analogy helps to explain the stabilizing effect of rotation with respect to the Ri = -0.25 case, even though the latter case does not represent a pure strain flow in a rotating frame.

Bertoglio, Charnay, and Mathieu (1979) and Bertoglio (1982) made a linearized spectral analysis of homogeneous turbulent shear flows in a rotating frame. The initial spectrum corresponds to the experiment of Comte-Bellot and Corrsin (1971) and is the same one used in our simulations. The initial nondimensional shear rate is SQ^2/ε = 43.46. Their analysis used the two-point correlation equations with mean shear in a rotating frame and $-0.5 \leq \Omega/S \leq 0.5$. In these simulations, the triple velocity correlations were neglected, periodic boundary conditions were applied, and no coordinate transformation was used; thus, the transfer of energy between eddies of various sizes was omitted. These equations, like all rapid distortion models, do not represent the long time evolution of the turbulence, but they are useful at shorter times.

Their turbulence intensity, Reynolds shear stresses, and averaged pressure-strain terms are smooth "Gaussian-shaped" functions of Ω/S; they reach a maximum when Ω/S = 1/4. However, the maximum magnitudes of $< u_1^2 >$ and $< u_2^2 >$ are obtained for Ω/S = 1/12 and Ω/S = 5/12, respectively. The averaged pressure-strain terms ϕ_{ij} show relative maxima where the corresponding Reynolds stresses are maximum.

In summary, numerical and experimental evidence indicates that max-imum growth of turbulence intensity obtains when $Ri = -0.25$ ($\Omega/S = 1/4$). Rotation destabilizes the turbulence when $Ri < 0$, stabilizes the turbulence when $Ri > 0$, and is neutral when $Ri = 0$. However, the limits $Ri = 0$ when $\Omega/S = 1/2$ or $\Omega/S = 0$ represent different physi-cal flows; the former one is a shear flow in a rotating system, while the latter one is a pure shear flow in a fixed system.

The effect of rotation on turbulence production can be understood by first considering the case of pure strain. In this case, the turbu-lence intensity increases in the direction(s) undergoing compression and decreases in the directions suffering extension. This can be explained by vortex-stretching arguments and causes the principal axes of the Reynolds stress tensor to be aligned with those of the imposed strain. As the turbulence is distorted by the strain, it becomes more capable of absorbing energy from the imposed strain flow. This would lead to expo-nential growth but is limited by nonlinear effects, including spectral transfer and pressure redistribution. When rotation is added to this flow, the principal axes of the Reynolds stress are rotated away from those of the strain field. The resulting misalignment of the principal axes of the strain and the Reynolds stress reduces the efficiency with which the turbulence can absorb energy from the strain field and reduces its rate of growth.

We shall analyze homogeneous turbulent shear flows in solid-body rotation using large eddy simulation.

9.2 Large Eddy Simulation Results

We shall make large eddy simulations of homogeneous turbulent shear flow subject to solid body rotation. The rotation is about the x_3-axis (in either the fixed or rotating coordinate system), while the shear rate is in the rotating frame of reference.

The equations of motion and the numerical method were described in Chapter II; the shearing transformation is used. The pseudospectral method was used on a $32 \times 32 \times 32$ grid. The initial conditions of the turbulence were $Q^2 = 0.1539 \ m^2s^{-2}$, $\varepsilon = 0.4919 \ m^2s^{-3}$, and the initial energy spectrum with $\Delta_f = 0.03$ m is shown in Fig. 4.2; they correspond

to the experiment of Comte-Bellot and Corrsin (1971). Two subgrid-scale models were used, and they are described in the captions of Figs. 9.1a and 9.1b. Figures with subindex a use the Smagorinsky model with $c_s = 0.19$, while figures with subindex b use the Smagorinsky and scale-similarity model with $c_s = 0.165$ and $c_r = 1.1$. The values of the imposed rotation rate Ω and shear rate S are given in Table 9.1. These flows represent an ample range of the most important effects on homogeneous sheared turbulence. They include the case with the the most destabilizing effects of rotation (Ri = -0.25, Ω/S = 1/4), the neutral effects of rotation (Ri = 0, Ω/S = 1/2), no system rotation or pure shear flow (Ri = 0, Ω/S = 0), pure rotation or no mean strain effects (Ri = ∞), and "isotropic" turbulence or no mean velocity gradients (S = Ω = 0).

Table 9.1

Rotation Rate Ω and Shear Rate S Used

$(\alpha = 12.9 \ s^{-1})$

Ω	S	Ri	$\Omega Q_0^2/\varepsilon_0$	$S Q_0^2/\varepsilon_0$
0	0	—	0	0
0	α	0	0	4.036
$\alpha/2$	α	0	2.018	4.036
$\alpha/4$	α	-1/4	1.009	4.036
$-\alpha/2$	0	∞	-1.018	0

No attempt to defilter the numerical results has been made, due to the lack of data to which the results could be compared.

Figure 9.1 shows the time evolution of the turbulence intensity for the cases shown in Table 9.1. In these simulations the flow field was allowed to develop from $St = -2.2$ through $St = 0$, before the shear and/or rotation were applied. As expected, maximum increase of the turbulence intensity is obtained when Ri = -0.25 (Ω/S = 1/4). In contrast to Bradshaw's (1969) and Ferziger and Shaanan's (1976) analyses, the turbulence intensity increases faster in the pure shear flow (Ri = 0, Ω/S = 0) than in the case of shear in a rotating frame (Ri = 0, Ω/S = 1/2). The case of pure rotation $S = 0$ and $\Omega = -\alpha/2$ shows only small

difference from that of the decay of isotropic turbulence, because the rotation rate is small compared to those in the cases simulated in Chapter VII.

Figure 9.2 shows the time evolution of the shear component of the Reynolds stress anisotropy b_{12}. The growth of the turbulence intensities shown in Fig. 9.1 can be largely explained by the behavior of the shear stress, which in turn governs the production of turbulence. This is especially significant in the $Ri = 0$ with $\Omega/S = 0$ and $\Omega/S = 1/2$, because there are no other significant differences in the turbulence statistics of these two cases, as will be seen in the following figures.

Figures 9.3, 9.4, and 9.5 show the time history of the normal components of the Reynolds stress anisotropy tensor; they are relatively small, except when $Ri = 0$. As could be anticipated by examining the production terms in the Reynolds stress equations, $b_{11} \approx - b_{22} > 0$ and $b_{33} \approx 0$ in the case of pure shear $(\Omega/S = 0)$, while $b_{22} \approx -b_{11} > 0$ and $b_{33} \approx 0$ in the case of shear in a rotating frame $(\Omega/S = 1/2)$. The absolute magnitudes are of the same order of magnitude in both cases. A similar analysis of the production terms of the Reynolds stress equations indicates that $2b_{11} \approx 2b_{22} \approx -b_{33} > 0$ in the case of shear in a rotating frame $(Ri = -0.25, \Omega/S = 1/4)$, as shown in Figs. 7.3 for $\alpha t > 3$; however, for $Ri = -0.25$, the absolute magnitudes of b_{11} and b_{22} are much smaller than the absolute magnitudes obtained for $Ri = 0$. These figures also show the Coriolis effects on the normal stresses in the case of pure rotation when $Ri = \infty$ $(S = 0)$, as compared to the isotropic case when $\Omega = S = 0$.

Figures 9.6 and 9.7 show the time history of the production and dissipation of turbulence, respectively, nondimensionalized by the dissipation at $\alpha t = 0$. There is a large increase in both the production and dissipation for $Ri = -0.25$ $(\Omega/S = 1/4)$, with the larger increase in the production. Production seems to reach an asymptote for $Ri = 0$; $P/\varepsilon_o \approx 2.1$ in the case of pure shear $(\Omega/S = 0)$, while $P/\varepsilon_o \approx 1$ in the case of shear in a rotating frame $(\Omega/S = 1/2)$. On the other hand, dissipation shows a relatively slow variation with time for these cases, a small increase in the former case and a small decrease in the latter one. The differences in the production are mainly due to the

differences in the shear stresses, as shown previously; the differences in the dissipation are mainly due to the growth of the length scales, as will be shown in Figs. 9.19, 9.20, and 9.21. The fastest decay of the dissipation obtains in the case of "isotropic" turbulence ($S = \Omega = 0$) and pure rotation ($S = 0$), being a little slower in the latter case. There is, of course, zero production in these two cases. Finally, Figs. 9.6 and 9.7 show the relative significance of the mean strain rate and the mean rotation rate on production and dissipation in the cases of pure shear, $Ri = 0$ ($S = \alpha$, $\Omega = 0$), and pure rotation, $Ri = \infty$ ($S = 0$, $\Omega = -\alpha/2$).

Figures 9.8 and 9.9 show the time history of the production for $< \overline{u_1^2}/2 >$ and $< \overline{u_2^2}/2 >$, respectively, nondimensionalized by the total dissipation at $\alpha t = 0$. As should be expected, the production rates are nearly equal and increase nearly exponentially in the case of shear in a rotating frame when $Ri = -0.25$ ($\Omega/S = 1/4$). The other cases have already been analyzed in Figs. 9.6 and 9.7. There is production of $< \overline{u_1^2}/2 >$ in the case of pure shear when ($Ri = 0$, $\Omega/S = 0$) and of $< \overline{u_2^2}/2 >$ in the case of shear in a rotating frame ($Ri = 0$, $\Omega/S = 1/2$).

Figures 9.10, 9.11, and 9.12 show the time history of the dissipation of $< \overline{u_1^2}/2 >$, $< \overline{u_2^2}/2 >$, and $< \overline{u_3^2}/2 >$, respectively, nondimensionalized by the total dissipation at $\alpha t = 0$. These are smaller than the non-zero components of the production shown in Figs. 9.8 and 9.9. Dissipation increases almost linearly and equally for all the components for $Ri = -0.15$ ($\Omega/S = 1/4$). On the other hand, dissipation increases only for $< \overline{u_1^2}/2 >$ only in the case of pure shear for $Ri = 0$ ($\Omega/S = 0$), but is nearly constant or decreases with time in all the other cases.

Figures 9.13, 9.14, and 9.15 show the time history of the pressure strain for $< \overline{u_1^2}/2 >$, $< \overline{u_2^2}/2 >$, and $< \overline{u_3^2}/2 >$, respectively, nondimensionalized by the total dissipation at $\alpha t = 0$. The absolute magnitudes of the pressure-strain components increase almost linearly with time and are larger than the corresponding dissipation components when $Ri = -0.25$ ($\Omega/S = 1/4$). On the other hand, they are nearly constant and have absolute magnitudes similar to those of the corresponding

dissipation components when $Ri = 0$ ($\Omega/S = 0$ and $\Omega/S = 1/2$). In all the shear cases, the pressure-strain components subtract energy from the first two components of the turbulent kinetic energy and add energy to the third.

In summary, the energy balances indicate that $< \overline{u_1^2}/2 >$ and $< \overline{u_2^2}/2 >$ increase with time due to the production and $< \overline{u_3^2}/2 >$ increases due to the pressure strain in the case of shear in a rotating frame ($Ri = -0.25$, $\Omega/S = 1/4$). On the other hand, for $Ri = 0$ (either $\Omega/S = 0$ or $\Omega/S = 1/2$) the pressure-strain and dissipation almost balance each other for $< \overline{u_3^2}/2 >$, but do not balance the production component for either $< \overline{u_1^2}/2 >$ or $< \overline{u_2^2}/2 >$. The main difference between these two last cases lies in the larger production in the case of pure shear flow.

Figures 9.16, 9.17, and 9.18 show the time history of the Taylor microscales, $\lambda_{11,1}$, $\lambda_{22,1}$, $\lambda_{33,1}$, nondimensionalized by the filter width, respectively. All these length scales are measured in the rotating frame when the system rotation is not zero. Maximum growth of the length scales obtains when $Ri = -0.25$ in all cases; however, $\lambda_{33,1}$ is approximately half of the other two microscales. Strong growth of the length scales is also obtained when $Ri = 0$. The longest length scale is associated with the component of the turbulence with th largest production; thus, $\lambda_{11,1}$ is largest when $\Omega/S = 0$, and $\lambda_{22,1}$ is largest when $\Omega/S = 1/2$, while $\lambda_{33,1}$ is the smallest and similar in all the shear cases.

Figures 9.19, 9.20, and 9.21 show the time history of the integral length scales $L_{11,1}$, $L_{22,1}$, $L_{33,1}$. The behavior of the integral length scales is similar to that of the Taylor microscales, but the magnitudes are larger.

Figures 9.22, 9.23, and 9.24 show the time history of the normal velocity-derivative skewnesses. Maximum negative skewness (-0.4) is obtained for isotropic turbulence ($\Omega = S = 0$). The magnitude of the skewness is strongly reduced in the case of pure rotation ($S = 0$ and $\Omega = -\alpha/2$), especially in the rotation direction. For $Ri = 0$, significant differences are observed between the pure shear flow ($\Omega = 0$, $S = \alpha$) and the shear flow in a rotating frame ($\Omega = \alpha/2$, $S = \alpha$). In the

former case, the magnitude of the skewness is only slightly reduced in the $\tilde{x}_1$-direction, positive in the $\tilde{x}_2$-direction, and small and negative in the $\tilde{x}_3$-direction. In the latter case, the magnitude of the skewness is reduced to less than half the isotropic value in the $\tilde{x}_1$-direction, nearly zero in the $\tilde{x}_2$-direction, and similar to the preceding case in the $\tilde{x}_3$-direction. In the case $Ri = -0.25$, the skewness is reduced to nearly zero in all directions, indicating that the energy transfer to the small scales has been greatly diminished.

9.3 Conclusions

Our simulations indicate that Bradshaw (1968) and Ferziger and Shannan (1976) are correct in saying that the most energetic homogeneous turbulent shear flow in a rotating frame obtains when $Ri = -0.25$ ($\Omega/S = 1/4$). However, their formulations do not represent the behavior over the full range of the ratio of shear and rotation rates. In particular, there are significant differences in the turbulence statistics between the two $Ri = 0$ cases, namely, pure homogeneous shear flow ($\Omega/S = 0$) and homogeneous shear turbulence in a rotating system ($\Omega/S = 1/2$). While the normal components of the Reynolds stress anisotropy tensor and the length scales show similar behavior in both cases, the system rotation generates smaller shear stress, production, turbulence intensity, and velocity-derivative skewness. These differences are due to the nonlinear interactions of the turbulence under the system rotation, which increases the pressure-strain correlation in the generation of the shear stress and diminishes the energy transfer to the small scales. Turbulence models of the future should take into account these effects, in order to be able to predict homogeneous turbulent shear flows in a rotating frame.

Lastly, we remark that development of turbulence modeling for engineering applications on shear flows in solid-body rotation should also consider the large anisotropy and rates of change of the length scales. No current model, other than that in development by Donaldson (1973) and Sandri et al. (1981) and a recent one by Reynolds (1982) includes this feature.

Chapter X

CONCLUSIONS

This investigation has focused on three-dimensional large eddy simulation of homogeneous turbulent flows.

The physical bases of large eddy simulation have been analyzed, leading to the conclusion that the best information for modeling the subgrid-scale turbulence is obtained from the smaller resolved eddies.

A "defiltering" method that is able to predict the characteristic scales of full turbulence with accuracy has been proposed. This method has been tested against experimental results on homogeneous isotropic, rotating, and sheared turbulence.

Previous authors assumed that the velocity scale to be used in the eddy viscosity is the r.m.s. subgrid-scale turbulence intensity. We have shown that the velocity scale obtained from the smaller resolved eddies is a better choice. Several eddy viscosity models based on this idea have been proposed. These models are essentially equivalent to the Smagorinsky (1963) and vorticity models for eddy viscosity, according to tests based on full and large eddy simulations. However, they may have other advantages. For example, one of these models is independent of the filter width and may be useful in inhomogeneous or transitional flows.

A new subgrid scale Reynolds stress model, which we called scale similarity model, has been proposed and tested. This model is not of the eddy viscosity type and is based on the smaller eddies of the large eddies. It represents the subgrid scale Reynolds stresses better than previous models, according to tests based on full simulations of homogeneous isotropic and shear turbulent flows. It does not correlate with eddy viscosity models and is not dissipative. A linear combination of the scale similarity and eddy viscosity models predicts turbulence statistics better than eddy viscosity models for homogeneous isotropic, rotating, and sheared turbulence.

The effects of rotation on homogeneous isotropic turbulence have been studied. The experimental results of Wigeland and Nagib (1978)

95

have been predicted with accuracy. The main effects of rotation on turbulence have been found. Rotation destroys the phase coherence between the turbulent eddies in the energy cascade process, and inhibits the net transfer of energy from the large eddies to the smaller eddies. The length scales of turbulence increase at a faster rate in the presence of increased rotation, especially the transverse length scales in the rotation direction. The apparently contradictory experimental results of Traugott (1958), Ibbetson and Tritton (1975), and Wigeland and Nagib (1978) about faster and slower decay of turbulence intensity in the presence of increased rotation rates have been explained. Experimental turbulence generating grids increase the initial dissipation and turbulence intensity as the rate of rotation increases, and this masks part of the effects the experiments are designed to display. The simulations do not suffer from this difficulty, and we were able to sort out the competing effects.

A two-equation model for the time-averaged turbulence intensity and rate of dissipation has been proposed. This model predicts accurately all of the experimental results of Wigeland and Nagib (1978) on the time evolution of turbulence intensity at different constant rates of rotation. This model may also be useful for modeling buoyancy and streamline curvature effects, according to an analogy made by Bradshaw (1969).

Large-eddy simulation of the experiments of Champagne, Harris, and Corrsin (1970) on homogeneous turbulent shear flow has been performed. The time evolution of turbulent kinetic energy has been predicted with accuracy, and the results may be valuable for developing turbulence models. This simulation also shows qualitative agreement with full simulations at low Reynolds numbers made by Shirani (1981) and Rogallo (1981).

A model for time-averaged Reynolds stresses has been proposed. This model is an extension and modification of the model proposed by Reynolds (1976). It is superior to the models proposed by Reynolds (1976) and Wilcox and Rubesin (1980) and similar to the one proposed by Launder, Reece, and Rodi (1975) for predicting homogeneous strained and sheared turbulence; it is also the only one that can predict homogeneous rotating turbulent flows.

Lastly, large eddy simulations of homogeneous shear flows in rotating systems have been carried out. These simulations have been focused on the destabilizing effects of system rotation on turbulence when the Richardson number $Ri < 0$. As in previous analyses, the most destabilizing case has been found for $Ri = -0.25$, which Ferziger and Shaanan (1976) showed to be the case in which turbulent stresses and strains are aligned. Contrary to common belief, we have shown that the limiting cases when $Ri = 0$ are not equivalent; that is, a homogeneous shear flow in a rotating system with $\Omega/S = 1/2$ develops more slowly than a pure homogeneous shear flow with the same mean shear rate and initial conditions. These differences are not predicted by using linear spectral analysis (Bertoglio (1981)), or by the mixing length model proposed by Bradshaw (1969) and Johnston et al. (1972). These simulations also show that, for pure homogeneous shear flow, the mean strain rate effects predominate over the mean rotation rate effects. Similarly, for homogeneous shear flow in a rotating system, the nonlinear effects of the mean shear rate and system rotation are significant.

Turbulence Intensity

3-D Initial Energy Spectrum
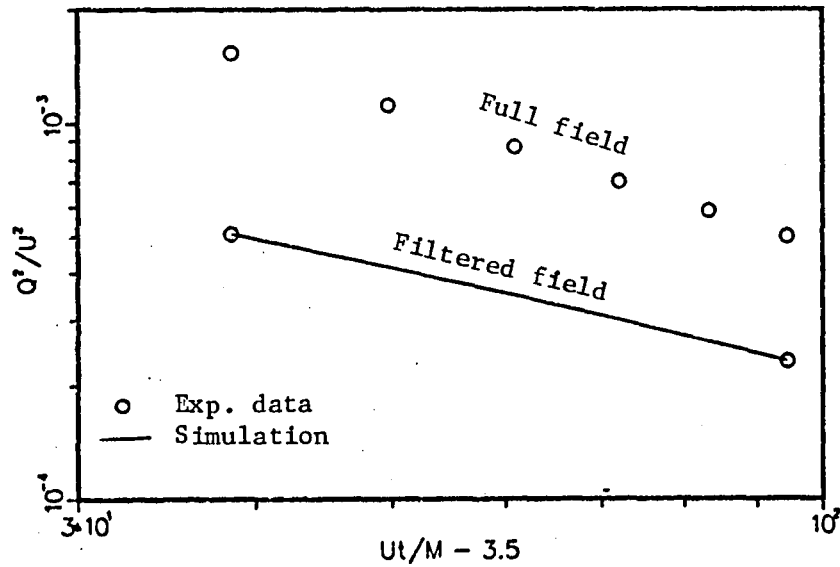
Fig. 4.1. Decay of the turbulence intensity in homogeneous isotropic turbulence. Large eddy simulation with Smagorinsky's (1963) model, $c_s = 0.21$, $\Delta_f = 0.03$ m, $32 \times 32 \times 32$ grid, pseudospectral methods, second-order central difference for model terms. Experimental data of Comte-Bellot and Corrsin (1971), $U = 10$ ms^{-1} and $M = 0.0508$ m.
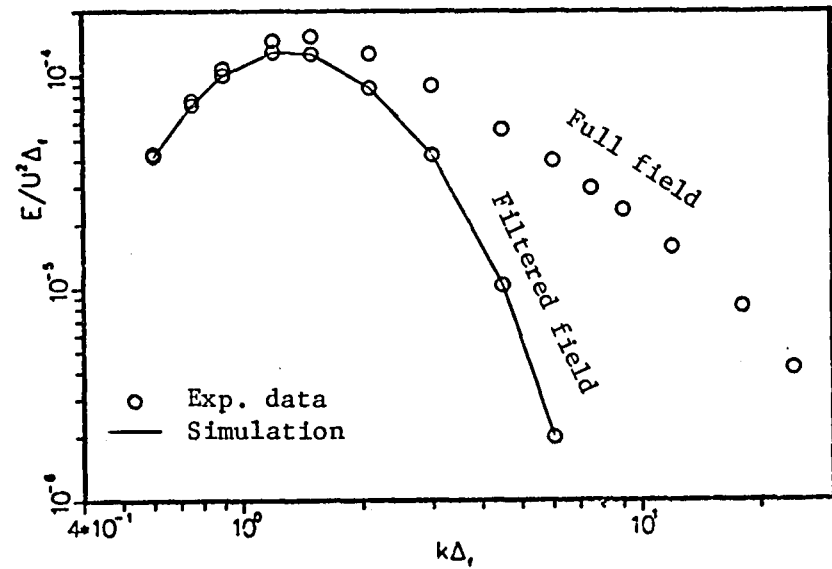
Fig. 4.2. Initial three-dimensional energy spectrum of Fig. 4.1 at $Ut/M = 42$.

3-D Final Energy Spectrum
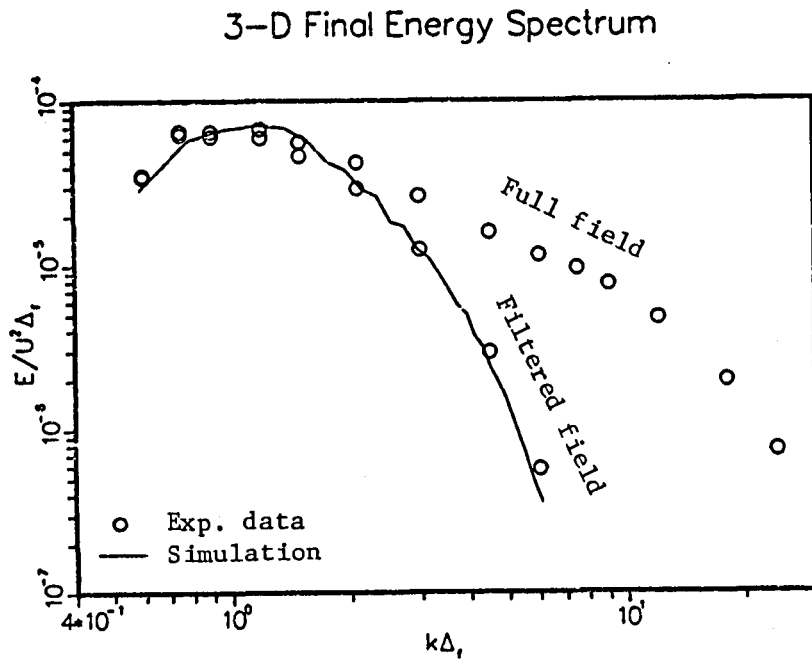
SGS Velocity Scale

Fig. 4.3. Final three-dimensional energy spectrum of Fig. 4.1 at $Ut/M = 98$.
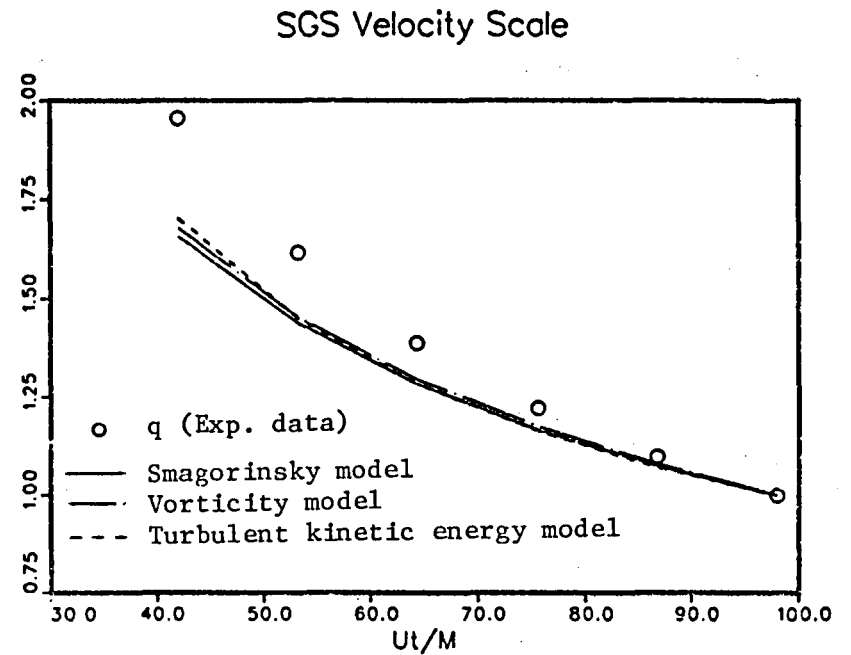
Fig. 4.4. Comparison of the time history of the r.m.s. of the subgrid-velocity scale q and eddy viscosity . Both variables are nondimensionalized with their respective values at $U_t/M = 98$. $q = \sqrt{Q^2 - Q_f^2}$ is obtained from data shown in Fig. 4.1.
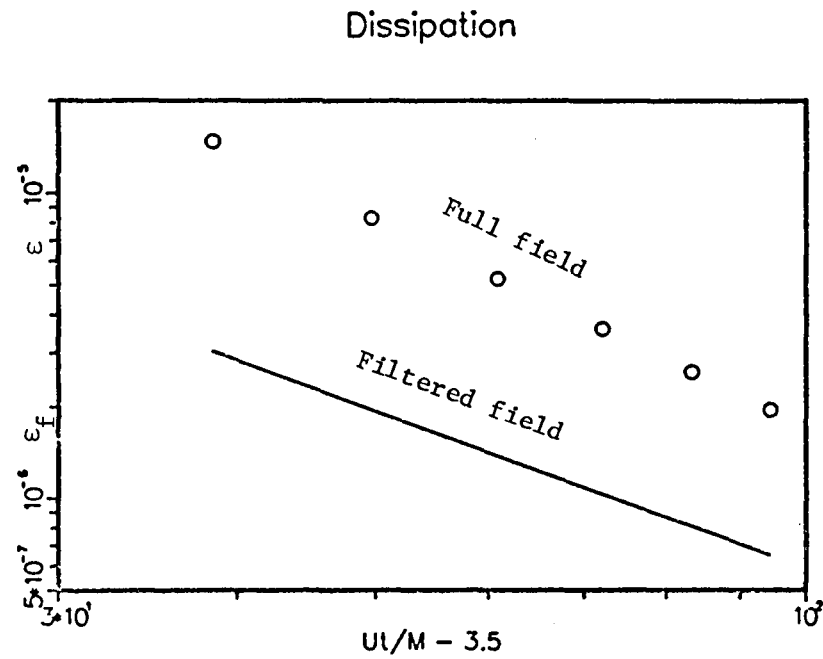
Dissipation

Fig. 4.5. Time history of the decay of the energy
dissipation rates ε and ε_f of the
full and filtered turbulence intensities
shown in Fig. 4.1, respectively.
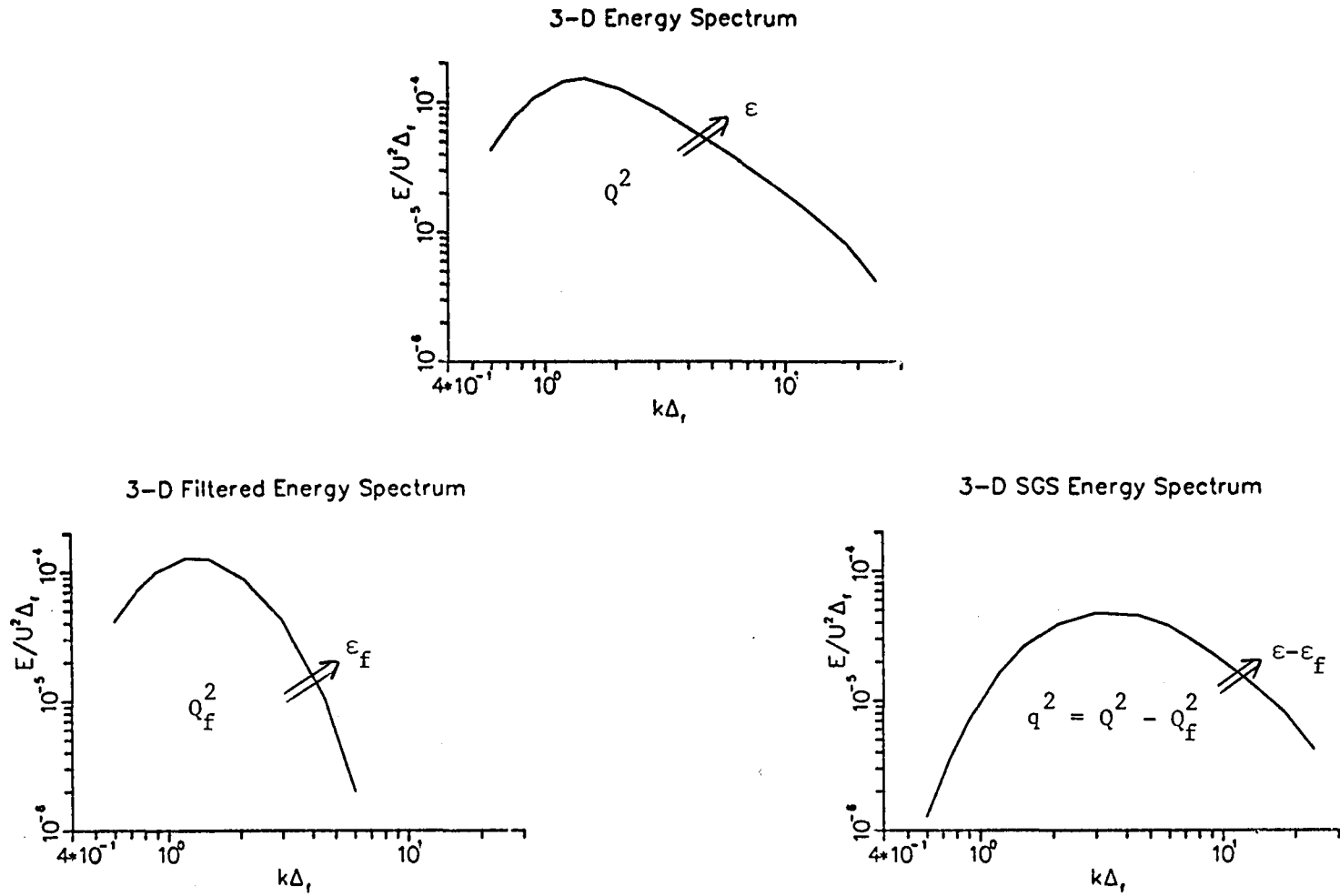
Fig. 5.1. Three-dimensional energy spectra of the full, filtered, and subgrid-scale flow fields showing schematic energy balances for the decay of isotropic turbulence.

Large Length—scale Ratio

SGS Scaling

$$\frac{q^2}{(2\epsilon\Delta_f)^{2/3}}$$
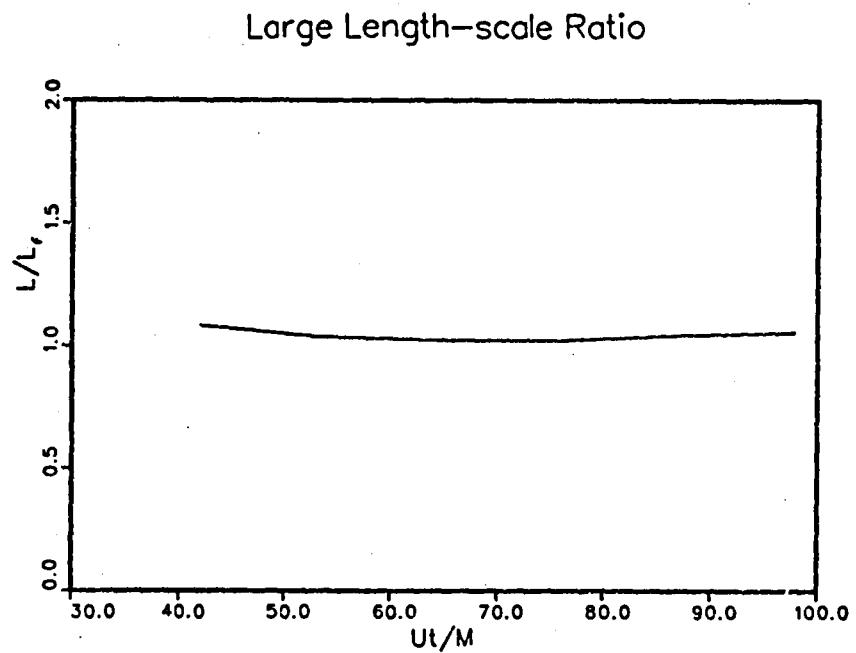
Fig. 5.2.   Time history of the ratio of the
large length scales of the full and
filtered flow fields, L/L_f.
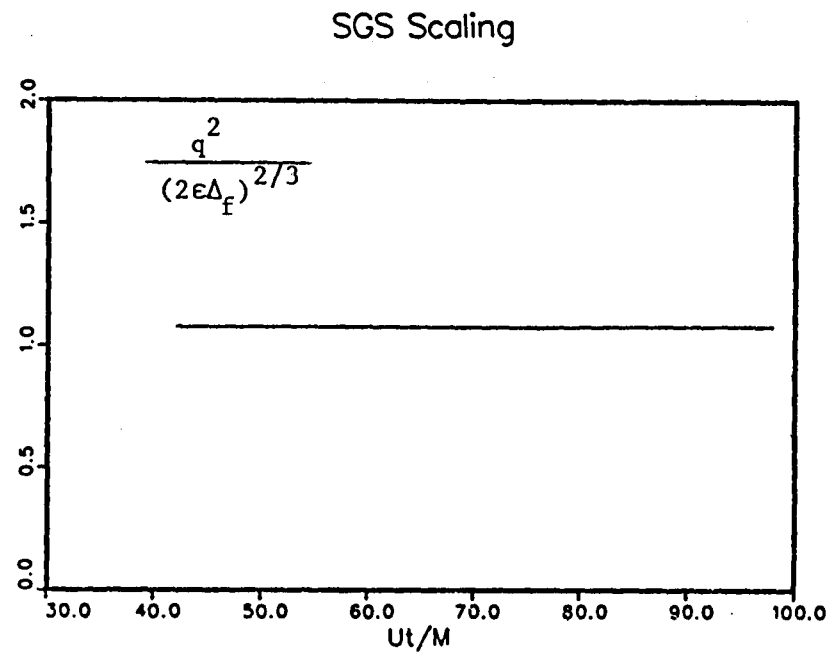
Fig. 5.3.   Time history of the scaling constant of
the subgrid scale flow field.

Turbulence Intensity in Isotropic Flow

Q^2/U^2

$Ut/M - 3.5$

Full field

Filtered field

o   Exp. data
- - -   Simulation
———   'Defiltering' prediction

Turbulence Intensity in Rotating Flow

$10^{-1} \cdot U_3^2/Q^2$

Ut/M

o   Exp. data
———   'Defiltering' prediction

$\Omega = 20$

$\Omega = 0$

$\Omega = 80$
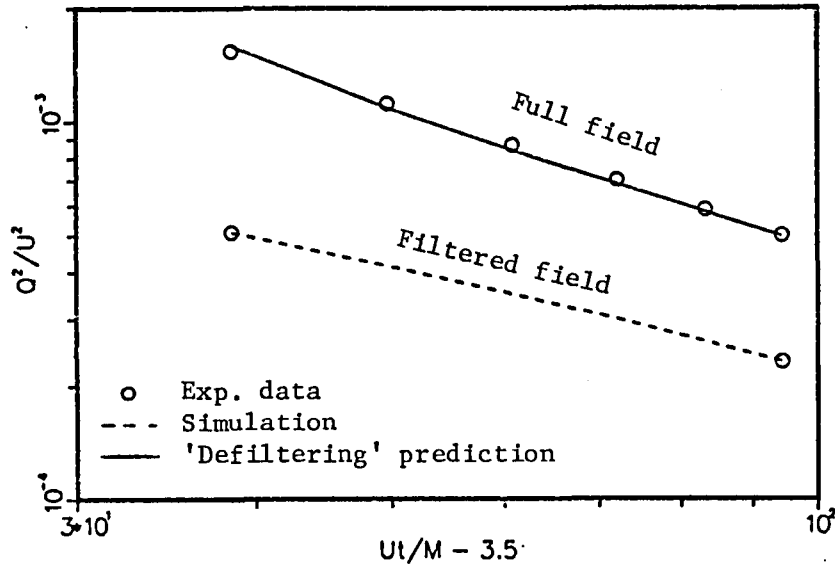
Fig. 5.4. Prediction of the full turbulence
intensity of the experiment of Comte-
Bellot and Corrsin (1971) in homogen-
eous isotropic turbulence. "Defilter-
ing" prediction is obtained from Eq.
(5-12). Other nomenclature same as
Fig. 4.1.
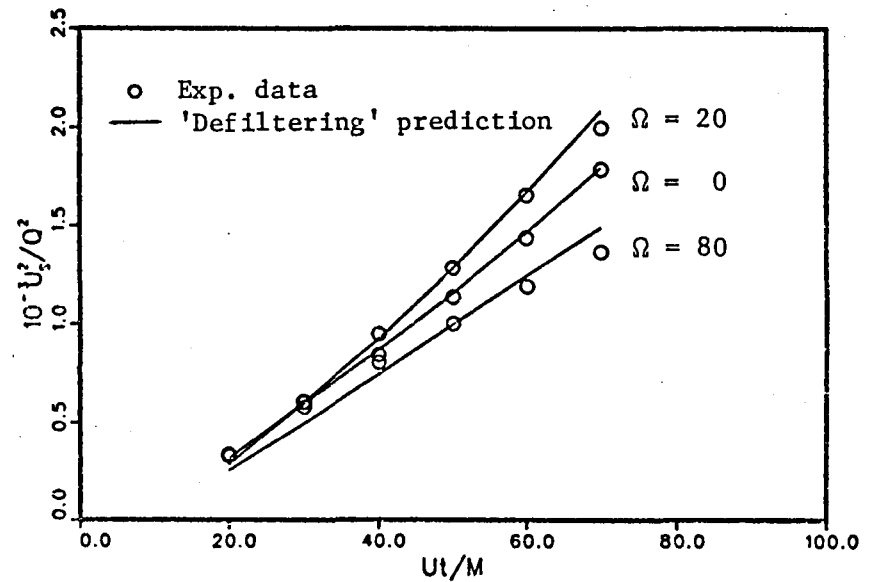
Fig. 5.5. Prediction of the full turbulence in-
tensity of the experimental results of
Wigeland and Nagib (1978.) on homogene-
ous, rotating turbulence with U = 6
m/s, M = 0.0625, and Ω = 0, 20, and
80 s^{-1}. Large eddy simulation as
described in caption of Fig. 4.1.

Turbulence Intensity in Shear Flow
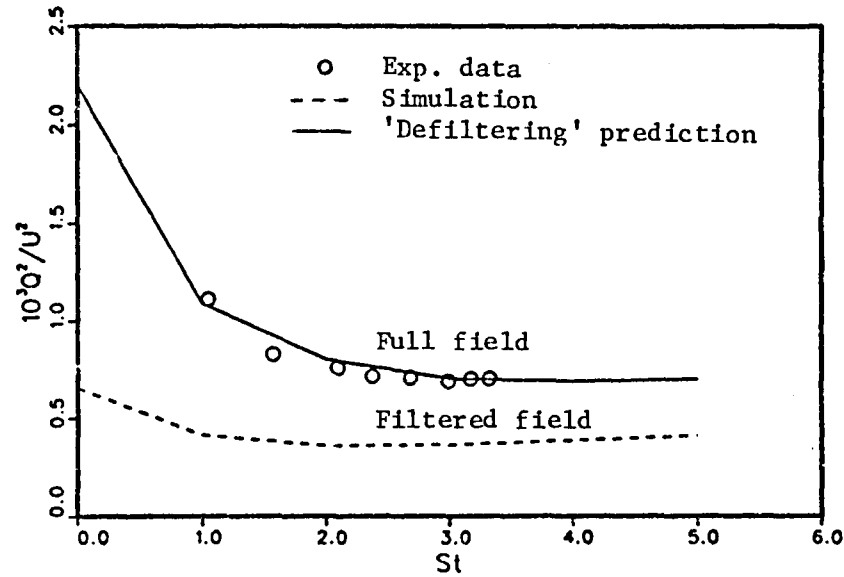
Fig. 5.6. Prediction of the full turbulence intensity of the experimental results of Champagne, Harris and Corrsin (1970) on homogeneous sheared turbulence with $U = 12.4$ m/s and shear rate $S = 12.9$ s^{-1}. Large eddy simulation as described in caption of Fig. 4.1a.
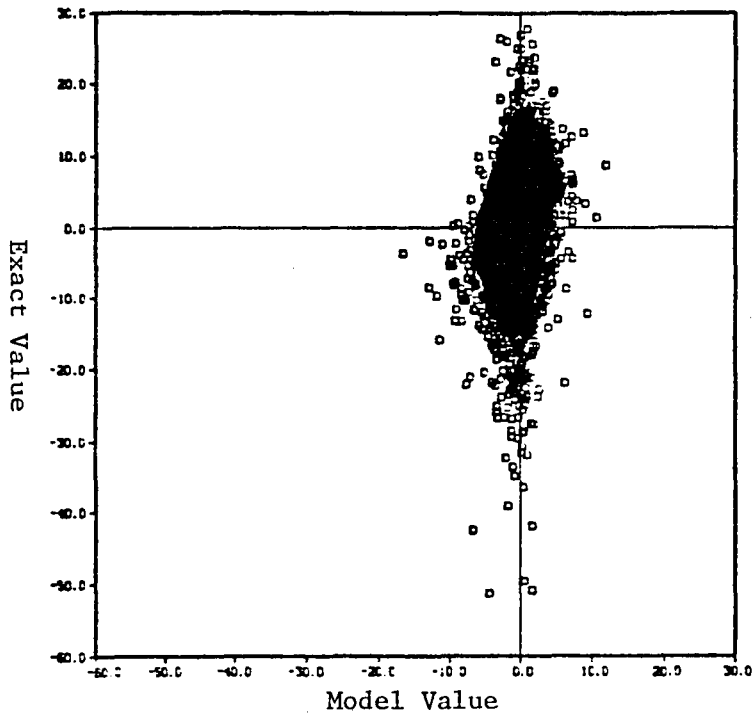
Fig. 6.1a. Smagorinsky model. "Exact" vs. model values of the subgrid-scale Reynolds stress τ_{11} in homogeneous isotropic turbulence. $R_\lambda = 38$ and $R_{SGS} = 180$.
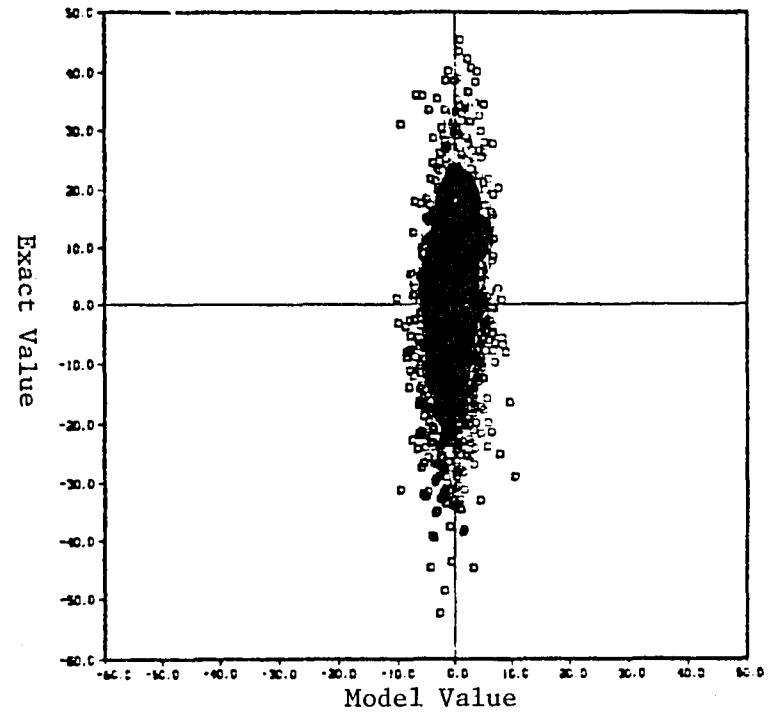
Fig. 6.1b. Smagorinsky model. "Exact" vs. model values of the divergence of the subgrid-scale Reynolds stress $\partial\tau_{1j}/\partial x_j$ in homogeneous isotropic turbulence. $R_\lambda = 38$ and $R_{SGS} = 180$.
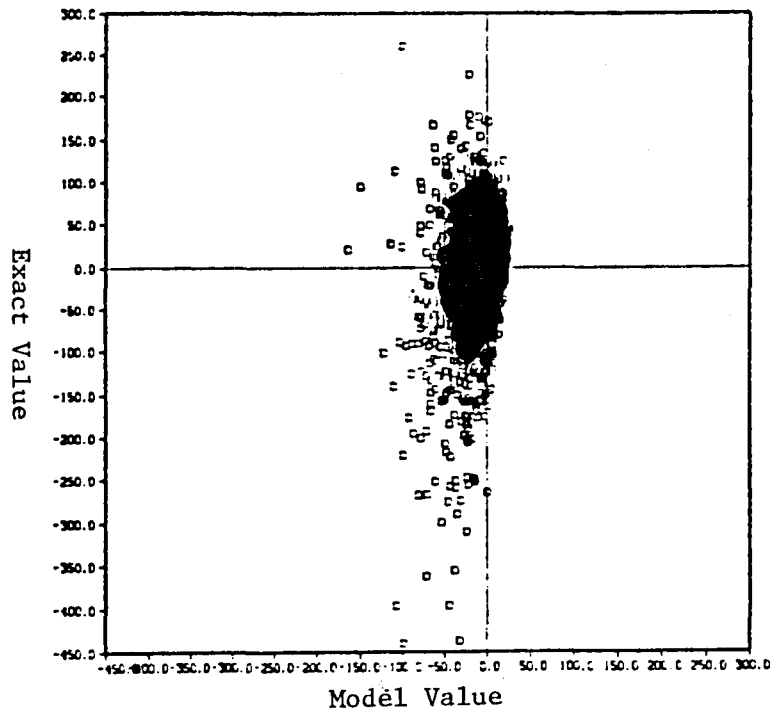
Fig. 6.1c. Smagorinsky model. "Exact" models of the dissipation caused by the subgrid-scale Reynolds stress $\overline{u}_i \partial \tau_{ij}/\partial x_j$ in homogeneous isotropic turbulence. $R_\lambda = 38$ and $R_{SGS} = 180$.
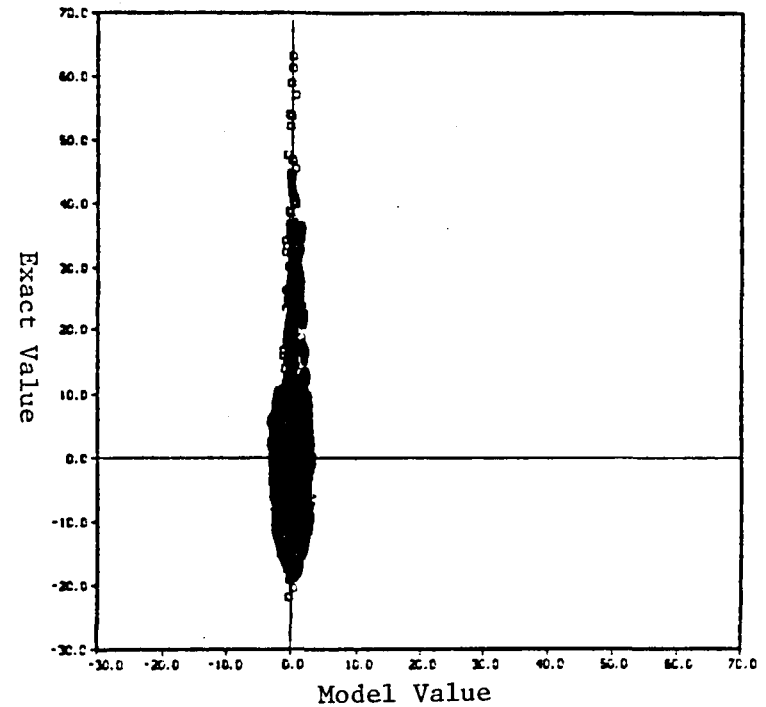
Fig. 6.2a. Smagorinsky model. "Exact" vs. model values of the subgrid-scale Reynolds stress τ_{12} in homogeneous sheared turbulence. $S = 34$ and $R_{SGS} = 204$.
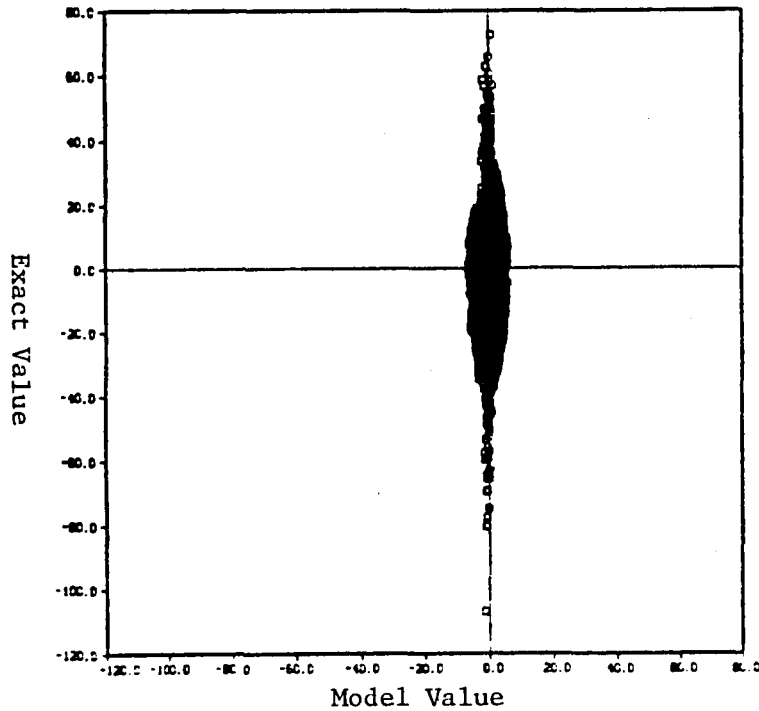
Fig. 6.2b. Smagorinsky model. "Exact" vs. model values of the divergence of the subgrid-scale Reynolds stress $\partial \tau_{ij}/\partial x_j$ in homogeneous sheared turbulence. $S = 34$ and $R_{SGS} = 204$.
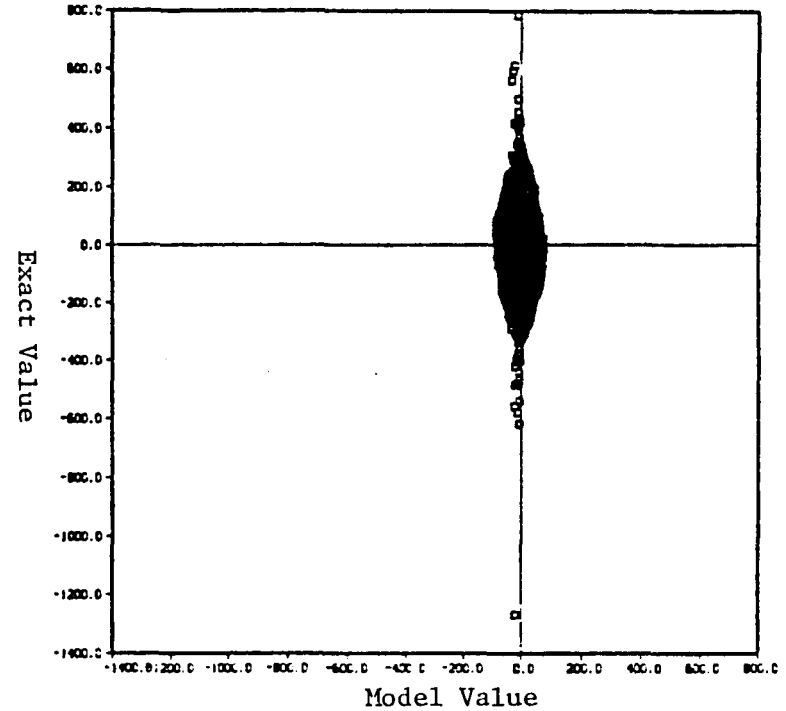
Fig. 6.2c. Smagorinsky model. "Exact" vs. model values of the dissipation due to the subgrid-scale Reynolds stress $\overline{u}_i \partial \tau_{ij}/\partial x_j$ in homogeneous sheared turbulence. $S = 34$ and $R_{SGS} = 204$.
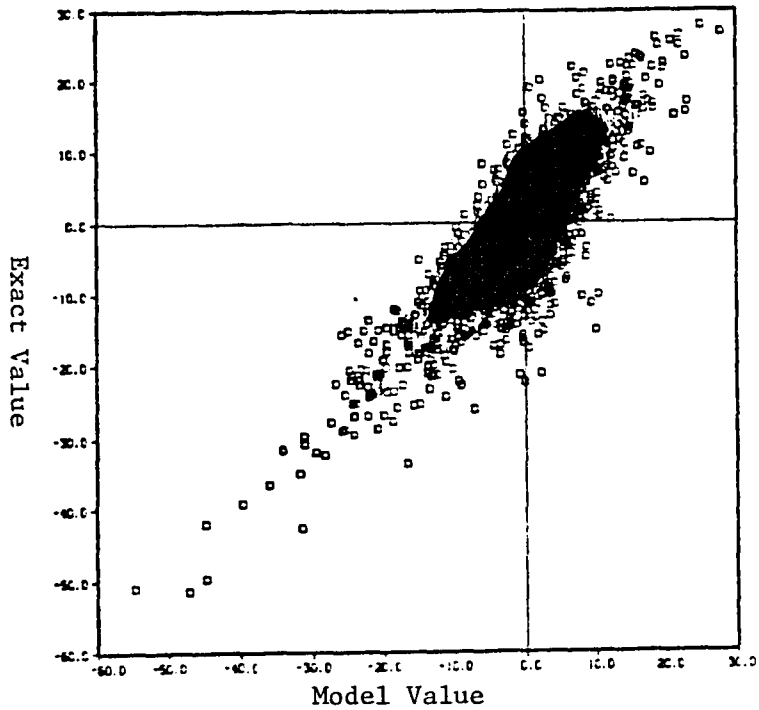
Fig. 6.3a. Scale similarity model. "Exact" vs. model values of the subgrid-scale Reynolds stress τ_{11} in homogeneous isotropic turbulence. $R_\lambda = 38$ and $R_{SGS} = 180$.
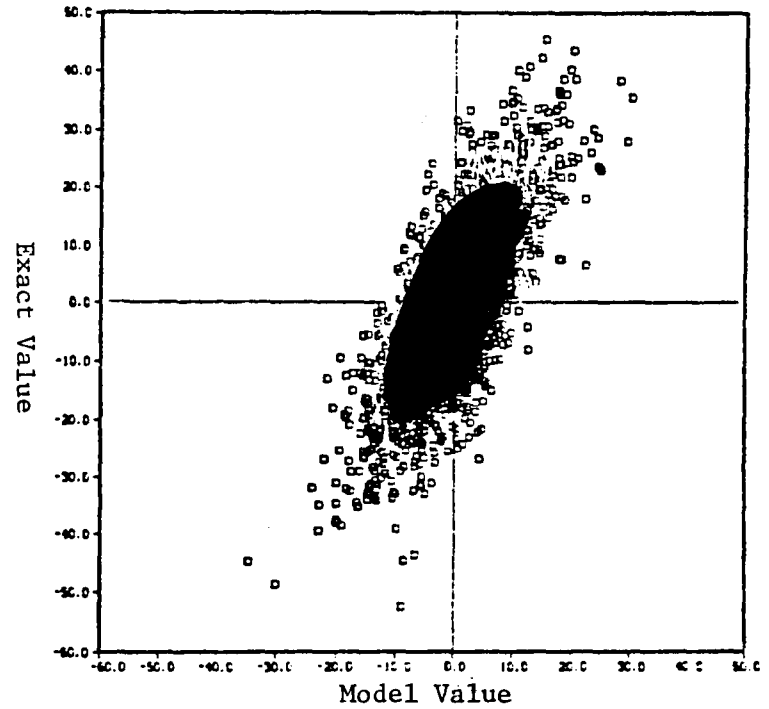
Fig. 6.3b. Scale similarity model. "Exact" vs. model values of the divergence of the subgrid-scale Reynolds stress $\partial\tau_{1j}/\partial x_j$ in homogeneous isotropic turbulence. $R_\lambda = 38$ and $R_{SGS} = 180$.

Model Value
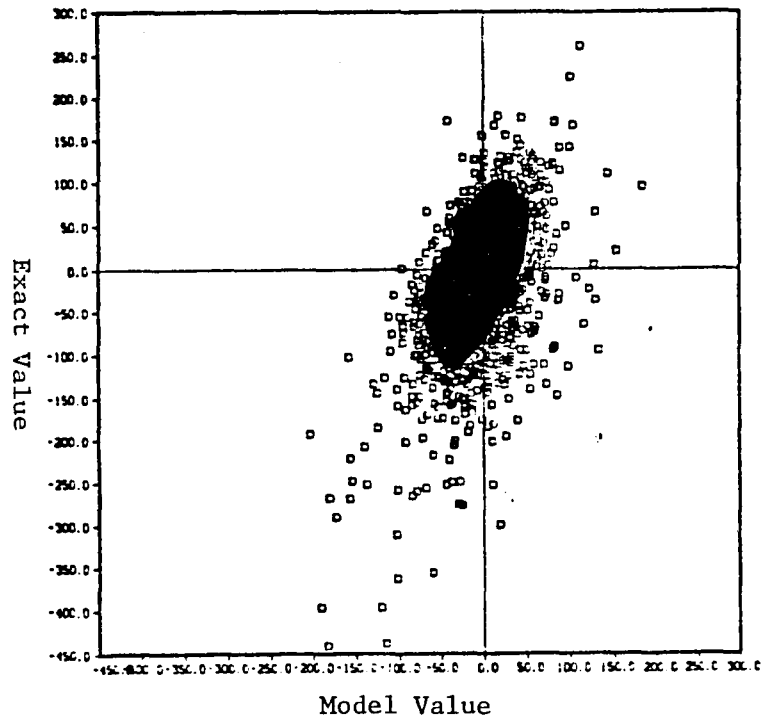
Model Value

Fig. 6.3c. Scale similarity model. "Exact" vs. model values of the dissipation due to the subgrid-scale Reynolds stress $\bar{u}_i \partial \tau_{ij}/\partial x_j$ in homogeneous isotropic turbulence. $R_\lambda = 38$ and $R_{SGS} = 180$.
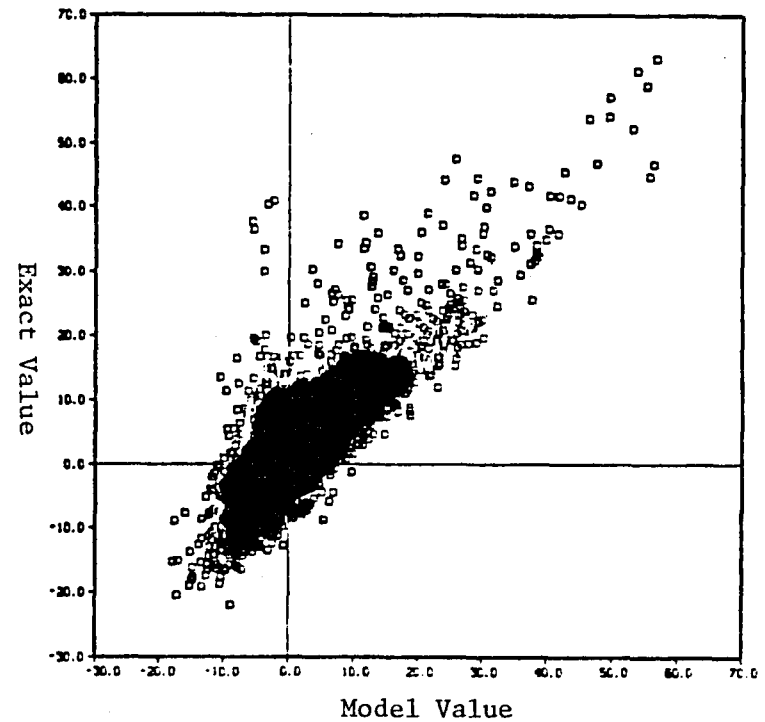
Fig. 6.4a. Scale similarity model. "Exact" vs. model values of the subgrid-scale Reynolds stress τ_{12} in homogeneous sheared turbulence. $S = 34$ and $R_{SGS} = 204$.
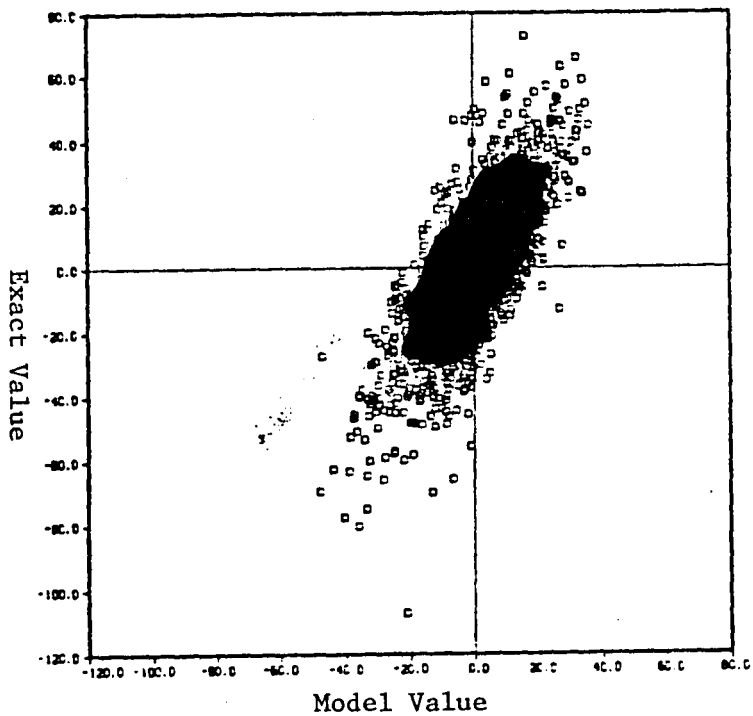
Fig. 6.4b. Scale similarity model. "Exact vs. model values of the divergence of the subgrid-scale Reynolds stress $\partial\tau_{ij}/\partial x_j$ in homogeneous sheared turbulence. $S = 34$ and $R_{SGS} = 204$.
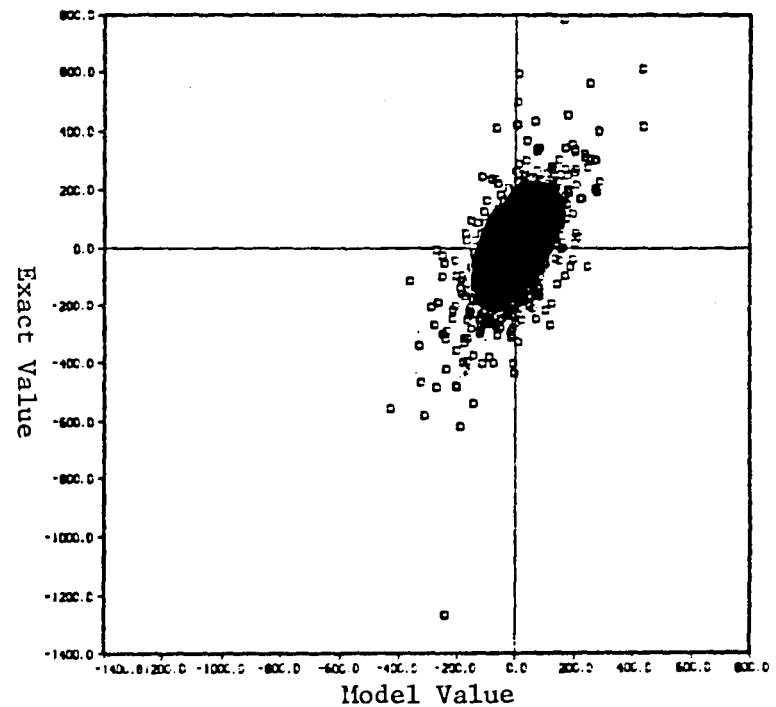
Fig. 6.4c. Scale similarity model. "Exact" vs. model values of the dissipation due to the subgrid-scale Reynolds stress $\overline{u_i \partial\tau_{ij}/\partial x_j}$ in homogeneous sheared turbulence. $S = 34$ and $R_{SGS} = 204$.
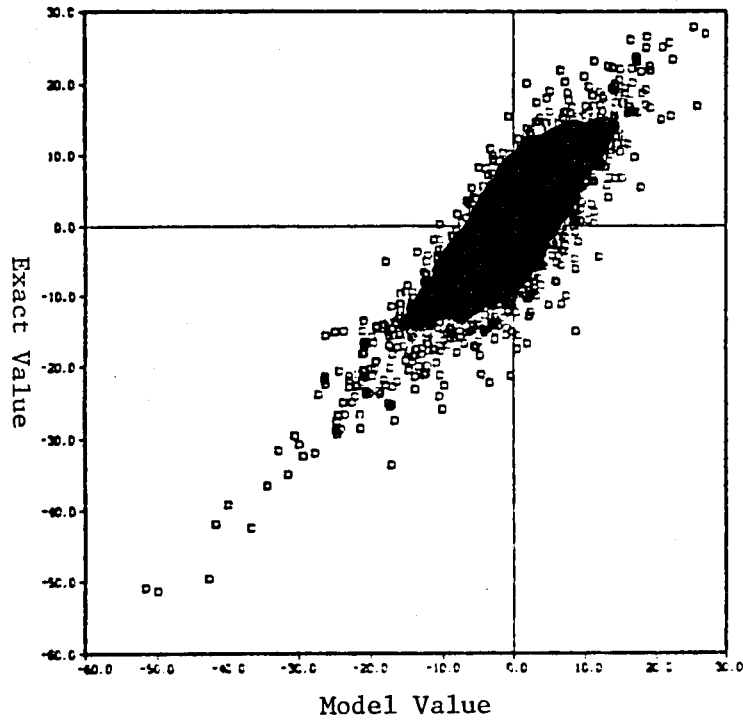
Fig. 6.5a. Scale similarity and Smagorinsky model. "Exact" vs. model values of the subgrid-scale Reynolds stress τ_{11} in homogeneous isotropic turbulence. $R_\lambda = 38$ and $R_{SGS} = 180$.
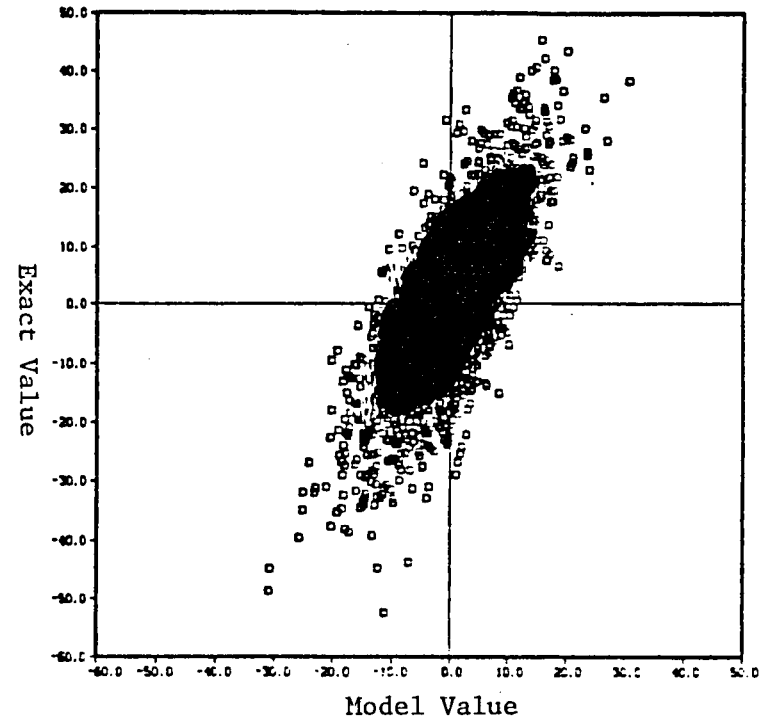
Fig. 6.5b. Scale similarity and Smagorinsky model. "Exact" vs. model values of the divergence of the subgrid-scale Reynolds stress $\partial \tau_{ij}/\partial x_j$ in homogeneous isotropic turbulence. $R_\lambda = 38$ and $R_{SGS} = 180$.
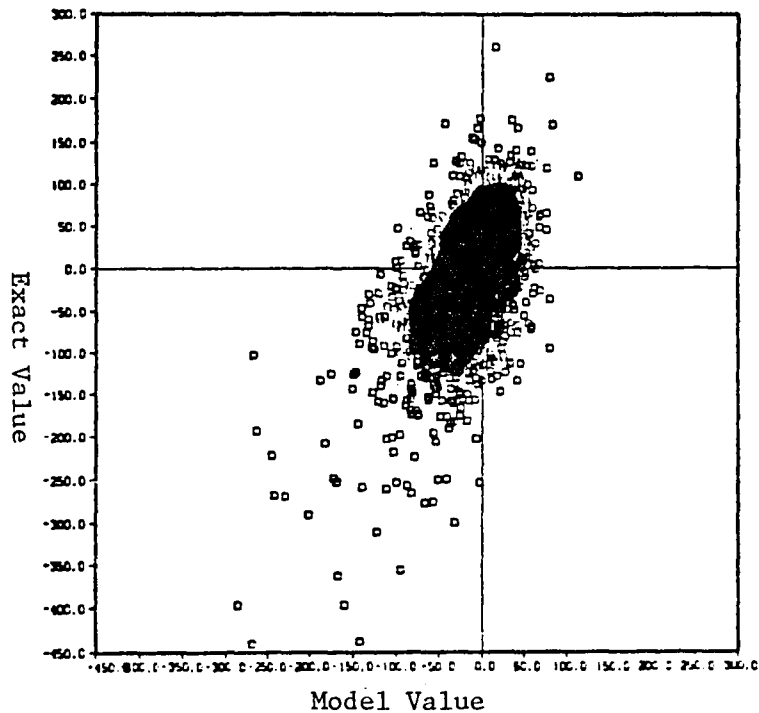
Fig. 6.5c. Scale similarity and Smagorinsky model. "Exact" vs. model values of the dissipation due to the subgrid-scale Reynolds stress $\bar{u}_i \partial \tau_{ij}/\partial x_j$ in homogeneous isotopic turbulence. $R_\lambda = 38$ and $R_{SGS} = 180$.
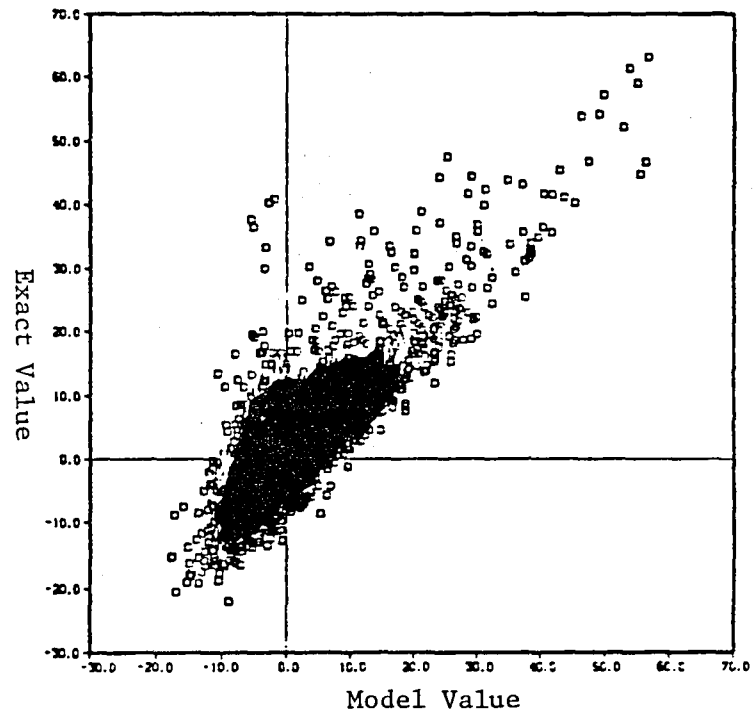
Fig. 6.6a. Scale similarity and Smagorinsky model. "Exact" vs. model values of the subgrid scale Reynolds stress τ_{12} in homogeneous sheared turbulence. $S = 34$ and $R_{SGS} = 204$.
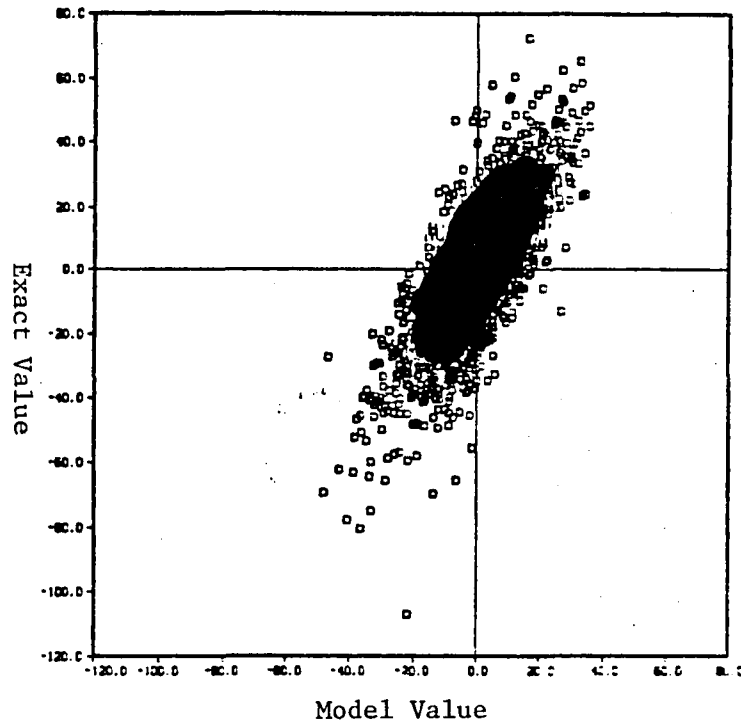
Fig. 6.6b. Scale similarity and Smagorinsky model. "Exact" vs. model values of the divergence of the subgrid-scale Reynolds stress $\partial \tau_{ij}/\partial x_j$ in homogeneous sheared turbulence. $S = 34$ and $R_{SGS} = 204$.
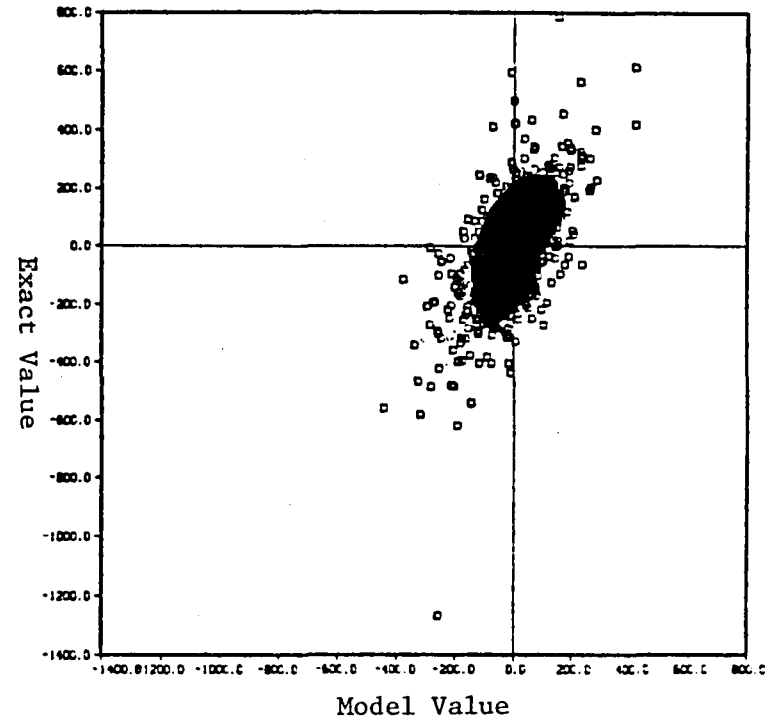
Fig. 6.6c. Scale similarity and Smagorinsky model. "Exact" vs. model values of the dissipation due to the subgrid-scale Reynolds stress $\overline{u}_i \partial \tau_{ij}/\partial x_j$ in homogeneous sheared turbulence. $S = 34$ and $R_{SGS} = 204$.

114
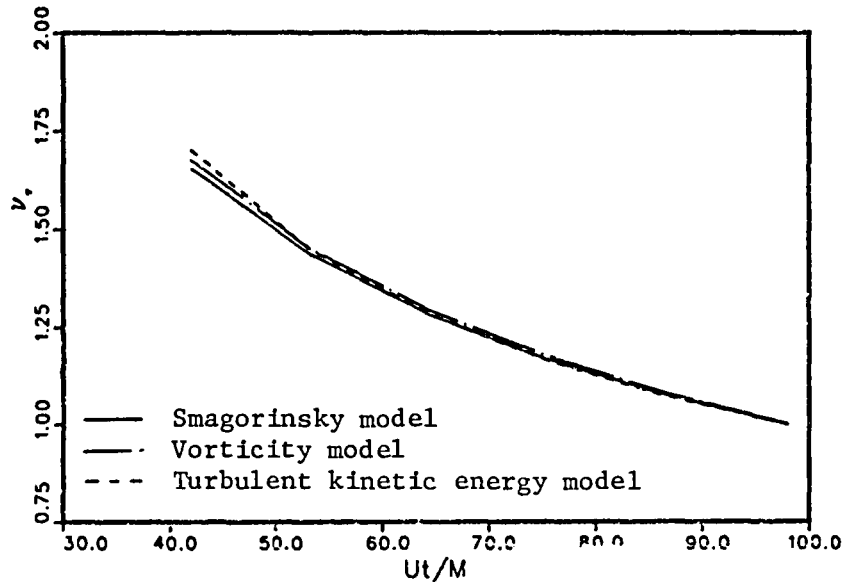
Eddy Viscosity

Fig. 6.7a. Decay of the spatially averaged eddy viscosity in homogeneous isotropic turbulence. Large eddy simulation as described in caption of Fig. 4.1; Smagorinsky model constant c_s = 0.21; vorticity model constant, c_v = 0.21; TKE model constant, c_q = 0.16.
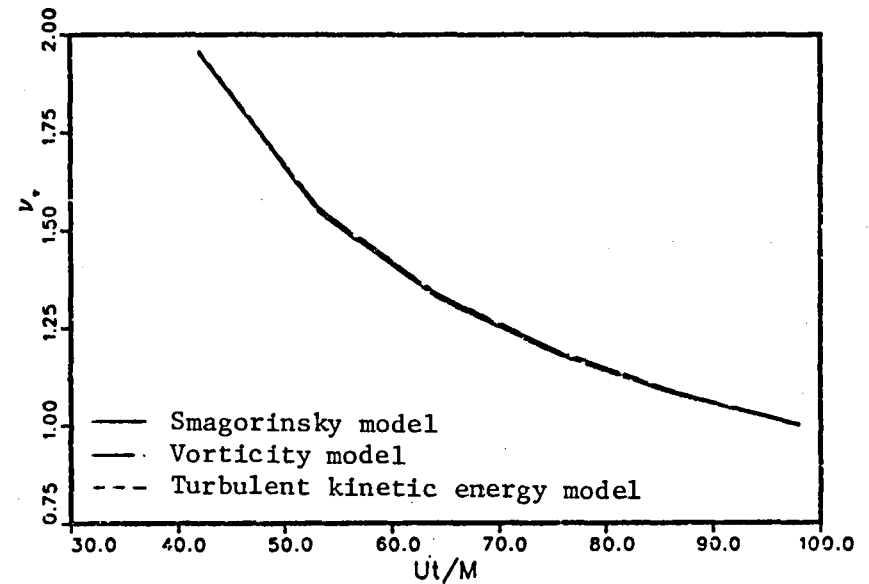
Fig. 6.7b. Decay of the spatially averaged eddy viscosity in homogeneous isotropic turbulence (see caption of Fig. 4.1). Large eddy simulation with pseudospectral method. Smagorinsky model constant, c_s = 0.19; vorticity model constant, c_v = 0.19; TKE model constant, c_q = 0.145.

3-D Energy Spectrum

Exp. data
Simulation (pseudospectral)
Simulation (pseudospectral, second-order central diff. for model terms)

Filtered Turbulence Intensity

Exp. data
Simulation without scale-similarity model
Simulation with scale-similarity model
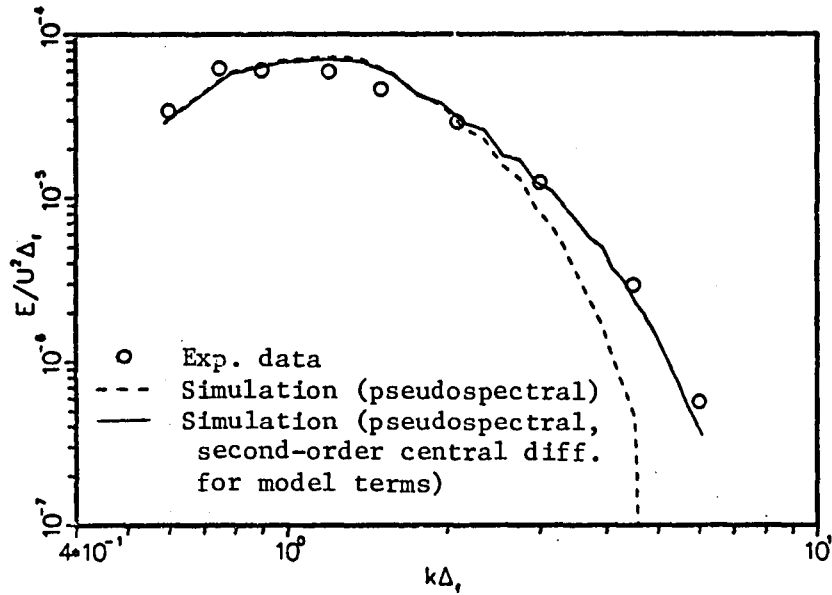
Fig. 6.8. Three-dimensional energy spectrum of the filtered flow field of homogeneous isotropic turbulence at $U_t/M = 98$ in Fig. 6.7. Large eddy simulation with Smagorinsky model.
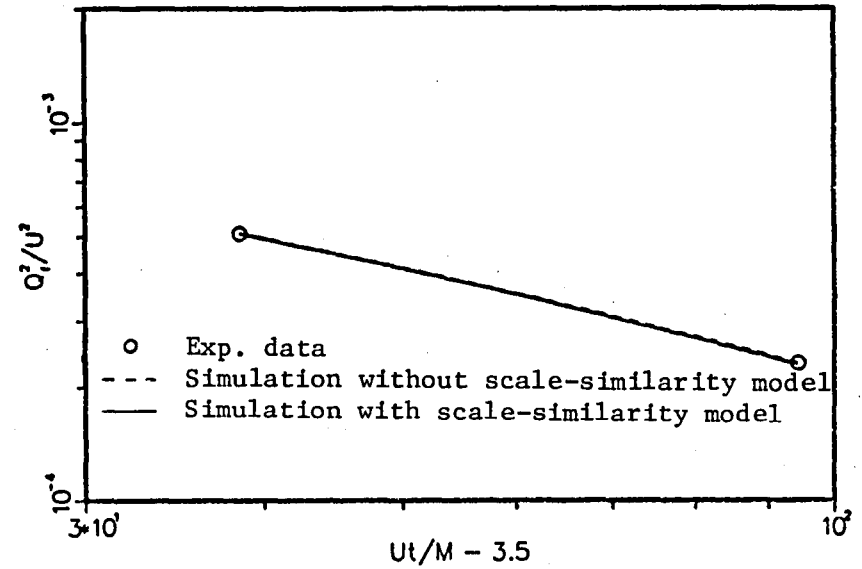
Fig. 6.9. Decay of the turbulence intensity of filtered flow field in homogeneous isotropic turbulence. Experimental values of Comte-Bellot and Corrsin. (1971). Large eddy simulation, pseudospectral method: Smagorinsky model constant, $c_s = 0.19$; Smagorinsky and scale similarity model constants, $c_s = 0.16$ and $c_r = 1.1$.

3-D Energy Spectrum

Velocity-Derivative Skewness
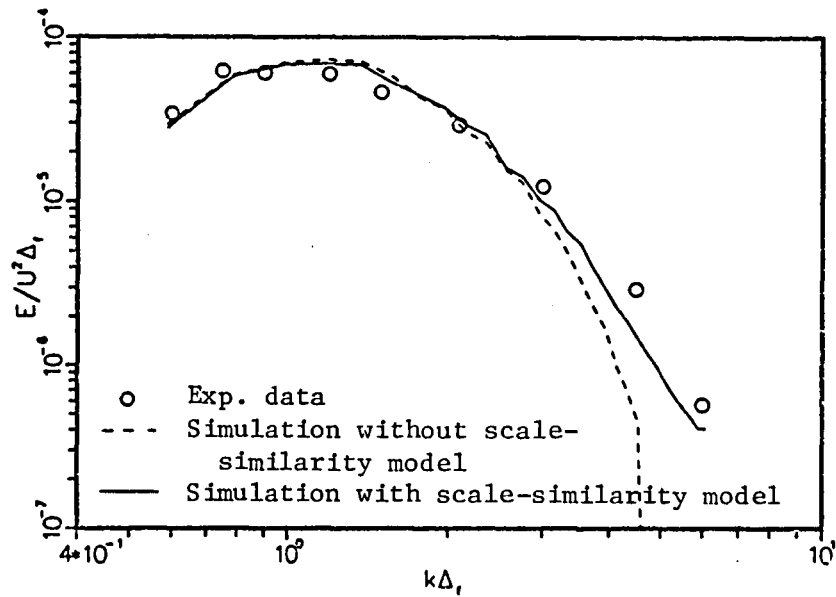
Fig. 6.10. Three-dimensional energy spectrum of the filtered flow field in homogeneous isotropic turbulence at $U_t/M = 98$ of Fig. 6.9.
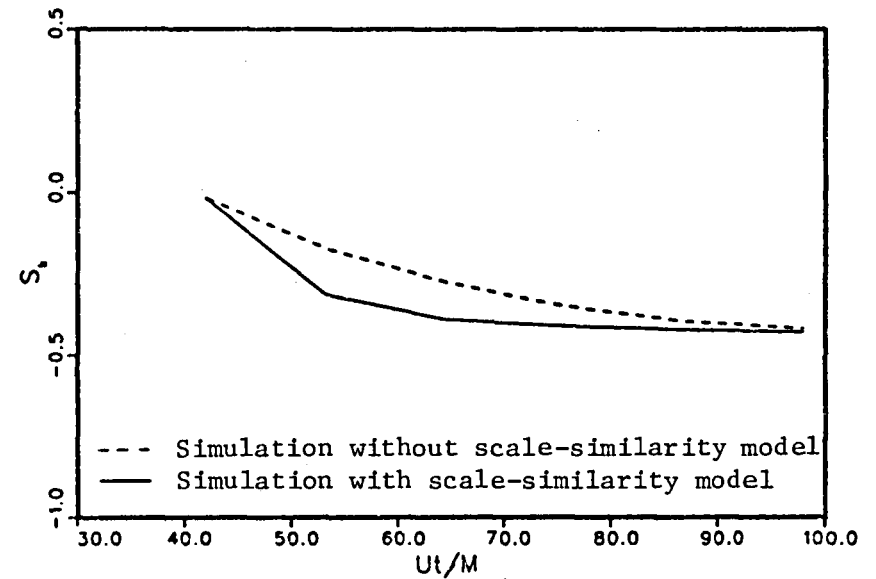
Fig. 6.11. Time history of the velocity-derivative skewness of the filtered flow field in the homogeneous isotropic turbulence flow of Fig. 6.9.

Filtered Turbulence Intensity
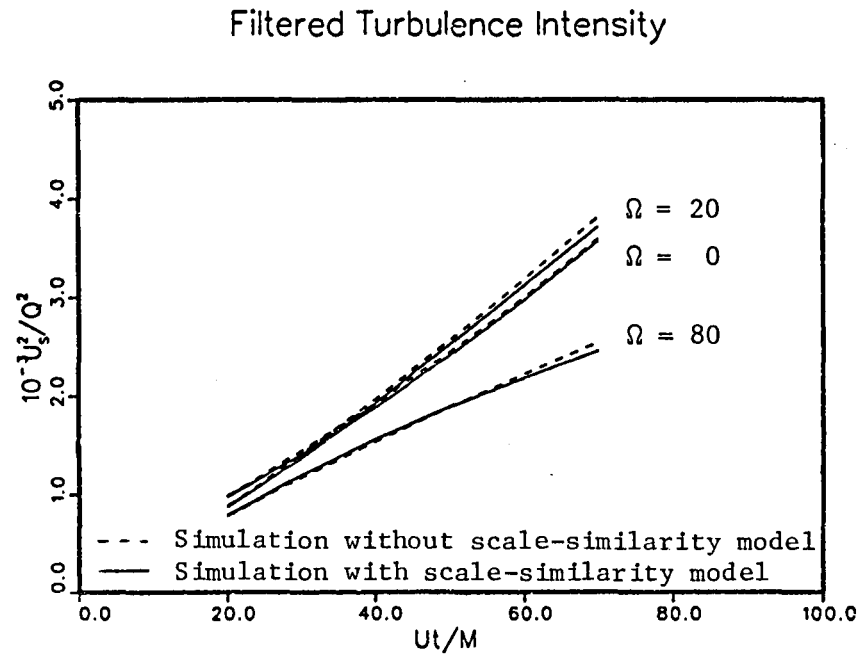
Fig. 6.12. Decay of the turbulence intensity of
the filtered flow field in homogeneous
rotating turbulence (See Fig. 5.5).
Large eddy simulation, pseudospectral
method, second-order central differ-
ence for model terms. Smagorinsky
model constant, c_s = 0.21; Smagor-
insky and scale similarity model
constants, c_s = 0.19 and c_r = 1.1.

Velocity–Derivative Skewness
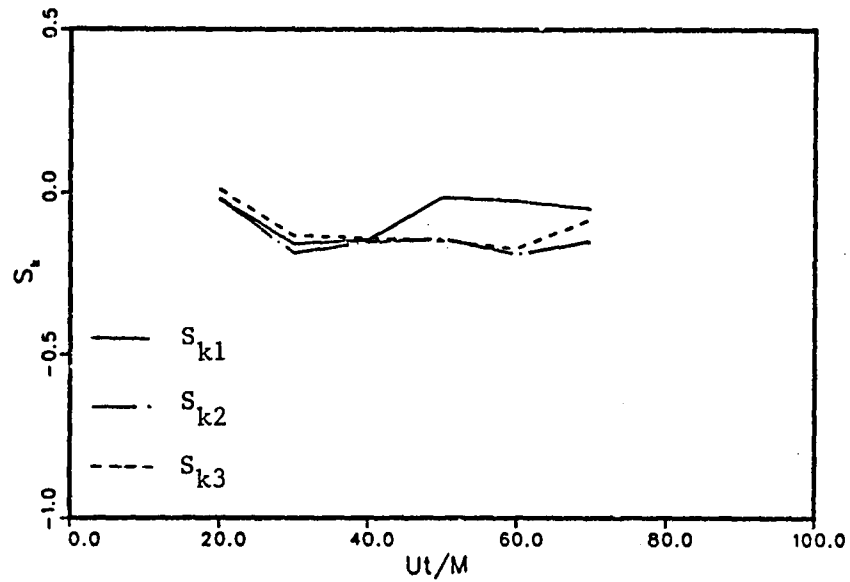
Fig. 6.13a. Time history of the velocity-derivative skewness in the rotation direction in the case $\Omega = 80$ s^{-1} with the Smagorinsky model of Fig. 6.12.
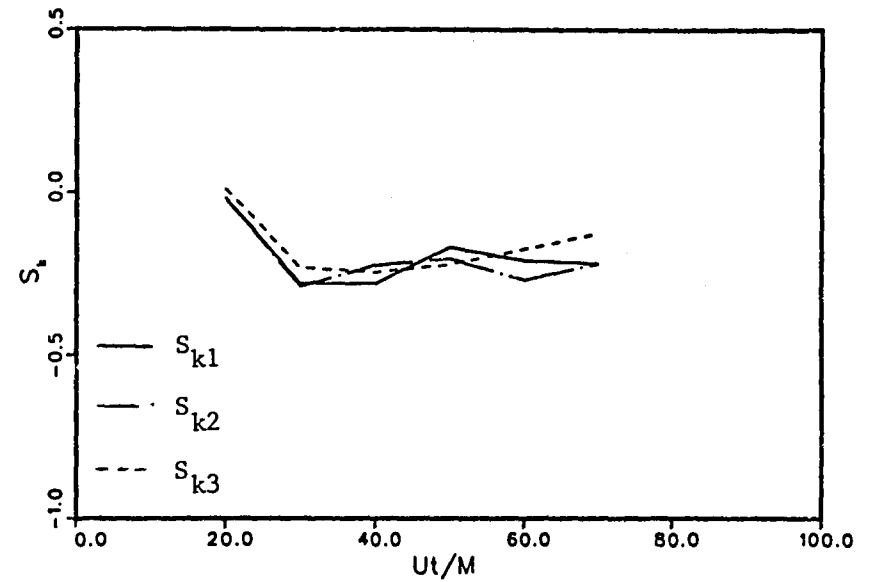
Fig. 6.13b. Time history of the velocity-derivative skewness in the rotation direction in the case $\Omega = 80$ s^{-1} with the Smagorinsky model and scale similarity model of Fig. 6.12.

Turbulence Intensity in Shear Flow
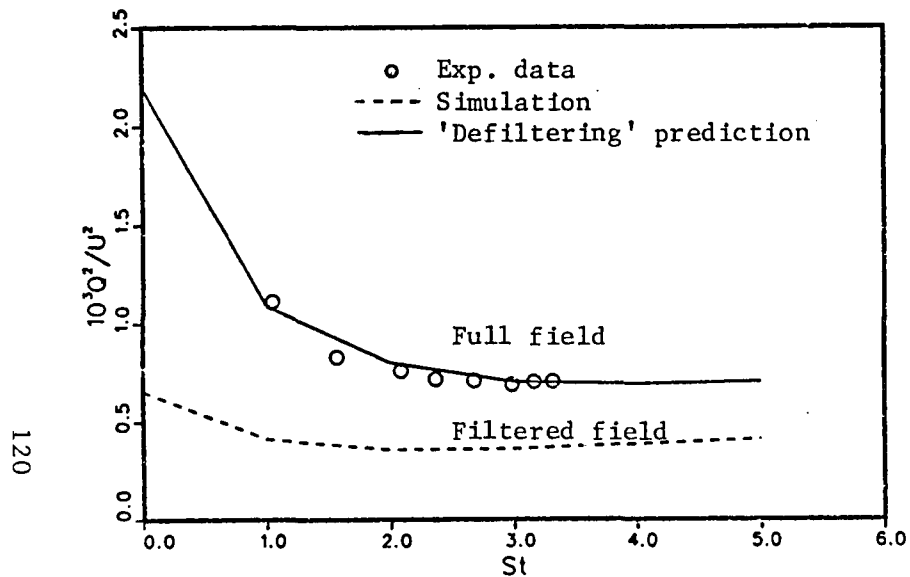
Fig. 6.14a. Time history of the turbulence intensity of the full and filtered flow field in homogeneous shear flow. $S = 12.9$ s^{-1}, $U = 12.4$ m/s. Large eddy simulation, pseudospectral method, second-order central difference for model terms, Smagorinsky model $c_s = 0.21$. "Defiltering" method, Eq. (5-12).

Turbulence Intensity in Shear Flow
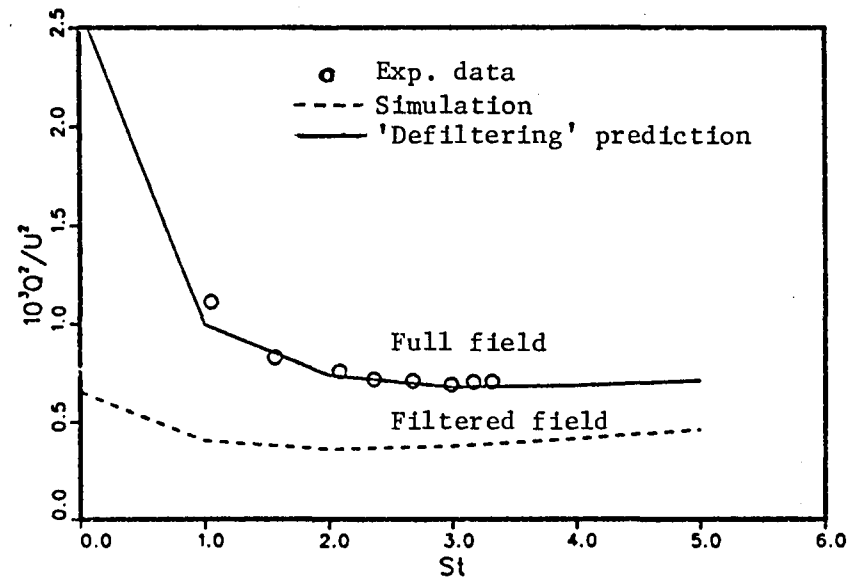
Fig. 6.14b. Time history of the turbulence intensity of the full and filtered flow field in homogeneous shear flow. $S = 12.9$ s^{-1}. Experimental results of Champagne, Harris and Corrsin (1970), $U = 12.4$ m/s. Large eddy simulation, pseudospectral method, second-order central difference for model terms, Smagorinsky and scale similarity model, $c_s = 0.19$ and $c_r = 1.1$. "Defiltering" method, Eq. (5-12).

Turbulence Intensity

Turbulence Intensity
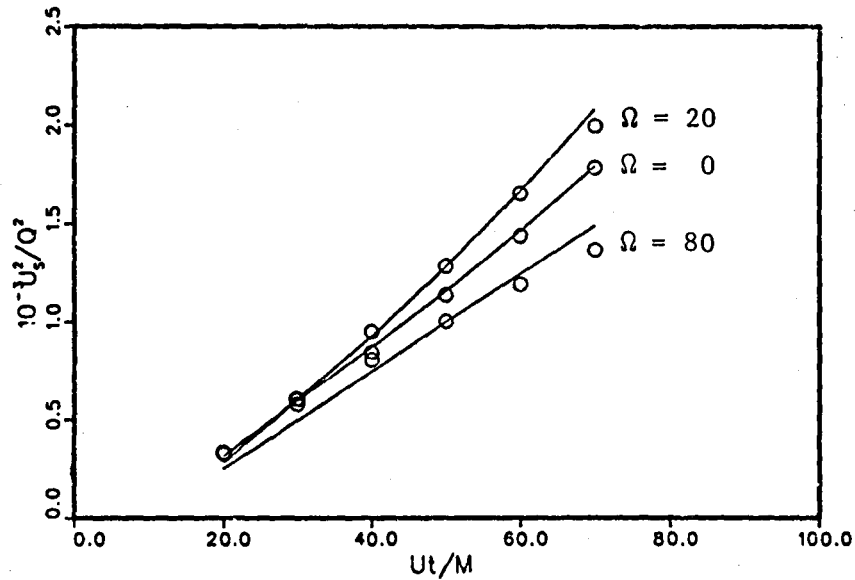
Fig. 7.1.   Time history of the inverse of the full turbulence intensity in homogeneous rotating turbulence. Comparison of "defiltered" results of large eddy simulation with experimental data of Wigeland and Nagib (1978). The initial energy and dissipation rates are matched to the experimental values shown in Table 7.2.
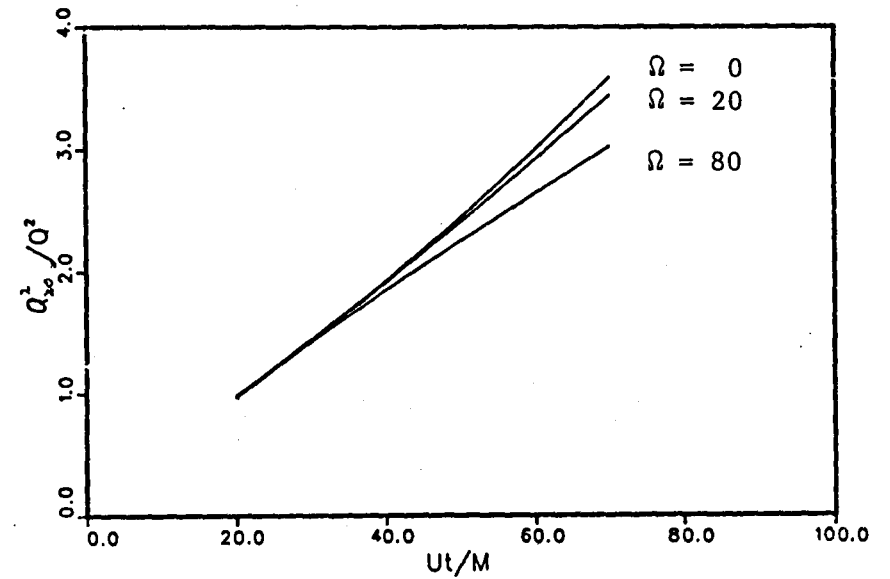
Fig. 7.2.   Time history of the inverse of the full turbulence intensity in homogeneous rotating turbulence. All cases have the same initial conditions as the $\Omega = 0$ case shown in Fig. 7.1.

Length Scale
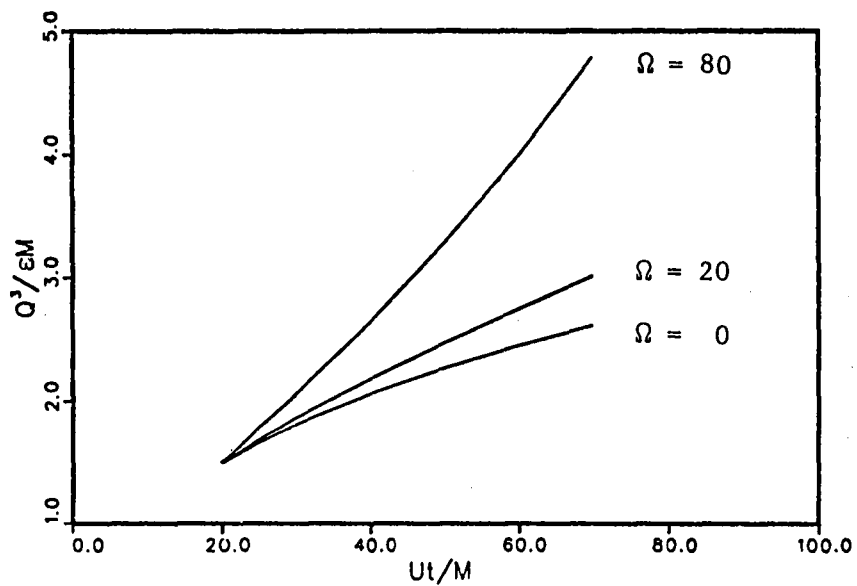
Fig. 7.3. Growth of the average length scale in the homogeneous rotating flows of Fig. 7.2.

Turbulence Intensity

Energy Components
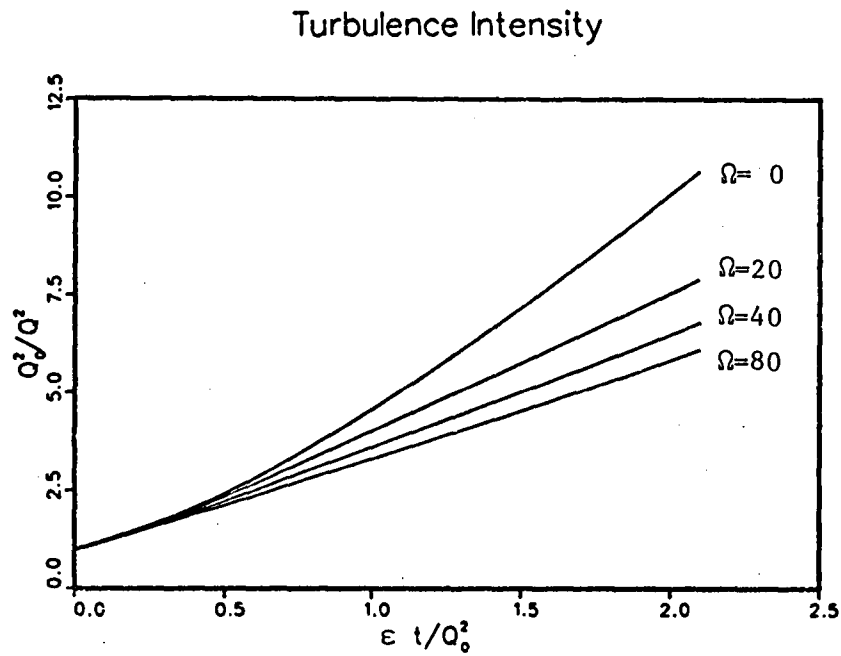
Fig. 7.4. Full simulation of the decay of the turbulence intensity in homogeneous turbulent flows.
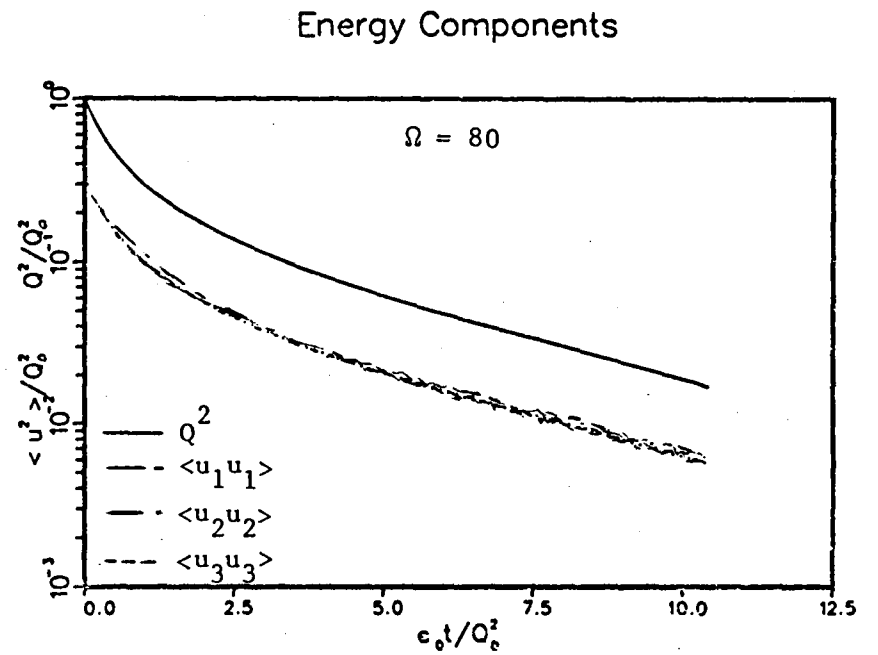
Fig. 7.5. Time history of the components of the turbulence intensity in the $\Omega = 80$ s^{-1} case of Fig. 7.4.

Integral Length Scales
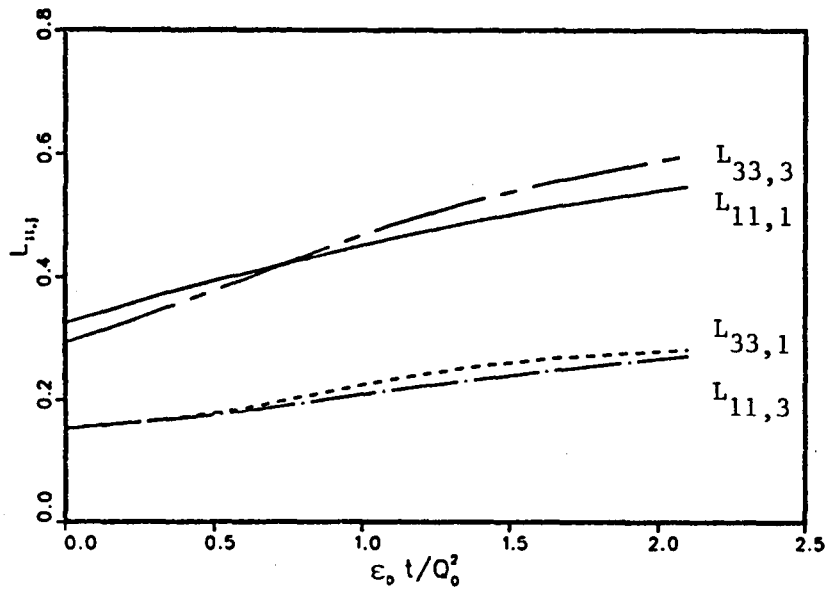
Fig. 7.6a. Growth of the integral length scales in homogeneous isotropic turbulence in the $\Omega = 0$ s^{-1} case of Fig. 7.4.

Integral Length Scales
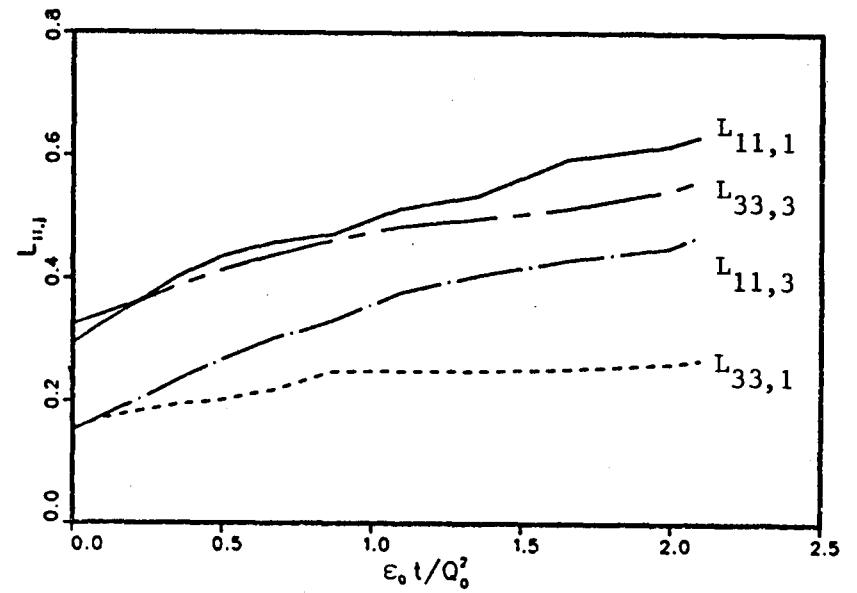
Fig. 7.6b. Growth of integral length scales in homogeneous rotating turbulence in the $\Omega = 80$ s^{-1} case of Fig. 7.4.

Turbulence Intensity

Turbulence Intensity
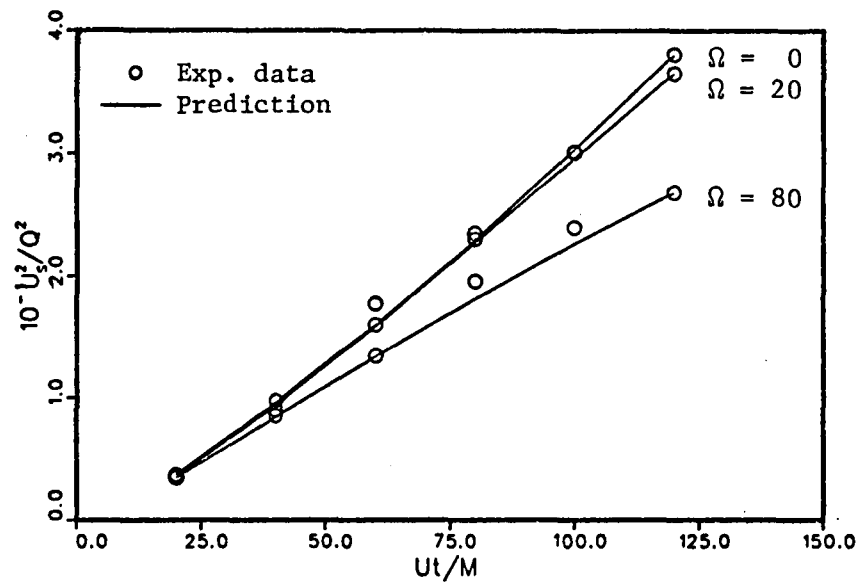
Fig. 7.7a. Two-equation model prediction of Wige-
land and Nagib's (1978) experimental
results on the decay of homogeneous
rotating turbulence. Case A of Table
7.3.
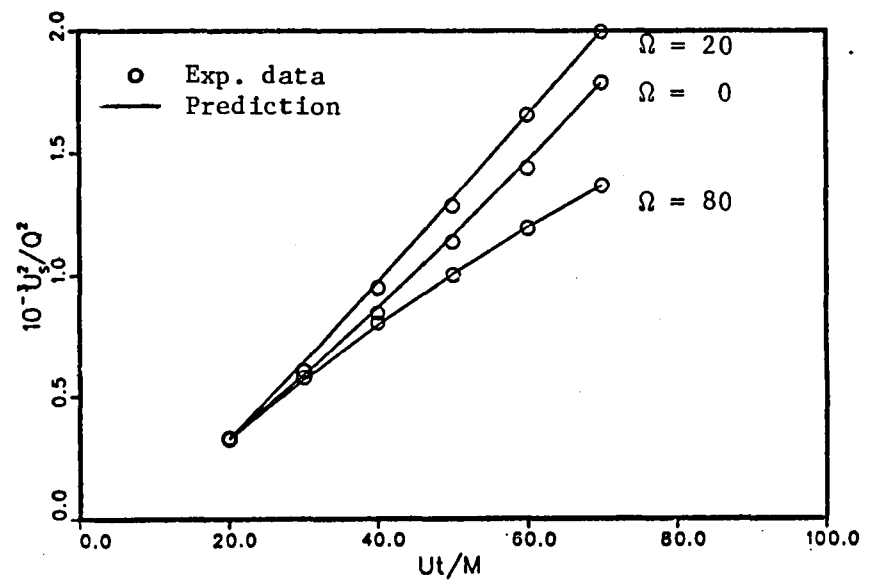
Fig. 7.7b. Two-equation model prediction of Wige-
land and Nagib's (1978) experimental
results on the decay of homogeneous
rotating turbulence. Case B of Table
7.3.

Turbulence Intensity
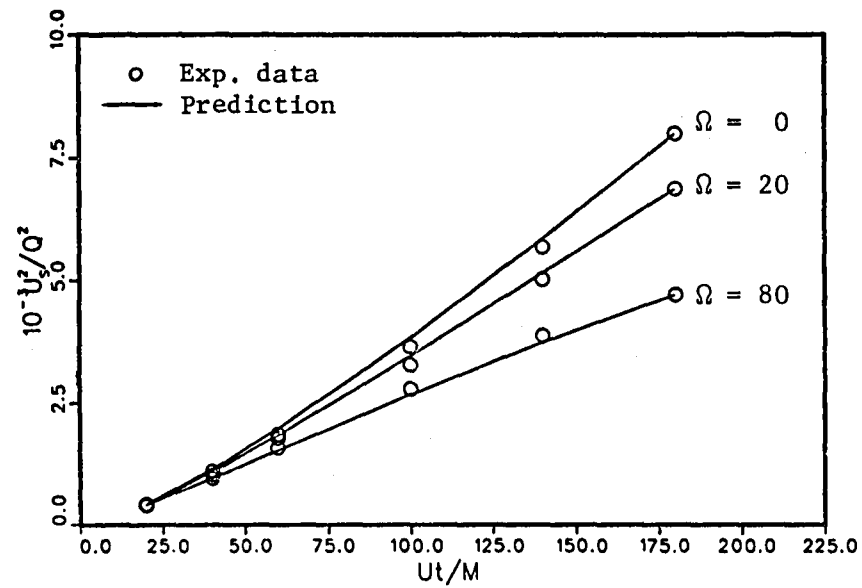
Fig. 7.7c. Two-equation model prediction of Wige-
land and Nagib's (1978) experimental
results on the decay of homogeneous
rotating turbulence. Case C of Table
7.3.

Turbulence Intensity in Shear Flow
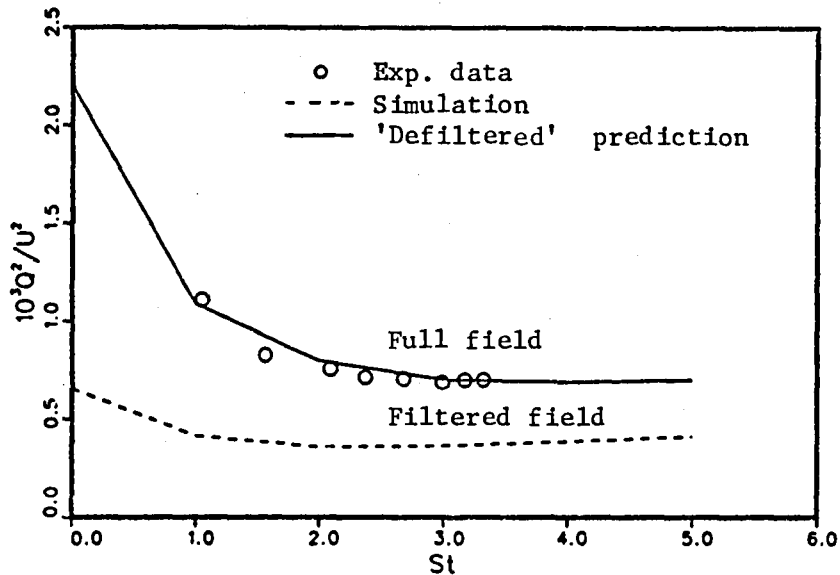
Fig. 8.1a. Time history of full and filtered turbulence intensities of homogeneous shear turbulent flow with $U = 12.4$ m/s and $S = 12.9$ s^{-1}. Comparison of experimental results of Champagnbe, Harris, and Corrsin (1970) and large eddy simulation with pseudospectral method and Smagorinsky model, $c_s = 0.19$.

Turbulence Intensity in Shear Flow
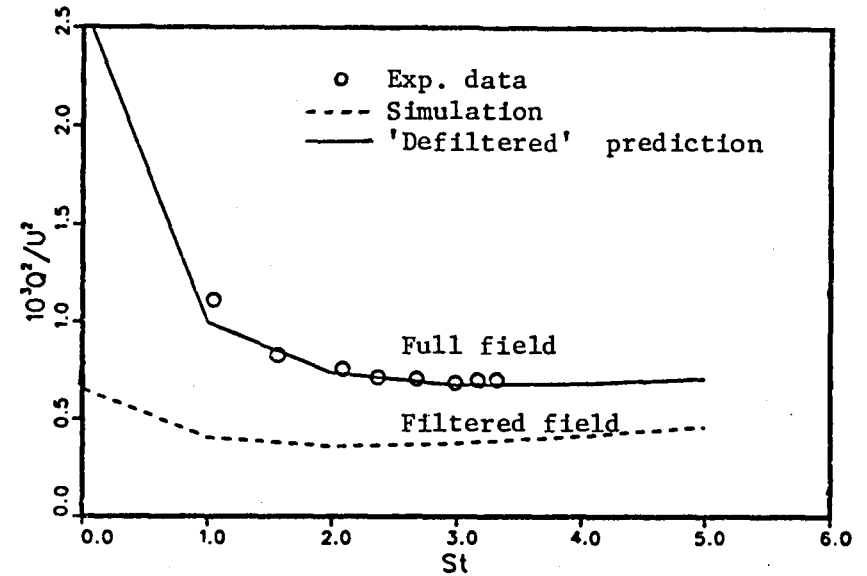
Fig. 8.1b. Time history of full and filtered turbulence intensities of homogeneous shear turbulent flow with $U = 12.4$ m/s and $S = 12.9$ s^{-1}. Comparison of experimental results of Champagne, Harris, and Corrsin (1970) and large eddy simulation with pseudospectral method and Smagorinsky and scale similarity models, $c_s = 0.19$ and $c_r = 1.1$.

Reynolds Stress Anisotropy
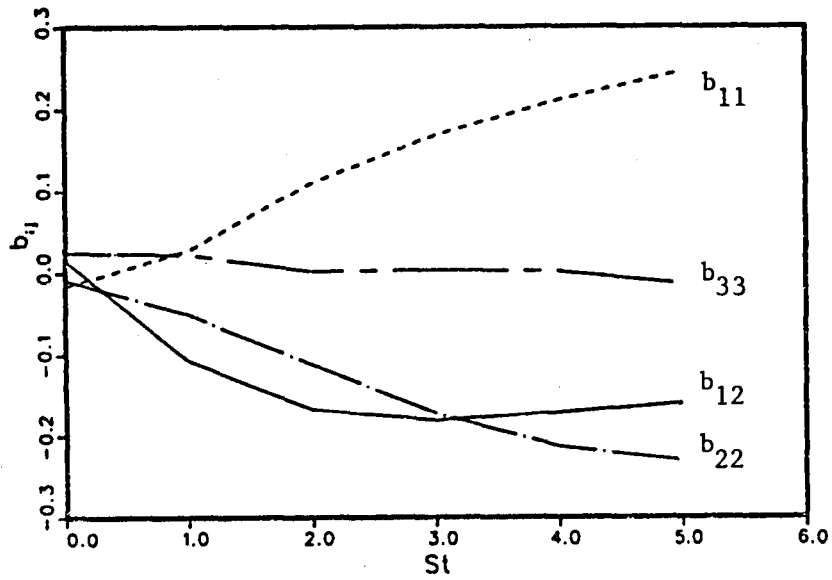
Reynolds Stress Anisotropy

Fig. 8.2a. Time history of the components of the
Reynolds stress anisotropy tensor of
the filtered flow field shown in Fig.
8.1a.
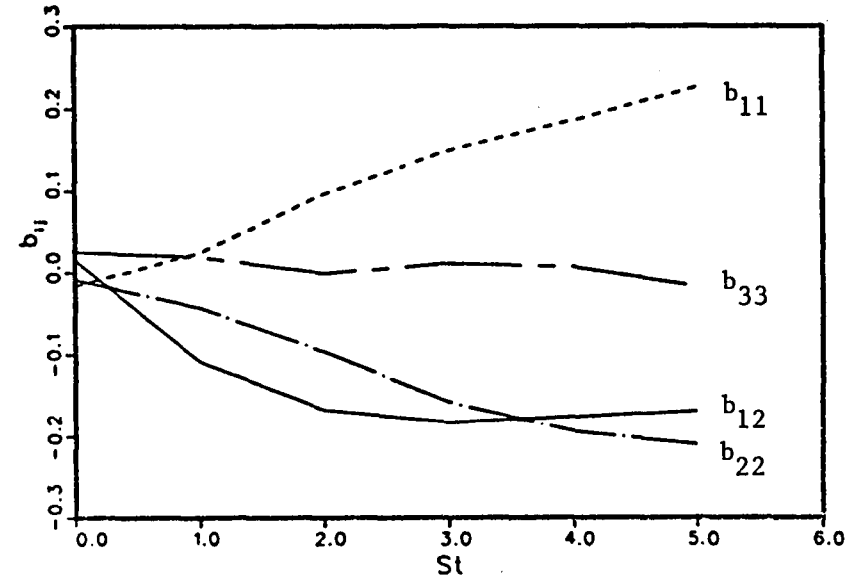
Fig. 8.2b. Time history of the components of the
Reynolds stress anisotropy tensor of
the filtered flow field shown in Fig.
8.1b.

Reynolds Stress Anisotropy
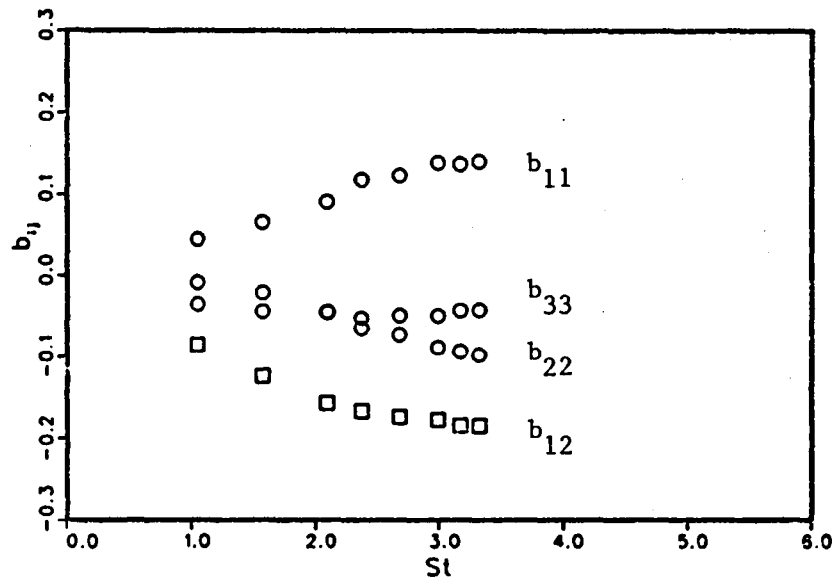
Fig. 8.2c. Time history of the components of the
Reynolds stress anisotropy tensor of
the full flow field obtained from the
experimental data of Champagne,
Harris, and Corrsin (1970) shown in
Fig. 8.1.

Energy Balance $< \bar{u}_1^2 >$

Production

Dissipation

'convection'   Rate of change

Redistribution

Energy Balance $< \bar{u}_1^2 >$

Production

Rate of change

Dissipation

Redistribution

- - - - 'convection' + scale-similarity term

St

St
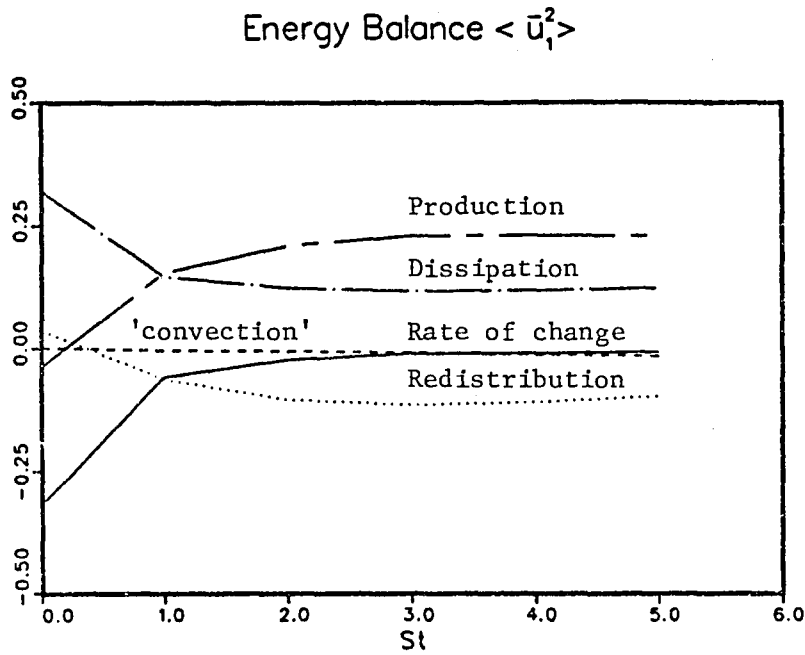
Fig. 8.4a. Time history of each spatially aver-
aged term of the $< \bar{u}_1^2 >$ equation of
the filtered flow field shown in Fig.
8.1a.
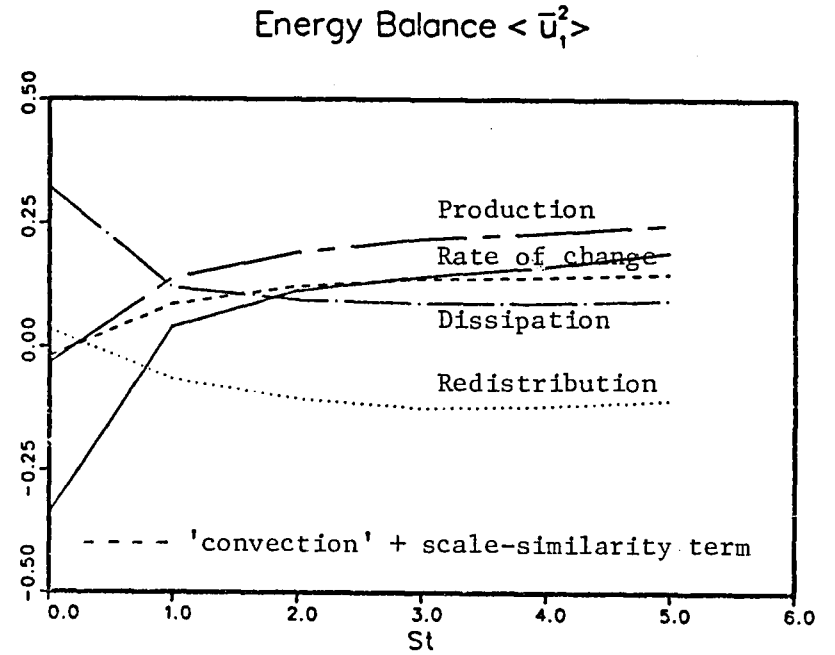
Fig. 8.4b. Time history of each spatially aver-
aged term of the $< \bar{u}_1^2 >$ equation of
the filtered flow field shown in Fig.
8.1b.

Energy Balance
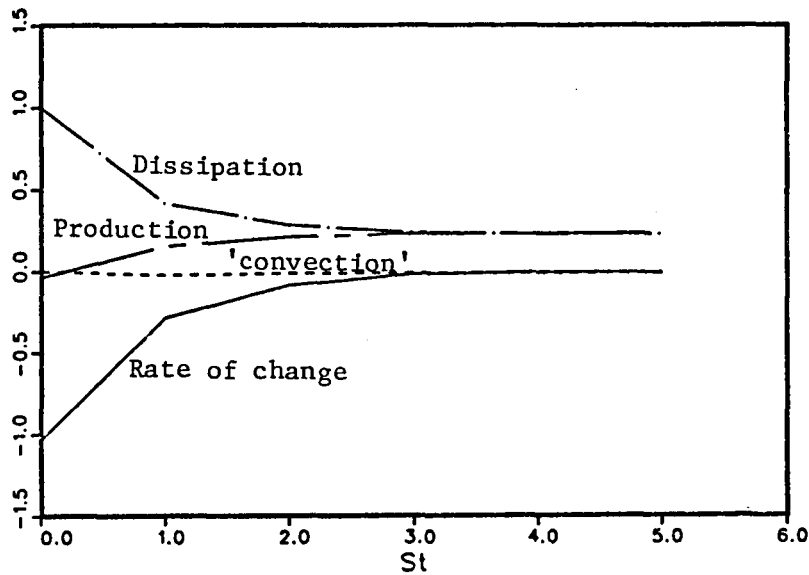
Energy Balance

Fig. 8.3a. Time history of each spatially aver-
aged term of the turbulent kinetic
energy equation of the filtered flow
field shown in Fig. 8.1a.

Fig. 8.3b. Time history of each spatially aver-
aged term of the turbulent kinetic
energy equation of the filtered flow
field shown in Fig. 8.1b.

131

Energy Balance $< \bar{u}_2^2 >$

Energy Balance $< \bar{u}_2^2 >$
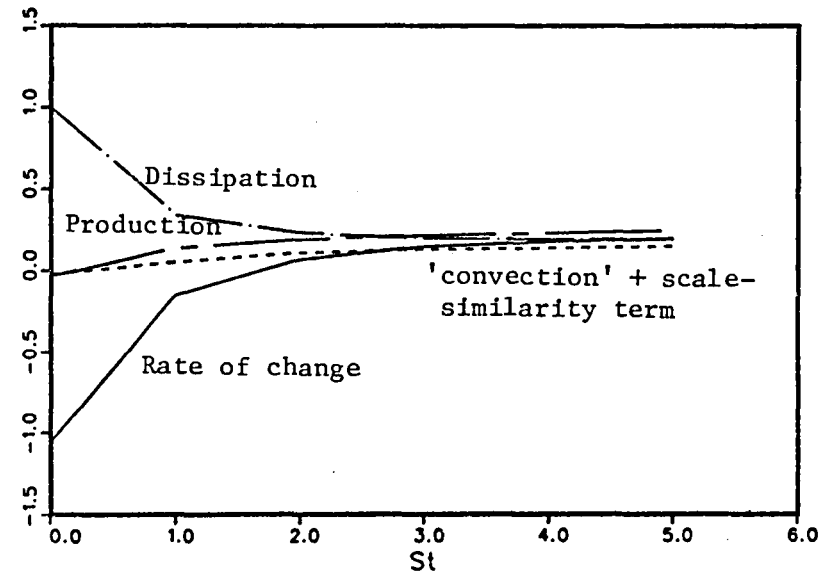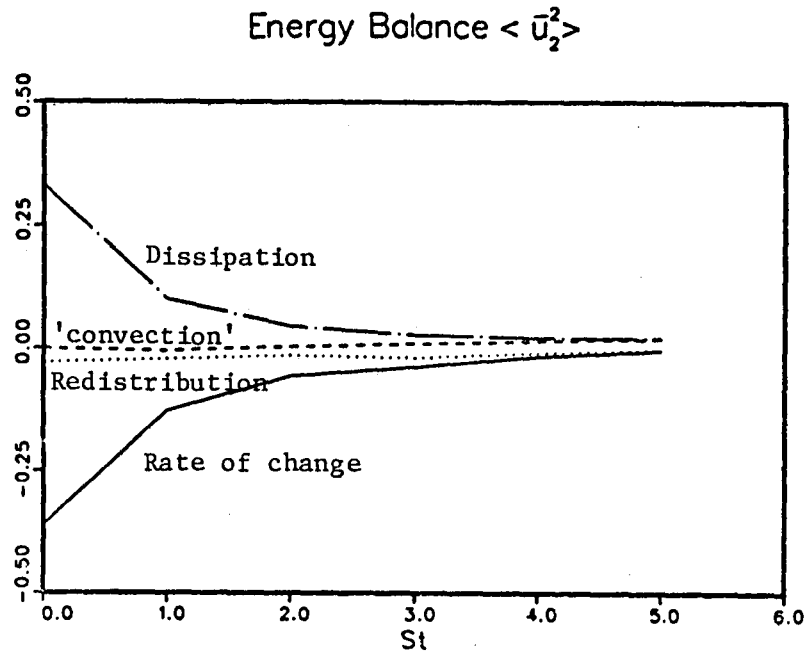
Fig. 8.5a. Time history of each spatially aver-
aged term of the $< \overline{u}_2^{-2} >$ equation of
the filtered flow field shown in Fig.
8.1a.

Fig. 8.5b. Time history of each spatially aver-
aged term of the $< \overline{u}_2^{-2} >$ equation of
the filtered flow field shown in Fig.
8.1b.

Energy Balance $< \bar{u}_3^2 >$

Dissipation

Redistribution

'convection'

Rate of change

St

Energy Balance $< \bar{u}_3^2 >$

Dissipation

Redistribution

'convection' + scale-similarity term

Rate of change

St
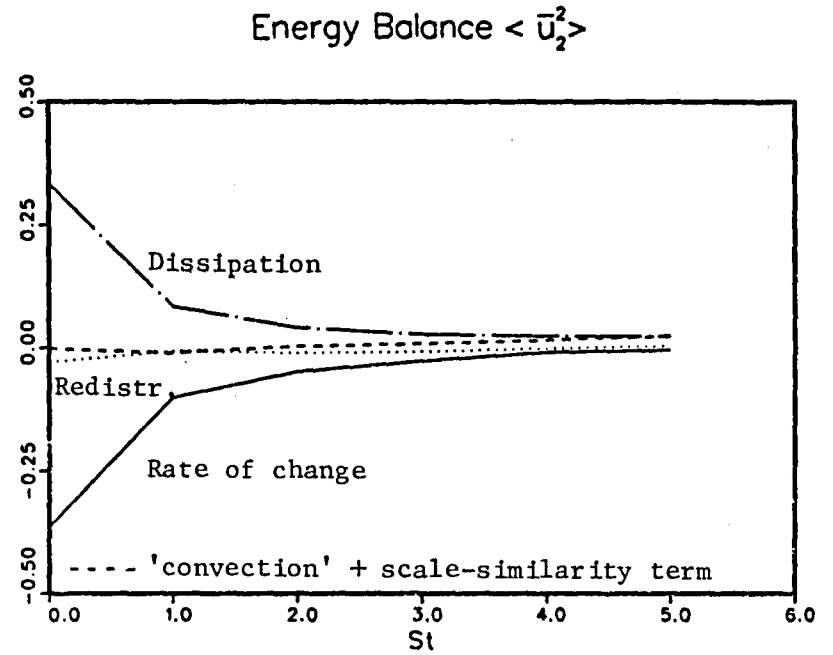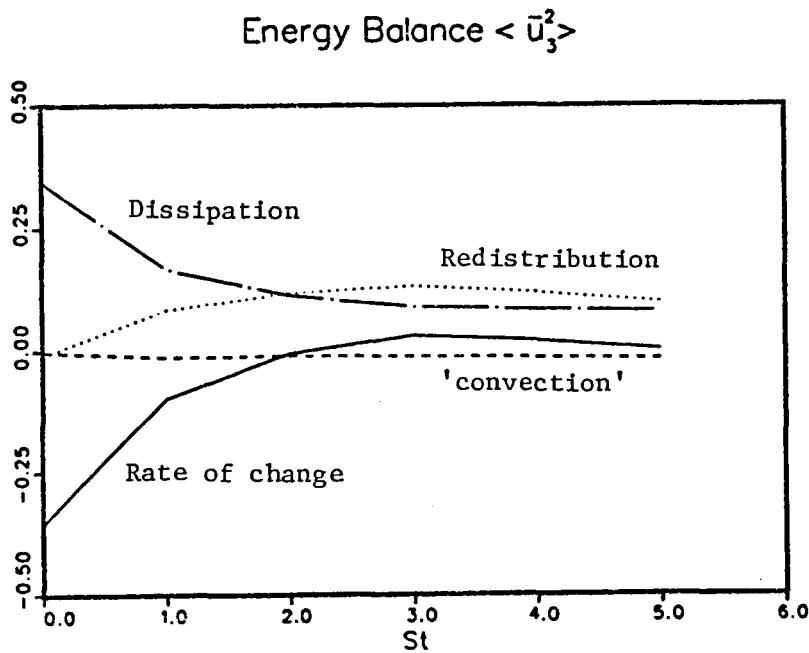
Fig. 8.6a. Time history of each spatially aver-
aged term of the $< \bar{u}_3^2 >$ equation of
the filtered flow field shown in Fig.
8.1a.
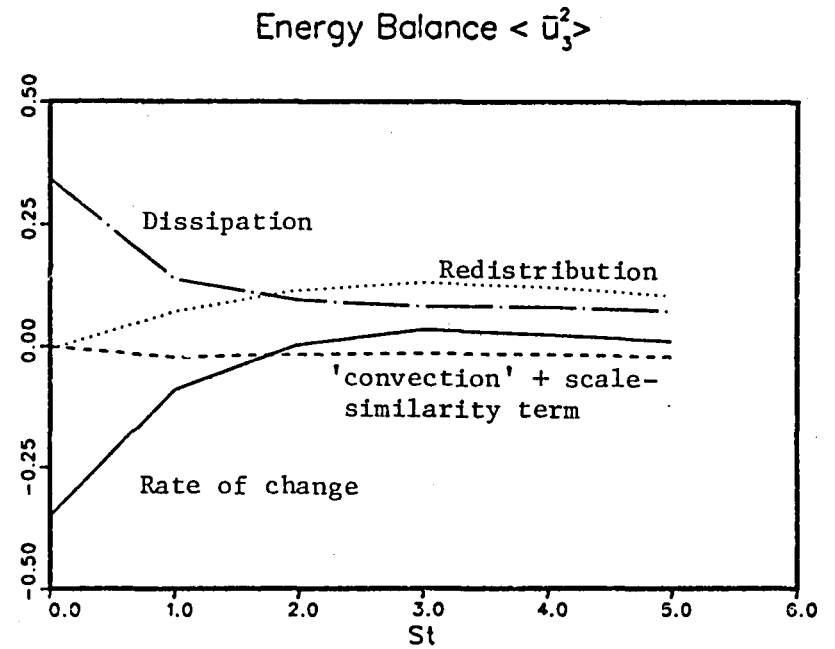
Fig. 8.6b. Time history of each spatially aver-
aged term of the $< \bar{u}_3^2 >$ equation of
the filtered flow field shown in Fig.
8.1b.

Plane Strain Flow $\Gamma = 12.9\ s^{-1}$

Plane Strain Flow $\Gamma = 12.9\ s^{-1}$

o   Exp. data
—— New model
—·— R model
—··— LRR model
----- WR model
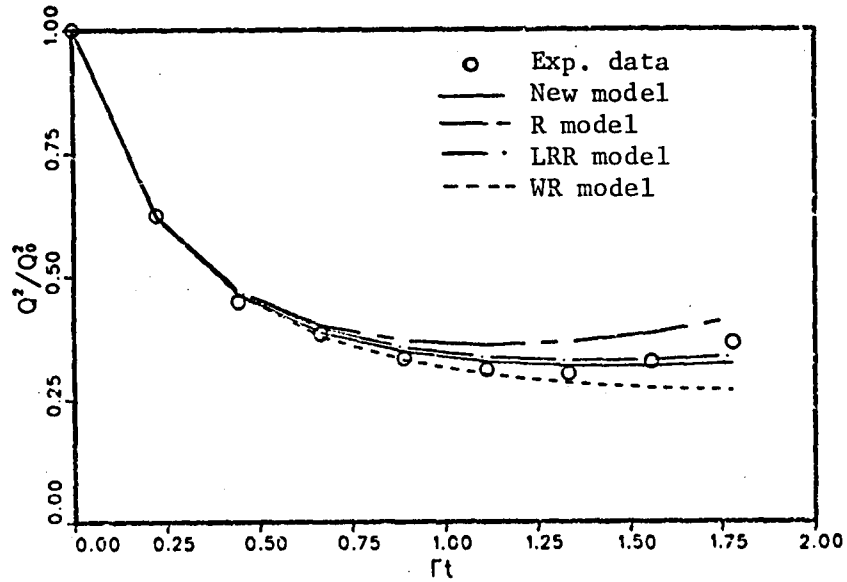
Fig. 8.7a. Time-averaged Reynolds stress model prediction of the turbulent intensity of the experimental results of Tucker and Reynolds (1976) on homogeneous turbulence subject to a mean plane strain rate, $\Gamma = 4.45\ s^{-1}$.
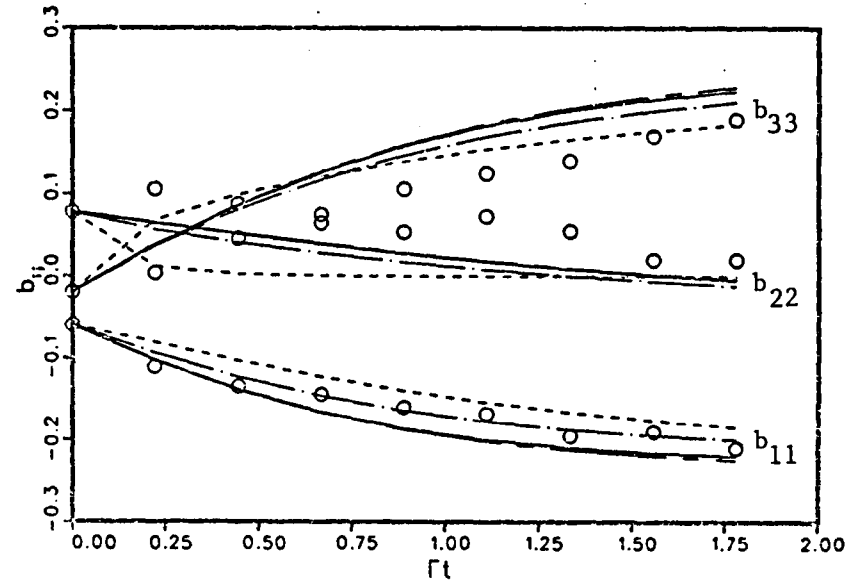
Fig. 8.7b. Time-averaged Reynolds stress model prediction of the components of the Reynolds stress anisotropy tensor of the flow of Fig. 8.7a; the lines are as in the previous figure.

Plane Strain Flow $\Gamma = 32.23\ s^{-1}$

Plane Strain Flow $\Gamma = 32.23\ s^{-1}$
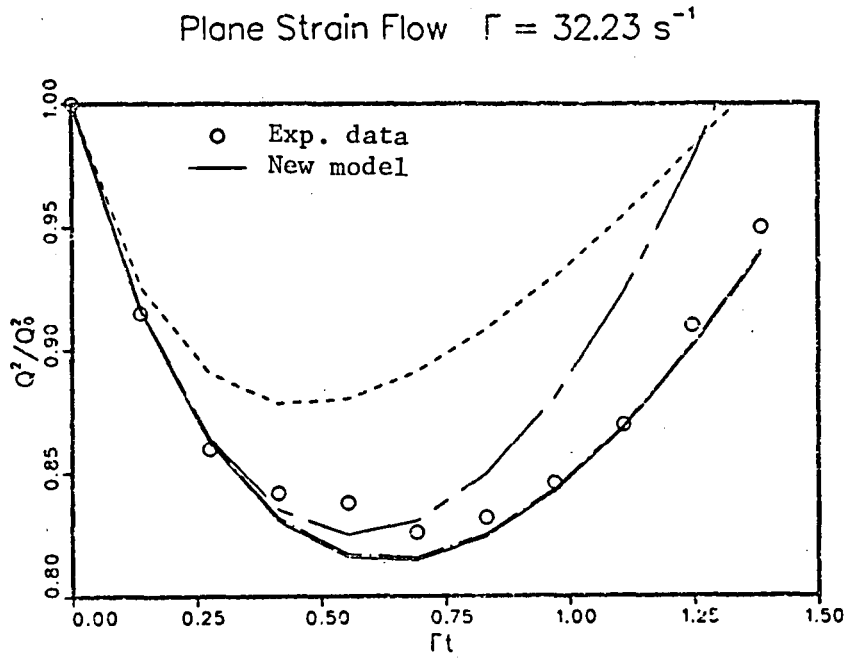
Fig. 8.8a. Time-averaged Reynolds stress model prediction of the turbulence intensity of the experimental results of Gence and Matheiu (1979) on homogeneous turbulence subject to a mean axisymmetric strain rate, $\Gamma = 32.23\ s^{-1}$. See Fig. 8.7 for symbols.
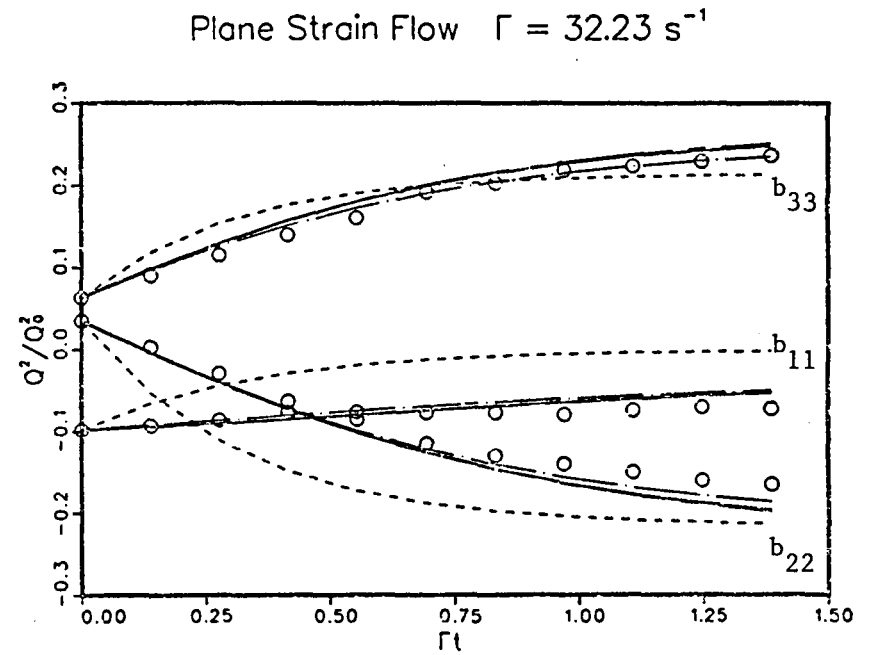
Fig. 8.8b. Time-averaged Reynolds stress model prediction of the components of the Reynolds stress anisotropy tensor of the flow of Fig. 8.8a.

Shear Flow   S = 12.9 s⁻¹

$\bigcirc \langle u_1^2\rangle$, $\square \langle u_2^2\rangle$, $\triangle \langle u_3^2\rangle$, $\nabla \langle -u_1 u_2\rangle$ Exp. data

—————   New model
—— · ——   LRR

Shear Flow   S = 12.9 s⁻¹

$\bigcirc \langle u_1^2\rangle$, $\square \langle u_2^2\rangle$, $\triangle \langle u_3^2\rangle$, $\nabla \langle -u_1 u_2\rangle$ Exp. data

- - - - -   WR
—— —   R

136
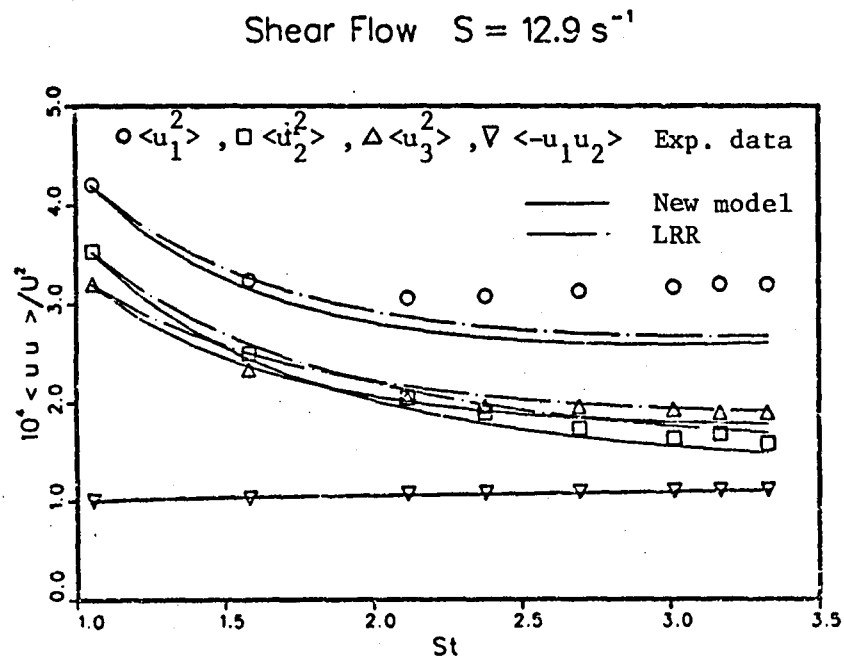
Fig. 8.9a.   Time-averaged Reynolds stress model prediction of the components of the turbulence intensity and shear stress of the experimental results of Champagne, Harris, and Corrsin (1970) on homogeneous turbulence subject to a mean shear rate, $S = 12.9 \text{ s}^{-1}$.
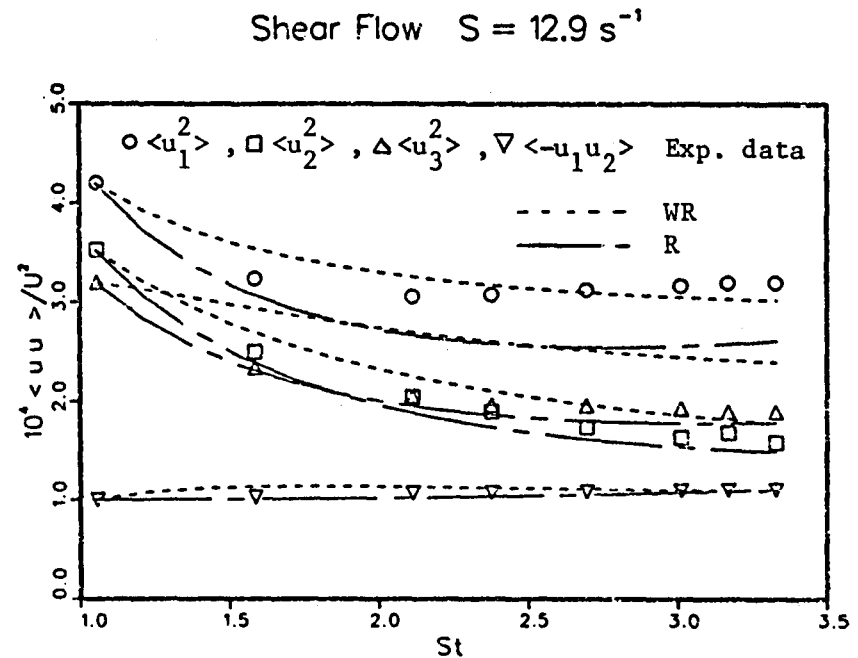
Fig. 8.9b.   Time-averaged Reynolds stress model prediction of the components of the turbulence intensity and shear stress of the experiment of Fig. 8.9a.

Shear Flow   S = 48.0 s^{-1}

Shear Flow   S = 48.0 s^{-1}
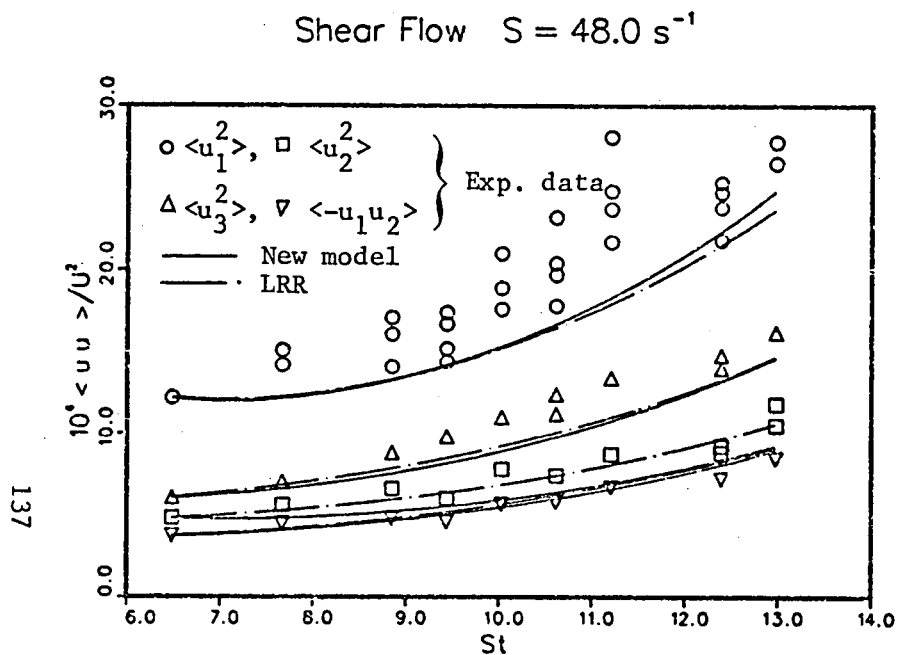
Fig. 8.10a. Time-averaged Reynolds stress model prediction of the components of the turbulence intensity and shear stress of the experimental results of Harris, Graham, and Corrsin (1977) on homogeneous turbulence subject to a mean shear rate, S = 44.0 s^{-1}.
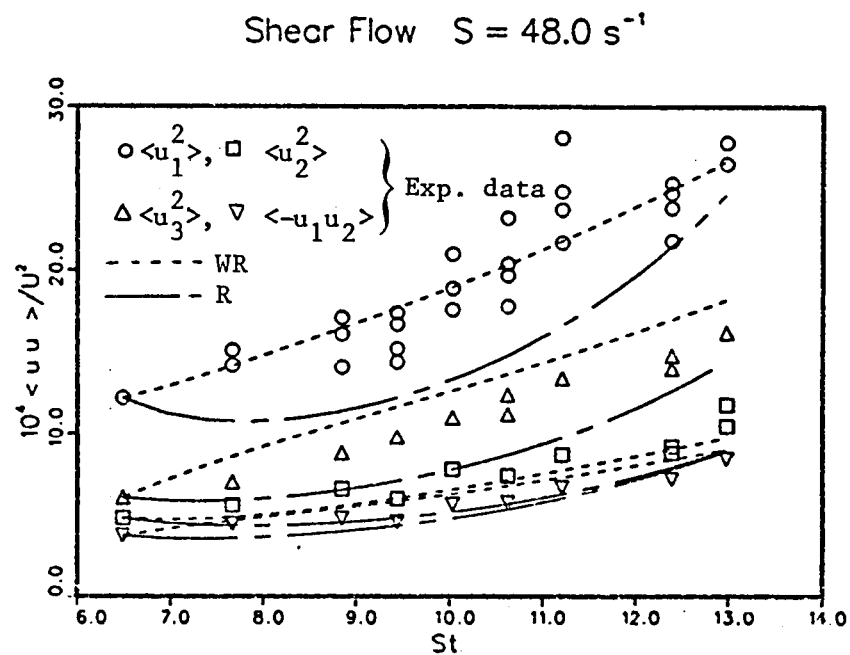
Fig. 8.10b. Time-averaged Reynolds stress model prediction of the components of the turbulence intensity and shear stress of the flow of Fig. 8.10a.

137
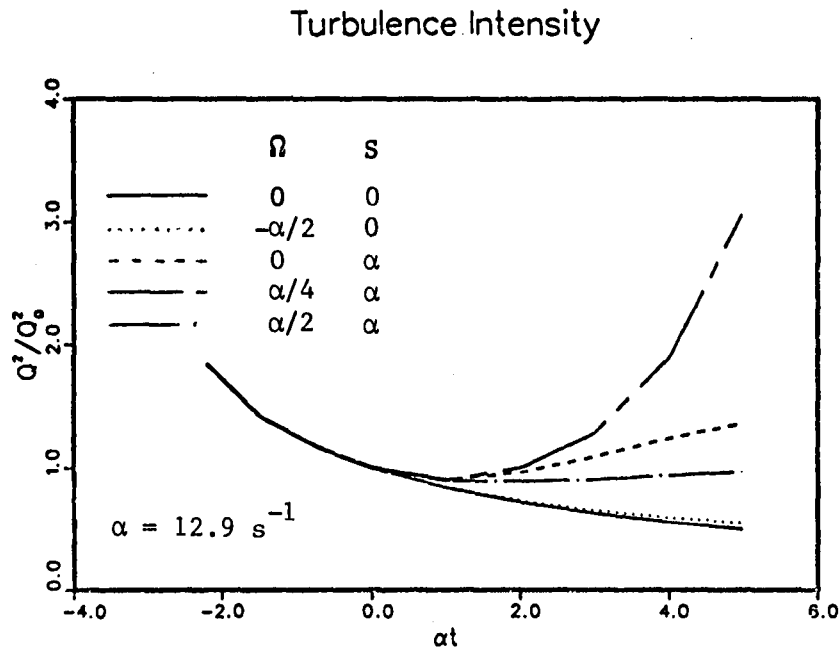
Fig. 9.1a. Time history of the turbulence intensity of homogeneous shear turbulent flows in the presence of system rotation. Large eddy simulation, pseudospectral method, Smagorinsky model, $c_s = 0.19$.
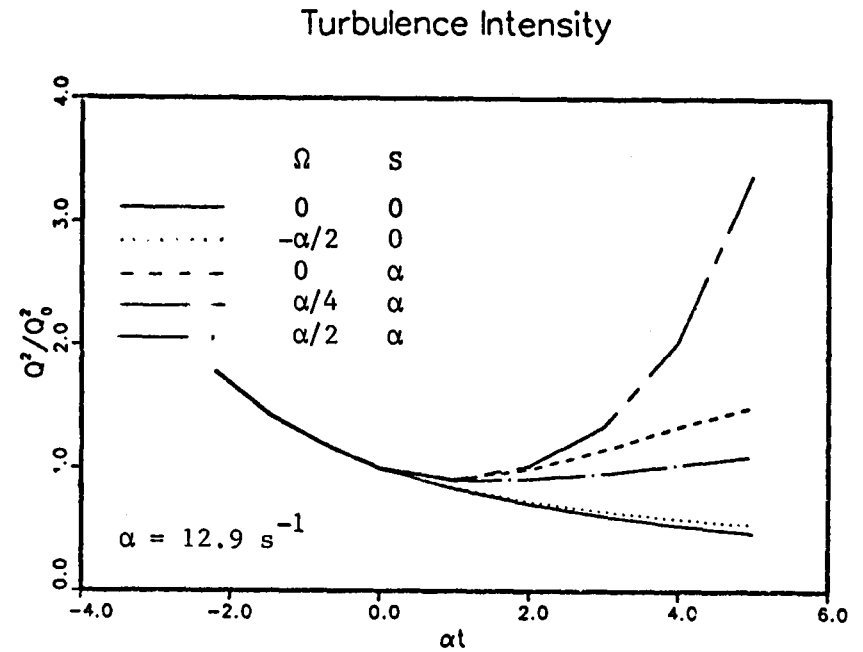
Fig. 9.1b. Time history of the turbulence intensity of homogeneous shear turbulent flows in the presence of system rotation. Large eddy simulation, pseudospectral method, Smagorinsky and scale similarity model, $c_s = 0.16$ and $c_r = 1.1$.

138

Reynolds Stress Anisotropy b_{12}

Reynolds Stress Anisotropy b_{12}
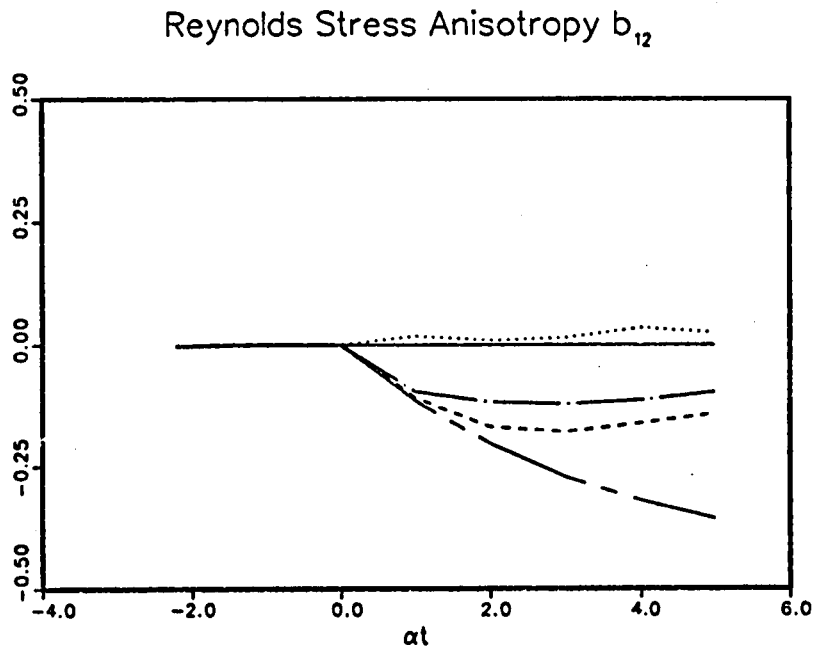
Fig. 9.2a. Time history of the shear stress ani-
sotropy of the turbulent flows shown
in Fig. 9.1a.
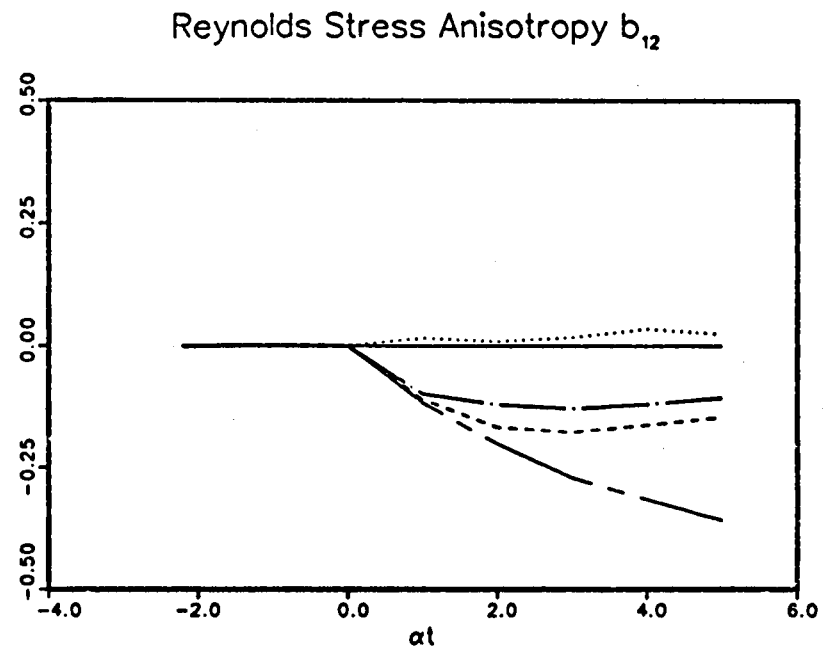
Fig. 9.2b. Time history of the shear stress of
the turbulent flows shown in Fig.
9.1b.

Reynolds Stress Anisotropy b_{11}

Reynolds Stress Anisotropy b_{11}
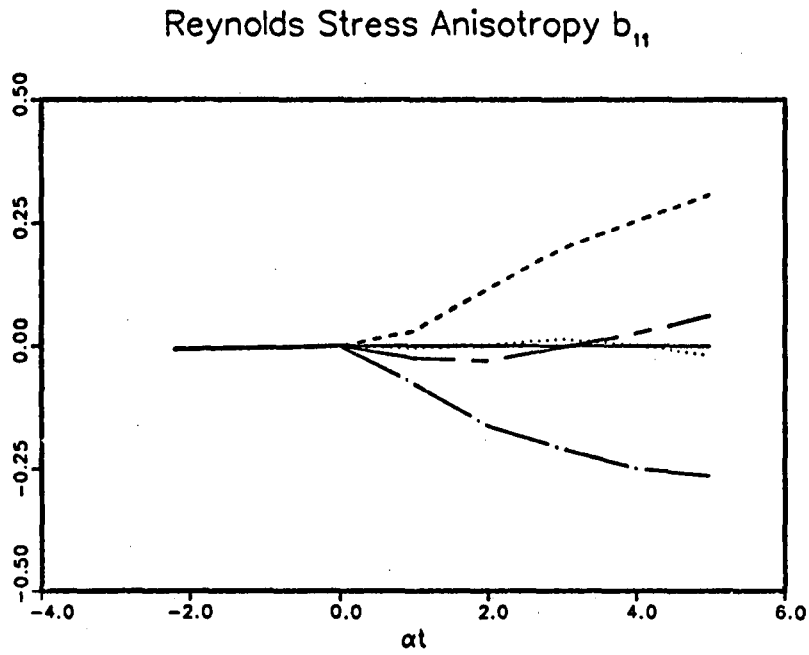
Fig. 9.3b. Time history of the component b_{11} of the Reynolds stress anisotropy tensor of the turbulent flows shown in Fig. 9.1b.

Fig. 9.3a. Time history of the component b_{11} of the Reynolds stress anisotropy tensor of the turbulent flows shown in Fig. 9.1a.
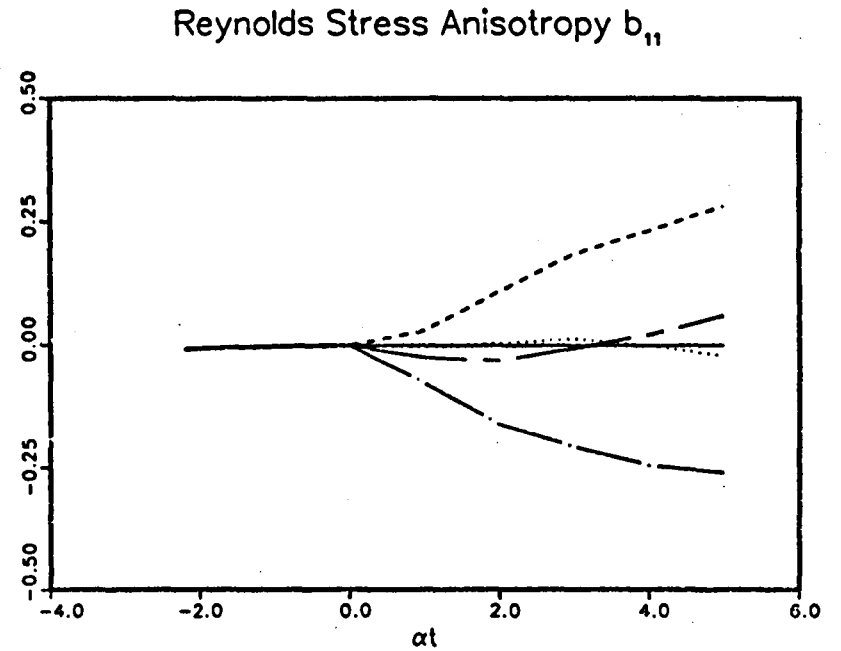
Reynolds Stress Anisotropy b_{22}

Reynolds Stress Anisotropy b_{22}
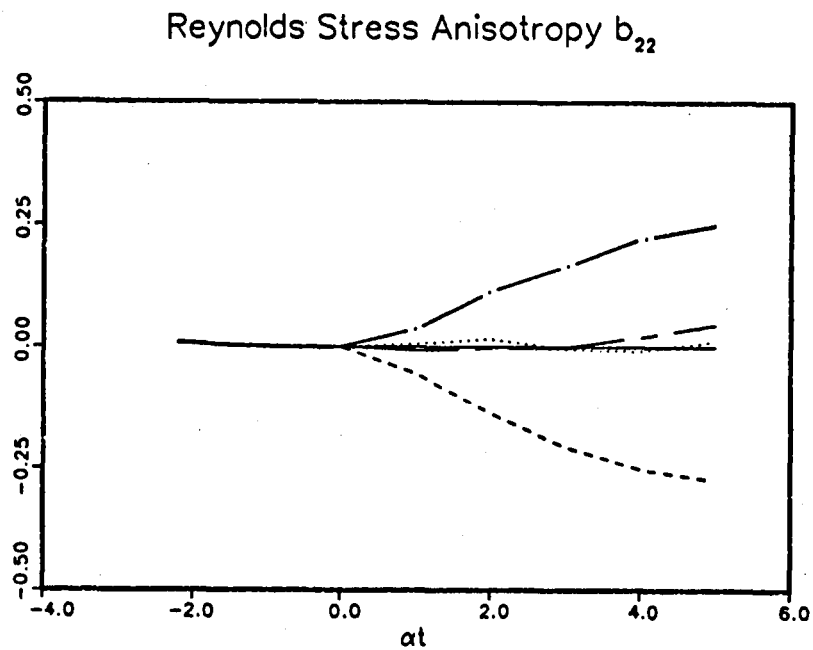
Fig. 9.4a. Time history of the component b_{22} of the Reynolds stress anisotropy tensor of the turbulent flows shown in Fig. 9.1a.

Fig. 9.4b. Time history of the component b_{22} of the Reynolds stress anisotropy tensor of the turbulent flows shown in Fig. 9.1b.
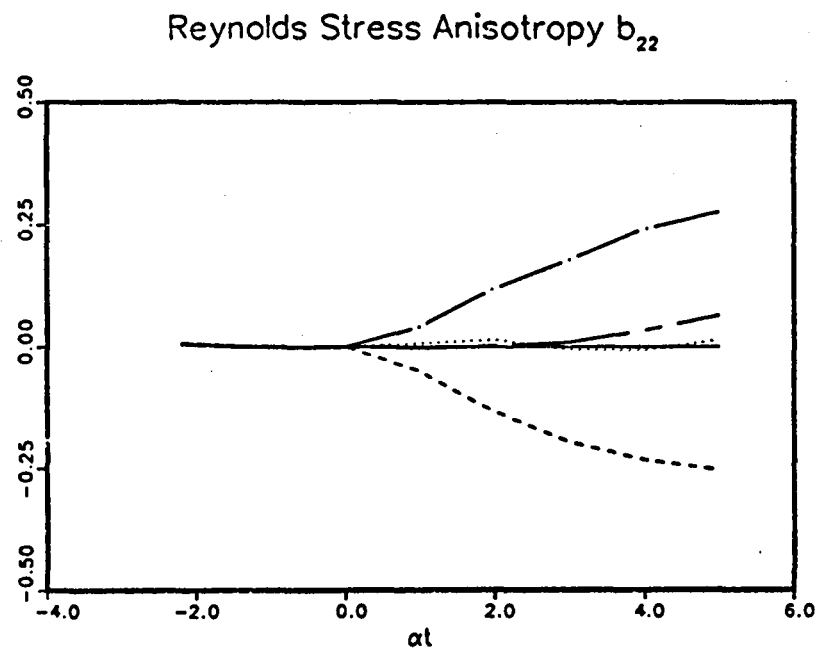
Reynolds Stress Anisotropy b_{33}

Reynolds Stress Anisotropy b_{33}
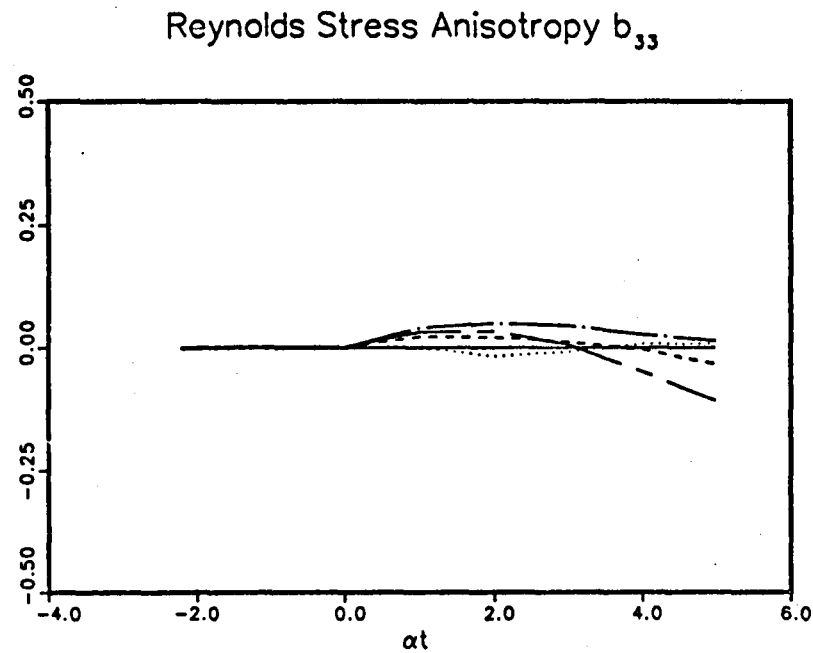
Fig. 9.5a.   Time history of the component b_{33} of the Reynolds stress anisotropy tensor of the turbulent flows shown in Fig. 9.1a.

Fig. 9.5b.   Time history of the component b_{33} of the Reynolds stress anisotropy tensor of the turbulent flows shown in Fig. 9.1b.

Energy Production

Energy Production
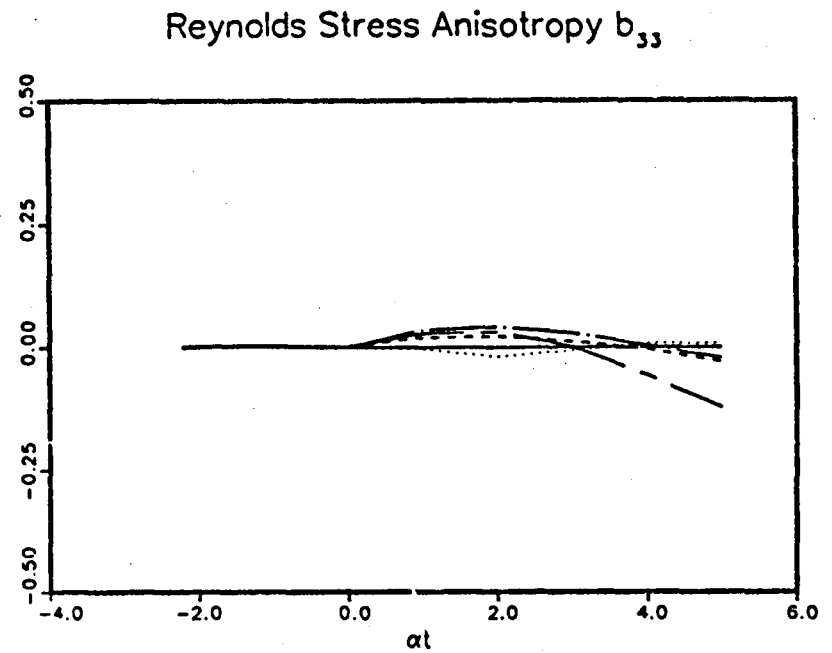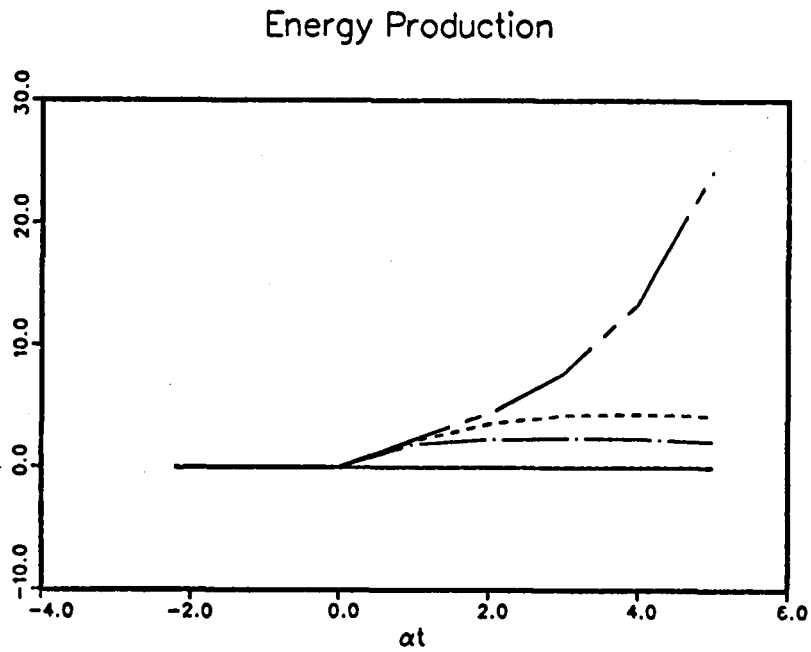
Fig. 9.6a. Time history of the production rate of turbulence, nondimensionalized by the dissipation rate at $\alpha t = 0$, of the turbulent flows shown in Fig. 9.1a.
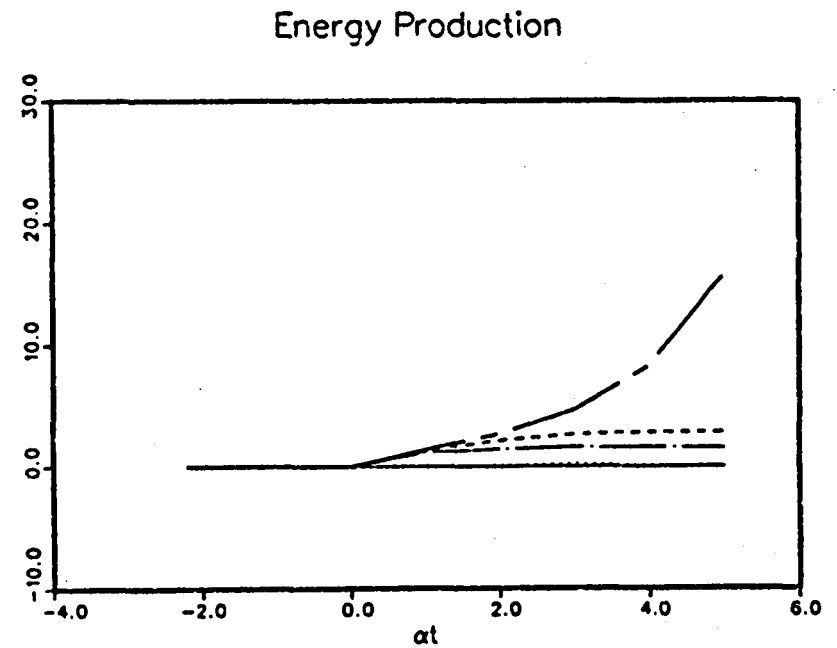
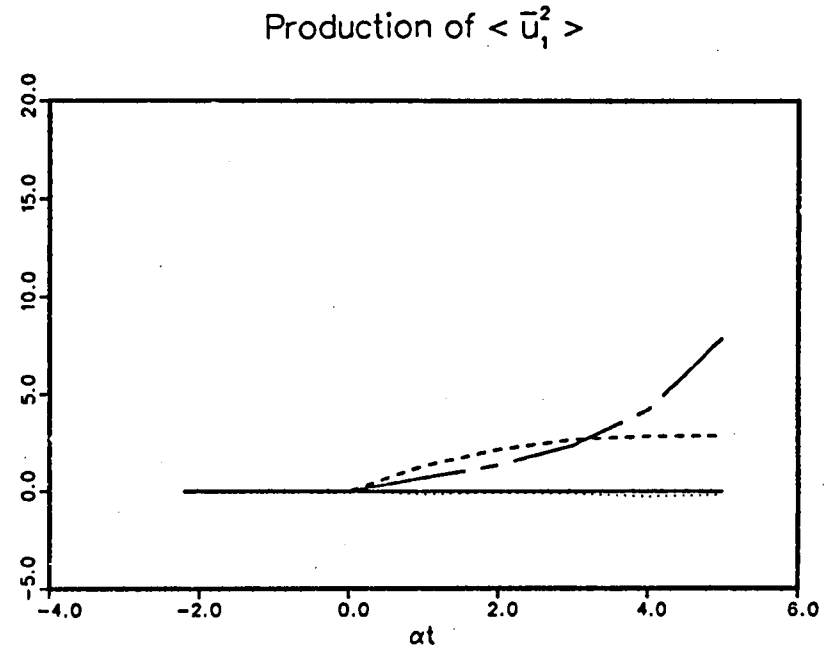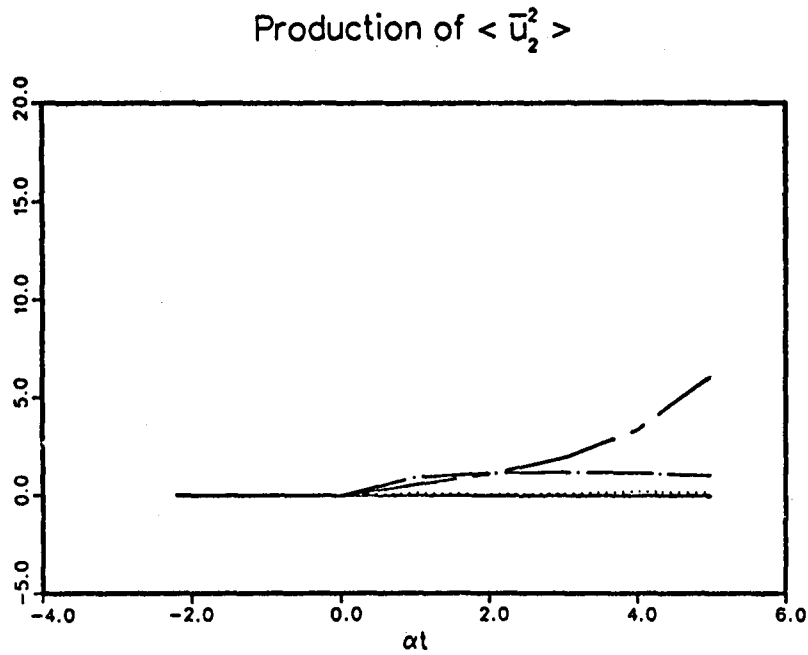Fig. 9.6b. Time history of the production rate of turbulence, nondimensionalized by the dissipation rate at $\alpha t = 0$, of the turbulent flwos shown in Fig. 9.1b.

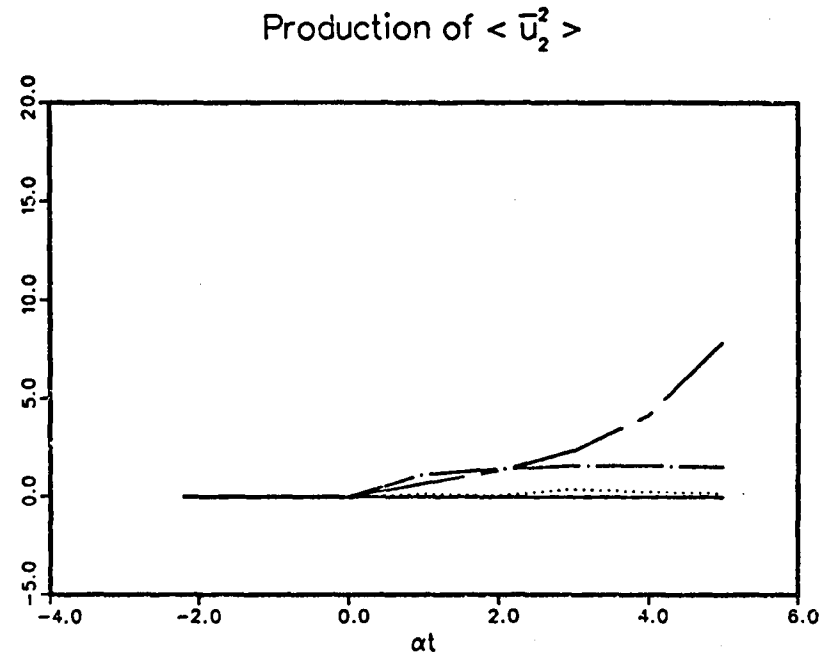## Energy Dissipation

Energy Dissipation
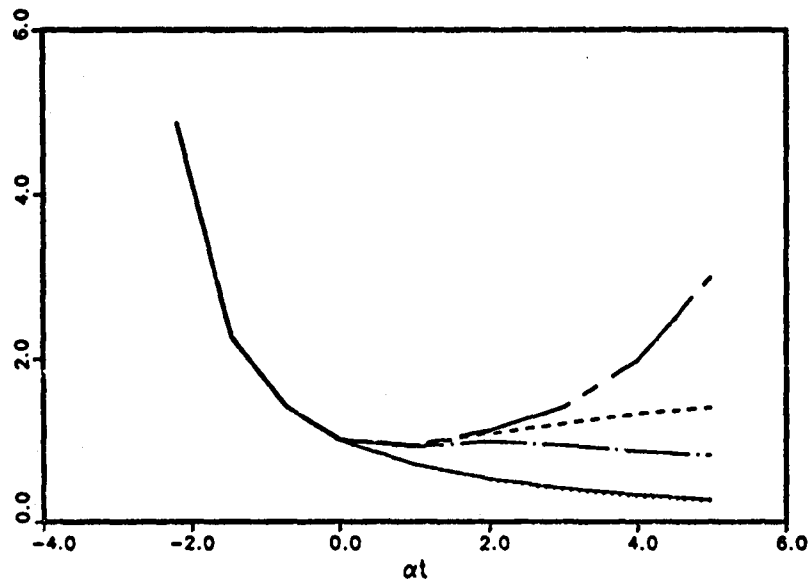
Fig. 9.7a. Time history of the dissipation rate of turbulence, nondimensionalized by the dissipation rate at $\alpha t = 0$, of the turbulent flows shown in Fig. 9.1a.

Fig. 9.7b. Time history of the dissipation rate of turbulence, nondimensionalized by the dissipation rate at $\alpha t = 0$, of the turbulent flows shown in Fig. 9.1b.

Production of $< \bar{u}_1^2 >$

Production of $< \bar{u}_1^2 >$
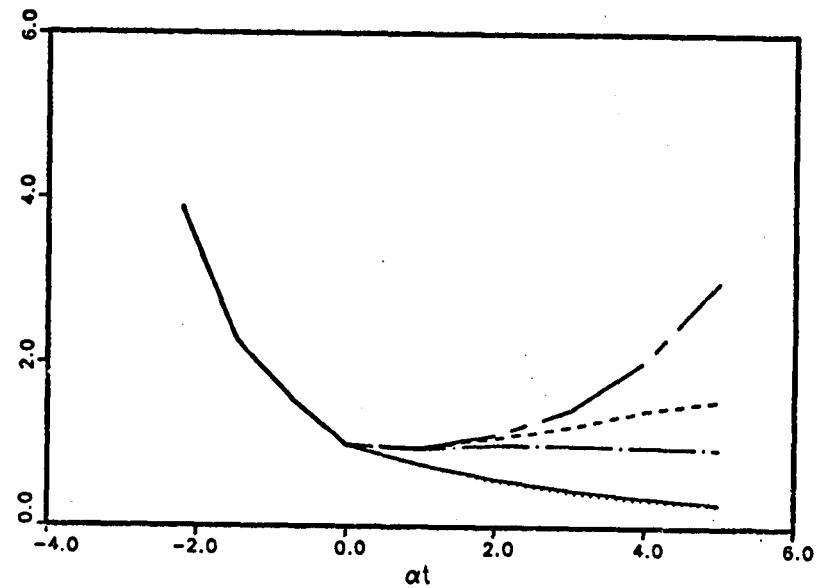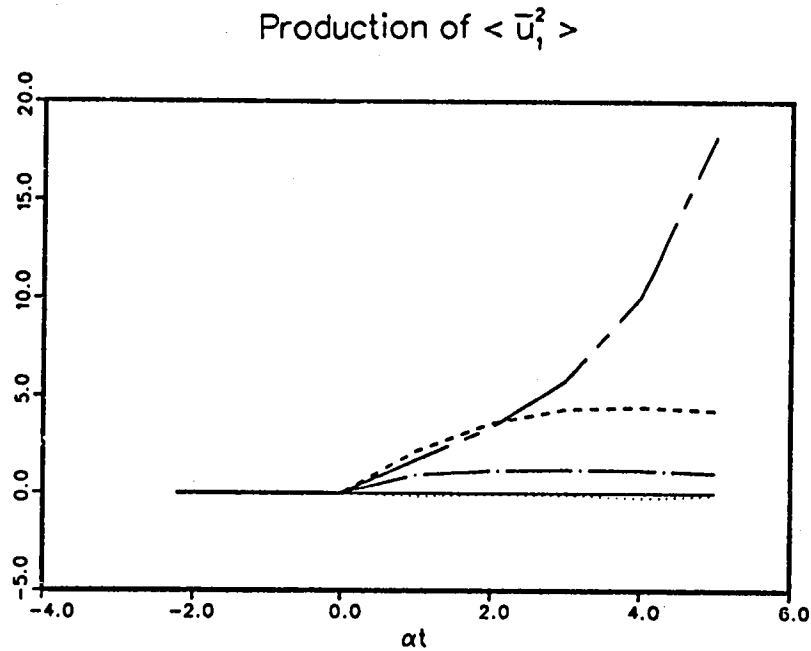
Fig. 9.8a. Time history of the component P_{11} of the production rate of turbulence, nondimensionalized by the dissipation rate at $\alpha t = 0$, of the turbulent flows shown in Fig. 9.1a.
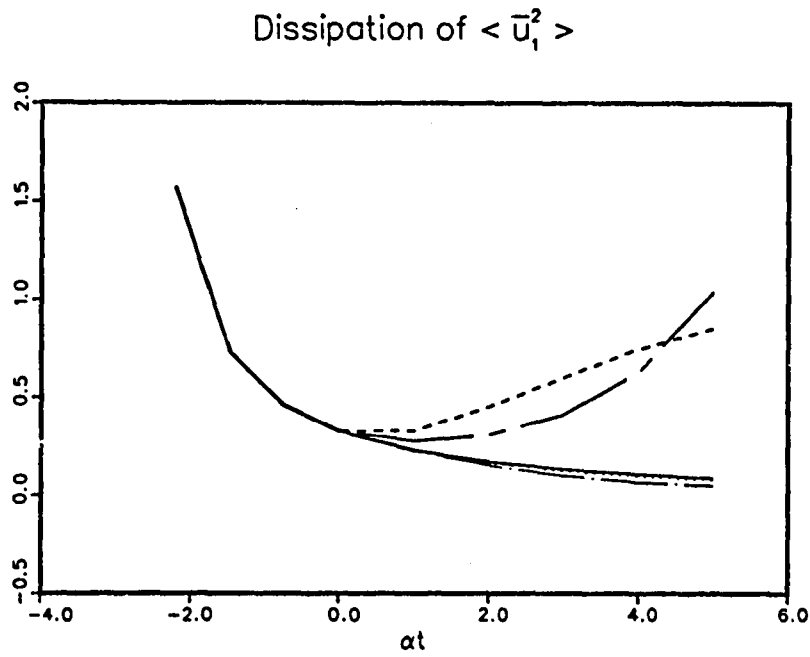
Fig. 9.8b. Time history of the component P_{11} of the production rate of turbulence, nondimensionalized by the dissipation rate at $\alpha t = 0$, of the turbulent flows shown in Fig. 9.1b.

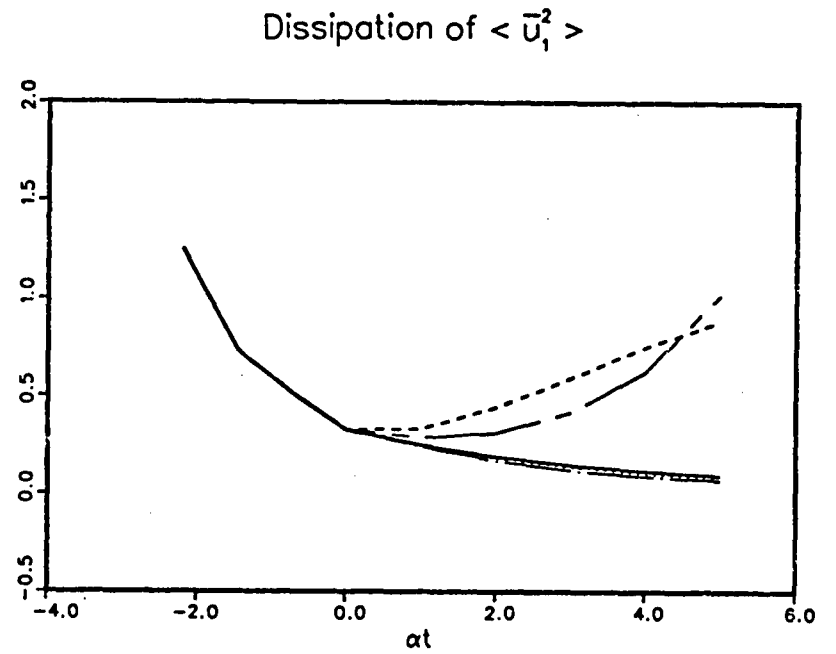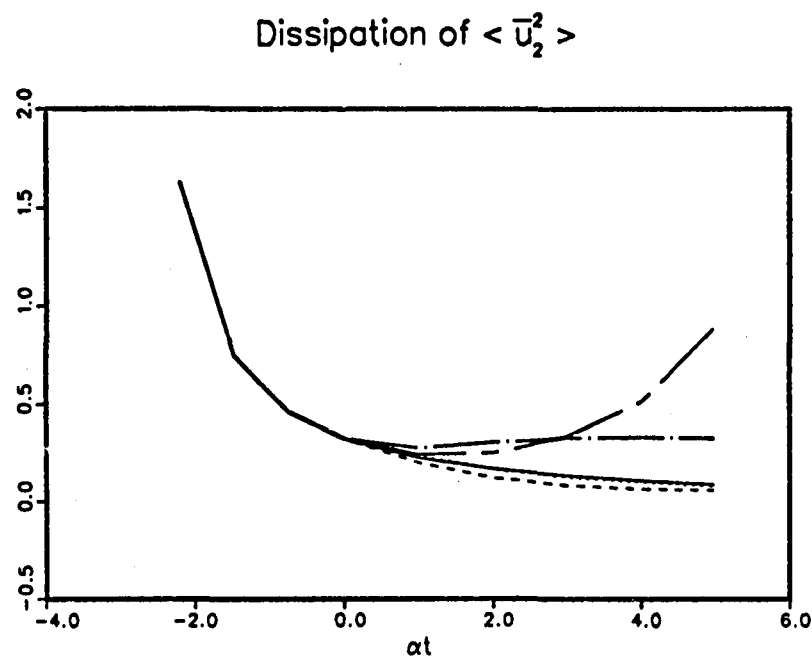Production of $< \bar{u}_2^2 >$

Production of $< \bar{u}_2^2 >$

Fig. 9.9a. Time history of the component P_{22} of the production rate of turbulence, nondimensionalized by the dissipation rate at $\alpha t = 0$, of the turbulent flows shown in Fig. 9.1a.

Fig. 9.9b. Time history of the component P_{22} of the production rate of turbulence, nondimensionalized by the dissipation rate at $\alpha t = 0$, of the turbulent flows shown in Fig. 9.1b.

Dissipation of $< \bar{u}_1^2 >$

Dissipation of $< \bar{u}_1^2 >$

Fig. 9.10a. Time history of the component ε_{11} of
the dissipation rate of turbulence,
nondimensionalized by the dissipation
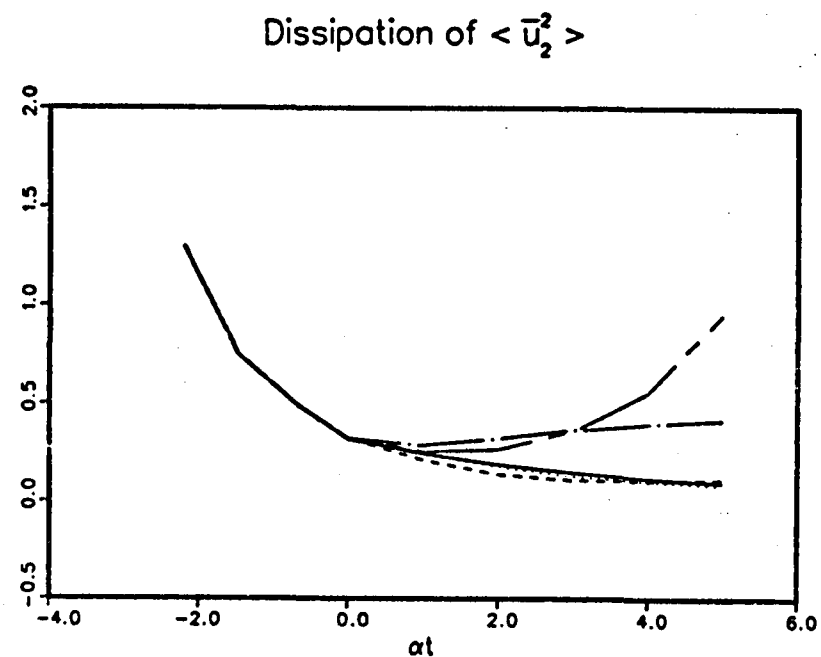rate at $\alpha t = 0$, of the turbulent
flows shown in Fig. 9.1a.

Fig. 9.10b. Time history of the component ε_{11} of
the dissipation rate of turbulence,
nondimensionalized by the dissipation
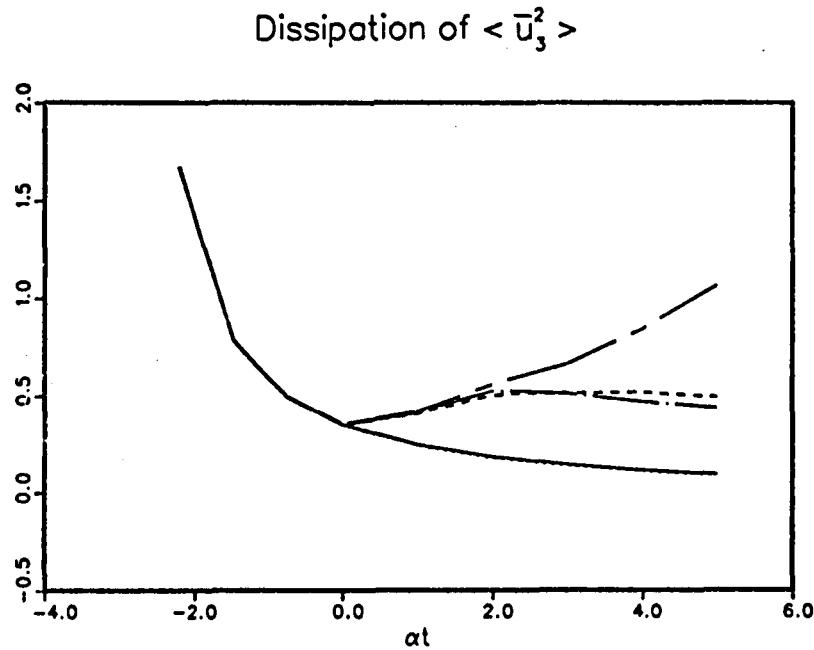rate at $\alpha t = 0$, of the turbulent
flows shown in Fig. 9.1b.

Dissipation of $< \bar{u}_2^2 >$

Dissipation of $< \bar{u}_2^2 >$

Fig. 9.11a. Time history of the component ε_{22} of the dissipation rate of turbulence, nondimensionalized by the dissipation rate at $\alpha t = 0$, of the turbulent flows shown in Fig. 9.1a.

Fig. 9.11b. Time history of the component ε_{22} of the dissipation rate of turbulence, nondimensionalized by the dissipation rate at $\alpha t = 0$, of the turbulent flows shown in Fig. 9.1b.
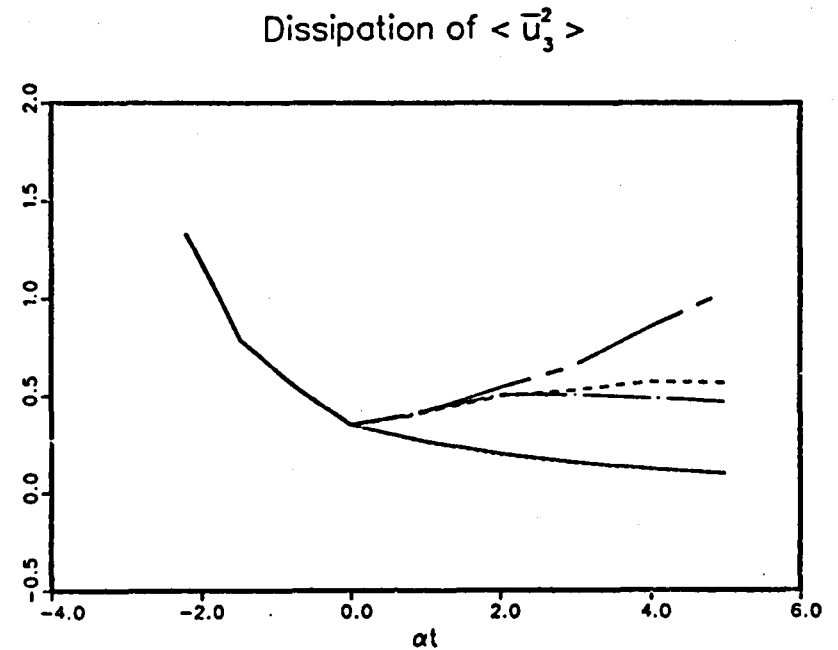
Dissipation of $< \bar{u}_3^2 >$

Dissipation of $< \bar{u}_3^2 >$

Fig. 9.12a. Time history of the component ε_{33} of the dissipation rate of turbulence, nondimensionalized by the dissipation rate at $\alpha t = 0$, of the turbulent flows shown in Fig. 9.1a.

Fig. 9.12b. Time history of the component ε_{33} of the dissipation rate of turbulence, nondimensionalized by the dissipation rate at $\alpha t = 0$, of the turbulent flows shown in FIg. 9.1b.

149

Pressure–Strain of $< \bar{u}_1^2 >$

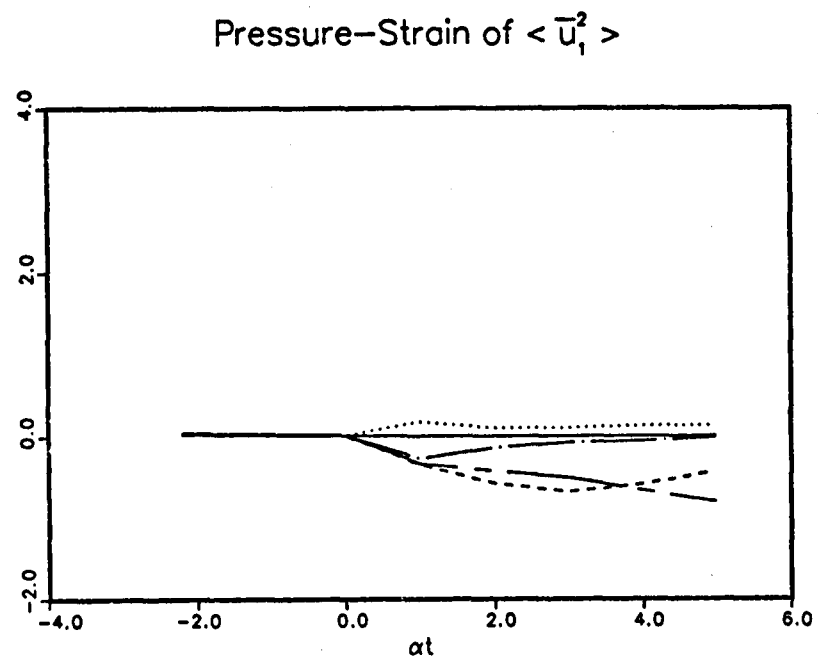Pressure–Strain of $< \bar{u}_1^2 >$

Fig. 9.13a. Time history of the component ϕ_{11} of the pressure strain rate of turbulence, nondimensionalized by the dissipation rate at $\alpha t = 0$, of the turbulent flows shown in Fig. 9.1a.
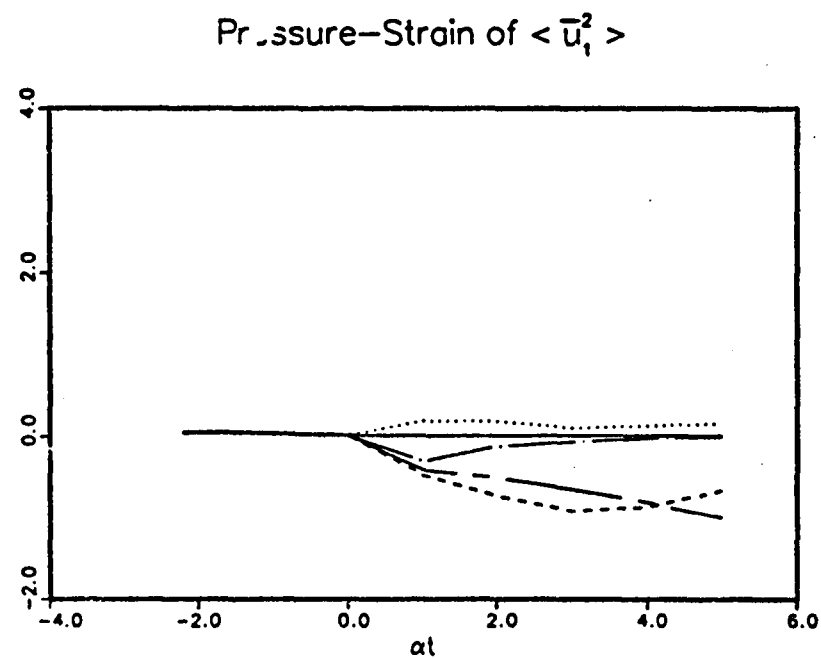
Fig. 9.13b. Time history of the component ϕ_{11} of the pressure strain rate of turbulence, nondimensionalized by the dissipation rate at $\alpha t = 0$, of the turbulent flows shown in FIg. 9.1b.
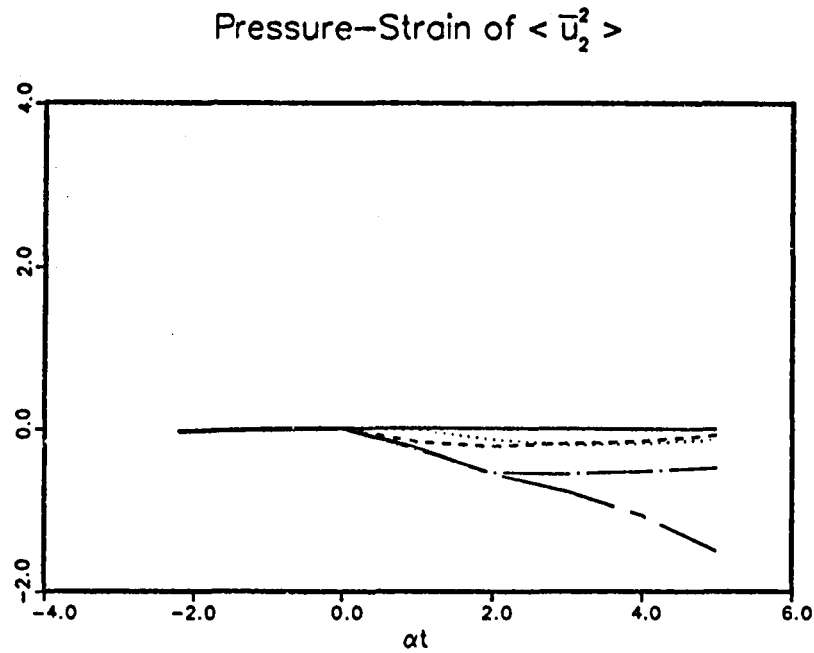
Pressure–Strain of $< \overline{u}_2^2 >$

Pressure–Strain of $< \overline{u}_2^2 >$

Fig. 9.14a. Time history of the component ϕ_{22} of the pressure strain rate of turbulence, nondimensionalized by the dissipation rate at $\alpha t = 0$, of the turbulent flows shown in Fig. 9.1a.
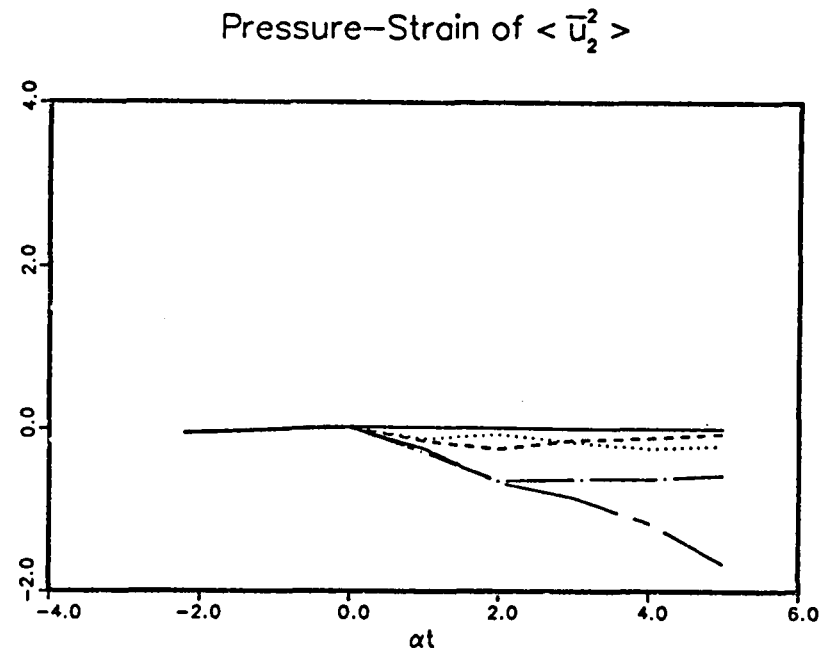
Fig. 9.14b. Time history of the component ϕ_{22} of the pressure strain rate of turbulence, nondimensionalized by the dissipation rate at $\alpha t = 0$, of the turbulent flows shown in FIg. 9.1b.

Pressure–Strain of $< \bar{u}_3^2 >$
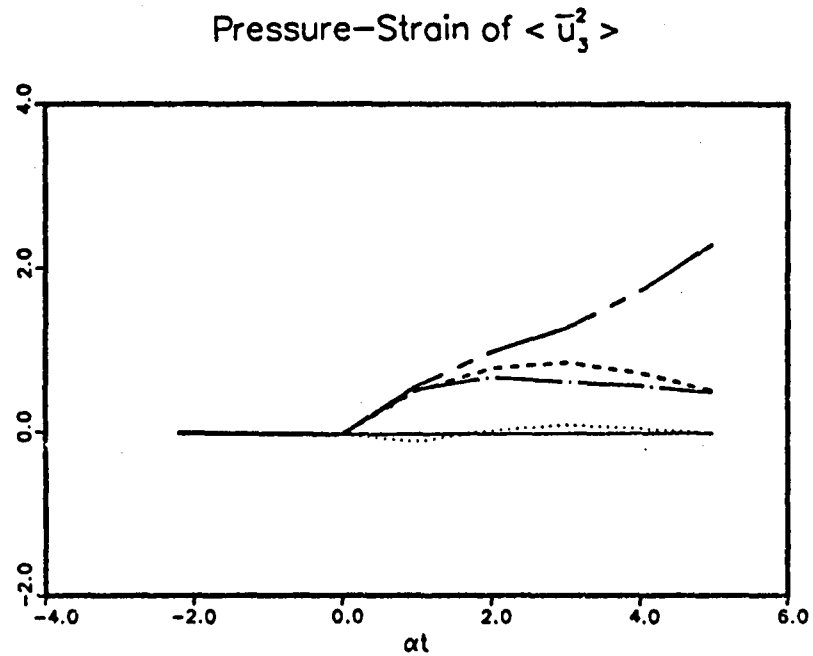
Pressure–Strain of $< \bar{u}_3^2 >$

Fig. 9.15a. Time history of the component ϕ_{33} of the pressure strain rate of turbulence, nondimensionalized by the dissipation rate at $\alpha t = 0$, of the turbulent flows shown in Fig. 9.1a.
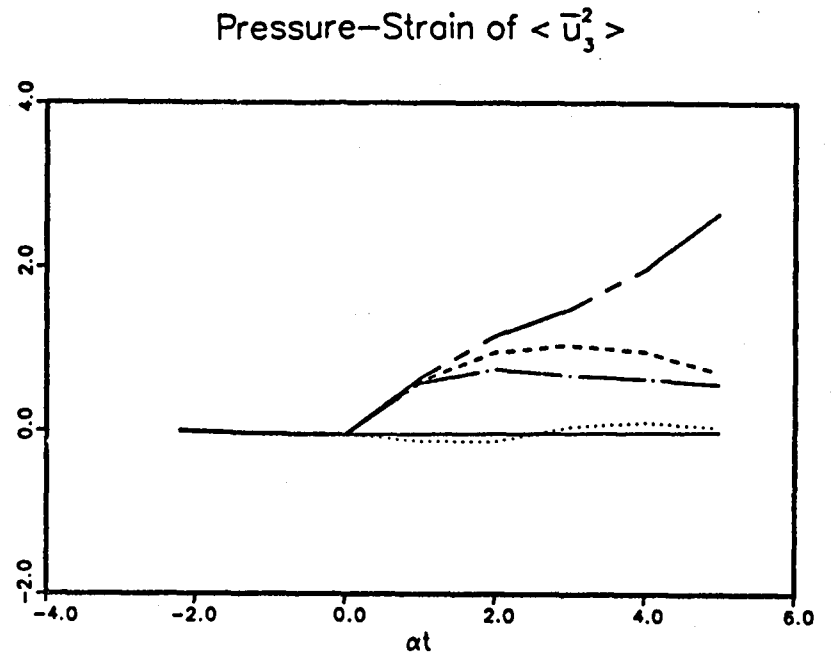
Fig. 9.15b. Time history of the component ϕ_{33} of the pressure strain rate of turbulence, nondimensionalized by the dissipation rate at $\alpha t = 0$, of the turbulent flows shown in FIg. 9.1b.

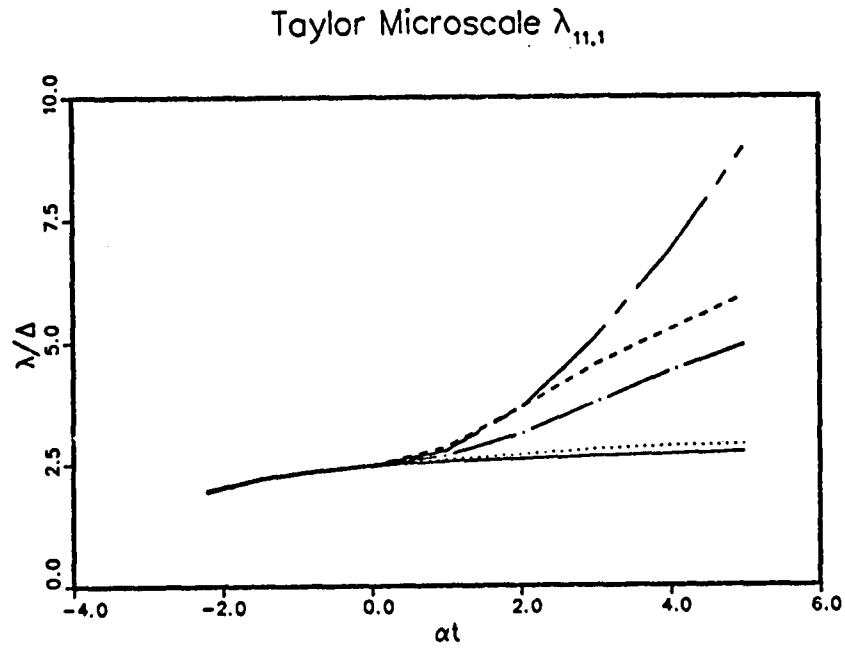Taylor Microscale $\lambda_{11,1}$

Taylor Microscale $\lambda_{11,1}$

Fig. 9.16a. Time history of the Taylor microscale, $\lambda_{11,1}$, of the turbulent flows shown in Fig. 9.1a.

Fig. 9.16b. Time history of the Taylor microscale $\lambda_{11,1}$, of the turbulent flows shown in Fig. 9.1b.

Taylor Microscale $\lambda_{22,1}$

Fig. 9.17a. Time history of the Taylor microscale, $\lambda_{22,1}$, of the turbulent flows shown in Fig. 9.1a.

Taylor Microscale $\lambda_{22,1}$

Fig. 9.17b. Time history of the Taylor microscale, $\lambda_{22,1}$, of the turbulent flows shown in Fig. 9.1b.

Taylor Microscale $\lambda_{33,1}$

Taylor Microscale $\lambda_{33,1}$

Fig. 9.18a. Time history of the Taylor microscale, $\lambda_{33,1}$, of the turbulent flows shown in Fig. 9.1a.

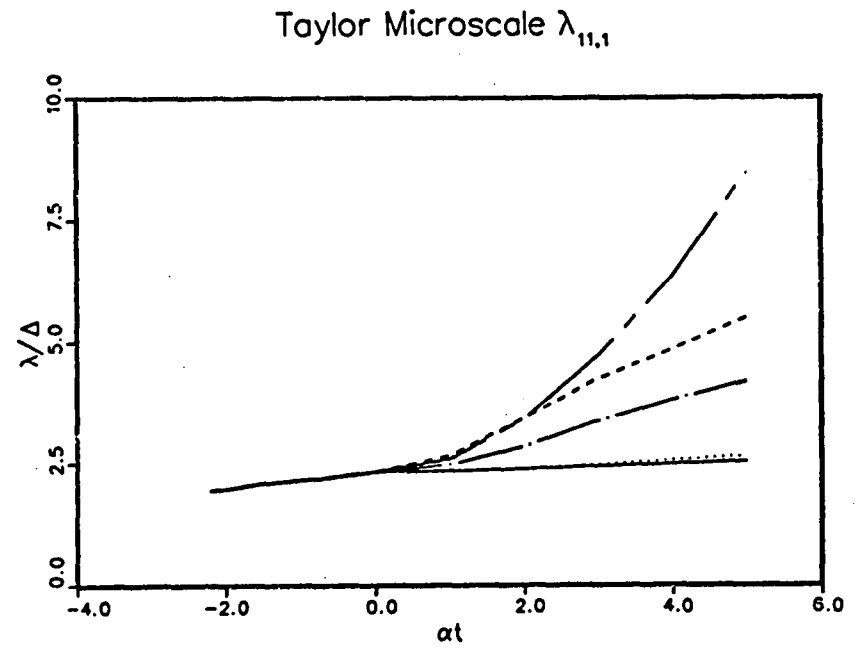Fig. 9.18b. Time history of the Taylor microscale, $\lambda_{33,1}$, of the turbulent flows shown in Fig. 9.1b.
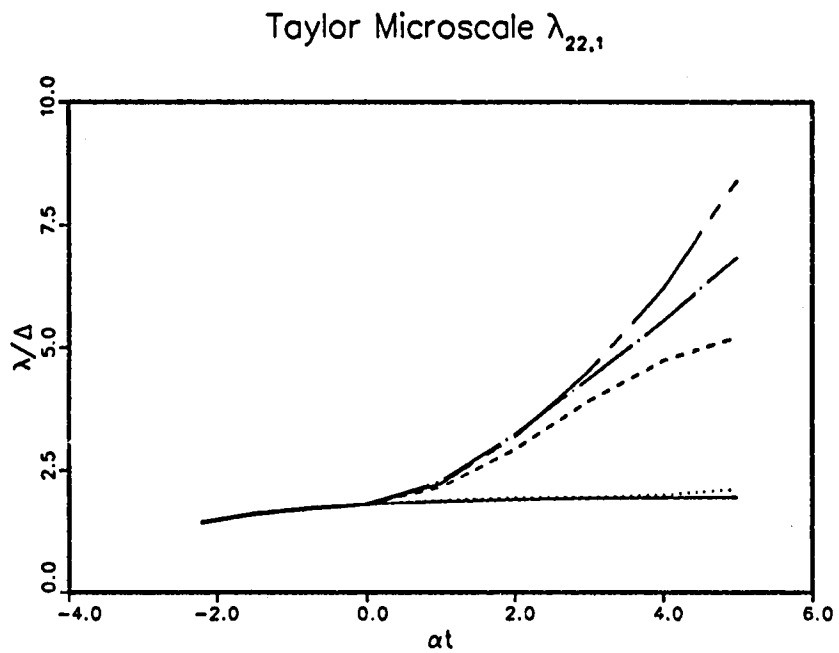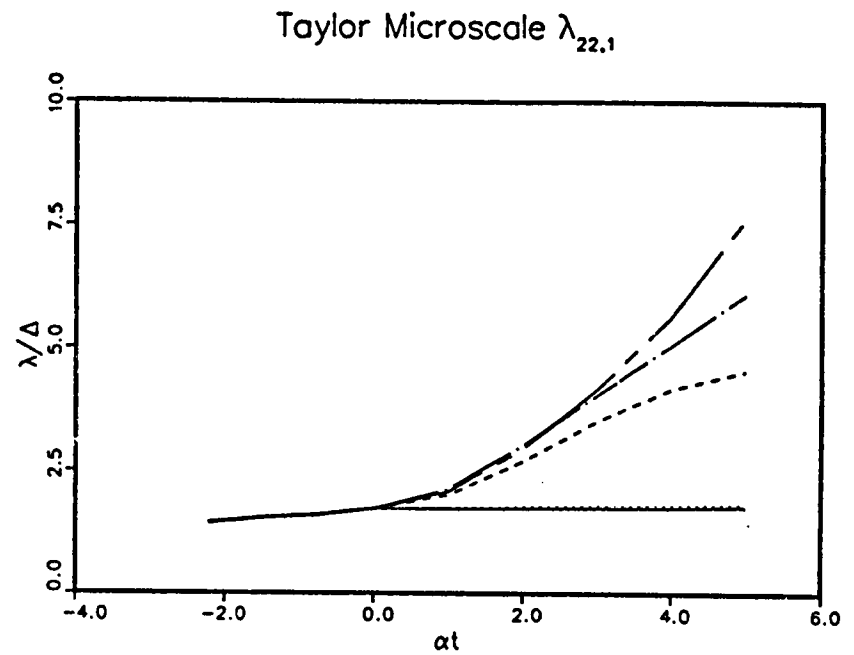
Integral Length—Scale $L_{11,1}$

Integral Length—Scale $L_{11,1}$

Fig. 9.19a. Time history of the integral length scale, $L_{11,1}$, of the turbulent flows shown in Fig. 9.1a.

Fig. 9.19b. Time history of the integral length scale, $L_{11,1}$, of the turbulent flows shown in FIg. 9.1b.

Integral Length–Scale $L_{22,1}$

Integral Length–Scale $L_{22,1}$
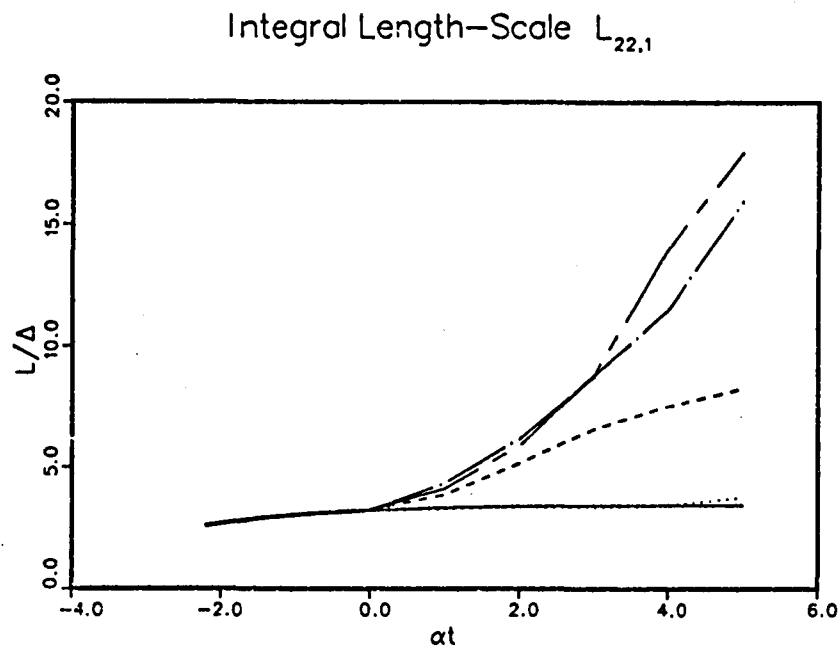
Fig. 9.20a. Time history of the integral length scale, $L_{22,1}$, of the turbulent flows shown in Fig. 9.1a.

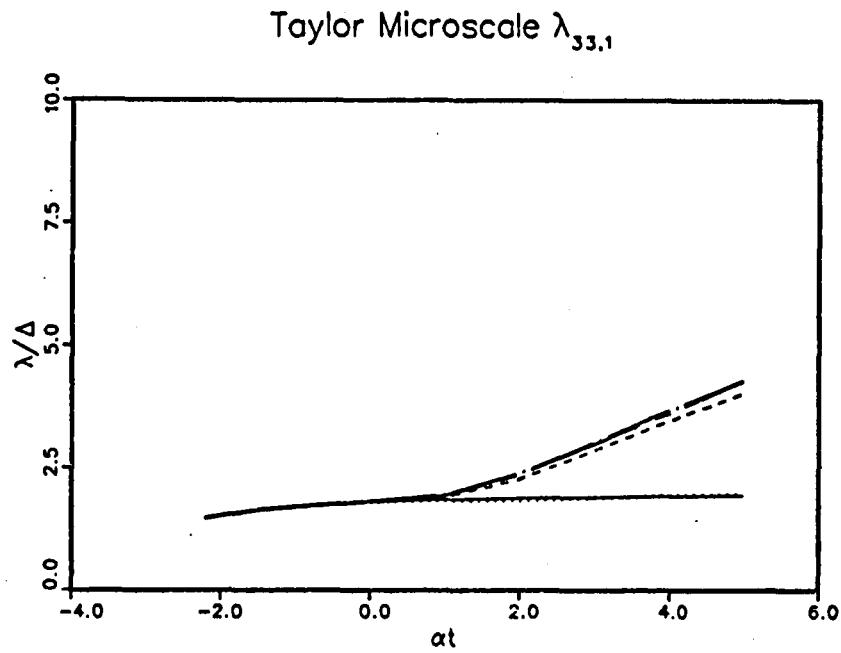Fig. 9.20b. Time history of the integral length scale, $L_{22,1}$, of the turbulent flows shown in Fig. 9.1b.
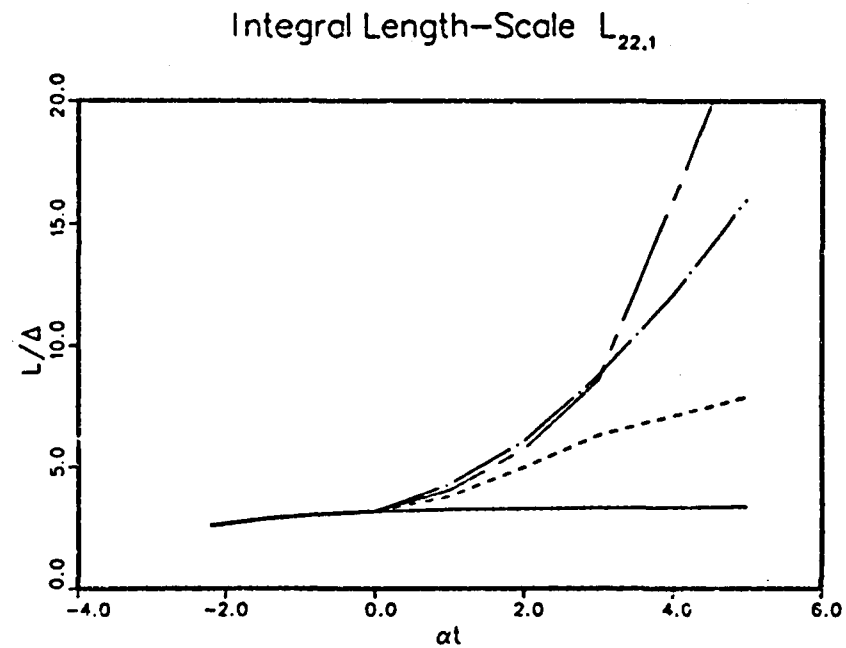
Integral Length—Scale $L_{33,1}$

Integral Length—Scale $L_{33,1}$
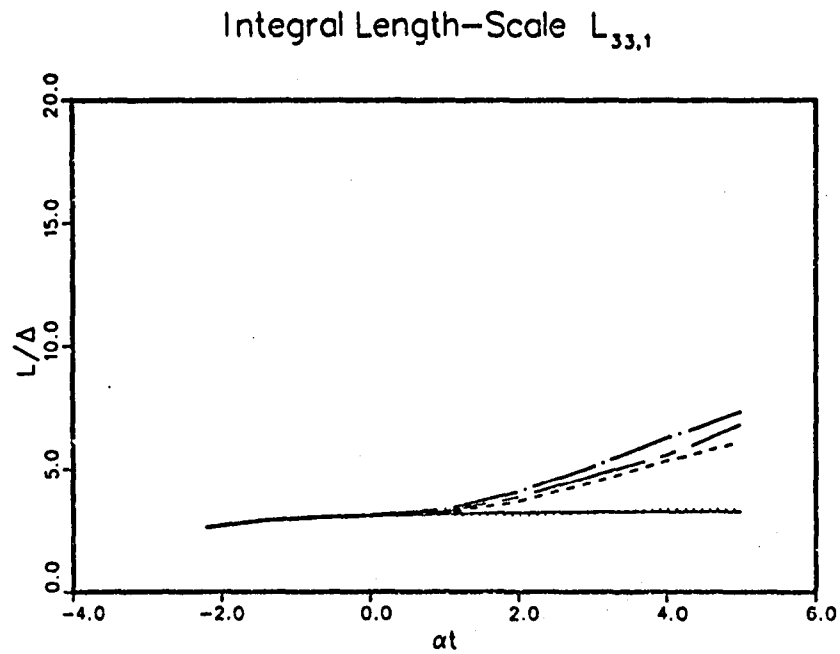
Fig. 9.21a. Time history of the integral length
scale, $L_{33,1}$, of the turbulent flows
shown in Fig. 9.1a.
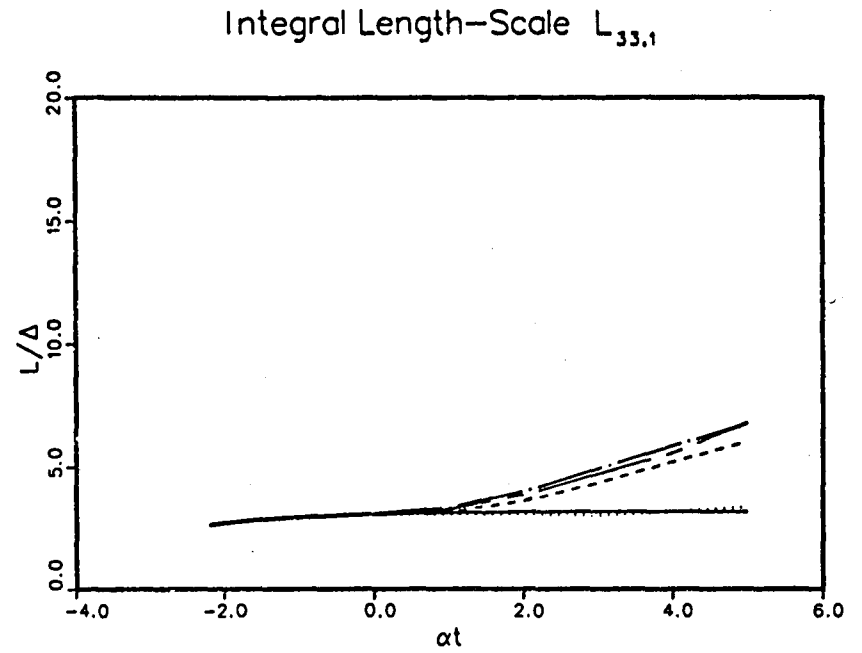
Fig. 9.21b. Time history of the integral length
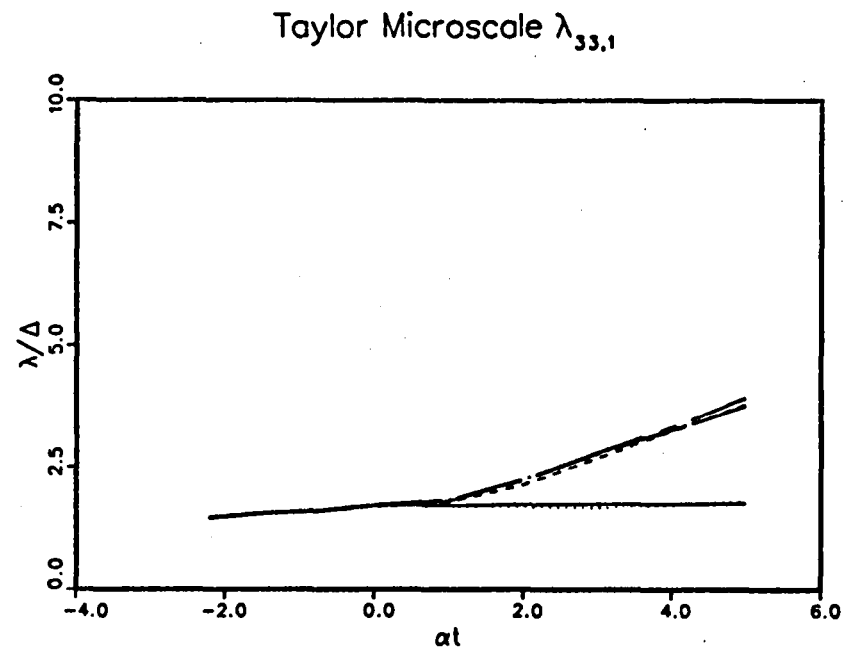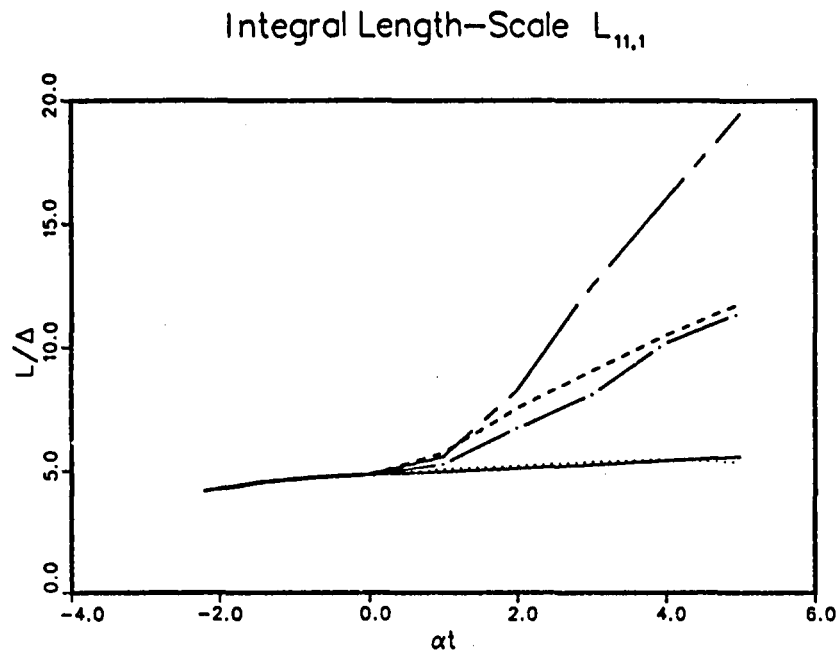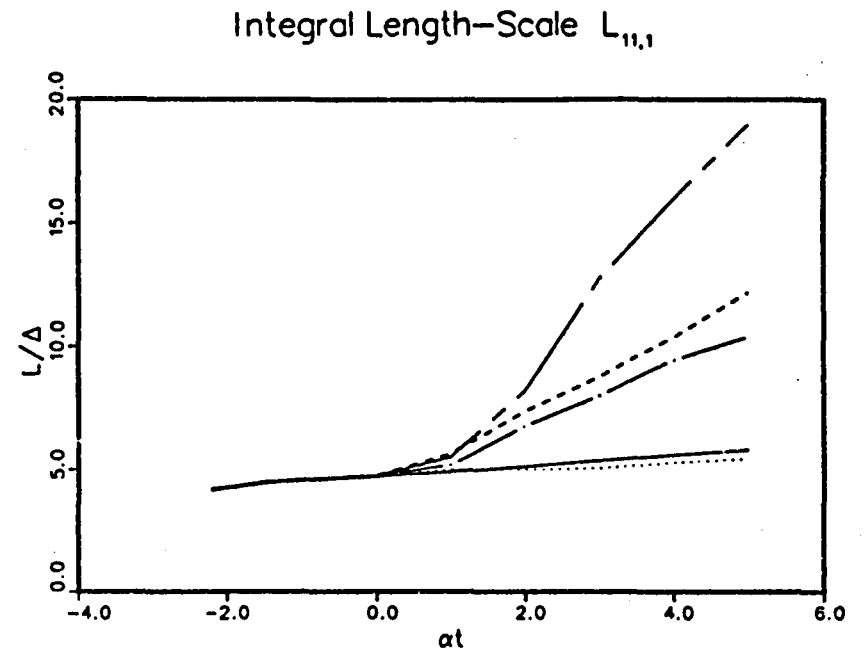scale, $L_{33,1}$, of the turbulent flows
shown in Fig. 9.1b.

Velocity—Derivative Skewness S_{K1}

Velocity—Derivative Skewness S_{K1}

Fig. 9.22a. Time history of the u_1 velocity-derivative skewness in the 3rd direction of the turbulent flows shown in Fig. 9.1a.

Fig. 9.22b. Time history of the u_1 velocity-derivative skewness in the 3rd direction of the turbulent flows shown in Fig. 9.1b.

Velocity–Derivative Skewness S_{K2}

Fig. 9.23a. Time history of the u_2 velocity-derivative skewness in the 3rd direction of the turbulent flows shown in Fig. 9.1a.

Velocity–Derivative Skewness S_{K2}

Fig. 9.23b. Time history of the u_2 velocity-derivative skewness in the 3rd direction of the turbulent flows shown in Fig. 9.1b.

160

Velocity—Derivative Skewness $S_{\kappa 3}$

Velocity—Derivative Skewness $S_{\kappa 3}$

Fig. 9.24a. Time history of the u_3 velocity-derivative skewness in the 3rd direction of the turbulent flows shown in Fig. 9.1a.

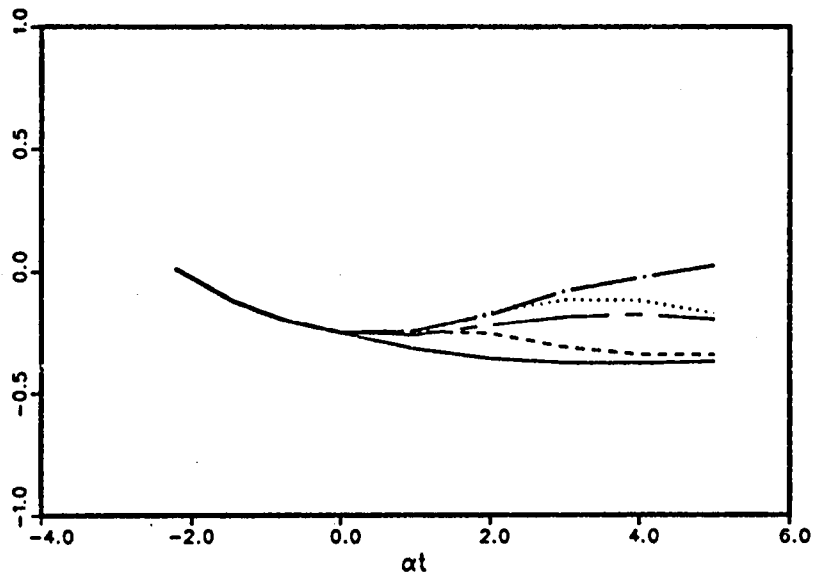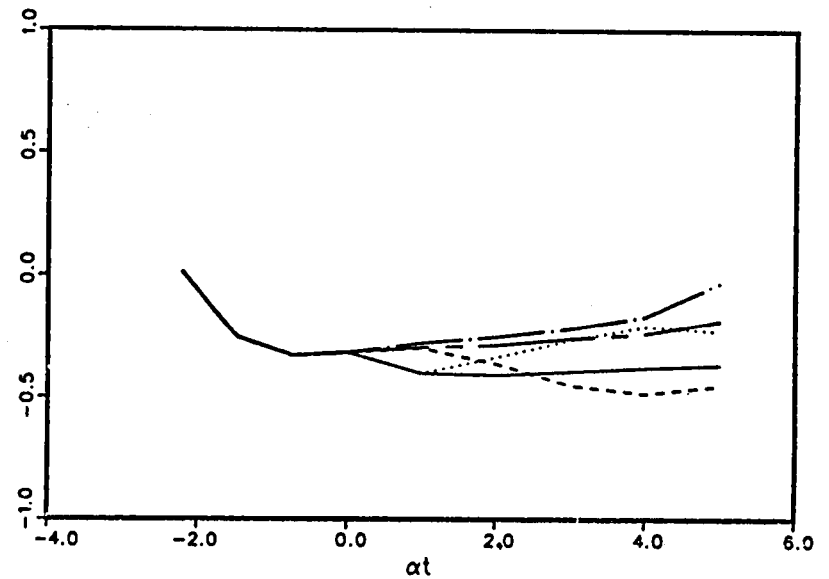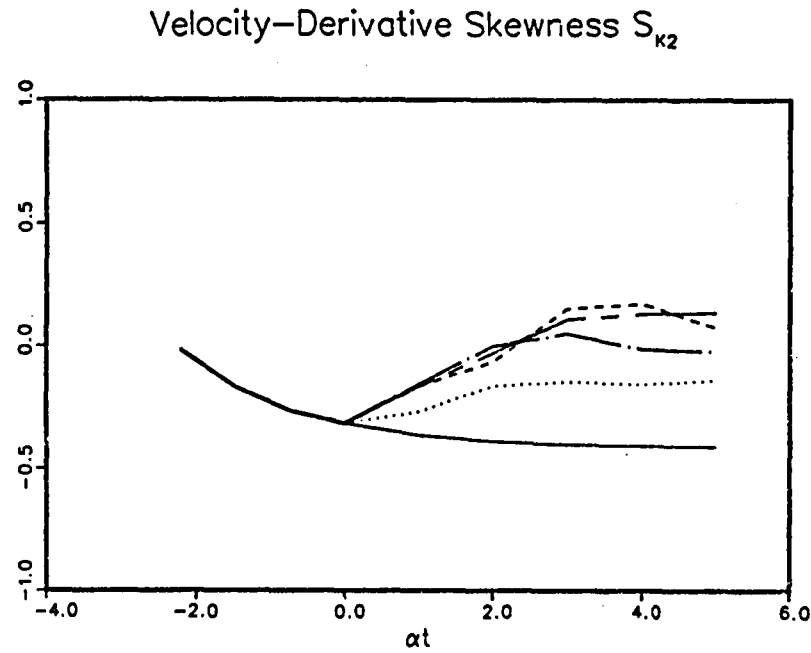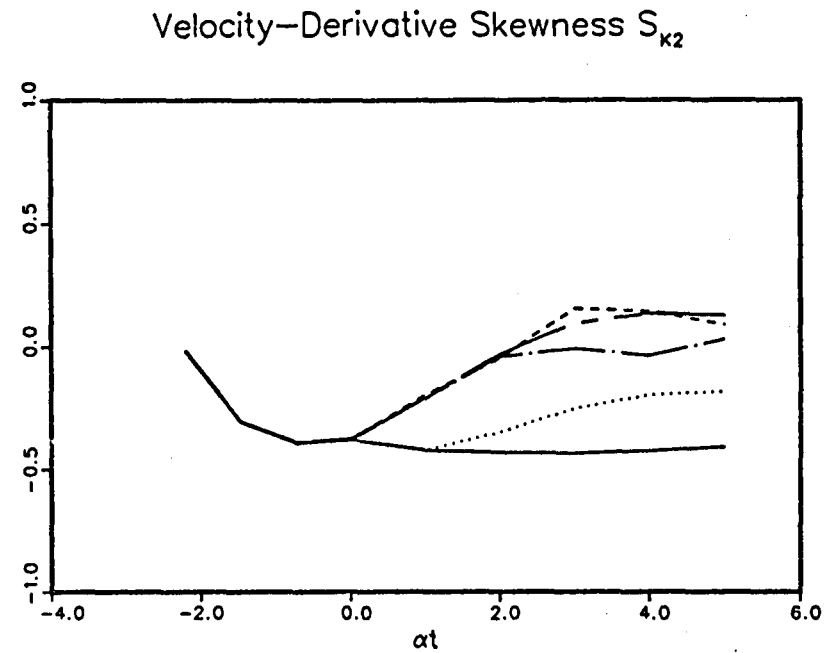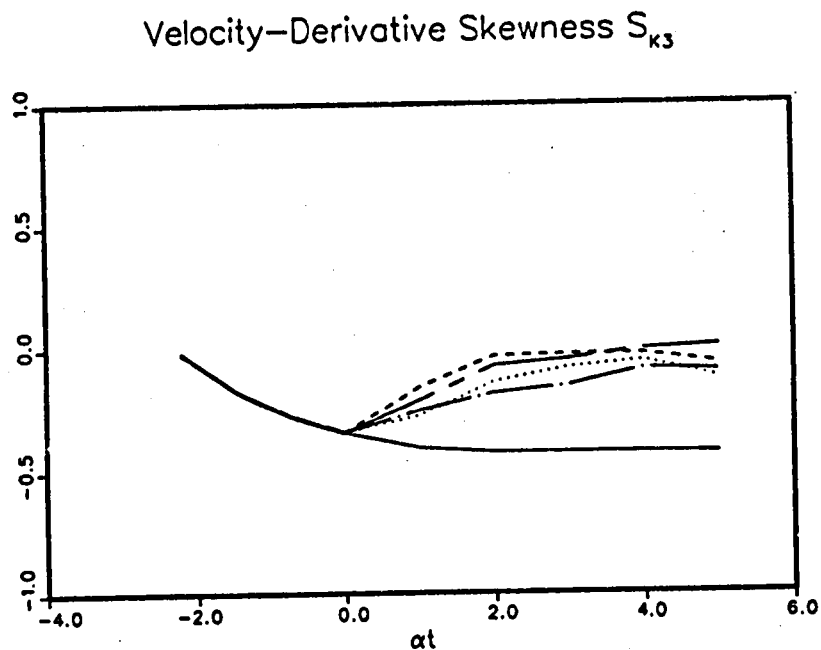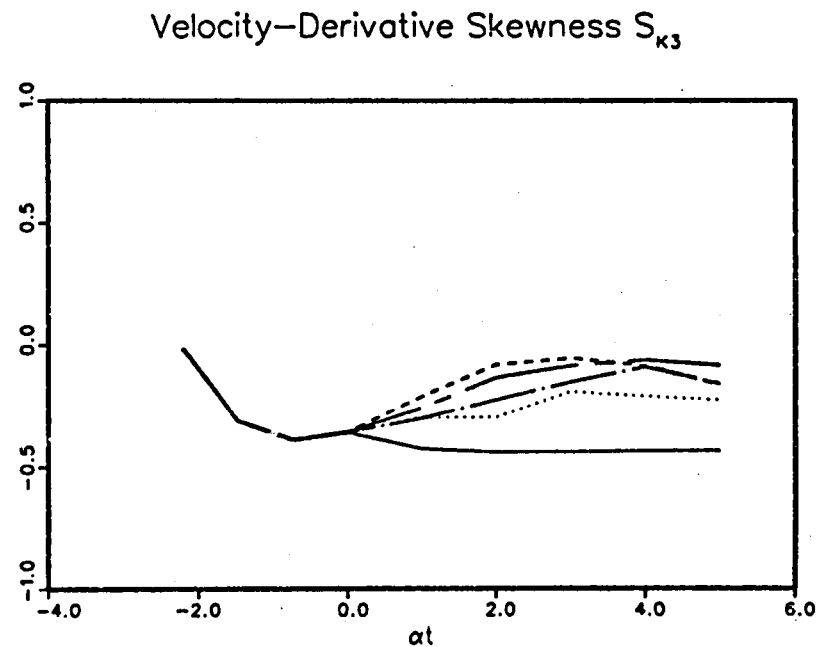Fig. 9.24b. Time history of the u_3 velocity-derivative skewness in the 3rd direction of the turbulent flows shown in Fig. 9.1b.

Appendix A

"EXACT" TESTS OF SUBGRID-SCALE TURBULENCE MODELS

Tests of subgrid-scale turbulence models, based on "exact" solutions obtained from full simulations of homogeneous turbulent flows, were presented in Chapter V. In this appendix, we shall present the equations for the correlation coefficients and the methods of obtaining model constants.

As described in Chapter V, model predictions of the subgrid-scale Reynolds stresses are compared against the "exact" solutions. This comparison is done on the tensor, vector, and scalar levels suggested by Clark et al. (1977); these are, respectively, comparisons with

$$\tau_{ij} \quad , \quad \frac{\partial \tau_{ij}}{\partial x_j} \quad , \quad \text{and} \quad \bar{u}_i \frac{\partial \tau_{ij}}{\partial x_j}$$

In contrast to Clark et al. (1977) and McMillan et al. (1978), we test combinations of turbulent models; i.e., linear combinations of eddy viscosity models, scale-similarity models, and other ones described in Chapter 5. At any point in the flow, each of these models can be represented by

$$\underline{Y}_1 = \sum_{j=2}^{m+1} \beta_j \underline{Y}_j + \underline{E} \tag{A-1}$$

where

$\underline{Y}_1$ is the "exact" quantity obtained from the full simulation.

$\underline{Y}_j$, $j = 2$, $m + 1$ are quantities derived from the large-scale field which one used in the turbulence model. For example, Y_2 might be the Smagorinsky model and Y_3 the scale-similarity model.

β_j, $j = 2$, $m + 1$ are the constants,

m is the number of component models in the composite model, and

$\underline{E}$ is the error, i.e., the difference between the "exact" and predicted quantity.

Assessment of the accuracy of the model in representing the spatial variations of the "exact" quantities is done by means of a multiple correlation coefficient, $C_{1 \cdot 2,3 \ldots m+1}$, where

$$c^2_{1 \cdot 2,3 \ldots m+1} = 1 - \frac{|C|}{\tilde{c}_{11}} \qquad (A-2)$$

and

$|C|$ is the determinant of the matrix C defined below,

$\tilde{C}_{ik}$ is the co-factor of the ik element in the matrix C, and

$C = (C_{ik})$ is the matrix whose elements are the zero-order correlations r_{ik} defined below.

The zero-order correlation C_{ik} denotes the simple correlation coefficient between Y_i and Y_k and is defined by:

$$r^2_{ik} = \langle y_i y_k \rangle / (S_i S_k) \qquad (A-3)$$

where

$S_i = \langle y^2_i \rangle^{1/2}$ is the zero-order standard deviation of Y_i,

$y_i = Y_i - \langle Y_i \rangle$ is the local fluctuation of Y_i,

$\langle Y_i \rangle$ is the spatial average of Y_i over the entire field, and

n is the sample size or number of points in the grid.

The absolute value of the correlation coefficients varies between 0 and 1. It takes the value 0 if the model is totally unrelated to the "exact" quantity, and 1 if the model is exactly proportional to the "exact" quantities. These correlation coefficients are independent of the values used for the model constants β_j. there are several methods of detemining the constants, as described in Chapter V. In particular, we used three different methods: (1) doing LES and fitting the constant so as to predict the experimental decay of the mean turbulent kinetic energy, (2) equating the mean values of the "exact" and modeled values of the subgrid-scale Reynolds stresses on the scalar level, and (3) using least-square statistics on solutions of the full simulations.

The first two methods allow the model to predict the decay of the turbulent kinetic energy, while the third minimizes the mean-square error $\underline{E}$ of the prediction given by Eq. (B-1). The equation used to evaluate the model constants using least-square statistics is

$$\beta_j = -\frac{S_1}{S_j} \frac{\tilde{C}_{1j}}{\tilde{C}_{11}} \qquad (A-4)$$

with no index summation. This Eq. (A-4) provides values of the model constants for the subgrid-scale Reynolds stresses at each of the three test levels. The values used in Chapter V were obtained from the scalar level.

Appendix B

DISCARDED SUBGRID-SCALE TURBULENCE MODELS

The following subgrid-scale turbulence models were discarded because they do not increase the correlation coefficient between the "exact" Reynolds stresses obtained from full simulations and modeled quantities, using the Smagorinsky and scale-similarity model.

The model

$$R_{ij} = \left(M_{ik}\bar{\delta}_{jk} + M_{jk}\bar{S}_{ik} - \frac{2}{3}\delta_{ij}M_{\ell k}\bar{S}_{\ell k}\right)/|\bar{S}| \tag{B-1}$$

where

$$\bar{S}_{ij} = \frac{1}{2}\frac{\partial\bar{u}_i}{\partial x_j} + \frac{\partial\bar{u}_j}{\partial x_i}$$

$$|\bar{S}| = \left(2\bar{\delta}_{ij}\bar{S}_{ij}\right)^{1/2}$$

and

$$M_{ij} = \overline{\bar{u}_i\bar{u}_j} - \bar{\bar{u}}_i\bar{\bar{u}}_j$$

or

$$M_{ij} = \left(\bar{u}_i - \bar{\bar{u}}_i\right)\left(\bar{u}_j - \bar{\bar{u}}_j\right)$$

represent a nonlinear combination of the scale-similarity model and an eddy-viscosity model. However, this model yields least-squared statistics similar to those of eddy-viscosity models in homogeneous isotropic and homogeneous sheared turbulence. Furthermore, no improvement is obtained by adding this model to the ones used in the text.

The next turbulence models

$$R_{ij} = c\frac{q_f^2}{|\bar{S}|^2}D_{ij} \tag{B-2}$$

167

where

$$D_{ij} = \frac{\partial \overline{u}_i}{\partial x_k} \frac{\partial \overline{u}_j}{\partial x_k}$$

or

$$D_{ij} = \frac{\partial \overline{u}_i}{\partial x_k} \frac{\partial \overline{u}_j}{\partial x_k} - \frac{\partial \overline{\overline{u}}_i}{\partial x_k} \frac{\partial \overline{\overline{u}}_j}{\partial x_k}$$

and

$$q_f^2 = \left(\overline{\overline{u}_i \overline{u}_i} - \overline{\overline{u}}_i \overline{\overline{u}}_i \right)$$

are based on the structural form of the dissipation terms of the Navier-Stokes equations.

These models yield statistics inferior to those of eddy viscosity models in isotropic turbulence, but superior to them in homogeneous sheared turbulence. However, the statistics show almost no improvement when this kind of model is added to the combination of the scale-similarity and eddy-viscosity models. These models are also not strictly dissipative; therefore, it is not worthwhile to replace the eddy-viscosity model by this kind of model.

168

References

Antonopoulos-Domis, M. (1981), "Large Eddy Simulation of a Passive Scalar in Isotropic Turbulence," J. Fluid Mech. 104, 55-79.

Bardina, J., J. H. Ferziger, and W. C. Reynolds (1980), "Improved Subgrid-Scale Models for Large-Eddy Simulation," AIAA 13th Fluid & Plasma Dynamics Conference, AIAA Paper 80-1357.

Batchelor, G. K. (1953), The Theory of Homogeneous Turbulence, Cambridge University Press, Cambridge.

Batchelor, G. K. (1967), An Introduction to Fluid Dynamics, Cambridge University Press, Cambridge.

Bertoglio, J. P. (1982), "Homogeneous Turbulent Field within a Rotating Frame," AIAA J., 20, 9, 1175-1181.

Bradshaw, P. (1969), "The Analogy between Streamline Curvature and Buoyancy in Turbulent Shear Flow," J. Fluid Mech. 36, 177-191.

Cain, A. B., W. C. Reynolds, and J. H. Ferziger (1981), "A Three-Dimensional Simulation of Transition and Early Turbulence in a Time-Developing Mixing Layer," Report TF-15, Thermosciences Div., Dept. of Mech. Engrg., Stanford University, Stanford, CA.

Champagne, F. H., V. G. Harris, and S. Corrsin (1970), "Experiments on Nearly Homogeneous Turbulent Shear Flow," J. Fluid Mech. 41, 81-140.

Chung, M. K., and R. J. Adrian (1979), "Evaluation of Variable Coefficients in Second-Order Turbulence Models," 2nd Symp. on Turbulent Shear Flows, Imperial College, London, July 2-4, 10.43-10.48.

Clark, R. A., J. H. Ferziger, and W. C. Reynolds (1977), "Evaluation of Subgrid Scale Turbulence Models Using a Fully Simulated Turbulent Flow," Report TF-9, Thermosciences Div., Dept. of Mech. Engrg., Stanford University, Stanford, CA. Also, J. Fluid Mech. 91, 1-16.

Comte-Bellot, G., and S. Corrsin (1971), "Simple Eulerian Time Correlation of Full- and Narrow-Band Velocity Signals in Grid-Generated 'Isotropic' Turbulence," J. Fluid Mech. 48, 273-337.

Cooley, J. W., and J. W. Tukey (1965), "An Algorithm for the Machine Calculation of Complex Fourier Series," Math. Comput. 19, 90, 297-301.

Deardorff, J. W. (1970), "A Numerical Study of Three-Dimensional Turbulent Channel Flow at Large Reynolds Numbers," J. Fluid Mech. 41, 453-480.

Deardorff, J. W. (1971), "On the Magnitude of the Subgrid Scale Eddy Coefficient," J. Comp. Phys. 7, 120-133.

Deissler, R. G. (1961), "Effects of Inhomogeneity and of Shear Flow in Weak Turbulent Fields," Phys. Fluids, 4, 1187-1198.

Deissler, R. G. (1970), "Effect of Initial Condition on Weak Homogeneous Turbulence with Uniform Shear," Phys. Fluids, 13, 1868-1869.

Deissler, R. G. (1972), "Growth of Turbulence in the Presence of Shear," Phys. Fluids, 15, 1918-1920.

Donaldson, C. duP (1973), "Construction of a Dynamic Model of the Production of Atmospheric Turbulence and the Dispersal of Atmospheric Pollutants," Workshop on Micrometeorology (D. A. Haergen, ed.), Amer. Meteorological Society, Boston, 313-392.

Feiereisen, W. J., W. C. Reynolds, and J. H. Ferziger (1981), "Numerical Simulation of a Compressible, Homogeneous, Turbulent Shear Flow," Report TF-13, Thermosciences Div., Dept. of Mech. Engrg., Stanford University, Stanford, CA.

Ferziger, J. H. (1981), "Higher-Level Simulations of Turbulent Flows," Report TF-16, Thermosciences Div., Dept. of Mech. Engrg., Stanford University, Stanford, CA.

Ferziger, J. H., and D. C. Leslie (1979), "Large Eddy Simulation--A Predictive Approach to Turbulent Flow Computation," AIAA Computational Fluid Dynamics Conference, AIAA Paper 79-1441.

Ferziger, J. H., and S. Shaanan (1976), "Effect of Anisotropy and Rotation on Turbulence Production," Phys. Fluids, 19, 596-597.

Ferziger, J. H., and S. Shaanan (1981), "Reply to the Comments by D. J. Tritton," Phys. Fluids, 24, 1923.

Gence, J. N., and J. Mathieu (1979), "On the Application of Successive Plane Strains to Grid-Generated Turbulence," J. Fluid Mech. 93, 501-513.

Greenspan, H. P. (1968), The Theory of Rotating Fluids, Cambridge University Press, Cambridge.

Grotzbach, G., and U. Schumann (1979), "Direct Numerical Simulation of Turbulent Velocity-, Pressure-, and Temperature-Fields in Channel Flows," in Turbulent Shear Flows I (F. Durst, B. E. Launder, and F. W. Schmidt, eds.), Springer-Verlag New York, Inc., New York, NY, 379-385.

Halleen, R. M ., and J. P. Johnston (1967), "The Influence of Rotation on Flow in a Long Rectangular Channel--An Experimental Study," Report MD-18, Thermosciences Div., Dept. of Mech. Engrg., Stanford University, Stanford, CA.

Harris, V. G., J. A. H. Graham, and S. Corrsin (1977), "Further Experiments in Nearly Homogeneous Turbulent Shear Flow," J. Fluid Mech. 81, 657-687.

Herring, J. R. (1977), "Subgrid Scale Modeling--An Introduction and Overview," in Turbulent Shear Flows I (F. Durst, B. E. Launder, and F. W. Schmidt, eds.), Springer-Verlag New York, Inc., New York, NY, 347-352.

Ibbetson, A., and D. J. Tritton (1975), "Experiments on Turbulence in a Rotating Fluid," J. Fluid Mech. 68, 639-672.

Johnston, J. (1972), Econometric Methods, McGraw-Hill, New York, NY.

Johnston, J. P., R. M. Halleen, and P. K. Lezius (1972), "Effects of Spanwise Rotation on the Structure of Two-Dimensional, Fully Developed, Turbulent Channel Flow," J. Fluid Mech. 56, 533-557.

Jones, W. P., and B. E. Launder (1972), "The Prediction of Laminarization with a Two-Equation Model of Turbulence," Int. J. Heat & Mass Transfer, 15, 301-314.

Kim, J., and P. Moin (1979), "Large Eddy Simulation of Turbulent Channel Flow--ILLIAC IV Calculation," in Turbulent Boundary Layers--Experiments, Theory, and Modeling, The Hague, Netherlands, AGARD Conf. Proc. No. 271, 14.

Kline, S. J., B. J. Cantwell, and G. M. Lilley (1981), The 1980-81 AFOSR-HTTM-Stanford Conference on Complex Turbulent Flows: A Comparison of Computation and Experiment, Vol. 1 published in 1981, Volumes 2 and 3 to be published, Thermosciences Div., Dept. of Mech. Engrg., Stanford University, Stanford, CA.

Kwak, D., W. C. Reynolds, and J. H. Ferziger (1981), "Three-Dimensional Time-Dependent Computation of Turbulent Flows," Report TF-5, Thermosciences Div., Dept. of Mech. Engrg., Stanford University, Stanford, CA.

Launder, B. E. (1980), "Turbulence Transport Models for Numerical Computation of Complex Turbulent Flows, ME-213, Dept. of Mech. Engrg., University of California, Davis, CA.

Launder, B. E., G. J. Reece, and W. Rodi (1975), "Progress in the Development of a Reynolds-Stress Turbulence Closure," J. Fluid Mech. 68, 537-566.

Launder, B. E., C. H. Priddin, and B. I. Sharma (1977), "The Calculation of Turbulent Boundary Layers on Spinning and Curved Surfaces," J. Fluids Engrg., ASME, 231-239. (what volume?)

Leonard, A. (1974), "On the Energy Cascade in Large-Eddy Simulations of Turbulent Fluid Flows," Adv. in Geophysics, 18A, 237-248.

Lilly, D. K. (1966), "On the Application of the Eddy Viscosity Concept in the Inertial Sub-Range of Turbulence," NCAR (National Center for Atmospheric Research), Manuscript No. 123, Boulder, Colorado.

Lin, A., and M. Wolfstein (1980), "Tensorial Volume of Turbulence," Phys. Fluids, 23, 644-646.

171

Lumley, J. L. (1978), "Computational Modeling of Turbulent Flows," Adv. in Appl. Mech. 18, 123-176.

Mansour, N. N., P. Moin, W. C. Reynolds, and J. H. Ferziger (1977), "Improved Methods for Large Eddy Simulation of Turbulence," in Turbulent Shear Flows I (F. Durst, B. E. Launder, and F. W. Schmidt, eds.), Springer-Verlag New York, Inc., New York, NY, 386-401.

Mansour, N. N., J. H. Ferziger, and W. C. Reynolds (1978), "Large Eddy Simulation of a Turbulent Mixing Layer," Report TF-11, Thermosciences Div., Dept. of Mech. Engrg., Stanford University, Stanford, CA.

McMillan, O. J., and J. H. Ferziger (1979), "Direct Testing of Subgrid Scale Models," AIAA J., 17, 1340-1346.

McMillan, O. J., J. H. Ferziger, and R. S. Rogallo (1980), "Tests of New Subgrid-Scale Models in Strained Turbulence," AIAA 13th Fluid & Plasma Dynamics Conference, AIAA Paper 80-1339.

Moin, P., W. C. Reynolds, and J. H. Ferziger (1978), "Large Eddy Simulation of Incompressible Turbulent Channel Flow," Report TF-12, Thermosciences Div., Dept. of Mech. Engrg., Stanford University, Stanford, CA.

Moin, P., and J. Kim (1981), "Numerical Investigation of Turbulent Channel Flow," J. Fluid Mech. 118, 341-377. Also, NASA TM-81309.

Mulhearn, P. J., and R. E. Luxton (1975), "The Development of Turbulence Structure in a Uniform Shear Flow," J. Fluid Mech. 68, 577-590.

Orszag, S. A., and G. S. Patterson (1972), "Numerical Simulation of Three-Dimensional, Homogeneous, Isotropic Turbulence," Phys. Rev. Lett. 28, 76.

Pao, Y. H. (1965), "Structure of Turbulent Velocity and Scalar Fields at Large Wave Numbers," Phys. Fluids, 8, 1063-1075.

Pedlovsky, J. (1979), Geophysical Fluid Dynamics, Springer-Verlag New York, Inc., New York, NY.

Pulliam, T. H., and H. Lomax (1979), "Simulation of Three-Dimensional Compressible Viscous Flow on the ILLIAC IV Computer," 17th Aerospace Sciences Meeting, Paper 79-0206, Jan. 15-17, New Orleans, LA.

Reynolds, W. C. (1976), "Computation of Turbulent Flows," Annual Review of Fluid Mechanics, 8, 183-208.

Reynolds, W. C. (1982), "Physical and Analytical Foundations, Concepts, and New Directions in Turbulence Modeling and Simulation," to appear in Proceedings of Ecole d' Eté d' Analyse Numérique-Modélisation Numérique de la Turbulence, Clamart, France.

Reynolds, W. C. (1983), private communication.

Rodi, W. (1979), " Influence of Buoyancy and Rotation on Equations for the Turbulent Length Scale," 2nd Int. Symp. Turbulent Shear Flows, London, 10.37-13.42.

Rodi, W. (1981), "Progress in Turbulence Modeling for Incompressible Flows," AIAA 19th Aerospace Sciences Meeting, AIAA Paper 81-0045.

Rogallo, R. S. (1977), "An ILLIAC Program for the Numerical Simulation of Homogeneous Incompressible Turbulence," NASA TM-73203.

Rogallo, R. S. (1981), "Numerical Experiments in Homogeneous Turbulence," NASA TM-81315.

Rose, W. G. (1966), "Results of an Attempt to Generate a Homogeneous Turbulent Shear Flow," J. Fluid Mech. 25, 97-120.

Rose, W. G. (1970), "Interaction of Grid Turbulence with a Uniform Mean Shear," J. Fluid Mech. 44, 767-780.

Sandri, G., and C. Cerasoli (1981), "Fundamental Research in Turbulent Modeling, Part 1: Theory, Part 2: Experiment," A.R.A.P. Report No. 438. Also published as AFOSR-TR-81-0332, February, 1981.

Schumann, U. (1973), "A Procedure for the Direct Numerical Simulation of Turbulent Flows in Plane and Annular Channels and Its Application in the Development of Turbulence Models," dissertation, Univ. of Karlsruhe, NASA Tech. Translation, NASA TT T-15391.

Schumann, U. (1975), "Subgrid Scale Model for Finite Difference Simulations of Turbulent Flow in Plane Channels and Annuli," J. Comp. Phys. 18, 376-404.

Shaanan, S., J. H. Ferziger, and W. C. Reynolds (1977), "Numerical Simulation of Turbulence in the Presence of Shear," Report TF-6, Thermosciences Div., Dept. of Mech Engrg., Stanford University, Stanford, CA.

Shirani, E., J. H. Ferziger, and W. C. Reynolds (1977), "Mixing of a Passive Scalar in Isotropic and Sheared Homogeneous Turbulence," Report TF-15, Thermosciences Div., Dept. of Mech. Engrg., Stanford University, Stanford, CA.

Smagorinsky, J. (1963), "General Circulation Experiments with the Primitive Equations. I. The Basic Experiment," Monthly Weather Review, 91, 99-164.

Tavoularis, S., and S. Corrsin (1981), "Experiments in Nearly Homogeneous Turbulent Shear Flow with a Uniform Mean Temperature Gradient," J. Fluid Mech. 104, 311-347 and 349-367.

Tennekes, H., and J. L. Lumley (1978), A First Course in Turbulence, 5th printing, MIT Press, Cambridge, Mass.

Townsend, A. A. (1976), The Structure of Turbulent Shear Flow,, Cambridge University Press, Cambridge.

Traugott, S. C. (1958), "Influence of Solid-Body Rotation on Screen-Produced Turbulence," NACA Technical Note 4135.

Tritton, D. J. (19891), "Comments on 'Effect of Anisotropy and Rotation on Turbulence Production,'" Phys. Fluids, 24, 1921-1922.

Tucker, H., and A. J. Reynolds (1968), "The Distortion of Turbulence by Irrotational Strain," J. Fluid Mech. 32, 657-673.

Uberoi, M. S., and S. Wallis (1966), "Small Axisymmetric Contraction of Grid Turbulence," J. Fluid Mech. 24, 539-543.

Wigeland, R. A., and H. M. Nagib (1978), "Grid-Generated Turbulence with and without Rotation about the Streamwise Direction," IIT Fluids and Heat Transfer Report R78-1.

Wilcox, D. C., and M. W. Rubesin (1980), "Progress in Turbulence Modeling for Complex Flow Fields, Including Effects of Compressibiity," NASA TP-1517.

End of Document